Remote Sensing of Localized Ion Acoustic Waves with Multistatic Passive Radar

Melissa G. Meyer

A dissertation submitted in partial fulfillment of
the requirements for the degree of

Doctor of Philosophy

University of Washington

2006

Program Authorized to Offer Degree: Electrical Engineering

University of Washington
Graduate School

This is to certify that I have examined this copy of a doctoral dissertation by

Melissa G. Meyer

and have found that it is complete and satisfactory in all respects,
and that any and all revisions required by the final
examining committee have been made.

Chair of the Supervisory Committee:

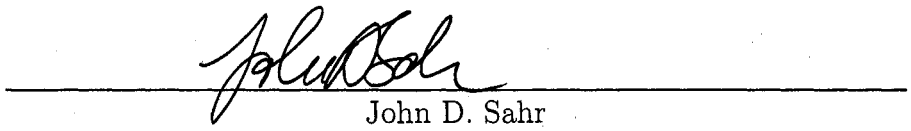

John D. Sahr

Reading Committee:

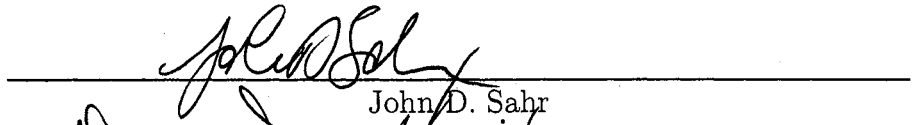

John D. Sahr

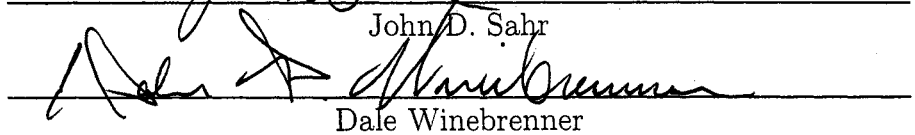

Dale Winebrenner

Brian Nelson

Date: 7 August 2006

In presenting this dissertation in partial fulfillment of the requirements for the doctoral degree at the University of Washington, I agree that the Library shall make its copies freely available for inspection. I further agree that extensive copying of this dissertation is allowable only for scholarly purposes, consistent with "fair use" as prescribed in the U.S. Copyright Law. Requests for copying or reproduction of this dissertation may be referred to Proquest Information and Learning, 300 North Zeeb Road, Ann Arbor, MI 48106-1346, 1-800-521-0600, to whom the author has granted "the right to reproduce and sell (a) copies of the manuscript in microform and/or (b) printed copies of the manuscript made from microform."

Signature 

Date 10 August 2006

University of Washington

Abstract

Remote Sensing of Localized Ion Acoustic Waves with Multistatic Passive Radar

Melissa G. Meyer

Chair of the Supervisory Committee:
Professor John D. Sahr
Electrical Engineering

Our goal is to contribute to the understanding of ionospheric E region physics by developing a linear fluid theory of E region plasma density irregularities as well as new experimental techniques for radar remote sensing of these irregularities.

We derive a new form of the Farley-Buneman (ionospheric two-stream) instability dispersion relation based on a model of perturbed quantities as spatially localized plane wave packets. The motivation for this work is (1) a desire to understand the instability behavior and resulting radar observations in a new theoretical framework that is "aware" of spatially-localized effects; (2) to investigate the coupling of energy into spatial Fourier components and propagation directions other than those of the instability waves themselves.

We also describe our development of a passive VHF radar used to observe plasma irregularities into a multistatic, distributed system capable of performing new experiments. The experiments we describe are "spatially diverse," are the first of their kind with passive radar, and provide an important proof of concept for other scientists in the aeronomy community who hope to implement large-scale versions of distributed, passive radio remote sensing instruments.

TABLE OF CONTENTS

LIST OF FIGURES

LIST OF TABLES

GLOSSARY / FREQUENTLY USED ACRONYMS

ACE: The Advanced Composition Explorer, a satellite measuring solar wind parameters.

CME: Coronal mass ejection: a violent explosion of material from the sun's surface, usually associated with a sunspot.

CW: Continuous wave. A continuous (non pulsed) transmission.

DASI: Distributed Arrays of Small Instruments. A new initiative in ground-based solar and space physics research.

EISCAT: The European Incoherent Scatter radar. A tristatic ISR system consisting of UHF and VHF transmit stations in Tromsø, Norway, plus receiving stations in Kiruna, Sweden, and Sodankylä, Finland. The ESR (EISCAT Svalbard Radar) is another UHF station, located in the Svalbard archipelago, added in 1994.

EWU: Eastern Washington University, where one of the MRR receivers is located.

FARLEY-BUNEMAN INSTABILITY: The ionospheric two-stream plasma instability, first described by Farley in 1963 and also Buneman.

FFT: Fast Fourier Transform. An efficient algorithm for computing the discrete Fourier transform of a time series.

FM: Frequency modulation. A scheme for encoding information into the instantaneous frequency of a carrier signal.

GPS: Global Positioning System.

IMF: Interplanetary Magnetic Field. The sun's magnetic field, carried outwards by the solar wind.

ISIS: Intercepted Signals for Ionospheric Science. A multistatic passive radar project headed by Dr. Frank Lind at MIT Haystack Observatory.

ISR: Incoherent Scatter Radar. A radar powerful enough to detect thermal fluctuations of ionospheric plasma.

MAGNETOSPHERE: The Earth's magnetic force field, and the particles and currents trapped within.

MAGNETOPAUSE: The edge, or boundary, of the magnetosphere.

MAGNETOSHEATH: An area of shocked solar wind flowing around the magnetosphere.

MATLAB: A commercial numerical computation and visualization software tool.

MHD: Magnetohydrodynamic; referring to the treatment of plasmas with the fluid equations.

MRO: Manastash Ridge Observatory, MRR's namesake and where its scatter-receiving antennas are located.

MRR: The Manastash Ridge Radar, designed and developed at the University of Washington.

NOAA: The National Oceanic and Atmospheric Administration.

PEDERSEN DRIFT: Charged particle drift due to an external electric field.

PLASMA: Charged (ionized) particles; called the fourth state of matter.

RX: Stands for "receiver."

SUPERDARN: The Super Dual Auroral Radar Network (originally just "DARN"). A network of HF radars in both the northern and southern polar regions which use observations of F-region plasma instabilities to map plasma convection in the polar caps.

TX: Stands for "transmitter."

UW: University of Washington, where this work was conducted, and where one of the MRR receivers is located.

ACKNOWLEDGMENTS

I wish to thank my committee members – John Sahr, Dale Winebrenner, Brian Nelson, Anthea Coster, and Anis Bawarshi – for their patience, enthusiasm, encouragement, and careful review of my work. John in particular has been a great inspiration, role model, and friend.

Frank Lind, Phil Erickson, John Foster, Rich Christie, Paul Crilly, Dennis Freeman, and J.-P. St.-Maurice provided extremely useful discussions and good company in general. To Gary Bust, Radha Poovendran, and also John S., Phil, and Anthea, who served as my professional references: you helped me get the job that made it necessary for me to finish this degree! Thank you... I think.

I would also like to thank: Chucai "Cliff" Zhou for showing me how to be a grad student; Andy Morabito and Zac Berkowitz for being fun fellow grad students; my best friends Andrew and Sarah Petersen, for boundless love and support; Steve Swanson and Spoon for 2 great years; and Lena and Adam for sharing a house and life in Seattle with me. Best wishes to you all.

My great appreciation goes to the UKC sea kayakers for excellent camaraderie and many memorable experiences; the Wavescalar group for cathartic foosball and ping pong sessions; my Dad, Mom, brother and sister for supporting me while I pursued this dream in the great Northwest, and also John and Bobbie Sahr, Bob and Michiko Petersen, and Frankye Jones and her husband Brock, who are like family to me. Last but not least, I would like to thank the Michigan Tech ECE faculty for hiring me even though I got their time zone wrong the first time through.

During my time in graduate school, I have made great progress in both figuring out who I want to be and in becoming that person. It is a lifelong process, but I am very pleased with how I have grown since my arrival here 5 years ago. I want to thank everyone for this opportunity, and for your friendship, which has influenced me so profoundly.

This material is based upon work supported by the National Science Foundation under Grant No. 0310233. I also thank NSF for 3 years of support through a Graduate Research Fellowship, Intel for 2 years of support through a Master's Award Program (IMAP) Fellowship, and the ARCS (Achievement Rewards for College Scientists) Foundation for additional support. I am grateful to F. J. Rich (Air Force Research Laboratory, Hanscom AFB, Massachusetts) for providing DMSP F13 satellite data.

DEDICATION

An Introduction to RADAR

As Shakespeare's apprentice might have written it

For John, the original sonnet lecturer

Inspired by Professor Sahr, I wrote
this radar lecture that's composed in verse.
I offer it to him for use, and note
with thanks that it was his idea first.

Dear class, listen to me while I reveal
to you the strange magic of skyborne waves
and how obscurity they ably peel
away, from how it is the world behaves.

Through soundless snow and howling wind they sail
along untouched; until such time they meet
an obstacle that blocks their forward trail.
Deflected from their path, the waves retreat.

Some scatter wildly; others go straight back.
The latter are the ones we use to track.

A system that can harness waves like this
is called a radar – that's an acronym.
Detecting target ranges is the gist –
and it still works when other lights grow dim.

How is it that we make this work, you ask?
It's not too hard, as you will find with time.
To understand the waves is our first task.
(What's tough is making words like 'radar' rhyme!)

They're not unusual, just radio –
electric and magnetic energy.
Like light, which surely you already know,
these waves provide another way to see.

Though typically, they're lower frequency.
But waves can come in many shapes – you'll see.

The basic concept is a game of catch:
we throw a wave of radio, then wait
for its return. We're looking for a match
in everything we snatch: the first wave's mate.

The distance waves traverse is meaningful.
We know how fast the radio can go,
so, round trip time from start to obstacle
plus rebound trip is what we need to know.

That's how we find reflecting things, and learn
their distance too. Sometimes we get confused
if several waves are in the air per turn.
So which one came from where? We need more clues.

The pitcher in this game of catch is called
a transmitter; receivers grab the ball.

So now, what types of things can radars see?
Well, aeroplanes, and tanks and trains; all kinds
of transportation means. Ships on the sea
and cars on streets, but that's not all we'll find.

A weather radar's eye sees snow and ice,
rains on parades, and warns of thunderstorms.
Still other radars map the planet. Slice
by slice they scan precisely all landforms.

We need to know of UFOs – in case ...
they come. And missile plumes, and planet moons,
the satellites we shouldn't lose, in space.
Remember shooting stars? We see those too.

Plus wind down-shears and in the atmosphere
up high, mysterious effects appear.

There's turbulence where different tides collide;
Aurora Borealis dance the skies;
and even the electrons cannot hide
activities from radar's watchful eyes.

So there you have it, Ladies, Gents; stay tuned.
This fascinating tale continues soon.
If you're like me, you'll love this stuff. I hope
I've whet your appetite. Did you take notes?

I wrote this poem for you, Dear John, to show
my gratitude for all the things you did.
You taught me everything I need to know,
but most importantly, you are my friend.

At all those times when physics hurt my head
how fun it was to play with words instead.

Melissa Meyer
UW EE Ph.D. student
2001–2006

Chapter 1

INTRODUCTION

The motivation for this work is two-fold: advancing the state of the art in remote sensing technology and conducting fundamental research on the Earth's ionosphere and its coupling to the space environment. We can best describe the field of this research as radio science: an engaging area of study in which innovative technology development is driven by scientific inquiry. We use radio science to study localized plasma instabilities in the ionosphere, and compare experimental observations with the predictions of fluid theory.

1.1 The Radar Aurora

Studies of this particular type began as investigations of the "radar aurora," an unexplained significant backscatter of radio energy from the high latitude and equatorial regions of the ionosphere. The radar aurora obtained its name through its strong correlation with the visual aurora, driven by field-aligned currents dissipating energy as heat in the upper atmosphere.

The physical explanation for the radar aurora - plasma density irregularities caused by a streaming instability in the E region - was first described for the equatorial electrojet by Farley with kinetic theory [23]. Farley's theory led to decades of experimental and theoretical effort to determine the behavior of the instability and the properties of the resulting coherent radar backscatter.

Over the years several "features" have been added to the fluid theory of the ionospheric/modified two-stream instability (also called the Farley-Buneman instability, after the first two authors to describe it). Many of these additions to the theory have been in response to a need to explain experimental observations. We will discuss the background of the fluid theory in Chapter 4 of this dissertation, and also propose our own modest extension in Chapter 5.

The E region of the ionosphere - the stage for our study of plasma behavior - covers the altitudes of about 90–180 km. A very small fraction of the particles in the E region are ionized by energetic photons from the sun during daylight hours; the region (insofar as it is defined as an ionized layer) largely vanishes at night. A key characteristic of the E region plasma is the fact that electrons are magnetized by the Earth's magnetic field, while the ions are dominated by collisions with neutral particles. This discrepancy between the behaviors of oppositely charged particles can destabilize the plasma, with interesting results.

1.1.1 Radar Observations of Ionospheric Irregularities

Besides being simply interesting physical phenomena, plasma disturbances have an important practical significance as they can severely disrupt trans-ionospheric communications (such as GPS signals and satellite-relayed media). Remote sensing is the only feasible way to routinely experimentally study the evolution and effects of these disturbances: the relevant altitude (approximately 100 km) is too high for weather balloons and too low for satellites; rockets are too costly to use regularly.

It has been over four decades since Farley explained the radar aurora in 1963. Since then, many radar experiments have been conducted, and several of these radars are still operating today. Common subjects of experimental studies of the radar aurora include the interpretation of Doppler spectra; scattering cross section estimates for

the density irregularities; the effects of radar observation geometry and magnetic field geometry on observations and spectra of the irregularities; and the effects of different transmitter frequencies on the backscatter intensity and Doppler spectra of the irregularities (*i. e.*, studies of the irregularity k-spectrum).

In his introduction to E-region coherent backscatter studies, Schlegel [113] outlined a critical challenge in interpreting radar scatter from auroral electrojet plasma irregularities: there is no satisfying plasma physics forward model which provides detailed Doppler spectra. This stands in sharp contrast to the case for incoherent scatter from thermal plasma populations, for which a detailed theory exists [7]. In the former case, the plasma is evidently in a turbulent state, with nonlinear dynamics playing a substantial role in the evolution of the plasma; in the latter case the plasma is in near thermal equilibrium, with linear dynamics and dissipation leading to an adequate description.

Therefore, much of our knowledge of auroral electrojet irregularities arises from essentially phenomenological studies of radar backscatter observations, which are sometimes supplemented with *in situ* measurements of plasma parameters and structures, such as in the ERRRIS campaign [97]. Several studies have been conducted with coherent scatter radars in which a large number of irregularity observations are characterized by their Doppler moments and analyzed statistically [115, 129, 49, 21, 36, 77]. The type 1 and 2 nomenclature for irregularity classification originated from frequently occurring Doppler features in studies (originally equatorial, then later auroral) such as these [39]. Much effort has been made to associate the "irregularity types" and their Doppler spectral features with physical phenomena and plasma instability mechanisms. While theoretical progress continues, more experimental observations of ionospheric plasma density irregularities can only help to develop our understanding of them. A brief review of E region VHF Doppler statistical studies, as well as the

first contribution of this kind from a passive radar, are given by Meyer *et al.* [75].

Several excellent, complete reviews of both experimental and theoretical work done on ionospheric plasma density irregularities have been made in the past couple decades by Fejer and Kelley [26], Haldoupis [39], and Sahr and Fejer [109]. A very thorough description of the field's beginnings, starting with the first observations by Eckersley in 1937 and continuing into the 1990s, is given by Lind in his Ph.D. dissertation [72].

1.2 The University of Washington Passive Radar

Over the past decade, the author's research group at the University of Washington (UW) has designed and built a distributed passive radar system for observing and studying ionospheric plasma instabilities. Our radar takes advantage of existing RF energy in the environment to illuminate targets and monitors the scattered electromagnetic waves with three spatially distributed receivers. The result is a high quality (virtually ambiguity-free), inexpensive surveillance tool, useful in atmospheric physics as well as other applications. Until recently, this passive radar was the only one of its kind in the world. In Chapter 3, we describe the UW passive radar in detail.

1.3 Project Goals and Organization

A challenging but satisfying aspect of this research is its multidisciplinary nature. We have developed technology as well as scientific experiments. We also contribute some new plasma physics theory. The thought processes required to develop these different bodies of work can be substantially different, and our goals for the different research topics, though complimentary, are separate.

Our primary engineering goals in this project are to develop a passive, coherent, multistatic radar as a new scientific instrument; demonstrate the capabilities of such an instrument for geophysical studies and surveillance in general; identify system

configurations and operational requirements for different applications; and design new experiments for multistatic passive radar. As a space science experimentalist, our goals are to design appropriate instruments and experiments to take advantage of new technologies; offer the theorists in the field observations with better resolution, less ambiguity, and more kinds of information; and support the next-generation ionosphere and space weather models by providing more continuous data with longer temporal coverage and larger spatial coverage. Of course, we also interpret our own data and attempt to contribute to the understanding of ionospheric processes and plasma instabilities.

The dissertation is organized as follows. Chapters 2 and 3 provide background information about the two broad disciplines we address in this work: space plasma physics and passive radar technology. In Chapter 4, we present a linear fluid theory and brief summary of the characteristics of the Farley-Buneman ionospheric two-stream instability. We propose and explore a simple modification of the linear fluid theory – a spatially-limited disturbance model – in Chapter 5. Chapter 6 introduces our experimental contributions with an additional passive radar receiver, making the UW radar multistatic; Chapter 7 discusses actual results from several experiments we performed with the new system. Finally, Chapter 8 concludes the dissertation. We relegate the details of some derivations presented in the text to Appendix A.

Chapter 2

THE EARTH'S IONOSPHERE AND SPACE ENVIRONMENT

Until being introduced to the rich and complex study of space plasma physics, one might be inclined to imagine the Earth as a ball of rock, surrounded by a thin layer of gas, revolving about a similarly bounded star in the vacuum of space.

In fact, the Earth is positioned within the atmosphere of the sun (the solar corona) and is subject to a wide variety of "space weather" in addition to being merely warmed by the sun's electromagnetic rays from a distance of 1 astronomical unit (1.5×10^{11} m). Most of the time, space weather effects are delivered by the solar wind, which boils continuously off the sun in all directions. The solar wind is a magnetized plasma composed primarily of protons (H^+), alpha particles (He^{++}), and accompanying electrons [95]; these charged particles carry the solar magnetic field with them into the solar system, where it is renamed the interplanetary magnetic field (IMF). The Earth, with its own magnetic field, presents an obstacle to the solar wind and IMF, which are normally supersonic ($\approx$400 km/sec). Thus begin many fascinating sun-Earth interactions which are noticed by humans in many forms, including beautiful lights in the sky, disruptions in communication technology, and disturbances in power distribution; the effects of these interactions are measured and studied with telescopes, satellites, magnetometers, radars, and many other scientific instruments.

2.1 *Magnetosphere Gross Structure*

The outermost feature of the Earth's immediate space environment is its bow shock, in which the collisionless, supersonic (and superalfvénic) solar wind reacts to the obstacle of the Earth's magnetic field. The bow shock is located where the solar wind pressure and terrestrial magnetic field pressure are balanced:

$$v_{\mathrm{sw}}^2 nm + B_{\mathrm{sw}}^2/2\mu_0 = B_{\mathrm{Earth}}^2/2\mu_0 \tag{2.1}$$

(Plasma thermal pressure is very low just within the magnetopause.) The solar wind flow is compressed, heated, and slowed so that it can be deflected around the Earth's magnetosphere (essentially Earth's force field against energetic particle beams: not just for Trekkies); the area of shocked solar wind is called the magnetosheath [61].

The geomagnetic field structure is essentially a dipole, with $\mathbf{B}$ outside the Earth directed northward; it is believed to be generated by dynamo action due to liquid metal convection in the Earth's core. The magnetic dipole shape of the magnetosphere is deformed by the constant pressure from the solar wind, as shown in Figure 2.1: it is compressed on the dayside and stretched into a tail on the nightside. The outer- and inner-most magnetic field lines map to different latitudes on the Earth's surface. The inner field lines (up to 3–5 Earth radii ($R_E \approx 6375$ km) out, except in the sunward direction, where the magnetic field is highly compressed due to solar wind pressure) maintain their approximate dipole shape and map to the lower and mid-latitudes (approximately $0 - 60°$ latitude). The outer field lines are most affected by solar "weather," are deformed in shape, and correspond to areas of visible activity in the high latitude upper atmosphere – most notably, the aurora. Finally, the polar cap field lines, from 70–75 degrees latitude and north/southward, are "open" field lines: one end is anchored to the Earth while the other end has connected to the IMF in the solar wind. The process by which two separate magnetic fields – in this

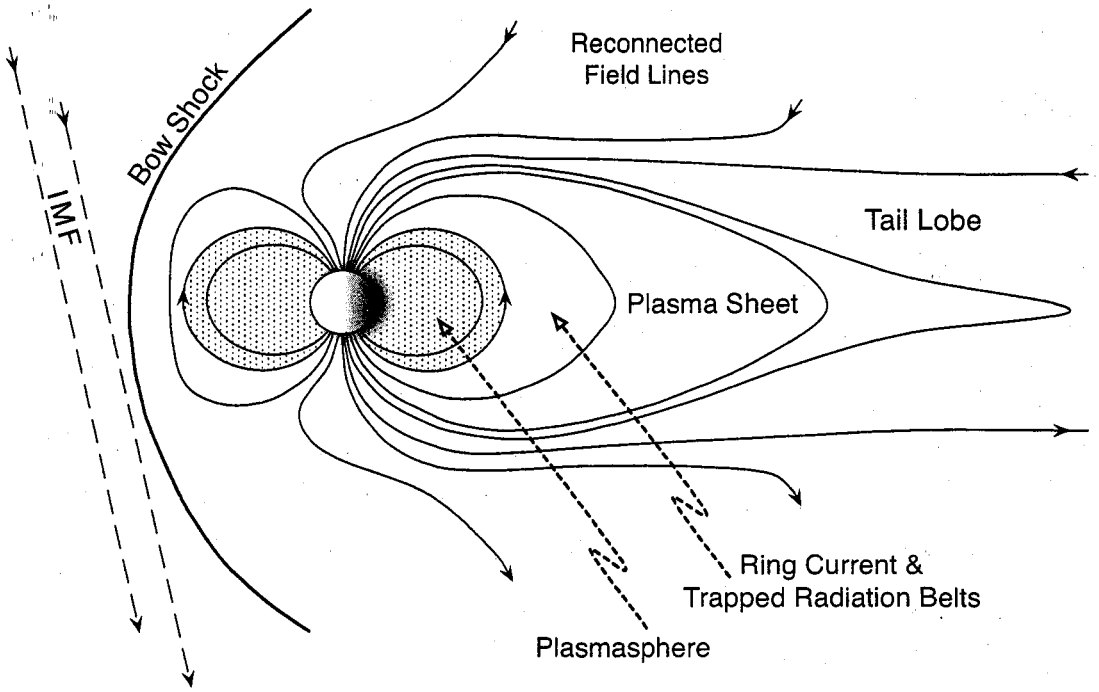

Figure 2.1: A cartoon illustration of the Earth's magnetosphere, shown here in a noon-midnight meridian view, with the sun to the left. The IMF is the interplanetary magnetic field, shown here arriving at Earth with a southward orientation.

case, the IMF, ultimately anchored to the sun, and the terrestrial field – can become mixed is called reconnection. Magnetic reconnection is a fascinating and complicated theory whose details have not yet been altogether ironed out [99]. A discussion of reconnection is beyond the scope of this work; however, it is an integral part of a readily understandable model of the dynamic magnetosphere, which we present here in a "handwaving" sense.

2.1.1 Magnetospheric Convection

It is convenient to describe magnetospheric geometry and behavior in terms of magnetic field lines, but a more rigorous physical explanation deals with the motion of the plasma itself. However, due to the collisionless, high-conductivity nature of space plasmas, a "frozen-in flux" assumption can be made in MHD (fluid) treatment, in which the total magnetic flux crossing a defined surface in the plasma fluid remains constant [61]. Therefore, we are able to describe magnetic field lines as if they move, loaded with plasma, through the system themselves.

Space scientists hypothesize that magnetic reconnection occurs at the sunward-facing magnetopause, when the interplanetary magnetic field, carried by the solar wind, is driven against the Earth's (or another planet's) magnetosphere. The outermost field lines, which map to Earth's highest latitudes, are the first to be affected. Some of the IMF field lines slip around the magnetosphere intact. However, others "reconnect," forming hybrid field lines which have one end connected to the Earth (at either the north or south polar cap) and the other flowing with the solar wind past the Earth (*cf.* Figure 2.1). Both the terrestrial field and the IMF lines are loaded with plasma (sometimes called flux tubes), so plasma is convected across the polar caps, and this results in a Hall-effect electric field, oriented in the dawn-dusk direction. Also, because of the reconnected field lines, this process is an important mechanism

by which solar material enters the Earth's magnetosphere.

On the nightside, the reconnected field lines are carried past the Earth in the solar wind flow, stretching the magnetosphere into a long tail behind Earth. Eventually, magnetic tension brings oppositely directed hybrid field lines from the north and south together, and reconnection occurs again, resulting in an unbroken interplanetary field that can continue through the solar system and a whole terrestrial field line that can relax toward the Earth.

Dungey proposed this model for magnetospheric "convection" in 1961 [20]. The general ideas are widely accepted in the space science community because they can self-consistently account for many phenomena observed on the Earth, such as the aurora. For example, when the reconnected, loaded field lines in the geomagnetic tail snap back, they catapult plasma (some of it originally from the solar wind) toward the Earth. Some of this plasma precipitates when it reaches the ionosphere (via bounce motion along the reconnected field line). We see the energy it deposits there as the colorful display of excited electrons losing energy levels, known as the Northern (Southern) Lights, or Aurora Borealis (Australis). Thus, the auroral oval latitudes specify the outermost closed terrestrial field lines.

2.1.2 Interaction with Solar and Space Weather

The orientation of the IMF (particularly the north-south component, which is either parallel or antiparallel to the Earth's field) strongly influences the magnetospheric convection process. If the IMF is oriented in a southward direction (i.e., opposite that of Earth's field), reconnection, and the number of open field lines, are enhanced and the auroral ovals expand equatorward. However, when the IMF points northward, the resulting convection patterns are more complex, the magnetosphere is "closed" (more impervious to solar particles), and the auroral ovals are smaller and less intense

[95].

Due to the approximate north-south symmetry of the dipole-shaped terrestrial magnetic field, magnetospheric behavior in the northern hemisphere is mirrored in the southern hemisphere. To first order, we expect geomagnetic effects to occur on both the north and south ends of field lines, and magnetic conjugate point studies are popular with ground-based experimentation. For example, Chisham *et al.* used conjugate SuperDARN radar observations to study the magnetic reconnection mechanism at magnetic local noon by comparing differences between the northern and southern ionospheric convection responses to changes in IMF direction [15].

So far we have described magnetospheric convection as if it were always in a steady state, but actually the entire system is quite dynamic, continually responding to transient changes in the solar wind and other space weather effects, such as coronal mass ejections (CMEs). An increase in solar wind pressure (which may come as enhanced speed, density, temperature, or magnetic flux density, or combinations of the above – *cf.* equation 2.1) can temporarily increase the auroral oval width, decreasing the polar cap area [10].

A combination of southward IMF and increased solar wind pressure causes a sudden increase in energy flow from the solar wind into the Earth system. The resulting sequence of reactions is called a magnetospheric substorm [61]. Substorms have many features that can be observed on the Earth's surface, including more intense auroras which occur at lower latitudes, and strong magnetic disturbances, which can be measured by ground-based magnetometers, due to electric currents flowing in the upper atmosphere. When substorm conditions last for days, the ensuing geomagnetic activity is known as a magnetic storm.

During this work we monitored the solar wind conditions closely (using real-time solar wind reporting from the ACE satellite [120] and Kp predictions and the Space

Weather Forecast from NOAA's Space Environment Center) in hopes of always detecting the onset of magnetic substorms and storms. Operating a radar with a field of view between 50° and 55° latitude, yet with the purpose of observing high latitude, aurora-related phenomena, means that we must be prepared to observe whenever Nature is ready to show us interesting things. (The undisturbed auroral oval typically lies between 60° to 70° latitude [61].)

"Inclement" space weather is interesting from a scientific point of view, but it can also be hazardous to modern civilization on Earth, which is one practical reason to learn to understand and possibly predict it. Showers of energetic particles associated with CMEs and magnetospheric storms are dangerous to both astronauts and equipment in orbit. Satellites have been lost during magnetic storms, costing billions of dollars and inconveniences in the form of disrupted communications on Earth [64]. Further, the ionosphere becomes a very noisy channel to electromagnetic signals travelling through it during "interesting" space weather; this can destroy reliability in satellite data products (notably GPS positioning), and confuse radio astronomy observations. The huge currents (millions of amperes) that flow in the ionosphere and around the Earth are noticeable to sensitive magnetic instruments and can cause problems in power distribution systems through magnetic coupling with power lines.

2.1.3 Current Systems in the Magnetosphere

Many current systems exist in the magnetosphere, caused by the complex interactions of different plasma populations and magnetic fields. For example, current sheets must exist at boundaries between regions of oppositely directed magnetic fields. Such boundaries include Earth's magnetopause (the boundary between the terrestrial field and the solar wind / IMF, associated with the Chapman-Ferraro current [61]); the low latitude region of the geomagnetic tail (the boundary between the northern and

southern lobes of the drawn-out nightside geomagnetic field); and a similar boundary near the sun's ecliptic plane, which results in an interplanetary current sheet that looks like a ballerina's tutu [83, 95].

Currents must also flow when potential differences arise between different regions of space. Electric fields can appear due to the Lorentz force and "guiding center" particle motions which act oppositely on particles with different charge, as in the ring current [61]; the Hall-effect, which causes the dawn-dusk potential at the polar caps; and gradients in conductivity, which are more common in the ionosphere where particle densities are much higher. Figure 2.2 illustrates several of these major current systems.

All of the currents maintain equilibrium in the magnetosphere by reacting to space weather, transferring energy between physical systems, and eventually dissipating excess energy dumped into the Earth system by solar weather effects. The ionosphere, Earth's highest, partially ionized atmospheric layer, plays an important role as a "resistor" for this gigantic magnetospheric circuit. Field-aligned currents flowing around the Earth close in the ionosphere. The aurora are just one sign of the massive amount of energy that is dissipated as energized magnetospheric particles collide with the cold, dense atmospheric plasma co-rotating with the Earth.

2.2 Ionospheric Structure

The Earth, in addition to capturing some of the solar wind particles in its magnetic net, has its own plasma population, which resides in the upper layer of the atmosphere, starting at about 80 km and extending upward. This layer is aptly named the ionosphere. The ionospheric plasma is made up of atmospheric particles that have been ionized, mostly through photoionization by solar energy (the sun's radiation arrives at Earth with a power density of 1.4 kW per square meter [60]). Ionization

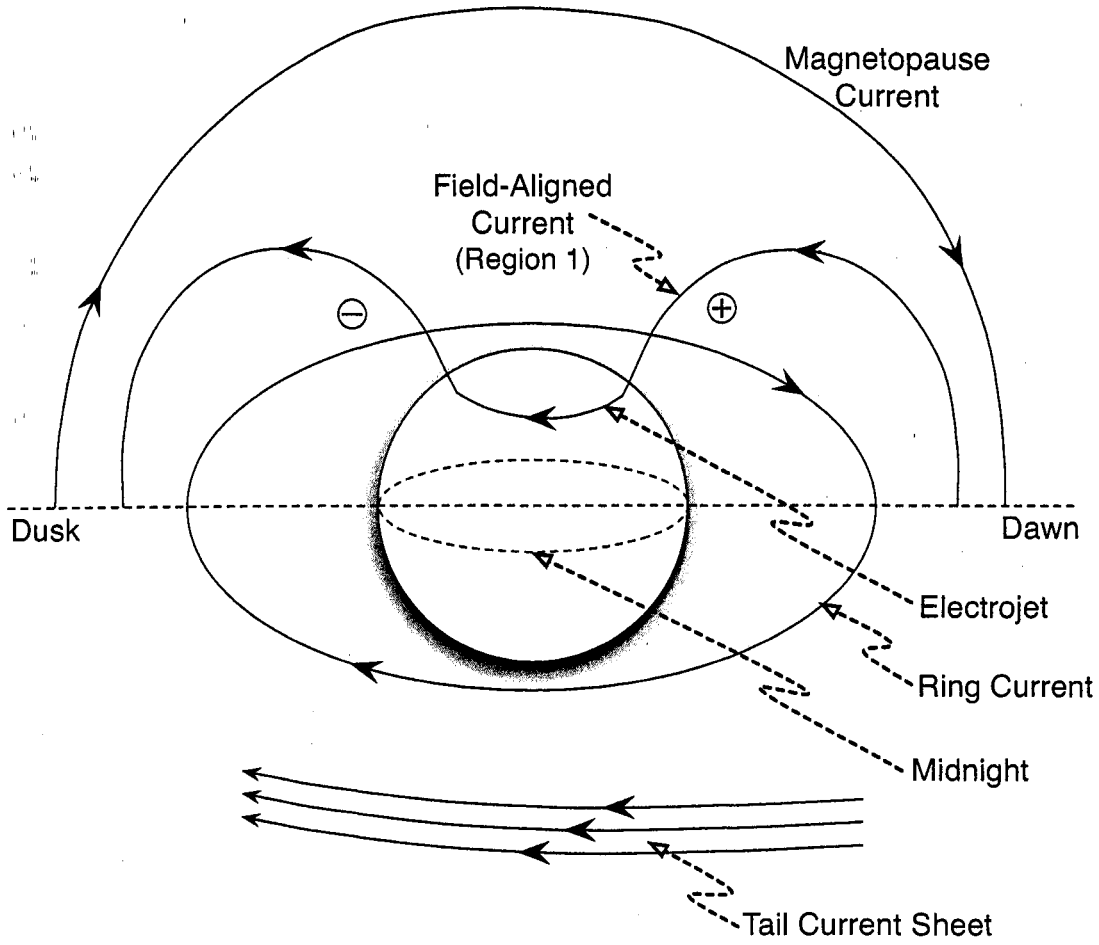

Figure 2.2: A cartoon illustration of major current systems in the Earth's magnetosphere. The Earth is shown from the nightside. The dawn-dusk electric field, due to magnetospheric convection, is indicated with positive and negative charge symbols. The electrojets in the ionosphere close field-aligned currents, causing both the aurora as well as plasma density irregularities visible to radar.

Table 2.1: A comparison of typical parameters for different types of plasmas: electron temperature, density, magnetic flux density strength, collision frequency, debye length, plasma parameter, and plasma beta. The ionosphere values are accurate for nighttime at high latitude and an altitude of 100 km. The solar wind values are accurate for a distance of 1 AU.

Plasma	T (°K)	n (cm^{-3})	B (nT)	ν (s^{-1})	λ_D (cm)	parameter	β
Ionosphere	230	2×10^3	48,000	2×10^4	2	2×10^4	10^{-8}
Solar wind	10^5	10	5	10^{-4}	700	3×10^9	3
Tokamak	10^8	10^{14}	10^{10}	4×10^4	7×10^{-3}	3×10^7	0.007

may also occur through collisions with other particles or cosmic rays. The percentage of particles that are ionized is actually rather low (up to 3% at high altitudes; as low as 10^{-7}% at altitudes of about 100 km) [60]; however, the relatively small population of charged particles can have profound effects on electromagnetic waves traveling through the ionosphere.

The ionospheric plasma is usually characterized as cold, dense, collisional, and low-beta (dominated by magnetic, as opposed to thermal, pressure). For reference, in Table 2.1 we compare typical parameters for plasmas in the nighttime E region ionosphere, the solar wind at 1 AU, and a tokamak fusion reactor [11, 95, 119, 9, 14]. The parameters we compare are: electron temperature, density, magnetic flux density strength, collision frequency, debye length, plasma parameter (number of particles in a debye cube), and plasma beta (ratio of plasma thermal pressure to magnetic pressure).

2.2.1 Vertical Structure

The Earth's atmospheric density changes exponentially with altitude; its scale height is approximately 8 km (*i. e.*, the density is reduced by a factor of e^{-1} over an altitude

increase of 8 km). Other important ionospheric parameters change with altitude as well, changing the physical behavior of the plasma at different altitudes. For example, with increasing height, particle collisions become less frequent; temperature, thermal speeds, and the acoustic speed increase; magnetic field strength slightly decreases; and the ion composition changes.

The ionosphere is divided into three major altitude layers, called the D, E, and F regions (sometimes the F layer is subdivided into F1 and F2). The E region (formerly the Heaviside layer) was named first in 1924 by Appleton, "E" for the radio electric fields that it reflects [101]. The F and D regions, above and below the E region, respectively, were named next. These three ionospheric regions, while lacking precise boundaries, each have distinguishing features and characteristic physical behavior.

The F region, at approximately 180 km and up, is composed mainly of atomic ions, with O^+ being the dominant species below about 1000 km, and H^+ more prevalent above that [72]. Atmospheric density has thinned significantly by 180 km, and this combined with the light atomic ions makes the F region plasma collisionless (*i. e.*, particle gyrofrequencies are much greater than collision frequencies). The E region is a transition region, in which the light electrons are still collisionless, but the much heavier ions are now dominated by collisions. Most of the ions in the E region are molecular, with O_2^+ (molecular weight of 32 u) and NO^+ (30 u) being approximately equally represented. The E region is usually said to extend from 90 km altitude up to 180 km. This is the layer to which we will direct most of our attention. Finally, the D region, below 90 km, is the lowest, and also has the lowest ionization density. Both positive and negative ions (mostly molecular) can be found. Due to the higher neutral density, both ions and electrons are dominated by collisions [60].

At nighttime, photoionization pauses until the next sunrise, and recombination processes steadily lower the ionosphere's plasma density. However, molecular and

atomic ions undergo different recombination processes. Dissociative recombination, which involves molecular ions, is a much faster ionization loss mechanism than radiative recombination, the equivalent process for atomic ions. Thus, the lower-altitude D and E regions normally disappear completely overnight (with the exception of the so-called sporadic E layers, which are narrow, intermittent layers of plasma formed of metal ions from meteor ablation [38]). The F region plasma, on the other hand, is not significantly depleted.

In Table 2.2, we summarize useful parameters for nighttime, E region ionospheric plasma for several altitudes [111, 119, 60, 72]. For further reference, the International Reference Ionosphere (IRI) model can be used to create plots of many parameters versus altitude [8].

2.2.2 Latitudinal Structure

Since the ionospheric plasma consists of charged particles, its behavior is strongly influenced by the Earth's magnetic field. The geomagnetic field, as we discussed above, has a complex structure, and latitudes on Earth map to different regions of the magnetosphere along magnetic field lines. Furthermore, while gravity organizes the atmosphere in a radially stratified fashion that is roughly similar over the entire Earth's surface, the magnetic field geometry changes with respect to the vertical atmospheric structure depending on latitude. For example, at the equator, the magnetic field and atmospheric density gradient are perpendicular to each other. At much higher latitudes, they are roughly parallel (northern hemisphere) or antiparallel (southern hemisphere). This leads to substantially different ionospheric behavior at different latitudes. Normally, studies of the ionosphere are divided into two major groups: low latitude / equatorial, and high latitude / auroral. However, more specific distinctions can be made. Figure 2.3 illustrates the major latitudinal zones of the

Table 2.2: Ionospheric parameters appropriate for the nighttime high latitude E region, given for several altitudes.

Parameter	90 km	100 km	120 km	150 km	units
density					
neutral (n_0)	4×10^{13}	6×10^{12}	6×10^{11}	8×10^{10}	cm^{-3}
electron (n_e)	630	2.0×10^3	1.3×10^3	1.1×10^3	cm^{-3}
collision frequency					
electron (ν_e)	3×10^5	7×10^4	4×10^3	2×10^3	s^{-1}
ion (ν_i)	3×10^4	5×10^3	2×10^2	50	s^{-1}
cyclotron frequency					
electron (Ω_e)	10^7	10^7	10^7	10^7	rad/sec
ion (Ω_i)	150	170	200	220	rad/sec
temperature					
neutral (T_n)	180	200	340	800	K
electron (T_e)	180	290	400	800	K
ion (T_i)	190	240	840	890	K
thermal speed					
electron ($v_{\mathrm{Th,e}}$)	55	62	78	110	km/s
ion ($v_{\mathrm{Th,i}}$)	230	250	330	420	m/s
ion acoustic speed (c_s)	360	440	630	770	m/s
mean free path					
electron ($v_{\mathrm{Th,e}}$)	30	80	800	5500	cm
ion ($v_{\mathrm{Th,i}}$)	1	5	70	800	cm

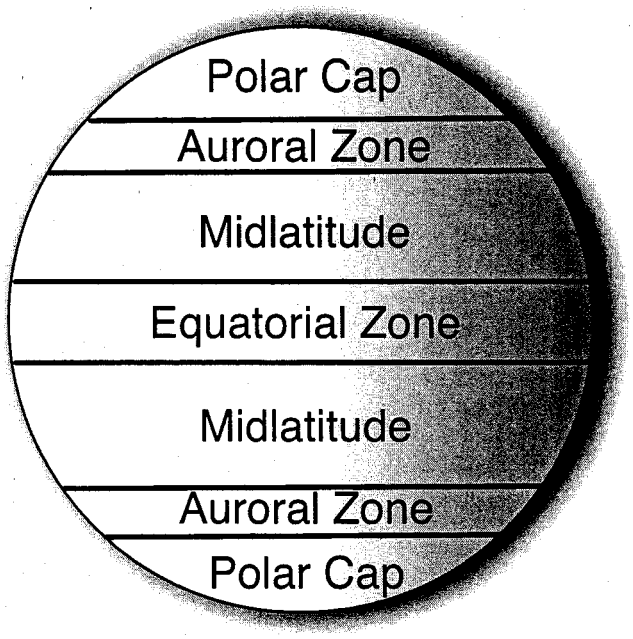

Figure 2.3: The major latitudinal zones of the Earth, corresponding to regions of similar magnetic field geometry. The auroral zones typically lie between 60° – 70° geodetic latitude.

Earth. The polar caps are regions in which the magnetic field lines are "open," or connected to the solar wind. The auroral zone, a region of energetic particle precipitation on recently reconnected field lines, is typically around 60° – 70° geodetic latitude [95]. In this study, due to the location of our coherent scatter radar, we will be mostly interested in high- and mid-latitude phenomena.

2.3 Midlatitude Magnetosphere-Ionosphere Coupling

The conditions to which field lines are exposed in space (possibly hundreds of Earth radii out) are strongly coupled to upper atmospheric behavior at the Earth itself. We are particularly interested in ionospheric behavior in the midlatitude region (approx-

imately 30–60° geographic latitude), because this is the area in which the MRR is sensitive to plasma behavior.

At midlatitudes, increasing altitudes map first through the outer plasmasphere and then into the tail lobes, which are magnetospheric regions of very low density that lie (on the nightside) between the magnetopause and the current sheet in the geomagnetic tail (*cf.* Figure 2.1). The tail lobes, with densities generally less than 0.1 cm^{-3} [61], are probably the highest vacuum anywhere in the solar system (excepting similar features on other planets with magnetospheres, such as Jupiter). Thus, GPS-measured total electron content (TEC)[1] at midlatitude is quite low compared to other areas, and the low-TEC region is called the "midlatitude trough." The low-latitude boundary of the auroral precipitation region marks the poleward edge of the midlatitude trough; on the equatorward boundary are the closed field lines which bound the plasmasphere – a bulge of dense ($n \approx 10^3$ cm^{-3}), cold[2] ($T \approx 1$ eV), co-rotating plasma centered about Earth's equator [61]. This large population of plasma is subject to significant perturbations in density when electric fields are applied, for example, during magnetic storms. Some of the plasmasphere can be redistributed to other regions as storm-enhanced density (SED) during disturbed geomagnetic conditions [13, 29].

2.3.1 The Sub-Auroral Polarization Stream

An important, relatively new model that explains northward electric fields, deep density troughs, and large-scale westward plasma drifts in the midlatitude, northern hemisphere ionosphere may also explain many of the plasma irregularity observations that the MRR (with sub-auroral field of view) has made. These effects are part of

[1]The GPS satellite orbit altitudes are 20200 km; thus, TEC is integrated plasma density from the Earth's surface out to about 4 R_E.

[2]The plasmasphere plasma is cold relative to other particles in the magnetosphere and solar wind. Ionospheric plasma is typically even less energetic. One electron volt (eV) is approximately 11000 Kelvin.

a positive feedback process and have been collectively named SAPS, for the Sub-Auroral Polarization Stream [35]. The SAPS behavior, characteristics, and causes are currently being studied extensively by the Millstone Hill Radar group [31, 32].

The feedback instability begins when current is driven, by external effects (*i. e.* storm conditions), through a midlatitude ionospheric region of low density (and therefore low conductivity). The electric field must intensify to maintain the current despite the low conductivity of the region. This heats the existing plasma, encouraging recombination and further reducing the density and conductivity in the region. In turn, the electric field must become stronger, feeding the instability mechanism.

The resulting observable effects are an enhanced, northward-pointing electric field and corresponding enhanced plasma drift in the sunward ($\mathbf{E}\times\mathbf{B}$) direction. The SAPS is the electric field, which occurs at F region heights, but can map down along field lines to the E region. Incoherent scatter radars can measure the sunward plasma drift associated with the SAPS, and coherent scatter radars can detect the plasma density irregularities which occur in regions with elevated electric field strength. We can detect the SAPS signatures of depleted density and enhanced sunward drift [35] with instruments onboard satellites in low Earth orbits. We present MRR observations of a SAPS event along with supporting satellite data in Chapter 7, Section 7.2.2.

Chapter 3

PASSIVE RADAR AND ITS GEOPHYSICAL APPLICATIONS

Systems which passively observe pre-existing illumination for scientific study or surveillance purposes have been in use for many years. Almost any signal imaginable can be used for passive remote sensing. Our eyes passively sense reflections and absorption of ambient light to determine the locations and characteristics of objects around us. Scientists have used whale song to perform ocean acoustic tomography [16]; lightning strikes to detect whistler waves[1] in the magnetosphere [59]; and vice versa (whistlers in spectrograms measured by *Voyager 1* indicate lightning in the Jovian atmosphere [112]).

Electromagnetic communications signals of all kinds can be made to serve double duty as illumination for radar applications. Recently, Howland used television broadcasts for aerospace tracking applications [52]; Lockheed Martin Corporation developed Silent Sentry^{TM}, a portable, passive surveillance system that relies on commercial FM radio stations [68]; Roke Manor Research Ltd created Celldar^{TM}, which exploits ubiquitous cellular phone signals for short-range, high resolution applications; Beley *et al.* used HF radio signals to study traveling ionospheric disturbances [6]; and Koch and Westphal have investigated the use of GPS satellite signals for air-defense radar [63], to name a few examples.

At the University of Washington, Sahr and Lind built the first bistatic passive

[1] electromagnetic waves which propagate parallel to magnetic field lines and which can have a resonance with gyrating electrons [61]

radar in the world [110]. Like the Lockheed Martin system, the UW passive radar detects the scatter of commercial FM radio broadcasts (near 100 MHz). Its primary purpose is to observe ionospheric plasma density irregularities [110, 71]. In the next section (3.1), we describe this radar in detail.

3.1 The Manastash Ridge Radar

The University of Washington radar, named the Manastash Ridge Radar (MRR) for the location of one of its receivers, is the first passive remote sensing instrument to provide range and power spectrum estimation in scattering studies of the ionosphere. We can also use it to detect aircraft and scatter from meteor trails. Sahr and Lind first described the MRR in 1997 [110]; it is designed to utilize commercial FM radio transmitters, since these are widely available, and provide a useful carrier frequency for the study of ionospheric plasma.

The MRR achieved first light from radio aurora in the summer of 1998 [71]. This was a happy occasion, since it has a field of view in the subauroral zone (approximately $56 - 63°$ geomagnetic latitude), and it was believed then that the auroral oval would have to expand far enough equatorward to dip into the MRR field of view for any "radar aurora" to be detected. (The field of view, over a region of Southwestern Canada, can be seen in Figure 3.1.) Now we realize that plasma irregularities can arise in the MRR view volume due to effects other than auroral precipitation and convection, and over the past 3 years the MRR has acquired quite an impressive number of "auroral" observations, considering its latitude.

The scattering mechanism by which coherent radars detect plasma features is Bragg scattering. An approximate conceptual explanation for Bragg scatter (with our ionospheric bias) is: enhancements (or rarefactions) of plasma density cause changes in index of refraction which can reflect electromagnetic waves, and density structures

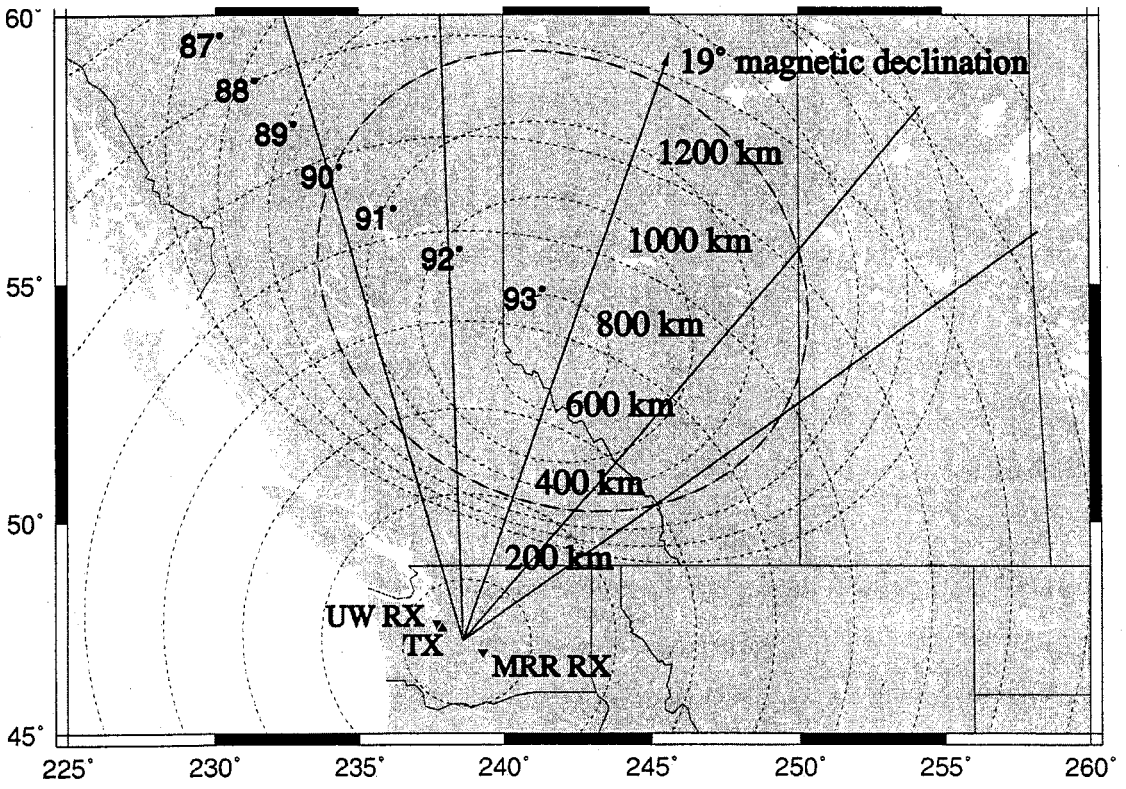

Figure 3.1: The MRR field of view with contours of constant range and magnetic aspect angle (near perpendicular) overlayed. The left and bottom edges show geographic latitude (north) and longitude (east). The locations of two receivers and one commercial transmitter are also shown.

can cause multiple small reflections to add coherently if they are of the appropriate wavelength (one half the wavelength of the incoming transmitter wave). Therefore, coherent radars receive scatter only from a particular spatial frequency component of the medium (structures of scale size near one half the transmitter wavelength). The MRR, at FM band frequencies of approximately 100 MHz, detects scatter from 1.5 meter-scale plasma density structures.

To operate the MRR, we record copies of signals broadcast by FM stations as well as the same signals after they have scattered back from interacting with targets. Since the radar is composed entirely of receivers, it is a passive system; it has been one of the first passive radars in the public domain and the first to be used for geophysical research. Rather than attempt to distinguish the direct-path and scattered signals, which may differ in power by as much as 100 dB, in a single receiver, we use separate receivers: one near the transmitter to provide the reference signal, and another located approximately 150 km away, behind the Cascade Mountains of Washington State, so that it is primarily exposed only to the scattered signal. This topology drastically reduces the dynamic range required of the receivers. Therefore, the system is inherently multistatic. The original reference receiver for the MRR is located in Seattle, Washington, while the scatter receiver is located at the Manastash Ridge Observatory (MRO) on Manastash Ridge, the radar's (and observatory's) namesake. The MRO is located at an elevation of approximately 1.2 km.

To recover the time series of the scattering target, we correlate the scattered signal with the reference FM signal (a matched filtering operation). We also perform a coherent integration before using common FFT analysis on the target time series. The usual MRR data product is the radar "cross-ambiguity," which, like self-ambiguity [70], shows correlation peaks in the two dimensions of time lag (range) and frequency (Doppler velocity). In this case, however, the correlation peaks represent detected

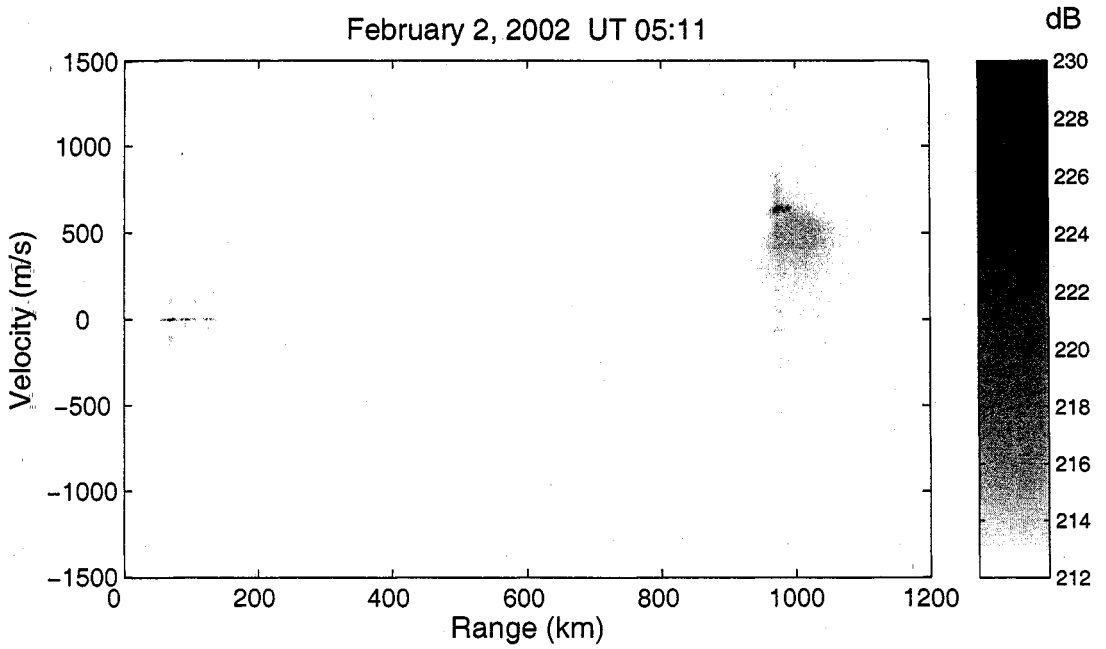

Figure 3.2: A range-Doppler diagram, or cross-ambiguity, the typical data product of MRR. Doppler power spectra are shown in vertical slices for 800 1.5-km ranges (lags). The greyscale is in dB, arbitrary units. Reflections from the Cascade mountain range can be seen at zero Doppler near 100 km; at a range of 1000 km, echoes due to ionospheric plasma turbulence are present.

targets rather than self-ambiguities in the illuminating signal. An example of MRR cross-ambiguity, or Doppler spectra versus range, can be seen in Figure 3.2.

The MRR provides full range and Doppler velocity information for 1.5 meter-scale waves and turbulence in the E region ionosphere. Meyer implemented a horizontal interferometer for the MRR in 2002 [76, 74], which provides resolution in the cross-beam direction (perpendicular to the radar line of sight), permitting the estimation of irregularity transverse structure. The MRR range resolution is 1.5 km; the (over-moded) interferometer provides azimuthal resolution corresponding to 2 km in width at a range of 1000 km. We typically use a Doppler resolution of 12 m/s and integrate

for 10 seconds.

3.1.1 Advantages of FM Illumination

There are many advantages to exploiting commercial FM broadcasts for radar illumination rather than operating a dedicated transmitter. One is simply expense: the cost of the transmitter itself is saved, as well as related costs of electricity and maintenance. No operating license must be obtained; no space must be secured for the transmitter to reside; and safety is almost a non-issue for receive-only systems. In addition to the convenience of utilizing someone else's transmitter, the commercial instruments are often powerful and omnidirectional, and their effective radiated power is high since they are CW, not pulsed.

The 100 MHz FM carrier frequency offers the opportunity to observe Bragg scatter at the 1.5-meter scale, bridging the gap between existing large datasets at 50 MHz and 140 MHz which do not agree well. FM radio passive radar is basically the only way to observe this scale size in North America, because of spectrum allocation and licensing obstacles. Also, 100 MHz signals are not strongly affected by either ionospheric refraction or atmospheric absorption.

Perhaps most importantly, the FM waveform is of high quality for radar applications, with excellent ambiguity characteristics (ability to uniquely detect targets in the time lag and frequency domains) in the average sense [48]. Usually, the waveform is such that the MRR is completely free of range aliasing. Of course, the broadcast signals constantly evolve in time, and we occasionally experience "bad ambiguity." Sahr has developed an algorithm for mitigating temporary waveform ambiguities in which the short-time autocorrelation function for the reference signal is monitored and sequences with long correlation times[2] are removed [unpublished work, 2004].

[2]The typical FM waveform has a correlation time of 5–10 μs, corresponding to a bandwidth of

The $\approx$ 100 kHz FM signal bandwidth yields a range resolution of 1.5 km, finer than any prior coherent radar data, and prevents Doppler aliasing (of targets moving up to $\pm$75 km/sec).

Essentially, the FM transmission acts like a stochastically coded long pulse [50], which is very useful for overspread[3] targets such as ion-acoustic turbulence in the ionosphere. The bandwidth of the FM transmission is large compared to inverse timescales of fluctuations in the ionospheric plasma, and this permits overspread target pulse compression. Pulse compression is a signal processing technique for achieving fine range resolution without sacrificing sensitivity [70]. Narrow pulse widths require a large receiver bandwidth, letting a lot of noise into the system and degrading detectability. Also, the amount of power a transmitter can expel in an extremely short pulse is limited, while a longer pulse can deposit more energy on a target. Therefore, longer pulses are modulated (usually in a bipolar phase scheme) by pulse sequences chosen specifically for their ambiguity function performance. After matched filtering, these long pulses perform as though they were very brief, but with the sensitivity advantages of long pulses. Serendipitously, commercial FM signals provide all of these desirable radar waveform features, in a stochastic sense. For future implementations of passive radar, HDTV signals seem quite promising; with a bandwidth of 6 MHz, they can potentially provide resolution as fine as 30 meters.

3.1.2 Operating the MRR

There are some practical challenges associated with operating a bistatic passive radar. First, we must decide to which FM station(s) to tune our receivers. We want to choose a loud, omni-directional transmitter near the reference receiver. On the other hand,

---

100–200 kHz.

[3]An overspread target is one which is simultaneously too distant and moving too fast to unambiguously resolve its range and frequency characteristics with a pulsed radar.

we require a relatively radio-quiet environment for the scattered signal receiver. This means choosing an FM channel for which a suitable transmitter is available near the reference receiver and whose channel is quiet at the scatter receiver site. Finding channels which satisfy these requirements can be difficult. Also, energy from other transmitters in the FM band can hurt the scatter receiver's dynamic range if they are powerful enough. In the future, we will add signal processing algorithms to the radar to reject sources of interference such as unwanted FM stations [133].

Next, both the reference and scattered data streams must be transferred via a network connection to a central location for processing. Currently, we transfer the scattered signals from the remote receiver at MRO to the University of Washington (the Seattle reference receiver location). The MRO data first come over a 500 kbps microwave link to the nearby Central Washington University and then are sent over the internet to the UW. This data transfer (particularly the microwave link portion) is currently the tightest bottleneck in the operation of MRR.

Our minimal MRR operation mode takes 10 second bursts of data every 4 minutes and processes one reference-scatter pair of channels for internet publishing, so users can keep abreast of activity on the radar. This limited default operation of MRR generates more than 8 gigabytes of data, causes sustained network traffic exceeding 130 kbps, and requires approximately 8 Mflops in sustained computation every day. While the passive radar computational load is easily handled by mainstream desktop computers available today, the bistatic network traffic is a significant limitation, particularly when transferring data from the observatory atop Manastash Ridge. Obtaining the scattered data from the mountain is the only barrier against operating the MRR in realtime.

Table 3.1: Latitude/longitude coordinates for some locations relevant to MRR.

Site	Latitude	Longitude	Comments
MRO	46.95° N	120.72° W	Central WA scatter RX location
UW	47.66° N	122.31° W	Western WA reference RX location
KBSG	47.50° N	121.98° W	Western WA TX; 97.3 MHz; 52 kW ERP
KJAQ	47.54° N	122.11° W	Western WA TX; 96.5 MHz; 100 kW ERP
KWJZ	47.50° N	121.97° W	Western WA TX; 98.9 MHz; 52 kW ERP
EWU	47.49° N	117.58° W	Eastern WA reference RX location
KKZX	47.59° N	117.30° W	Eastern WA TX; 98.9 MHz; 100 kW ERP
KKRS	47.59° N	117.89° W	Eastern WA TX; 97.3 MHz; 5.1 kW ERP
Mt. Rainier	46.85° N	121.76° W	Prominent ground clutter
KXLE	47.16° N	120.79° W	Calibration TX; 95.3 MHz; 51 kW ERP
KULE	47.31° N	119.60° W	Calibration TX; 92.3 MHz; 26 kW ERP

3.1.3 New Extensions of the MRR

In July of 2005, we added a second reference receiver in Eastern Washington State, making the MRR multistatic and providing the possibility of a significantly different view geometry. While the new receiver provides interesting new opportunities for radar observations and experiments, it also increases the complexity of the system and exacerbates the network traffic performance bottleneck mentioned above. We discuss this extension of the MRR system in detail in Chapter 6 and present observations with the three-receiver system in Chapter 7.

For reference, in table 3.1, we provide the latitude and longitude coordinates of each MRR receiver, several useful transmitters, and other relevant locations.

3.2 Passive Radar Scientific Contributions

Passive radar, like active coherent scatter radar, can be a powerful tool for space and ionospheric plasma physics studies. We group the scientific contributions of coherent scatter radars (both active and passive) into three broad categories: space weather, "macro-physics," and "micro-physics."

3.2.1 Space Weather

What we call space weather refers to the very large scale interactions that connect solar events to the Earth, through its magnetosphere and ionosphere, and the consequences felt at the Earth's surface of the coupling between these enormous systems. While satellites are probably the most useful platform for studying space weather, ground-based radar experimenters can help by identifying trends in their observations with respect to solar activity, or by providing supporting data during extreme events, like magnetic superstorms (for which the Dst geomagnetic index[4] is less than -300 nT) [117, 33].

Space weather, whose severity waxes and wanes with the 11-year solar cycle [84] (among other influences) is a research field in which long-term observations are useful. Passive radar is particularly well suited for uninterrupted, long-term remote sensing, since (to put it bluntly) science funding agencies do not have to pay for the continued operation of a transmitter. (Instead, we all contribute to passive radar's livelihood by listening to advertisements on the radio.) An example of a space weather-type study we performed with the MRR is illustrated in Figure 3.3.

---

[4]The Dst index represents the global magnetic storm level by averaging the geomagnetic field horizontal component at equatorial- and mid-latitudes worldwide [125]. A negative value indicates an enhanced ring current which in turn implies that a magnetic storm is occurring. The ring current usually cannot become large enough to make Dst negative unless the IMF is directed southward.

Since we can operate the MRR year-round, we may look for trends in our data with respect to the season, an option unavailable in event-driven campaigns. Figure 3.3 shows a histogram of irregularity occurrences during each month of the year. This histogram represents over 21,000 echoes detected during 24 consecutive months (years 2002 and 2003) of MRR observations. Clearly, many of the irregularity echoes occurred during the months of March, April, and May; June was also a very active month during the year 2003, but less so during 2002. We also find a prominent peak in activity during the months of October and November. This peak is primarily due to approximately 8000 irregularity detections (nearly 40% of the represented data) made during only three days in October/November 2003 (measurements from the "Halloween" geomagnetic superstorms of 2003). If these measurements are excluded (as shown with the dashed line in Figure 3.3), we see a secondary peak in activity near the autumn equinoctial months. This active spring/autumn trend is consistent with the well-documented Russell-McPherron effect [107], from which we expect maximum geomagnetic activity near the equinoctial months.

3.2.2 Macro-Physics

While space weather refers to events of global scale and beyond, we use the term "macro-physics" to describe observations of local, yet large- or meso-scale phenomena. For example, evidence of magnetosphere-ionosphere coupling (such as storm-enhanced ionospheric density) can sweep across large sections of the planet, but we can detect the "front," and observe part of the event, with coherent radar. Interesting electric field structures, symptoms of larger magnetospheric processes, may span the entire radar field of view, or develop over several hours.

The radar range-time intensity diagram (for example, see Figure 6.3, page 117) is a very useful tool for macro-physical studies since it consolidates a large amount

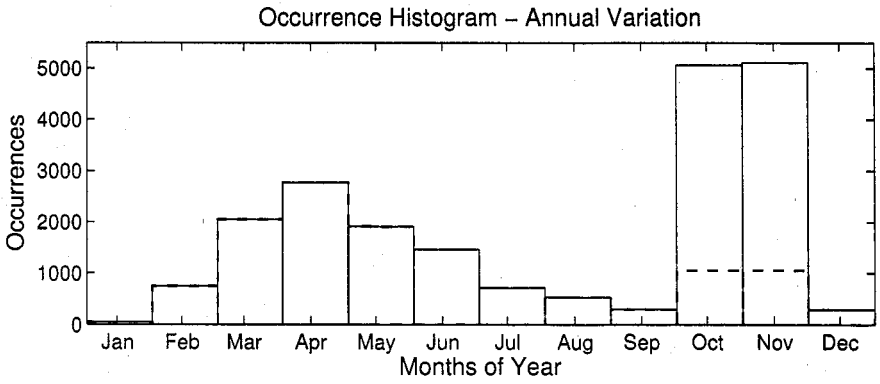

Figure 3.3: An occurrence histogram showing the seasonal dependence of irregularities observed by MRR in the years 2002 and 2003. The dashed line excludes approximately 8000 (of 21,000 total) measurements made during the severe magnetic storm events on three days during October and November 2003.

of data and in doing so conceals excess detail, so that "big picture" observations can be made. Also, we can more easily infer meaning from our radar observations when we are able to correlate our data with that of other space physics instruments, such as incoherent scatter radars, GPS receivers measuring total electron content, magnetometers, ionosondes, and *in situ* instruments on board satellites and rockets.

3.2.3 Micro-Physics

Finally, by "micro-physics," we mean the study of individual plasma instabilities: the primary purpose of most coherent scatter radar experiments. With the MRR, we continue to work toward understanding the ionospheric two stream instability and resulting plasma density irregularities by providing as many observations as possible under a wide range of geophysical conditions. Since we do not yet have a satisfying plasma physics model which predicts their radar spectral features, statistical studies of irregularity characteristics and behavior are still very important to the field, and

large data sets are useful for these studies (*e. g.*, the sub-auroral irregularity Doppler moment study by Meyer *et al.* [75]).

We present the following as an example of the micro-physics we can do with the MRR: we explain a trend in our data which was, at first, confusing. However, armed with an explanation, the same data corroborates theoretical predictions of irregularity behavior.

First, we show a two-dimensional histogram of irregularity occurrences versus range and mean Doppler shift (the greyscale represents the number of irregularity occurrences with a particular Doppler velocity and at a particular range) in Figure 3.4. We note an apparent Doppler velocity (irregularity phase speed) increase over the last 150 km of range (regardless of Doppler shift polarity). To explain this far-range speed-up feature of the data, we turn next to Figure 3.5, which is a cartoon (not to scale) of the MRR view volume showing the relationship between radar range and altitude. We can see that, as range increases, lower altitudes are shadowed by the limb of the Earth. At the farthest range gates marked in Figure 3.5, the MRR is only observing the higher altitudes of the E region. By about 1150 km range, the entire E region is cut off, and from Figure 3.4, we see the irregularity occurrences have ceased as well. (The ionospheric two-stream instability detected by the MRR only occurs over a certain altitude range in the E region – see Chapter 4, page 52.)

Thus, a correlation between higher altitudes and faster irregularity phase velocities would explain the speed-up feature of Figure 3.4, and indeed the two-stream instability theory, combined with ionospheric vertical structure, predicts this. The plasma temperature increases with altitude, which means that the ion acoustic speed (which is the threshold irregularity phase speed; see a derivation and discussion in Section 4.2.2) is also greater. Also, at higher altitudes, the atmospheric neutral density thins and ions become somewhat more mobile. This means that the instability driving

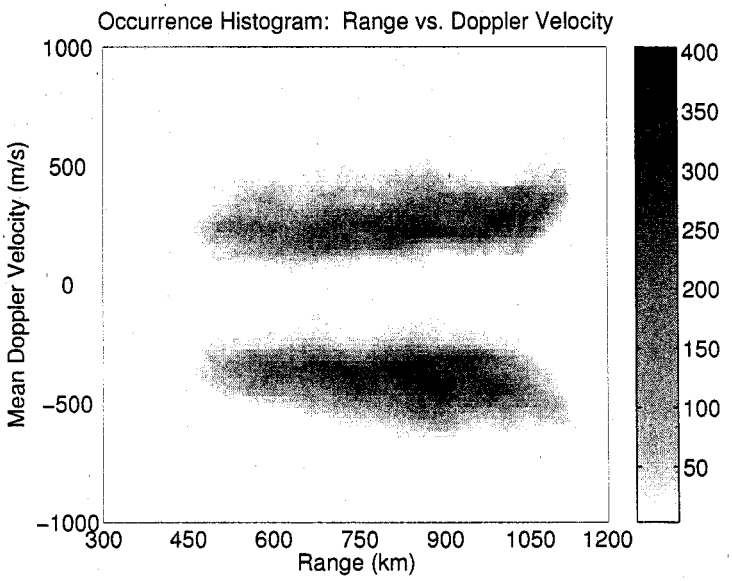

Figure 3.4: A two-dimensional histogram of irregularity occurrences versus range and mean Doppler shift. The greyscale is number of occurrences. This figure represents nearly 500,000 irregularity observations during the magnetic storm of 17-27 July 2004.

force – the relative electron-ion drift – must be faster, requiring a stronger electric field. These two circumstances both serve to increase the average phase velocity of irregularities observed at high E region altitudes.

Not all the features of MRR irregularity observations can be explained so easily, but the iterative process of developing theories to account for experimental data is the basis for science.

3.3 Passive Remote Sensing Arrays

We have recently developed the MRR into a truly multistatic passive remote sensing instrument. We expect this trend to continue, with more receiver nodes being added, and multistatic algorithms, such as the ones presented here in Chapter 6, being fur-

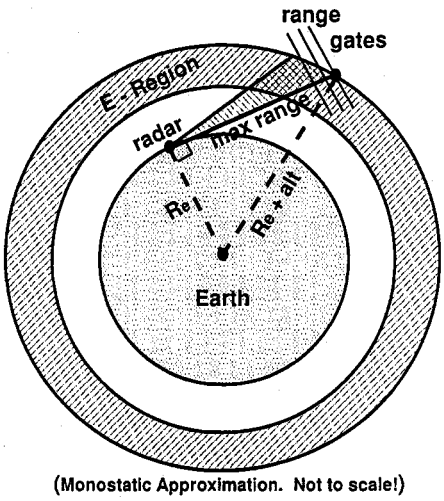

Figure 3.5: A diagram (not to scale) of the MRR view volume, showing the relationship between radar range and altitude. As range increases, lower altitudes are shadowed by the limb of the Earth.

ther developed. Distributed passive radar shows great potential for both geophysical as well as surveillance applications. We can do the same experiments with passive radar as we can with active systems; the data are of equal or better quality. Multistatic passive radar can provide simultaneous long time and wide area coverage, and accomplish both of these with fine temporal and spatial resolution. Also, passive radar surveillance cannot be detected, and multistatic networks and the simultaneous use of several different frequencies are both powerful anti-stealth techniques.

The multistatic MRR is an initial proof of concept for a new project, headed by Dr. Frank Lind at MIT Haystack Observatory, named ISIS (Intercepted Signals for Ionospheric Science). The ISIS project currently has 7 deployable passive radar receiver nodes; the plan is to dovetail them with the three existing MRR nodes to eventually create a distributed passive radar network along the US-Canada border, for continuous monitoring of the auroral oval and SAPS regions.

In turn, ISIS is one example, or subsystem, of a new initiative named DASI (Distributed Arrays of Small Instruments). The National Academy of Science decadal survey for solar and space physics mentions "large arrays of distributed instruments" and specifically DASI as new initiatives in ground-based research [90, 67]. Like the present-day network of GPS receivers, which is used to map total electron content on a nearly global scale [73], the individual receivers (or more generally, instruments) should be inexpensive, easy to control and maintain, and require little infrastructure so that users can focus their efforts on experiment design and the new scientific applications of such an array of instruments. The spatially distributed nature of a large network of instruments will enable large-scale remote sensing in a way that has never been possible before. Since dedicated transmitters are not required for passive instruments, those parts of DASI can operate continuously without interruption. We believe that these meta-instruments will define the future state of the art in ground-based geophysics as well as surveillance. They will eventually be able to observe a majority of the Earth and its environment, but it will take a lot of work to harness their full potential.

Chapter 4

FLUID THEORY OF HIGH LATITUDE E REGION PLASMAS

We begin our discussion of the theory behind the radar aurora by presenting a fluid theory that is applicable to plasma dynamics in the E region. Mathematically, we treat a fluid as a medium where all macroscopic quantities of interest are continuous functions of time and position [66]; assuming that the ionospheric plasma is a fluid means that we are interested in phenomena that vary on scales that are much greater than the time and length scales inherent to the plasma [11].

A fluid treatment of the ionosphere is reasonable if the time scales of interest are long compared with the inverse plasma frequency ($1/\omega_p$) and the period of a gyro-orbit ($2\pi/\Omega$) or the inverse collision frequency ($1/\nu$), depending on whether the plasma particles are magnetized or collisional. In the nighttime E region, the inverse plasma frequency is 0.4μs. Electrons are magnetized ($1/\Omega_e = 0.6\mu$s and $1/\nu_e = 50\mu$s) and ions are not ($1/\Omega_i = 63$ms and $1/\nu_i = 0.5$ms) [60]. The largest of these relevant time lengths is 0.5 ms; however, we are interested in plasma instabilities which occur over timescales of tens of milliseconds [41], so a fluid description is appropriate.

Likewise, the spatial scales of interest should be longer than the plasma Debye length, the thermal gyroradius, and/or the mean free path [14]. The E region nighttime Debye length is 2 cm; the thermal gyroradius is 8 mm for electrons and 2.5 meters for ions. However, the ions are dominated by collisions with other particles, and their mean free path is only 12 cm. The electron mean free path is 3-4 meters, but over this distance the electrons undergo many gyrations about the magnetic

field. Taking the largest of the scale lengths of dominant particle behavior, 12 cm, we arrive at a lower bound for fluid scale size of about 10×12 cm $= 1.2$ meters. This implies that radars observing the E region above an operating frequency of 125 MHz should use kinetic theory to interpret their observations, since these radars are sensitive to scale lengths of 1.2 meters and smaller. The majority of experimental electrojet irregularity studies have been conducted at 50 MHz (*e. g.* CUPRI [108]), 140 MHz (STARE [89]), and 150 MHz (SABRE [115]). The Manastash Ridge Radar, with an operating frequency between 88 MHz (1.7 m scale length) and 108 MHz (1.4 m), is just on the threshold between the fluid and kinetic plasma regimes, making it an intriguing tool for ionospheric research.

4.1 Fluid Equations for the E Region Ionosphere

If a plasma fluid treatment is appropriate, the governing equations of the system are the hydrodynamic equations plus Maxwell's equations, since plasmas are charged. We assume that the electromagnetic fields in the plasma vary on the same time and length scales as the plasma parameters; *i. e.*, the fields are related to bulk plasma motion, as in an MHD (magnetohydrodynamic) treatment [11].

This is in contrast to a kinetic treatment, in which statistical mechanics are used to keep up with a population of individual plasma particles in time, space, and phase space. Probably the most important equation in kinetic plasma physics is the Vlasov equation,

$$\frac{D}{Dt} f_s(\mathbf{r}, \mathbf{v}, t) = \frac{\partial}{\partial t} f_s + \mathbf{v} \cdot \nabla f_s + \frac{q_s}{m_s} (\mathbf{E} + \mathbf{v} \times \mathbf{B}) \cdot \nabla_v f_s = 0 \qquad (4.1)$$

which describes the evolution of the "distribution function" f_s of the plasma species s in six dimensional phase space and time ($\frac{D}{Dt}$ is a total time derivative). The Vlasov equation is often called the collisionless Boltzmann equation, since its right hand side (describing discontinuities in position and momentum) is zero. The fluid equations

(continuity and momentum) appropriate for plasmas can be derived from the Vlasov equation, using manipulations involving integrations over velocity space [85]. These equations, for particle species s, are given below:

$$\frac{\partial}{\partial t} n_s + \nabla \cdot (n_s \mathbf{u_s}) = 0 \qquad \text{(continuity)} \quad (4.2)$$

$$\frac{\partial}{\partial t}(n_s \mathbf{u_s}) + \nabla \cdot (n_s \mathbf{u_s} \mathbf{u_s}) = \frac{q_s}{m_s} n_s (\mathbf{E} + \mathbf{u_s} \times \mathbf{B}) - \frac{1}{m_s} \nabla p_s \qquad \text{(momentum)} \quad (4.3)$$

The fluid variables – density (n_s) and bulk flow ($\mathbf{u_s}$) – and fields $\mathbf{E}$ and $\mathbf{B}$ are functions of space ($\mathbf{r}$) and time (t) only. For our E region analysis, we will use the continuity and momentum equations for two plasma species: electrons and a single ion fluid with $q_i = +e$ and $m_i \approx 31 m_p$. This is a common assumption, since the E region ion population is dominated by NO^+ and O_2^+, which are very similar in mass. An exception is Lind [72], who worked out a three-fluid model with two ion species.

To close the system, we add a thermodynamic equation of state, one of Maxwell's equations (Faraday's law), and plasma quasi-neutrality, as several authors have done [124, 27, 111, 93, 54]:

$$p_s = \gamma_s k_B T_s n_s \qquad \text{(state equation)} \quad (4.4)$$

$$\nabla \times \mathbf{E} = -\frac{\partial}{\partial t} \mathbf{B} \qquad \text{(Faraday's law)} \quad (4.5)$$

$$\nabla \cdot \mathbf{J} = 0 \quad (\text{or } n_e = n_i \equiv n) \qquad \text{(quasi-neutrality)} \quad (4.6)$$

(Others have used Poisson's equation ($\nabla \cdot \epsilon \mathbf{E} = e(n_i - n_e)$) to tie the plasma species together, rather than assuming quasi-neutrality [69, 72].)

In simplifying the equations for our purposes, the most important E region distinction we make is a lack of magnetic influence on the ions (in equation 4.10). Also, electron inertia is often neglected ($D\mathbf{u_e}/Dt = 0$) as well as ion convection ($\nabla \cdot (n\mathbf{u_i}\mathbf{u_i}) = (\nabla \cdot \mathbf{u_i})(n\mathbf{u_i}) + (\mathbf{u_i} \cdot \nabla)(n\mathbf{u_i}) = 0$). The first statement means that the electrons react quickly enough to immediately balance any applied forces. The

second implies that the ion drift changes slowly as a function of space, and/or the background ion drift is negligible. These and other common assumptions for E region physics will be discussed further in sections 4.1.1 and 4.1.2. We also include collisional terms, which couple the plasma to the background neutral gas (still important at E region heights), through the collision frequencies ν_s. The two-fluid equations, simplified as discussed above, are then:

$$\frac{\partial}{\partial t}n + \nabla \cdot (n\mathbf{u_e}) = 0 \tag{4.7}$$

$$\frac{\partial}{\partial t}n + \nabla \cdot (n\mathbf{u_i}) = 0 \tag{4.8}$$

$$-\frac{e}{m_e}n\left(\mathbf{E} + \mathbf{u_e} \times \mathbf{B}\right) - \frac{\gamma_e k_B T_e}{m_e}\nabla n - \nu_e n\mathbf{u_e} = 0 \tag{4.9}$$

$$\frac{e}{m_i}n\mathbf{E} - \frac{\gamma_i k_B T_i}{m_i}\nabla n - \nu_i n\mathbf{u_i} = \frac{\partial}{\partial t}(n\mathbf{u_i}) \tag{4.10}$$

4.1.1 Discussion of Assumptions

We now describe features of the above fluid equations that characterize them for the E region ionosphere as opposed to other plasma environments. The key assumption, and the most important for our purpose in this document, is that the ions are unmagnetized, while electrons are. The rationale for this assumption is based on the gyrofrequency to collision frequency ratio: $\Omega_e/\nu_e \gg 1$, while $\Omega_i/\nu_i < 1$. A species is taken to be unmagnetized (unresponsive to magnetic forces) if its collision frequency is greater than its gyrofrequency (which can be thought of as a measure of how influential the magnetic field is to the species: $\Omega_s = q_s B/m_s$). Of course, models for collision processes can be very complex and we cannot know the most appropriate model or the exact value for ν_s. However, if we consider that the neutral density is far greater than either the electron or ion population, then we can say that collisions with neutrals dominate collision processes for either species, and ν_s will be proportional to n_n. The temperatures and collision frequencies for electrons and ions are

comparable; it is the greater ion mass that slows down Ω_i to the point where ions cannot, on average, make even a single gyro-orbit without being interrupted by a collision. Therefore, ion behavior is dominated by drifting along with neutral winds and drifting in response to applied electric fields. The electrons, on the other hand, are strongly magnetized with $\Omega_e/\nu_e \approx 500$.

An assumption about thermodynamic behavior must be made to utilize equation 4.4. Following Haldoupis and Schlegel [40], we assume the electrons are adiabatic ($\gamma_e = 5/3$ for 3-D, 2 for 2-D) and the ions, strongly coupled to the neutral heat reservoir through collisions, are isothermal ($\gamma_i = 1$). In replacing ∇p with $\gamma k_B T \nabla n$, we also assume that neither γ (ratio of specific heats) nor T (temperature) is a function of space; this is a valid assumption in the linear regime, or for small density perturbations ($\delta n/n \ll 1$).

In general, ionization and recombination effects cannot be ignored on the RHS of equations 4.7 and 4.8 for the E region, which is continuously ionized by solar radiation during daylight hours and which mostly disappears at night. However, following Lind [72], we assume that creation and destruction of ionized particles are balanced on the irregularity timescales in which we are interested. The average irregularity lifetime lasts tens of milliseconds [41]. We also do not consider electron density gradient effects; these are applicable at longer wavelengths than we detect with the MRR. Both density gradient and recombinational effects have been discussed by Fejer *et al.* [27]. Finally, we also disregard gravitational force and neutral particle drift.

4.1.2 Background (Zeroth-Order) Drifts

To study waves in the E region medium, we will use a perturbation method to linearize the fluid equations, keeping only first order terms. The perturbed quantities will be the density, electric field, and fluid velocities: $n \rightarrow n_0 + n_1$, $\mathbf{E} \rightarrow \mathbf{E_0} + \mathbf{E_1}$, and

$\mathbf{u_s} \rightarrow \mathbf{u_{s0}} + \mathbf{u_{s1}}$. We assume the system is electrostatic (the magnetic field is constant). This is consistent with our investigation of the longitudinal Farley-Buneman waves.

All zeroth-order terms are assumed to be in equilibrium and therefore their derivatives are zero. However, we can use the zeroth-order versions of the fluid equations to solve for the background electron and ion drifts, $\mathbf{u_{e0}}$ and $\mathbf{u_{i0}}$. These are important, because the source of free energy that drives the ionospheric two-stream instability is the background relative electron–ion drift, $\mathbf{V_d} \equiv \mathbf{u_{e0}} - \mathbf{u_{i0}}$. We would like to obtain an expression for $\mathbf{V_d}$. The zeroth-order momentum equations are:

$$\Omega_e n_0(\mathbf{E_0} + \mathbf{u_{e0}} \times \mathbf{B}) + \nu_e n_0 \mathbf{u_{e0}} = 0 \tag{4.11}$$

$$\Omega_i n_0 \mathbf{E_0} - \nu_i n_0 \mathbf{u_{i0}} = 0 \tag{4.12}$$

We can solve directly for the background ion drift due to an external electric field (the Pedersen drift):

$$\mathbf{u_{i0}} = \frac{\Omega_i \mathbf{E_0}}{B\nu_i} = \frac{e\mathbf{E_0}}{m_i \nu_i} \tag{4.13}$$

We obtained the second expression by re-substituting eB/m_i for the ion gyrofrequency, since it is peculiar to see the quantities Ω_i and B in an expression for unmagnetized ions.

Next, assuming the background electric field is perpendicular to the magnetic field ($\mathbf{E_0} \perp \mathbf{B}$), the zeroth-order electron drift is given by

$$\mathbf{u_{e0}} = -\frac{\Omega_e \nu_e \mathbf{E_0}}{B(\Omega_e^2 + \nu_e^2)} + \frac{\Omega_e^2(\mathbf{E_0} \times \mathbf{B})}{B^2(\Omega_e^2 + \nu_e^2)} \tag{4.14}$$

which is the electron Pedersen drift plus the $\mathbf{E} \times \mathbf{B}$ drift. The $\mathbf{E_0} \perp \mathbf{B}$ assumption is reasonable, since the conductivity along $\mathbf{B}$ is too large to sustain a constant electric field over the irregularity timescales of several milliseconds. Throughout this document, we will assume $\mathbf{E_0} = E_0 \hat{y}$ and $\mathbf{B} = B\hat{z}$, without loss of generality.

We can now solve for the relative electron–ion drift:

$$\mathbf{V_d} \equiv \mathbf{u_{e0}} - \mathbf{u_{i0}} \tag{4.15}$$

$$\approx -\mathbf{E_0}\left(\frac{\nu_e}{B\Omega_e}+\frac{\Omega_i}{B\nu_i}\right)+\frac{\mathbf{E_0}\times\mathbf{B}}{B^2} \tag{4.16}$$

$$\approx \frac{\mathbf{E_0}\times\mathbf{B}}{B^2} \tag{4.17}$$

The first approximation follows from the E region property that $\Omega_e \gg \nu_e$. Next, the relative Pedersen drift term ($\mathbf{E_0}$ term) is about two orders of magnitude smaller than the electron $\mathbf{E}\times\mathbf{B}$ drift, which has no ion counterpart. Therefore it is reasonable to approximate $\mathbf{V_d}$ as the electron $\mathbf{E}\times\mathbf{B}$ drift, and we use $\mathbf{V_d} = (E_0/B)\hat{x} = V_d\hat{x}$ interchangeably.

4.1.3 Derivation of the Ion Acoustic Differential Equation

Our goal is to use the foregoing fluid description of E region plasma to predict the characteristics and behavior of waves, or more generally, disturbances, in the plasma. First we will combine the coupled system of equations into a single expression, which we will next linearize using the perturbation method mentioned above. Finally, we assume a functional form for the perturbed fluid parameters and electric field. If the perturbation form is a plane wave, the resulting equation is a dispersion relation for the medium, which we can use to predict how and when growing wave modes (instabilities visible to coherent radars) may occur.

Following Sahr [111], we combine the ion fluid equations by solving the momentum equation for the ion flux $n\mathbf{u_i}$, taking the divergence of both sides, and making a substitution based on the continuity equation:

$$\frac{\partial}{\partial t}(n\mathbf{u_i})+\nu_i n\mathbf{u_i} = \frac{e}{m_i}n\mathbf{E}-\frac{\gamma_i k_B T_i}{m_i}\nabla n \tag{4.18}$$

$$\left(\frac{\partial}{\partial t}+\nu_i\right)\underbrace{(\nabla\cdot(n\mathbf{u_i}))}_{=-\frac{\partial}{\partial t}n} = \frac{e}{m_i}\nabla\cdot(n\mathbf{E})-\frac{\gamma_i k_B T_i}{m_i}\nabla^2 n \tag{4.19}$$

$$-\frac{\partial}{\partial t}\left(\frac{\partial}{\partial t}+\nu_i\right)n = \frac{e}{m_i}\nabla\cdot(n\mathbf{E})-\frac{\gamma_i k_B T_i}{m_i}\nabla^2 n \tag{4.20}$$

As with the ion equations, we'll want to solve for the electron flux, $n\mathbf{u_e}$, to combine the electron continuity and momentum equations. To represent the electron momentum equation in a form that is more accommodating for the coming manipulations (again following Sahr [111]), we define a 3×3 matrix R such that $n\mathsf{R}\mathbf{u_e} = \frac{e}{m_e} n\mathbf{u_e} \times \mathbf{B} + \nu_e n\mathbf{u_e}$:

$$\mathsf{R} \equiv \begin{pmatrix} \nu_e & \Omega_e & 0 \\ -\Omega_e & \nu_e & 0 \\ 0 & 0 & \nu_e \end{pmatrix} \tag{4.21}$$

In this definition of R, we have assumed that $\mathbf{B} = B\hat{z}$, and we substituted the cyclotron frequency $\Omega_s = eB/m_s$ (note that Ω_s does not carry a charge sign).

The electron momentum equation then becomes:

$$\frac{e}{m_e} n\mathbf{u_e} \times \mathbf{B} + \nu_e n\mathbf{u_e} = n\mathsf{R}\mathbf{u_e} = -\frac{e}{m_e} n\mathbf{E} - \frac{\gamma_e k_B T_e}{m_e} \nabla n \tag{4.22}$$

and the electron flux is

$$n\mathbf{u_e} = \mathsf{R}^{-1} \left(-\frac{e}{m_e} n\mathbf{E} - \frac{\gamma_e k_B T_e}{m_e} \nabla n \right) \tag{4.23}$$

This requires us to calculate the inverse of R:

$$\mathsf{R}^{-1} = \frac{1}{\Omega_e^2 + \nu_e^2} \begin{pmatrix} \nu_e & -\Omega_e & 0 \\ \Omega_e & \nu_e & 0 \\ 0 & 0 & \frac{\Omega_e^2 + \nu_e^2}{\nu_e} \end{pmatrix} \approx \frac{1}{\Omega_e^2} \begin{pmatrix} \nu_e & -\Omega_e & 0 \\ \Omega_e & \nu_e & 0 \\ 0 & 0 & \frac{\Omega_e^2}{\nu_e} \end{pmatrix} \tag{4.24}$$

(In the second expression, we have used the simplification $\Omega_e^2 + \nu_e^2 \approx \Omega_e^2$.) Now we substitute the electron flux into the electron continuity equation to arrive at

$$\frac{\partial}{\partial t} n + \nabla \cdot \left[\mathsf{R}^{-1} \left(-\frac{en}{m_e} \mathbf{E} - \frac{\gamma_e k_B T_e}{m_e} \nabla n \right) \right] = 0 \tag{4.25}$$

We combine the electron and ion fluid equations by multiplying equation 4.20 by $\nu_e/(\Omega_e \Omega_i)$ and subtracting it from equation 4.25. Next, we impose small perturbations on the density and electric field, and keep only first-order, linear terms. (For

details, see section A.1.) The resulting single equation describing E region plasma, emphasizing ion acoustic type effects, is

$$\frac{\psi}{\nu_i}\left(\frac{\partial^2}{\partial t^2} - c_s^2\nabla_\perp^2\right) n_1 \;+\; (1+\psi)\frac{\partial}{\partial t}n_1 - \frac{v_{\mathrm{Th,e}}^2}{\nu_e}\frac{\partial^2}{\partial z^2}n_1 \\ +\; \mathbf{V_d}\cdot\nabla n_1 + \frac{n_0}{B}\left(\nabla\times\mathbf{E_1}\right)\cdot\hat{z} - n_0\nabla\cdot\mathbf{V}_\parallel = 0 \quad (4.26)$$

We have used the following definitions: ψ is the ionospheric "anisotropy parameter," equal to $\nu_e\nu_i/(\Omega_e\Omega_i)$, and very small ($\approx 0.025$) in the E region; c_s is the ion acoustic speed; $\nabla_\perp^2 = \partial^2/\partial x^2 + \partial^2/\partial y^2$; $v_{\mathrm{Th,e}}$ is the electron thermal speed, equal to $\sqrt{\gamma_e k_B T_e/m_e}$; $\mathbf{V_d} = \mathbf{E_0}\times\mathbf{B}/B^2$ (from 4.17); and $\mathbf{V}_\parallel$ is the electron parallel (to magnetic field) velocity, equal to $\left(\frac{\Omega_e}{B\nu_e}\right)(\mathbf{E_1}\cdot\hat{z})\hat{z}$.

This equation has two unknowns, namely, n_1 and $\mathbf{E_1}$. However, we can disregard the $\mathbf{E_1}$ terms, for the following reasons. Faraday's law, to first order, states that $\nabla\times\mathbf{E_1} = -\frac{\partial}{\partial t}\mathbf{B_1}$. However, since we are interested in longitudinal waves, we have assumed that the magnetic perturbation $\mathbf{B_1} = 0$, meaning $\nabla\times\mathbf{E_1}$ is negligible. Next, the $\mathbf{V}_\parallel$ term can be ignored, since very high conductivity along $\mathbf{B}$ means that $\mathbf{E}\cdot\hat{z}\approx 0$. Finally, we arrive at

$$\frac{\psi}{\nu_i}\left(\frac{\partial^2}{\partial t^2} - c_s^2\nabla_\perp^2\right) n_1 + (1+\psi)\frac{\partial}{\partial t}n_1 - \frac{v_{\mathrm{Th,e}}^2}{\nu_e}\frac{\partial^2}{\partial z^2}n_1 + \mathbf{V_d}\cdot\nabla n_1 = 0 \quad (4.27)$$

4.2 *The Ionospheric Two-Stream Instability*

Next, we substitute a plane wave form for the density perturbation: $n_1 = \tilde{n}_1 e^{-j\omega t + j\mathbf{k}\cdot\mathbf{r}}$. ($\tilde{n}_1$ is a small, complex constant amplitude.) Substituting this solution into equation 4.27 leads to a dispersion relation (relating the propagation vector $\mathbf{k}$ of a wave to its frequency of oscillation ω). We usually take k to be real and allow ω to be complex: $\omega_r + j\Gamma$. An instability occurs when a solution for ω exists such that the "growth rate" $\Gamma > 0$, so that the wave amplitude $|\exp(-j(\omega_r + j\Gamma)t)| \to \infty$ as $t\to\infty$. In

this case, a small perturbation in the plasma fluid (or distribution function) can grow exponentially until the linear approximation breaks down [96]. At this point, the density fluctuations may become pronounced enough to cause coherent backscatter that radars with modest power (for example, 50 kW, pulsed) can detect.

The so-called "coherent scatter radars" are sensitive to irregularities in plasma density caused by instabilities as described above. These radars are distinguished from the far more powerful incoherent scatter radars (ISRs), which can detect scatter from the thermal fluctuations of electrons and command a few MW in peak power.

There is one particular instability relevant to our study of the E region ionosphere with the MRR, a VHF coherent scatter radar. First described by Farley [23] with kinetic theory and Buneman [12] with fluid theory, this two-stream instability produces ion acoustic waves; one mode has a positive growth rate. The "Farley-Buneman" instability arises in the E region and depends on the characteristic "fast electrons, collisional ions" physics of that region. As we showed above with the zeroth-order drift equations, the relative electron–ion drift can become very large when an external electric field is applied to the plasma. The result is a two-stream instability which is strongly field-aligned (the supersonic electrons and resulting disturbances travel in directions almost completely perpendicular to $\mathbf{B}$).

The linear fluid equations above successfully predict this instability and many of its characteristics (approximately), such as its field-aligned nature, phase velocity and growth rate, and the $\mathbf{V_d}$ (or equivalently, $\mathbf{E}$) threshold required for wave growth. However, there are several aspects of the linear theory which are not adequate to describe experimental observations. For example, the backscatter spectrum is not predicted at all, including any "scattering cross section" type parameter or amplitude saturation level. We know that the phase velocity (measured as Doppler velocity by radars) depends loosely on the ion acoustic speed, but we have no way of measuring

(except through ISR and rocket experiments) the plasma temperature or predicting heating effects as the scattering volume goes unstable. Many of these problems are being pursued by tackling nonlinear theory (*e. g.*, as Hamza and St-Maurice have done [45, 46]) and running simulation experiments (such as those by Oppenheim *et al.* [93]). However, these studies are beyond the scope of this work.

4.2.1 The Ion Acoustic Dispersion Relation

The basic fluid dispersion relation for the Farley-Buneman instability can be derived from the linearized equation 4.27.

$$\frac{\psi}{\nu_i}\omega^2 + j(1+\psi)\omega - \left(j\mathbf{k}\cdot\mathbf{V_d} + \frac{\psi}{\nu_i}k_\perp^2 c_s^2 + \frac{v_{\mathrm{Th,e}}^2}{\nu_e}k_z^2\right) = 0 \tag{4.28}$$

Again, we let ω be complex with imaginary part Γ. We would like to solve for ω to determine the wave phase velocity and growth rate. Equation 4.28 is quadratic in ω, so we can solve it simply with the quadratic formula. However, the resulting expression is difficult to interpret; it involves a complicated square root term, and is not very useful for our purposes. Sahr [111] simplifies the solutions by using a Taylor expansion of the square root term, and uses the new expression to show that one of the two solutions for ω is very strongly damped, and can be ignored.

However, the usual method is to initially neglect the (ψ/ν_i) terms, since this factor is roughly 10^{-5} in the E region. Another common assumption is that $k_\perp \gg k_\parallel$, so we can let $k_z \to 0$. Then, we find

$$\omega_r = \frac{\mathbf{k}\cdot\mathbf{V_d}}{1+\psi} \tag{4.29}$$

Next, we substitute $\omega = \omega_r + j\Gamma$ into the dispersion relation (4.28), using equation 4.29 for ω_r where needed:

$$-\frac{\psi}{\nu_i}\omega_r^2 + \frac{\psi}{\nu_i}\Gamma^2 - j2\frac{\psi}{\nu_i}\Gamma\omega_r - j(1+\psi)\omega_r + (1+\psi)\Gamma + j\mathbf{k}\cdot\mathbf{V_d} + \frac{\psi}{\nu_i}k^2c_s^2 = 0 \tag{4.30}$$

The $(1+\psi)$ terms cancel; we assume $\Gamma \ll \omega_r$ so that we can ignore the Γ^2 term. Then taking the real part of equation 4.30, we get the rest of the solution for ω:

$$\Gamma = \frac{1}{1+\psi}\left[\frac{\psi}{\nu_i}(\omega_r^2 - k^2 c_s^2)\right] \tag{4.31}$$

Equations 4.29 and 4.31 represent the growing, or marginally damped, ion acoustic wave mode. We concentrate our analysis on this solution, since we cannot expect to observe the strongly damped mode with ground-based coherent radars.

The ratio $\omega_r/k = (\mathbf{k}\cdot\mathbf{V_d})/k(1+\psi)$ is the phase velocity of the longitudinal wave; radars measure this as a Doppler velocity when $\mathbf{k}_{\text{radar}}$ is appropriately related to $\mathbf{k}_{\text{wave}}$. If $\mathbf{V_d}$ can be measured, then we have a chance to estimate the applied electric field, which is related to $\mathbf{V_d}$ through equations 4.15. Approximating the relative electron-ion drift as the $\mathbf{E}\times\mathbf{B}$ velocity makes this estimation very straightforward, if not exactly accurate.

4.2.2 Instability Threshold

Growing plasma density irregularities occur when the the growth rate Γ is positive; we can calculate the threshold for instability in this way. We find that the following condition holds when coherent scatter radars detect Farley-Buneman irregularities:

$$\mathbf{k}\cdot\mathbf{V_d} > kc_s(1+\psi) \tag{4.32}$$

If the irregularity wavevector $\mathbf{k}$ is parallel to $\mathbf{V_d}$, the condition for instability is $V_d > c_s(1+\psi) \approx c_s$. In general, the angle θ between $\mathbf{k}_{\text{irr}}$ and $\mathbf{V_d}$ is called the flow angle, and we have $V_d\cos\theta > c_s(1+\psi)$. (The geometric relationships between $\mathbf{B}$, $\mathbf{E}$, $\mathbf{V_d}$, and $\mathbf{k}$ are illustrated in Figure 4.1.) Thus, the threshold drift velocity required for instability becomes much larger for waves at angles away from $\mathbf{V_d}$, and the phase velocity measured by radar remains near the acoustic speed c_s. However, this traditional "instability cone" interpretation has been questioned based on experimental results

[5], and instead, some scientists are concluding that $|\mathbf{V_d}|$ saturates near c_s, and slower phase speeds measured by radars observing at nonzero flow angles are due to line-of-sight (LOS) effects [J. Drexler, unpublished work, 2005]. In essence, scattering volumes have turbulent "multiple-scatter-direction" areas, that behave like specular reflection targets and travel very close to the $\mathbf{E} \times \mathbf{B}$ direction, rather than organized plane waves producing Bragg backscatter in a few well-defined, specific directions.

4.2.3 Magnetic Aspect Angle Sensitivity

The angle that a transmitter wavevector makes with linear scattering structures (such as rows of agricultural crops) or with the contour direction in stratified media (such as the magnetic field direction in the ionosphere) is called the aspect angle. Figure 4.1 shows the magnetic field aspect angle of an irregularity wave as well as its geometric orientation with respect to the electric field and $\mathbf{E} \times \mathbf{B}$ drift. (We have adopted the convention that a zero-degree aspect angle corresponds to a view angle normal to the stratified surface.)

Because of a dominant negative dependence on $k_\parallel$ (the wavevector component parallel to the magnetic field) in the Farley-Buneman irregularity growth rate [27], the waves are very strongly damped if $\mathbf{k}_\parallel$ is significant. (Thus, it is commonly assumed that $\mathbf{k}$ is equal to $\mathbf{k}_\perp$, as we have done here.) Therefore, we expect to receive backscatter from the two-stream irregularity waves only when the magnetic aspect angle is close to zero (when the radar wavevector is nearly perpendicular to the terrestrial magnetic field). Despite unmistakable predictions of strong magnetic aspect angle dependency in the linear plasma fluid theory, the tolerance is not well understood and confusing experimental data have been reported. Although in general an aspect angle greater than 2° away from perpendicular is considered "large," echoes from up to 14° off-perpendicular have been observed at 50 MHz [116] and at UHF (993

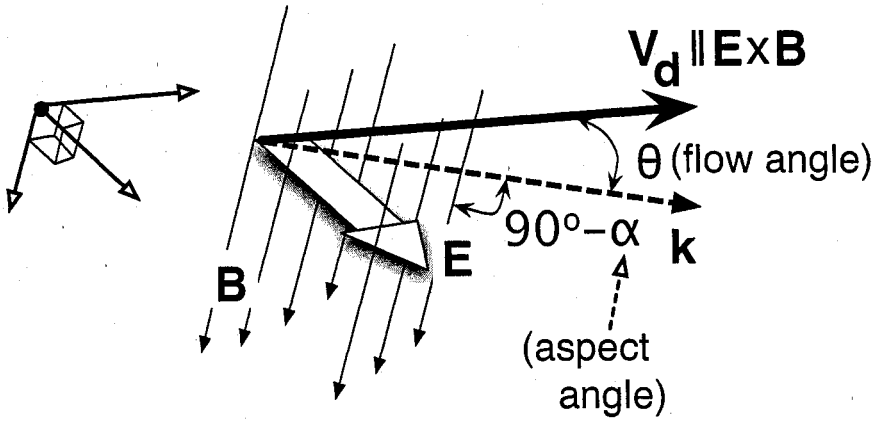

Figure 4.1: An illustration of the geometric relationships between magnetic field, electric field, electron drift velocity ($\mathbf{V_d}$), and an irregularity wavevector ($\mathbf{k}$). The flow angle is shown, marked as θ; the magnetic aspect angle is marked as α. $\mathbf{B}$, $\mathbf{E}$, and $\mathbf{V_d}$ (shown here in the $\mathbf{E} \times \mathbf{B}$ direction) make up three orthogonal directions. We use the convention that an aspect angle of 0° indicates a wavevector normal to the stratified surface.

MHz) Moorcroft and Schlegel detected coherent backscatter from a surprisingly high aspect angle of 6° [82]. Theoretical efforts to explain these observations focus on understanding the contributions of important nonlinear effects [44, 47]. Experimentally, scientists attempt to refine their techniques and reduce experimental ambiguities to make trustworthy measurements. Many authors have published aspect angle sensitivity rules for various operating frequencies (irregularity scale sizes). For example, Foster *et al.* report a dependence of -15 dB per degree away from perpendicularity [34]; their findings are based on experiments with the UHF Millstone Hill incoherent scatter radar, and thus are valid for irregularities of approximately 34 cm wavelength. Jackel *et al.* [55] measured magnetic aspect sensitivity with the EISCAT UHF radar system (16 cm irregularity wavelength), and found a variation of -5 dB/degree within 5°, decreasing to -3 dB/degree at 10°. A multitude of other observations at UHF as

well as VHF and HF have been reported; they do not often agree well and we do not try to summarize them here. At HF and low VHF radar frequencies, unusually large aspect angle observations are often attributed to refractive effects, and some authors have attempted to model these effects and correct their measurements for this problem [81, 128, 42].

The question of aspect sensitivity is a worthwhile object of study. Considering the speculation mentioned above about line-of-sight scatter from irregularities, and the result (given in Chapter 5) that a finite-sized wave packet irregularity model allows reduced backscatter to occur in arbitrary directions, we could view aspect sensitivity as related to the scattering coefficient for a particular line of sight rather than the amplitude of an off-perpendicular propagating wave. There are interesting implications for Doppler spectra as well; for example, waves propagating in off-perpendicular directions are more strongly damped, and therefore will have shorter lifetimes and wider spectra.

4.2.4 Instabilities as Tracers for Large Electric Fields

Another interpretation of equation 4.32, based on the importance of electric field in determining $\mathbf{V_d}$, is that an instability exists subject to the availability of an electric field $\mathbf{E_0}$ of sufficient magnitude to drive the electrons through the ions at a speed greater than the ion acoustic speed. At altitudes of 100 km, this works out to a field strength of 15–20 mV/m or greater [32]. Therefore, plasma density irregularities can be used as tracers for strong (above instability threshold) electric fields in the ionosphere. This allows coherent scatter radars to monitor electric field structures, and sometimes to estimate field magnitude and direction.

The Farley-Buneman instability mechanism is valid in the E region (approximately 90–180 km altitude) only; at higher altitudes the plasma temperature increases, re-

quiring prohibitively strong electric fields to drive the instability, and the ions are also increasingly better magnetized, reducing $\mathbf{V_d}$. At lower altitudes, as neutral density increases exponentially, collision frequencies for both species increase faster than their gyrofrequencies, and plasma density decreases as well.

4.3 Origin of Electric Fields in the Ionosphere

So far we have been concerned with what we like to call the "micro-physics" of E region plasma density irregularities. The application of external electric fields which drive the individual instabilities we study and observe with our radar requires us to consider, and allows us to make inferences about, the "macro-physical" effects which cause those electric fields to appear. For example, a model of magnetospheric convection may predict a strong electric field to be mapped down magnetic field lines to lower altitudes during certain times of day or under certain conditions which in turn could be dependent on solar activity. (We say more about magnetosphere-ionosphere coupling in section 2.3.) Thus, although an individual radar has a limited field of view, we have a chance to couple one instrument's measurements with many others and join a truly global effort in providing observations and evaluating large-scale models.

The spirit of this idea has been captured in the field of radio science by the SuperDARN community ([4], for example), and recently by Dr. Frank Lind in his proposal to put tens of receivers along the US-Canada border for use in passive radar surveillance of the midlatitude E region ionosphere [personal communication, 2005]. Lind's project is dubbed ISIS, for Intercepting Signals for Ionospheric Science. The MRR, originally designed and built by Sahr and Lind [110], is a small but growing version (now a part) of ISIS. We say more about distributed radar remote sensing in chapters 3 (page 35) and 6 (page 108) of this work.

In summary, we list several macro-physical processes that can cause instability-generating electric fields in the ionosphere. In the E region, neutral winds are collisionally coupled to ions, and thus tend to separate them from electrons, creating polarization electric fields [7]. At higher altitudes, localized polarization fields may also be generated on the edges of sharp density gradients at midlatitudes [121] or at the boundaries of regions of energetic electron precipitation at auroral latitudes [Lind, 2004, personal communication]. Electric fields also arise as a result of magnetospheric convection, as we mentioned above (*e. g.*, the 2-cell pattern over the polar cap). Because of the relatively high conductivity along magnetic field lines, electric fields generated in the magnetosphere will map along field lines down to lower altitudes. Electric fields in the ionosphere can also arise from dynamo processes as ionized material is moved through the terrestrial magnetic field, as in the equatorial electrojet.

Chapter 5

SPATIALLY LOCALIZED ANALYSIS OF IONOSPHERIC IRREGULARITIES

In this chapter we present new linear fluid theory for the high latitude E region based on modeling the two-stream instability disturbances as spatially-localized wave packets, rather than infinite plane waves.

5.1 Motivation for a New Model

The original motivation for deriving the ionospheric two-stream instability with wave packet perturbations was to understand the instability behavior and resulting radar data in a theoretical framework which is "aware" of spatially localized effects. First of all, the infinite-plane wave model for plasma disturbances, while mathematically convenient, is not particularly accurate in a physical sense, and may not even be a decent approximation of the instability form. A typical irregularity lifetime is 10 ms [41]; at 400 m/s it may affect a region 4 meters long, depending on the original area over which the instability conditions were met. On the other hand, the MRR range resolution is 1.5 km. Assuming an entire "active" range cell is filled by a plane wave or waves seems unreasonable. Also, Meyer [76] showed through interferometric imaging that the "hot spots" in the scattering regions observed by the MRR were quite limited in transverse (perpendicular to the radar beam) extent, sometimes only a few kilometers wide. While a few square kilometers is still rather a large area, especially compared to the plasma wavelength (1.5 meters in the case of MRR), it is far finer resolution than has previously been available in high-latitude VHF auroral

radar experiments (*e. g.*, CUPRI, which had a range resolution of 6 km [108]; STARE, 20 km [89]; and SABRE, 20 km [115]). We hypothesize that the scattering volumes observed by radars contain a limited population of individual instability instances, rather than an approximately uniform, large-area plane wave. Developing a body of theory to describe the behavior of spatially-localized instabilities in the high latitude E region is a step toward testing this hypothesis.

Understanding localization effects should also lead to insights into the energy dissipation mechanisms of the waves: for example, whether they are inherently dispersive or self-focusing. The fluid development given here shows promising descriptions of wave steepening and packet-shape-changing effects, which are surprising as they result from linear theory.

An interesting feature of our wave packet irregularity model is that it provides an opportunity to explicitly decouple the group and phase velocities. While the phase velocity is the usual ω/k, the group velocity is now effectively the drift velocity of the wave envelope, which can be specified as a model parameter. In the sections below, we compare this artificial group velocity with $\partial\omega/\partial\mathbf{k}$. This is useful for evaluating the appropriateness of the model, and in determining the conditions under which the wave envelope may change shape as it propagates. Also, it is possible to show that the instability wave packets have a "preferred" propagation velocity, which we determine.

Finally, we are intrigued by the ability of a spatially-limited wave packet perturbation model to produce backscatter given illumination from multiple directions, rather than backscattering in a single direction only, as in idealized Bragg scatter from plane waves. Modeling the instabilities in this way may lead to a better understanding of the Doppler shifts and flow angles measured by radars, and help account for other effects such as scatter from large aspect angles. We describe this last point in more detail in the following section.

5.1.1 *Bragg Scatter from Spatially-Limited Waves*

Radars detect Bragg scatter from plane waves in only one well-defined direction and scale-size ($\mathbf{k}_{\text{wave}} = -2\mathbf{k}_{\text{radar}}$, in the monostatic approximation). The traditional analysis method of Fourier transforming the medium gives the appearance of plane waves moving in any direction $\mathbf{k}$ takes. However, an alternate interpretation of the Farley-Buneman dispersion relation is that there is a single preferred direction of propagation for disturbances, $\mathbf{V_d} \approx \mathbf{E} \times \mathbf{B}$. In fact, Moorcroft [78] and Drexler *et al.* [18] have shown, using the Farley-Buneman dispersion relation, that the wave group velocity is completely independent of $\mathbf{k}$ for the field-aligned case ($k_{\|} = 0$), and that the phase velocity is just the projection of the group velocity in the direction of $\mathbf{k}$: $\mathbf{V_{ph}} = \hat{\mathbf{k}}\omega/k = (\hat{\mathbf{k}} \cdot (\partial\omega/\partial\mathbf{k}))\hat{\mathbf{k}} = (\hat{\mathbf{k}} \cdot \mathbf{V_g})\hat{\mathbf{k}}$.

Several attempts have been made to experimentally determine the relationship between $\mathbf{V_d}$ and phase velocity measurements. In other words, when radars detect coherent backscatter – for example, under instability threshold conditions – is $V_d \cos\theta \approx c_s$, with the radar measuring pure Bragg scatter from a plane wave pointed in the radar direction, or is $V_d \approx c_s$, with the radar measuring a line-of-sight (LOS) projection of a "hard target" velocity? (These experiments are complicated by the fact that the true acoustic speed is rarely known, except in experiments involving rocket flights or incoherent scatter radars.) The first case implies that Bragg scatter could be observed from waves with nearly any flow angle as long as V_d were large enough; physical limitations on the magnitude of $\mathbf{V_d}$ would then imply that we should observe scatter from waves with larger flow angles less frequently. So far, the experimental evidence on this topic is inconclusive, and difficult to obtain due to the necessity of knowing both $\mathbf{V_d}$ and precise scatterer locations. However, from a study using the EISCAT UHF radar system, Jackel *et al.* report that "observed coherent phase velocities from all three stations were found to be roughly consistent with LOS

measurements of a common E-region phase velocity vector" [55]. Also, Bahcivan *et al.* report Doppler shifts that closely follow $c_s \cos\theta$ in a rocket-radar combination study [5], which would imply that waves exist for below-threshold V_d if indeed the radar is observing pure plane wave scatter. Nielsen *et al.* report Doppler shifts that follow the component of the electron drift velocity (measured with EISCAT) along the coherent radar line of sight (STARE) [86]. These results seem to indicate that the phase velocity we measure is a LOS version of $V_d \approx c_s$. But this requires radars to be able to detect scatter from waves while observing them from directions that are not parallel to the wave $\mathbf{k}$. This possibility has been justified with the vague argument that an area of strong turbulence may have energy at many spatial Fourier components and rotated k-vectors. We propose that a simpler, linear model may give us the desired result of LOS scatter from Farley-Buneman waves as if they were specular targets. This model is simply a wavelet rather than a plane wave: we add an envelope function to the classical harmonic time and space dependence. The envelope may be reasonably specified as a number of different functions, or left as arbitrary during analysis. We will investigate specific wave packet envelopes in section 5.3.

We claim that the wave packet model allows radars to observe scatter from plane waves in arbitrary directions. To illustrate this, we turn to the wave equation in a medium with a first-order perturbation in the index of refraction:

$$\left[\nabla^2 - \frac{1}{V_{ph}^2}\frac{\partial^2}{\partial t^2}\right] u = 0 \tag{5.1}$$

$$\left[\nabla^2 - \frac{(1+\epsilon n(\mathbf{x},t))^2}{c^2}\frac{\partial^2}{\partial t^2}\right] u = 0 \tag{5.2}$$

Here, u is a representation of a wave amplitude. We will assume u varies harmonically in time as $\exp(-j\omega t)$ and is composed of an incident transmitter wave $\exp(j\mathbf{k_0}\cdot\mathbf{x})$ and some first-order arbitrary scatter $\epsilon u_1(\mathbf{x})$. (Note that we use the "physicists' convention" for the sign of ω and k in the wave.) Substituting this form for u into

the perturbed wave equation (5.2), we get

$$e^{-j\omega t}\left[-k_0^2 e^{j\mathbf{k_0}\cdot\mathbf{x}} + \epsilon\nabla^2 u_1(\mathbf{x}) + \frac{\omega^2}{c^2}(1 + 2\epsilon n(\mathbf{x},t) + \epsilon^2 n(\mathbf{x},t)^2)\left(e^{j\mathbf{k_0}\cdot\mathbf{x}} + \epsilon u_1(\mathbf{x})\right)\right] = 0 \tag{5.3}$$

$$-k_0^2 e^{j\mathbf{k_0}\cdot\mathbf{x}} + \epsilon\nabla^2 u_1(\mathbf{x}) + k_0^2 e^{j\mathbf{k_0}\cdot\mathbf{x}} + \epsilon k_0^2 u_1(\mathbf{x}) + 2\epsilon k_0^2 n(\mathbf{x},t) e^{j\mathbf{k_0}\cdot\mathbf{x}} = 0 \tag{5.4}$$

In equation 5.4, we have divided out $\exp(-j\omega t)$, used $\omega^2/c^2 = k_0^2$, and discarded the second-order terms involving ϵ^2. Next, we take the Fourier transform to get

$$-k_0^2 - \epsilon k^2 u_1(\mathbf{k}) + k_0^2 + \epsilon k_0^2 u_1(\mathbf{k}) + 2\epsilon k_0^2 n(\mathbf{k},\omega) * \delta(\mathbf{k} - \mathbf{k_0}) = 0 \tag{5.5}$$

$$u_1(\mathbf{k}) = \frac{2k_0^2 n(\mathbf{k} - \mathbf{k_0}, \omega)}{k^2 - k_0^2} \tag{5.6}$$

We can use equation 5.6 to show several interesting results. First, substituting $\mathbf{k} = -\mathbf{k_0}$ shows that the backscattered wave is extremely sensitive to structures with scale size $\lambda_{TX}/2$ (*i. e.*, $n(-2\mathbf{k_0})$). This is the well-known Bragg scatter result. (The unbounded denominator just shows that $u_1 = \exp(-j\mathbf{k_0}\cdot\mathbf{x})$ solves the wave equation when we ignore the small term involving u_1 and the perturbation of n.)

Next, if we choose n to be a plane wave with spatial frequency $\mathbf{k_1}$, then

$$u_1(\mathbf{k}) = \frac{2k_0^2\delta(\mathbf{k} - \mathbf{k_0} - \mathbf{k_1})}{k^2 - k_0^2} \tag{5.7}$$

and the backscatter $u_1(-\mathbf{k_0})$ is nonzero only if $\mathbf{k_1} = -2\mathbf{k_0}$: the plane wave propagation vector must be pointed at the radar receiver and of the correct scale size to be detected. However, if we now impose an isotropic, immobile, 3-D Gaussian envelope on the wave perturbation:

$$n(\mathbf{x}) = w(\mathbf{x})e^{j\mathbf{k_1}\cdot\mathbf{x}} \tag{5.8}$$

$$= \exp\left(-\frac{2}{L^2}\mathbf{x}\cdot\mathbf{x}\right)e^{j\mathbf{k_1}\cdot\mathbf{x}} \tag{5.9}$$

its Fourier transform is [1]:

$$n(\mathbf{k}) = \sqrt{\frac{\pi L^2}{2}}\exp\left(-\frac{L^2}{8}\mathbf{k}\cdot\mathbf{k}\right) * \delta(\mathbf{k} - \mathbf{k_1}) \tag{5.10}$$

and we obtain

$$u_1(\mathbf{k}) = \frac{2k_0^2\sqrt{\frac{\pi L^2}{2}}}{k^2 - k_0^2} \times \exp\left[\left(-\frac{L^2}{8}\right)\left(k^2 - 2\mathbf{k}\cdot\mathbf{k_0} - 2\mathbf{k}\cdot\mathbf{k_1} + k_0^2 + 2\mathbf{k_0}\cdot\mathbf{k_1} + k_1^2\right)\right] \tag{5.11}$$

$$u_1(-\mathbf{k_0}) = \frac{2k_0^2\sqrt{\frac{\pi L^2}{2}}}{k^2 - k_0^2} \exp\left[\left(-\frac{L^2}{8}\right)\left(4k_0^2 + 4\mathbf{k_0}\cdot\mathbf{k_1} + k_1^2\right)\right] \tag{5.12}$$

Now we can see that the maximum backscatter occurs when the Gaussian exponent $4k_0^2 + 4\mathbf{k_0}\cdot\mathbf{k_1} + k_1^2 = 0$. This is true when $\mathbf{k_1} = -2\mathbf{k_0}$, as before, but the backscatter still exists even when $\mathbf{k_0} \perp \mathbf{k_1}$.

Thus, modeling perturbations of a medium as wave packets allows us to expect radar backscatter from waves traveling in directions outside of the radar LOS. Moorcroft also comes to this conclusion by modeling electron density with wave packets in a study of scattering coefficient sensitivity to magnetic aspect angle [79]. Here, we model ionospheric two-stream waves as wave packets to determine the packets' behavior. We direct a large amount of attention to spatially-localized effects on wave packet phase (*i. e.* Doppler) and group velocities.

In addition to producing scatter in multiple directions, the wave packet model allows the *linear* coupling of energy into spatial Fourier components other than that of the primary wave (excited by the original streaming or gradient drift instability). This is because, in Fourier space, the localized plane wave is the Fourier transform of the envelope (which has finite bandwidth) centered at the plane wave frequency. While Sudan [124, 123] explains the transfer of energy from large to smaller wavelengths by nonlinear effects such as cascading eddies and wave steepening, the convolution with a finite bandwidth function in the frequency domain allows energy from the primary wave to spread into other scale sizes without resorting to turbulence. Of

course, nonlinear effects are definitely important for understanding the plasma density irregularities, whose amplitudes can reach up to 10% of the background density [100]. We just prefer to devise explanations with linear theory whenever possible, because it is more tractable.

Our primary goal in deriving the "spatially local" Farley-Buneman dispersion relation is to identify growing wave modes (*i. e.*, ones that can be detected with coherent radar) and understand the additional effects of the wave packet model parameters on the well-known phase velocity, growth rate, and instability threshold. Though it is not always feasible to obtain an analytic expression for the phase velocity and growth rate, we also solve the dispersion relation for ω numerically for sweeps of parameters, as Lind did [72].

5.2 Related Work

Previously Moorcroft investigated the effect on the radar scattering coefficient ($\sigma \propto |n_e(\mathbf{k})|^2$) of different electron density models based on wave packets of varying wavelength and orientation [79]. He considered scattering regions filled to a certain fraction with wave packets having several different distributions of features [80]. The primary focus of his work in these two papers [79, 80] is to understand magnetic aspect angle sensitivity and to attempt to explain experimental measurements of high (off-perpendicular) aspect angle echoes. Later, in 1992, Donovan and Moorcroft used the Gaussian wave-packet scattering model in a Monte Carlo study of multiple scattering in the auroral electrojet [17].

Using an "intermittency formulation" [43] of E region irregularity theory, St.–Maurice and Hamza introduced the concept of "blobs" and "holes" in 2001 [118]. They claim that while linearly unstable objects can be either plane waves or finite size irregularities, in the nonlinear regime plane waves must break into blobs and

holes due to rotation of the local wave electric field vector (when large amplitude perturbations in $\mathbf{E}$ are too significant to ignore). They obtained an expression for the "blob velocity" using a 3-D nonlinear fluid treatment: a group velocity given by the $\mathbf{E} \times \mathbf{B}$ drift, in which $\mathbf{E}$ is given by the rotated electric field inside the blob.

Drexler *et al.* describe a "nonlocal" theory of the Farley-Buneman instability which paradoxically is somewhat similar to our "localized" theory [18]. In their 2002 paper, "nonlocal" implies "convecting" and takes into consideration changes in the medium; the contrast is with plane wave theory which implicitly assumes that the medium is homogeneous. Actually, the anisotropy parameter ψ varies significantly over the altitude range which is unstable to Farley-Buneman turbulence, and this means that the wave frequency ω is also a function of location. Drexler *et al.* studied wave evolution after removing the constraint that ψ is constant, with the ultimate goal of shedding light on the apparent phase speed saturation at the ion acoustic velocity. They found that due to "nonlocal" (*i. e.* inhomogeneous medium) effects, waves necessarily take on "3-D characteristics" such as nonzero aspect angle and vertical group velocity, and finite instability volumes distort and short out along magnetic field lines [18]. They also derive a general expression for wave growth rate that includes a convective derivative of the wave amplitude; we come to a somewhat similar growth rate formulation below by substituting expressions for wave envelope amplitude directly into the differential equation describing the medium.

Ronchi *et al.* developed a similar nonlocal (inhomogeneous medium) theory in 1989 for larger scale gradient drift instabilities in the equatorial electrojet [106]. Others have used their nonlocal ideas when interpreting coherent scatter obtained at the Jicamarca Radio Observatory, which is near the magnetic equator [53].

There have been several studies of pulse–particle interactions in plasmas; for example, Akimoto studied the effect on ambient plasma of electrostatic and electro-

magnetic wave packets traveling through magnetized plasma populations with both theory and simulation [2].

Finally, our wave packet model may remind the reader of "solitons," or the solitary waves which are solutions to some nonlinear differential equations (such as the Korteweg–de Vries (KdV) equation [14]). These structures retain their wave envelope-like shape while propagating due to a precise balance of dispersion and nonlinearity [85]. Our wave packets and the model for their behavior are purely linear.

5.3 A Spatially Localized Fluid Model

We now derive the Farley-Buneman dispersion relation using linear fluid theory as before, except with the perturbation quantities n_1 and $\mathbf{E}_1$ modeled as plane waves ($e^{-j\omega t}e^{j\mathbf{k}\cdot\mathbf{x}}$) with an added envelope function. We will begin with a general 1-D treatment, and then discuss the specific Gaussian envelope case in depth, including a three dimensional treatment.

With the traditional plane wave solutions to the fluid equations, $\partial/\partial t \rightarrow -j\omega$ and $\nabla \rightarrow j\mathbf{k}$. Thus, the differential equation becomes algebraic in ω and $\mathbf{k}$. No wave packet envelope will be an eigenfunction of the linear fluid system, so we will have to deal with dependencies on space and time in our dispersion relation. While this may seem unusual, the very nature of the disturbance model – localized in space, convecting in time – means that the solutions for ω, or constraints imposed on the evolution of the disturbance, depend on where (and when) in the medium one seeks the solution. We discuss the nature of the space and time dependence for several cases below.

Although there are unavoidable analytic difficulties associated with the wave packet envelopes, we can still choose a convenient envelope function. An advantage to using an exponential (such as a Gaussian distribution-shaped function) for

the envelope is that, like the normal plane wave solutions, derivatives result in factors identical to the original wave disturbance. Since $\exp(\cdot) \neq 0$, we can factor out the actual wavelets from the first-order differential equations to yield coefficient equations.

We will still take k to be real-valued and allow ω to be complex. Thus, the wavelet will be windowed in space and have a lifetime characterized by growth and/or decay rates. A solution for $\omega = \omega_r + j\Gamma$ with a positive imaginary part indicates a growing wave mode, and one that is likely to be seen with a coherent radar system such as our own.

Finally, we should make a few "scale analysis" arguments to ensure that we consider only appropriate wave packet parameters. The wave packet model is valid only if the intrinsic packet size, which we denote L, is much larger than the irregularity wavelength. In other words, we require a wave packet to contain many wavelengths. Similarly, when considering radar observations of the wave packets we should assume that L is small compared to the scattering volume; otherwise, the spatially-localized effect is lost. As L gets very large, the irregularity behavior approaches the plane wave case. Also, since the localized dispersion relation is a function of space and time, we must take care to limit our analysis to regions where the wave packet amplitude is significant.

5.3.1 General Dispersion Relation in One Dimension

To begin our discussion of spatially localized irregularities, we derive the 1-D ion acoustic dispersion relation for a plane wave with an arbitrary envelope function. Starting with the 3-D differential equation for E region plasma given in equation 4.27, we simplify the system to 1-D by letting $\partial/\partial y = \partial/\partial z = 0$ ($\mathbf{k} \rightarrow k_x\hat{x}$). We have chosen the $\hat{x}$ direction because that is the direction of the $\mathbf{E_0} \times \mathbf{B}$ drift and of the most important part of $\mathbf{V_d}$, the source of energy for the Farley-Buneman instability.

(As before, we assume $\mathbf{B} = B\hat{z}$ and $\mathbf{E_0} = E_0\hat{y}$.)

We will denote the factors resulting from taking derivatives of the wave packet generally as $\mathcal{W}$ for time derivatives and $\mathcal{K}$ for spatial derivatives (see, for example, equations 5.15 and 5.16). If the envelope function is exponential, the wave packet itself is an understood nonzero multiplicative factor in the fluid equation. (Note that any arbitrary envelope function $\eta(t,x)$ can be written $\exp(\ln(\eta))$; therefore, with the caveat that one must be careful when $\eta = 0$, we do not lose generality by assuming the envelope is in exponential form.) The resulting equation is

$$\frac{\psi}{\nu_i}\left(\mathcal{W}^2 + \frac{\partial}{\partial t}\mathcal{W}\right) + (1+\psi)\mathcal{W} + V_d\mathcal{K} - \frac{\psi}{\nu_i}c_s^2\left(\mathcal{K}^2 + \frac{\partial}{\partial x}\mathcal{K}\right) = 0 \tag{5.13}$$

Now that we have a general form for the 1-D dispersion relation, we can make substitutions for $\mathcal{W}$ and $\mathcal{K}$ based on specific wave packet envelopes we wish to study. For any envelope other than unity (the pure plane wave case), there will be additional factor(s) introduced by the derivatives, which will complicate the dispersion relation. Our goal is to explore the impact of these new terms on the instability behavior.

5.3.2 Simple Gaussian Envelope in One Dimension

We first choose to investigate wave packets with a Gaussian-shaped envelope, given here in one dimension (x):

$$w(t,x) = e^{-j\omega t}e^{jkx}\exp\left(-\frac{2}{L^2}(x-vt)^2\right) \tag{5.14}$$

The wave packet center, vt, depends on time (the packet is moving). The wave packet velocity v is like a group velocity and L is the "two-standard-deviations" width; the majority of the wavelet energy is within $L/2$ meters of the window center. With the Gaussian envelope, the plane wave derivative factors in 1-D become

$$\frac{\partial}{\partial t} \;\rightarrow\; \mathcal{W} = -j\omega + \frac{4v}{L^2}(x-vt) \tag{5.15}$$

$$\frac{\partial}{\partial x} \rightarrow \mathcal{K} = jk - \frac{4}{L^2}(x - vt) \tag{5.16}$$

$$\frac{\partial^2}{\partial t^2} \rightarrow \mathcal{W}^2 + \frac{\partial}{\partial t}\mathcal{W} = -\omega^2 - j\frac{8}{L^2}v\omega(x - vt) + \frac{16}{L^4}v^2(x - vt)^2 - \frac{4v^2}{L^2} \tag{5.17}$$

$$\frac{\partial^2}{\partial x^2} \rightarrow \mathcal{K}^2 + \frac{\partial}{\partial x}\mathcal{K} = -k^2 - j\frac{8}{L^2}k(x - vt) + \frac{16}{L^4}(x - vt)^2 - \frac{4}{L^2} \tag{5.18}$$

The new factors contain dependence on time (t) and space (x), as well as the two new parameters L and v. We substitute this $\mathcal{W}$ and $\mathcal{K}$ into equation 5.13 to obtain the 1-D Gaussian wave packet dispersion relation. The resulting equation is a bit unruly; we present it in different ways below to illustrate certain features and possible solutions.

Organization of Terms by Relative Size

We have assumed that the intrinsic wave packet length $L \gg \lambda$, the irregularity scale length. Therefore, the quantity $1/L$ can be considered small compared to k. To illustrate the relative importance of terms in the dispersion relation, we organize it in factors of $1/L$. The Gaussian wave packet dispersion relation in 1-D is then

$$\begin{aligned}
L^0 \quad & \left[-\frac{\psi}{\nu_i}\omega^2 - j\left(1+\psi\right)\omega + jkV_d + \frac{\psi}{\nu_i}k^2c_s^2\right] + \\
L^{-2} \quad & (x - vt)\left[-j8v\frac{\psi}{\nu_i}\omega + j8\frac{\psi}{\nu_i}kc_s^2 + 4(1+\psi)v - 4V_d\right] - L^{-2}4\frac{\psi}{\nu_i}(v^2 - c_s^2) + \\
L^{-4} \quad & (x - vt)^2\left[16\frac{\psi}{\nu_i}(v^2 - c_s^2)\right] = 0
\end{aligned} \tag{5.19}$$

Note that if we let $L \rightarrow \infty$, we can recover the "original" (plane wave) dispersion relation; this is consistent with the role of L in the wave packet model. The L^0 term above is a one-dimensional version of the dispersion relation given in equation 4.28. In this sense, all the plane wave fluid theory to date has inherently assumed infinite disturbance scale length. To the extent that L is finite, the L^{-2} and L^{-4} terms represent corrections to existing theory based on the spatially localized model that we will discuss.

The Gaussian envelope is a particularly convenient model, because in this case, the space and time dependence is limited to the correction factors, as we see from equation 5.19. In other words, the consequences of the wave envelope not being an eigenfunction of the physical system are limited to extra additive terms in the dispersion relation; they do not "corrupt" the basic plane wave response. Furthermore, the x and t dependence is completely contained in the $(x-vt)$ terms, which cleanly factor out of the "medium dependence" expressions in both the L^{-2} and L^{-4} cases. However, the new parameter v (packet propagation speed) is present in several medium-related terms.

A Simple Substitution

For a first crack at interpreting equation 5.19, we would like to avoid dealing with the dependence on space and time, and concentrate on determining the roles of the new parameters v and L. Therefore, we consider a constant substitution for the factor $(x - vt)$. The Gaussian wave envelope is maximum – and the wave packet makes its most relevant contribution to radar backscatter – at its center, when $x = vt$. However, in this case, $(x - vt) = 0$, and we are left with only the L^0 (plane wave) dispersion relation plus the $L^{-2}(v^2 - c_s^2)$ term, which yields the marginally damped / growing solution

$$\omega_r = \frac{kV_d}{1+\psi} \tag{5.20}$$

$$\Gamma = \frac{1}{1+\psi}\frac{\psi}{\nu_i}\left(\omega_r^2 - k^2c_s^2 + \frac{4}{L^2}(v^2 - c_s^2)\right) \tag{5.21}$$

which is essentially unchanged from the pure plane wave solution (further support for the idea that we are adding "small corrections" to the traditional plane wave dispersion relation).

On the other hand, if $(x - vt)$ is large (if we consider a location far from the

packet center, or equivalently, a time long after the packet has left), the wave envelope amplitude is small and its effect is inconsequential. Therefore, we are most interested in locations that are within a distance from the packet center that is on the order of the packet scale size. This leads us to the approximation $|x - vt| \sim L$.

We can use the substitution $(x - vt) = \pm L$ as a "quick and dirty" simplification to aid in comprehending complex expressions. However, since $(x - vt)$ factors out of most of the L-correction terms above, we don't really need this crutch, at least for the 1-D Gaussian case. It is somewhat useful when confronted with full 3-D wave packet dispersion relations.

A Solution to the Gaussian Packet Dispersion Relation

Before we bring out the big guns to find an analytical solution for ω from the Gaussian wave packet dispersion relation, we consider a simple solution in which the L-terms go to zero separately. As we mentioned above, it is convenient that the quantity $(x - vt)$ factors mostly out of the L-terms; the one exception becomes zero under the same condition $(v = c_s)$ that causes the L^{-4}-term to vanish. This means we can set each L-term to zero independently of x and t, treating it like a traditional dispersion relation. Therefore, we proceed with setting the square-bracketed expressions in equation 5.19 to zero.

The L^{-4} term in particular is suggestive because we see immediately that setting $v = c_s$ will "solve" it. This result is intriguing because it implies that the packet group velocity v tends toward the ion acoustic speed; this corroborates much confusing experimental evidence which is not yet thoroughly addressed by theory (we say more on this topic under "Phase Velocity and the Ion Acoustic Speed," page 75, below).

Setting $v = c_s$ throughout the dispersion relation, we now attempt to choose ω such that the remaining L^0 and L^{-2} terms also become zero. Because of the different-

order derivatives of the envelope function, each L-term is multiplied by a different functional form: a Gaussian shape for L^0, and first- and second-derivatives of Gaussian shapes for the L^{-2} and L^{-4} terms, respectively. (The Gaussian functions themselves have been left out of equation 5.19 because they are nonzero factors common to all the L-terms.) The second of these is an odd function, while the other two are even (see Figure 5.1). That they will cancel simultaneously, with shared parameters in their coefficients, is not guaranteed. Our goal was to find a range of solutions for ω, and/or a range of parameter constraints, that minimizes the residual. However, we find that there is a single case that works. It is the normal plane wave solution ($\omega_r = \frac{1}{1+\psi} k V_d$; $\Gamma = \frac{1}{1+\psi}\frac{\psi}{\nu_i}(\omega_r^2 - k^2 c_s^2)$), but it only works at the plane wave instability threshold, $V_d = (1+\psi)c_s$. Therefore, for this special case, the plane wave with a Gaussian envelope is actually an eigenfunction of the physical system.

In fact, attempting to solve { L^{-4} term $= 0$, L^{-2} term $= 0$, L^0 term $= 0$ } simultaneously for v, ω and k simply yields the constraint $V_d = (1+\psi)c_s$, which is the plane wave instability threshold. This is because setting $v = c_s$ (using the L^{-4} term) forces the threshold constraint on the system: V_d must equal $(1+\psi)c_s$ to cancel the real part of the L^{-2} expression, and likewise ω must be the regular plane wave solution to cancel the imaginary part (as well as the L^0 term). As we will see shortly from the complete expression for the wave packet growth rate, one condition for the wave packet instability threshold is $v = V_d/(1+\psi)$. Then, setting $V_d = (1+\psi)c_s$ implies $v = c_s$.

In other words, except under the instability threshold conditions, the form of the solution for ω is different from the plane wave case, and we must solve the entire dispersion relation at once.

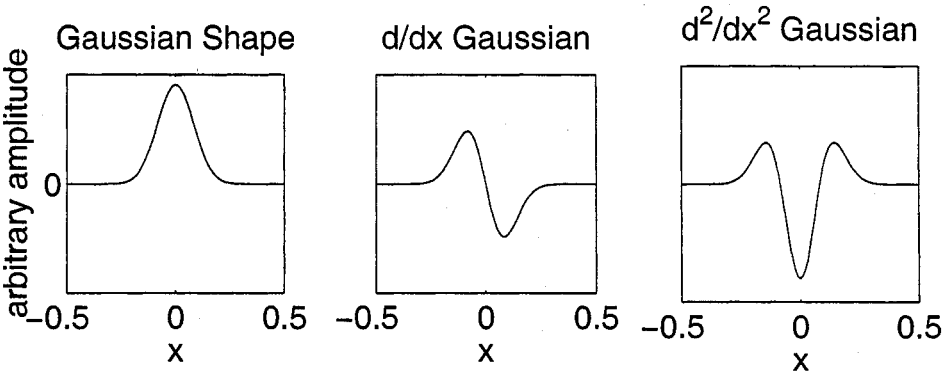

Figure 5.1: A Gaussian-shaped function (left plot), and its first and second derivatives.

The Complete Solution for the Gaussian Packet Dispersion Relation

Our technique for obtaining analytic, yet useful, solutions to the Gaussian wave packet dispersion relation is to use the quadratic formula (note that equation 5.19 is still quadratic in ω), and then compute series expansions of the ω solutions in the parameter ψ, which is small ($\psi = \nu_e\nu_i/(\Omega_e\Omega_i) \approx 0.03$ in the E region). We used a symbolic mathematics software package extensively for manipulating dispersion relations and their solutions. We choose to retain terms up through first order in ψ.

As in the usual plane wave theory, one of the two ω solutions represents a strongly damped wave mode: its growth rate Γ_{damped} contains the term $-\nu_i/\psi$, a large negative contribution (approximately -10^5 s^{-1}). The next most significant term in Γ_{damped} is $-\frac{\psi}{\nu_i}k^2(V_d^2 - c_s^2)$, negative when V_d exceeds the ion acoustic speed, thus ensuring that no growth occurs. We will ignore the strongly damped mode from this point forward. We present the real and imaginary parts of the solution representing the marginally damped / growing wave mode here:

$$\omega_r = (1-\psi)kV_d - 8\frac{\psi}{\nu_i}\frac{(x-vt)}{L^2}k(V_d^2 - c_s^2) + O(\psi^2) \tag{5.22}$$

$$\Gamma = \frac{\psi}{\nu_i}k^2(V_d^2 - c_s^2) + 4\frac{(x-vt)}{L^2}(V_d(1-\psi) - v) + \frac{4}{L^2}\frac{\psi}{\nu_i}(v^2 - c_s^2) - 16\frac{\psi}{\nu_i}\frac{(x-vt)^2}{L^4}(V_d^2 - c_s^2) + O(\psi^2) \tag{5.23}$$

First, we note that the L^{-2} and L^{-4} terms represent the new contributions due to the wave envelope. Treating the pure-plane wave dispersion relation similarly (expanding the quadratic formula solution about $\psi = 0$; keeping terms up to first order) yields

$$\omega_{r,\text{planewave}} = (1-\psi)kV_d + O(\psi^2) \tag{5.24}$$

$$\Gamma_{\text{planewave}} = \frac{\psi}{\nu_i}k^2(V_d^2 - c_s^2) + O(\psi^2) \tag{5.25}$$

Thus, if we let $L \to \infty$ in equations 5.22 and 5.23, we again recover the plane wave expression, a satisfying result.

As in the dispersion relation itself, the spatially-localized correction terms in ω_r and Γ depend on space and time. It turns out that these dependencies are important; it is from them that we derive most of our new insights from the spatially-localized theory. For example, just by inspection of the ω_r and Γ expressions, we see that the phase velocity, group velocity, and growth rate of the Farley-Buneman wave packets will be functions of space and time. This means that the wave pulses will change shape

over the duration of their lifetimes, even though they are not (to first order) dispersive (w_r has only k^1 terms). As the wave packet size L decreases, these effects become more pronounced, as expected. Normally we would expect to see such pulse-shape-changing behavior only in nonlinear analyses. We claim that using the wave envelopes, which are not eigenfunctions of the linear partial differential equation system, is a way of introducing "fake nonlinearity" into our analysis; it allows us to explore wave effects that depend on location (and/or time), in this case, up to second-order.

Wave Packet Phase and Group Velocity

Using equation 5.22 we can derive the phase velocity of the wave contained in the packet:

$$v_{\text{ph}} \equiv \frac{\omega_r}{k} = (1-\psi)V_d - 8\frac{\psi}{\nu_i}\frac{(x-vt)}{L^2}(V_d^2 - c_s^2) \tag{5.26}$$

If we let $L \to \infty$, and recall that $1/(1+\psi) = 1-\psi$ for small ψ, we can recover the 1-D version of the plane wave ω_r given in equation 4.29. The spatially-localized correction term depends on $(x-vt)$, and although it is small (with a factor of ψ/ν_i, approximately 10^{-5} seconds in the E region), it will cause the wave phase velocity to vary in space and time. We discuss this correction term in more detail after manipulating the wave velocity expressions a bit more.

In the 1-D, $O(\psi)$ case, the wave group velocity is the same as the phase velocity:

$$v_g \equiv \text{Re}\left\{\frac{\partial\omega}{\partial k}\right\} = (1-\psi)V_d - 8\frac{\psi}{\nu_i}\frac{(x-vt)}{L^2}(V_d^2 - c_s^2) \tag{5.27}$$

However, the model parameter v, the envelope velocity, can be considered a group velocity-like parameter, and we would prefer that v_g not be a function of v. So we let $v = v_g$ and re-solve for v_g. Then

$$v_g \text{ or } v \;=\; \frac{(1-\psi)V_d - 8\frac{\psi}{\nu_i}\frac{x}{L^2}(V_d^2 - c_s^2)}{1 - \underbrace{8\frac{\psi}{\nu_i}\frac{t}{L^2}(V_d^2 - c_s^2)}_{\text{small}}} \tag{5.28}$$

$$v_g \text{ or } v \approx (1-\psi)V_d + ((1-\psi)V_d t - x)\frac{8}{L^2}\frac{\psi}{\nu_i}(V_d^2 - c_s^2) \tag{5.29}$$

where we have used the geometric series expansion

$$\frac{a}{1-\epsilon} = a\,[1+\epsilon] + O(\epsilon^2)$$

with the quantity labeled "small" as ϵ and kept first order terms. We note that the ψ/ν_i terms are especially small because V_d is probably close to c_s.

Next, the phase velocity given in equation 5.26 is also a function of v, so for completeness, we substitute the new group/packet velocity expression (5.29) for v and re-solve for the phase velocity. Again keeping terms up to first order, we find

$$v_{\text{ph}} \approx (1-\psi)V_d + ((1-\psi)V_d t - x)\frac{8}{L^2}\frac{\psi}{\nu_i}(V_d^2 - c_s^2) \tag{5.30}$$

which is exactly the same as expression 5.29.

Finally, we can estimate the packet propagation speed v by a completely different method. We note that the growth rate (given by equation 5.23) depends on the factor $(x - vt)(V_d(1-\psi) - v)$. Change in growth rate over space and/or time could be a sign of propagation or perhaps even acceleration. Our numeric simulations of Farley-Buneman wave packets (section 5.3.3) confirm that the growth rate behavior changes for different values of v, and Γ switches from increasing in x to decreasing in x at a threshold value for v. If we choose $v > V_d$ (as in Figure 5.6), we see that Γ has a negative slope with respect to x, and if we choose $v < V_d$ (Figure 5.7), Γ has a positive slope over x.

By requiring the growth rate to be constant over space, a "preferred" or "stable" packet envelope velocity may emerge. Therefore, we set the derivative of Γ with respect to x to zero and solve for v (still keeping only first order terms):

$$\begin{aligned} \frac{\partial \Gamma}{\partial x} &= f(v) = 0 \\ \frac{\partial \Gamma}{\partial x} &= \frac{4}{L^2}(V_d(1-\psi) - v) - \frac{32}{L^4}\frac{\psi}{\nu_i}(V_d^2 - c_s^2)(x - vt) = 0 \qquad (5.31) \\ & \text{solve for } v\text{:} \\ v &\approx \underbrace{(1-\psi)V_d}_{\text{preferred}} + \underbrace{((1-\psi)V_d t - x)\,\frac{8}{L^2}\frac{\psi}{\nu_i}(V_d^2 - c_s^2)}_{\text{correction term}} \qquad (5.32) \end{aligned}$$

This technique has the very satisfying result that it yields exactly the same expression as that for v_g (with $v \equiv v_g$), given in equation 5.29, and for v_{ph}, given in equation 5.30. This is a strong suggestion that there is a "preferred" wave envelope propagation velocity v, which is the same as the group velocity of the wave contained in the packet, and that velocity is essentially equal to the relative electron-ion drift, V_d.

In all the wave velocity expressions, there is a small term that depends on location (the "correction term" in equation 5.32). The term is small due to its ψ/ν_i factor, but it nevertheless becomes more significant as L get smaller (as the disturbance is more localized). This term causes a shear in wave velocity (group, phase, and envelope) over space as follows:

$$\text{For } V_d > c_s\text{:} \begin{cases} \text{velocity slower for} & x > (1-\psi)V_d t \quad \text{(ahead of packet)} \\ \text{velocity faster for} & x < (1-\psi)V_d t \quad \text{(behind packet)} \end{cases} \qquad (5.33)$$

and the opposite results hold for $V_d < c_s$ (*i. e.*, if the packet propagates into a region in which V_d is sub-threshold, it will apparently undergo the opposite velocity shear before dissipating). This effect is more pronounced for greater $|V_d - c_s|$.

The velocity "divergence" is somewhat strange, since there are no corresponding dispersive terms in the velocity expressions (no dependence on k, at least to first order). However, the wave velocity is a function of position $(V_d t - x)$, which as we see from equation 5.33 has a dispersion-like effect. In fact, the wave packet has a range of associated wavenumbers due to its finite size; its k-bandwidth is approximately equal to $1/L$. Rearranging the growth rate expression (5.23) illustrates the fact that k is modified by the finite packet size. If the packet envelope velocity v is equal to its natural value V_d, we can write:

$$\Gamma \approx \frac{\psi}{\nu_i}(V_d^2 - c_s^2)\underbrace{\left(k^2 + \frac{4}{L^2} - \frac{16(x - V_d t)^2}{L^4}\right)}_{\text{new } k^2} \tag{5.34}$$

Comparing this expression with the original plane wave growth rate (equation 4.31), we see that the L-terms can be considered modifications to k^2. We note that $|x - V_d t| \leq L$ holds true when the wave packet has significant amplitude, so the range of k^2 over the finite-sized packet is:

$$\left(k^2 - \frac{12}{L^2}\right) \leq k^2 \leq \left(k^2 + \frac{4}{L^2}\right) \tag{5.35}$$

Phase Velocity and the Ion Acoustic Speed

Above, in our simple solution to the 1-D Gaussian packet dispersion relation, we found that the L^{-4} term solved independently implies $v = c_s$. This result was intriguing because, although much experimental evidence suggests that plasma irregularity phase velocities are limited to the ion acoustic speed c_s [26, 40], straightforward linear fluid theory predicts continuing wave phase velocity growth along with the driving electron drift. If V_d exceeds c_s (the instability threshold), we expect from linear theory that the Doppler shifts measured by radars will follow V_d, but instead they seem to remain approximately equal to c_s. The electron drift velocity has been shown to

significantly exceed the two-stream instability threshold, yet measured Doppler velocities still remain near the acoustic speed, as in a study by Nielsen *et al.* using the EISCAT UHF incoherent scatter radar in cooperation with the STARE coherent scatter auroral radar [86]. Many of the phase velocity experiments have been performed at equatorial latitudes [26], but the effect has also been documented at high latitudes [87, 88, 102]. The experimental results are somewhat dubious, since for the most part the experimenters have no way of actually measuring c_s, as Sahr and Fejer point out [109]. Even when the plasma temperatures are known (for example, if rocket or incoherent scatter radar data are available), we do not have an accurate expression for the sound speed in a non-isotropic, non-equilibrium plasma. Nevertheless, many theories have been proposed to explain the observations of waves whose phase velocities seem to be limited to the ion acoustic speed [18, 118, 45].

One rather handwaving, yet readily understood, explanation is that the largest waves producing the strongest radar backscatter (dominating the radar return) are those moving at threshold velocity, since they reach their maximum amplitude after propagating (and growing) through a region in which V_d exceeds c_s, and they cease to grow at the boundary of the unstable region, where $V_d = c_s$ [24]. A more complicated explanation, grounded in nonlinear fluid theory presented by Sudan [122, 123], is the idea that an "anomalous electron collision frequency" arises due to large amplitude-wave-enhanced diffusion across magnetic field lines. If the enhanced electron collision frequency is large enough, it could increase ψ such that the wave phase velocity $(V_d/(1+\psi))$ is limited (to c_s) [28]. Others have reached for a full nonlinear kinetic treatment to explain the effect [104].

The $(v^2 - c_s^2)$ terms in equation 5.19 suggested a possible explanation for phase speed saturation at c_s. However, it turns out that $v = c_s$ is only valid at exactly the instability threshold, in which case $V_d \approx c_s$. Since we have shown (in equation

5.32) that $v \approx V_d$, this particular aspect of the spatially-localized theory does not contribute any insight into the phenomenon of wave phase velocities – or at least measured Doppler velocities – being limited to c_s despite super-threshold V_d.

Wave Packet Instability Threshold

With the plane wave model as well as our own spatially-localized disturbance model, E region irregularities occur (and can be detected by radars) when the growth rate $\Gamma > 0$. Therefore, as in section 4.2, we solve for $\Gamma = 0$ to find the minimum conditions for wave packet instability. Consulting equation 5.23, reprinted here for convenience,

$$\Gamma = \frac{\psi}{\nu_i}k^2(V_d^2 - c_s^2) + 4\frac{(x-vt)}{L^2}(V_d(1-\psi) - v) + \frac{4}{L^2}\frac{\psi}{\nu_i}(v^2 - c_s^2) - 16\frac{\psi}{\nu_i}\frac{(x-vt)^2}{L^4}(V_d^2 - c_s^2)$$

there are four terms (which happen to be proportional to L^0, L^{-2}, and L^{-4}) that we must consider. We will set each term to zero separately, deriving four individual instability threshold conditions whose relative importance can be roughly estimated by noting factors of ψ/ν_i and $1/L$ (recall that we can make the approximation $|x - vt| \sim L$).

Letting $L \rightarrow \infty$ (leaving only the L^0 term) gives us the familiar plane wave instability threshold, $V_d \geq c_s$ (more or less a first-order factor of ψ). Setting $x = vt$ also yields the regular plane wave threshold, with the added constraint that $v \geq c_s$ from the 3rd term. However, from the 2nd term we again see an indication that the "preferred" wave packet propagation velocity, v, is equal to $V_d(1-\psi)$ (which should already be greater than c_s if an instability is to occur). It is interesting to note that this constraint for v is consistent with the dominant term in the expressions for v_{ph}, v_g, and v (equations 5.30, 5.29, and 5.32, respectively). The growth rate of the wave packet will either increase or decrease depending on the speed of v with respect to $V_d(1-\psi)$. However, there is also the complication that v shows up in the space-time dependence factor $(x - vt)$; thus, the sign of this term is also affected by spatial

location. Finally, setting the L^{-4} term to zero, we again see the condition $V_d = c_s$. However, the term is actually negative for $V_d > c_s$.

For reference, we make a rough estimate of the relevance of the four terms using typical values for MRR and a small ($L = 2\lambda$) packet size (so that the spatially-localized effects are as important as is reasonable). Using $\lambda = 1.5\text{m}$, we find $k \approx 4\text{m}^{-1}$ and $L \approx |x - vt| \approx 3\text{m}$. Then the L^0 term is proportional to $16 \times 10^{-5}(V_d^2 - c_s^2)$, while the L^{-4} term weighs in at $-\frac{1}{9}16 \times 10^{-5}(V_d^2 - c_s^2)$. In other words, the L^{-4} term has exactly opposite sign as the L^0 term, but is about one tenth its magnitude. Therefore, we can safely say that the instability turns on for $V_d > c_s$. The $(v^2 - c_s^2)L^{-2}$ term is four times smaller than the L^{-4} term. In contrast, the first L^{-2} term has a magnitude of approximately $1 \times (V_d - v)$, and it clearly dominates the growth rate if v is not very close to V_d. However, determining its sign is complicated, as we discuss elsewhere.

The fact that the L^{-4} term of the growth rate depends on x^2 means it has a particularly important contribution to wave envelope behavior, which we discuss next.

Wave Packet Steepening

An interesting consequence of the space and time dependence of the wave packet dispersion relation is that the growth rate and phase/group velocity change over the length of a wave packet (unless very specific threshold conditions are met). We have already explored the dependence of the growth rate on space and time in our derivation of the "preferred" value for the packet propagation velocity v by setting $\partial\Gamma/\partial x = 0$.

The growth rate depends on x to second order, however, so we actually have $\partial^2\Gamma/\partial x^2 \neq 0$. This implies that under the right conditions, the wave packet envelope will actually steepen – or flatten – depending on the sign of the second derivative:

$$\frac{\partial^2\Gamma}{\partial x^2} = -\frac{32}{L^4}\frac{\psi}{\nu_i}(V_d^2 - c_s^2) \tag{5.36}$$

If $V_d > c_s$, as will normally be the case when irregularities are present, $\partial^2\Gamma/\partial x^2$ will be negative (albeit small; there is a factor of ψ/ν_i in the expression). This means that the packet will steepen at its center (as long as $\partial\Gamma/\partial x$ changes sign at the same location as $\partial/\partial x$ of the wave envelope amplitude changes sign; this alignment is controlled by the value of v, as we will discuss below). Assuming we choose $v = V_d(1 - \psi)$ (the preferred packet velocity!) so that the growth rate and envelope humps are aligned, the growth rate is maximum at the packet center, and decreases on either side, gradually steepening the packet (*cf.* Figure 5.4).

On the other hand, if $V_d < c_s$, $\partial^2\Gamma/\partial x^2$ becomes positive (the growth rate parabola opens upward), and the packet flattens, since the minimum growth rate occurs at its center, and the Gaussian envelope decreases faster than the ψ/ν_i-size growth rate can affect it (as in Figure 5.5).

We interpret this result in the following way: a wave packet comes into existence when V_d exceeds the instability threshold (ion acoustic speed) in a certain region. While the system is being driven by a super-threshold electron drift, the wave grows and its envelope steepens. However, if the disturbance subsequently propagates into a region in which V_d is sub-threshold, it begins to dissipate (the packet flattens out and eventually disappears). These predictions are unique to our spatially-localized theory, since in the plane wave theory, neither ω_r nor Γ depends on x.

The packet propagation velocity v, a wave packet model parameter, also contributes to the packet-shape-changing effects if it is not set to its "preferred" value. Inspecting the equation for Γ, we see that its behavior versus x is equal to a constant; plus a parabola centered at $x = vt$ (which causes the steepening just discussed); plus a line whose slope depends on the size of v with respect to the preferred value $V_d(1-\psi)$. From equation 5.29 we see that the group velocity of the wave in the packet (at the envelope center; v_g changes very slightly over the length of the packet) is equal to

$V_d(1-\psi)$. Therefore, the disturbance center at time t will be located at $x = V_d(1-\psi)t$. If the growth rate parabola's center is to be aligned with the wave packet's center, then v (the model packet propagation velocity) must equal the packet's actual group velocity. Otherwise, the steepening/flattening effect on the packet will be asymmetric. Also, if $v \not\approx V_d(1-\psi)$, the linear term in Γ vastly distorts the steepening-parabola by adding a linear component to the growth rate (more significant than the parabola by about four orders of magnitude). The line has a positive slope (in x) if $v < V_d$ and a negative slope if $v > V_d$, and we get asymmetric growth (faster on the left, or "behind" the packet, if $v > V_d$; faster on the right if $v < V_d$). Examples of these effects can be seen in Figures 5.6 ($v > V_d$) and 5.7 ($v < V_d$).

Alternatively, we could interpret these "v-complications" as a sign that the wave packet model is unphysical unless we set $v = V_d(1 - \psi)$. From this point forward, we consider only cases in which the packet propagation velocity is set to its preferred speed, the wave group velocity.

These packet-shape-changing results are especially interesting because we are not aware of any other linear theory that predicts such behavior. For example, an ion acoustic wave with large amplitude will steepen into a sawtooth-shaped form due to ion acceleration by the wave electric field; this effect arises from the nonlinear term $\mathbf{u} \cdot \nabla \mathbf{u}$ in the ion momentum equation [14]. In linear theory, the ion acceleration due to $\mathbf{E}$ is taken into account, but not the displacement resulting from it, so steepening is not predicted.

We wish to avoid confusing the differential ion acceleration effect (which is truly nonlinear) with the steepening described by our packet theory, so we are careful to describe the $\partial^2\Gamma/\partial x^2 < 0$ effect as "envelope-" or "packet-steepening."

5.3.3 1-D Model Simulation

We now show a few plots of 1-D Gaussian wave packets for various model parameters. We have already referred to some of these figures in the text above. There are many parameters to explore (although not as many as in the 3-D case!). To summarize, the independent variables are x and t; the specified parameters are V_d, v, L, and the plasma λ (or k); and the relevant ionospheric parameters are ψ (and therefore ν_e, ν_i, Ω_e, and Ω_i) and c_s (which depends on electron and ion temperature, and to a lesser degree, on ion composition). We do not present plots in which we vary the ionospheric parameters, however; the most important of them is the ion acoustic speed, and it matters mainly by its difference from V_d, which we do vary.

The derived variables, which we plot, are Γ, $v_{\rm ph}$, v_g, and wave packet amplitude. The growth rate and phase velocity come directly from the imaginary and real parts of the solution for ω; in the 1-D case the wave group velocity and phase velocity are equal. We can find an expression for the wave packet amplitude using equation 5.14:

$$\text{packet amplitude } = e^{\Gamma t} \exp\left(-\frac{2}{L^2}(x - vt)^2\right) \tag{5.37}$$

(with Γ defined by equation 5.23).

Figure 5.2 shows wave packet amplitude versus both space (horizontal axis) and time (overlayed plots, time increasing to the right), for three different values of electron drift: barely above instability threshold (V_d = 430 m/s, top plot), above threshold (V_d = 600 m/s, middle plot), and strongly driven (V_d = 750 m/s, bottom plot). In the two more strongly driven cases, the wave growth is so fast it is difficult to see the packet propagation between consecutive time steps.

Figure 5.3 shows the evolution of a wave packet in space (vertical axis) and time (horizontal axis). The packet amplitude, growth rate, and phase velocity are shown as contour plots; here V_d is set to 500 m/s. We see that the growth rate is largest

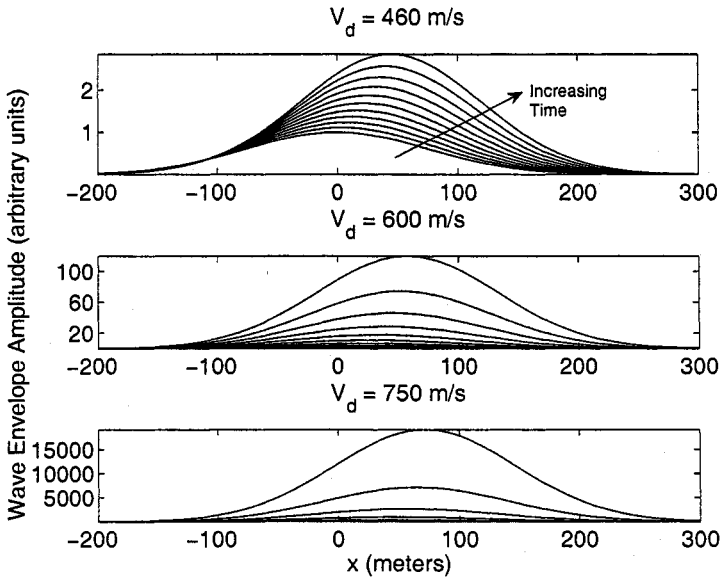

Figure 5.2: Packet evolution in space (horizontal axis) and time (plot overlays) for three different levels of electron drift: just above instability threshold (top), above threshold (middle), and strongly driven instability (bottom).

at the center of the packet, slightly falling off toward the edges; the phase velocity is greatest behind the packet center, and decreases toward the front of the propagating packet.

In both Figures 5.2 and 5.3, the packet size L is held constant at 10λ, with λ set to 1.5 meters. The packet envelope velocity is set to the wave group velocity, $(1-\psi)V_d$.

If we use the "proper" packet propagation velocity (so that $\partial\Gamma/\partial x \approx 0$), we can actually see the change in growth rate versus space change sign; this occurs at the center of the packet if v is exactly equal to $(1-\psi)V_d \approx 0.97V_d$ (a condition we see from equation 5.32). If V_d is above threshold, the wave envelope steepens, as in Figure 5.4; if V_d falls below threshold, the packet flattens and dissipates (Figure 5.5).

If v is not approximately the wave group velocity, the packet model is unphysical,

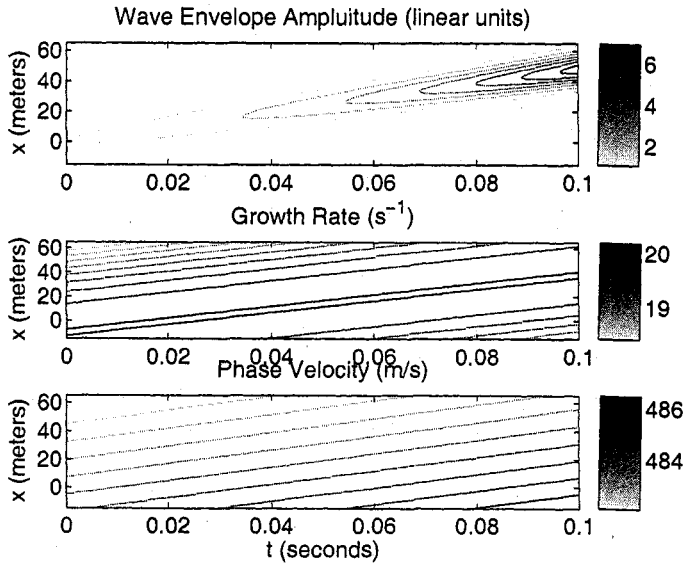

Figure 5.3: Contour plots of wave packet amplitude, growth rate, and phase/group velocity versus time (horizontal axis) and space (vertical axis). Here, $V_d = 500$ m/s, $\lambda = 1.5$m, and $L = 10\lambda$.

or at least does not make much sense; we can see this by observing the dependence of growth rate, phase velocity, and group velocity on space and time. For example, the wave envelope velocity in Figure 5.6 has been set to a value greater than V_d (the wave group velocity). In this case, the wave phase and group velocities decrease over the length of the packet in space, but increase with time. The wave growth rate decreases over the length of the packet.

In Figure 5.7, $v < V_d$, and the wave growth rate increases over the packet length, but the phase and group velocities decrease over both space and time.

These effects may change the shape of the wave packet slightly, but the growth rate and group velocity dependencies on space and time appear to somewhat cancel each other out. We do not believe the packet model is particularly useful if the envelope

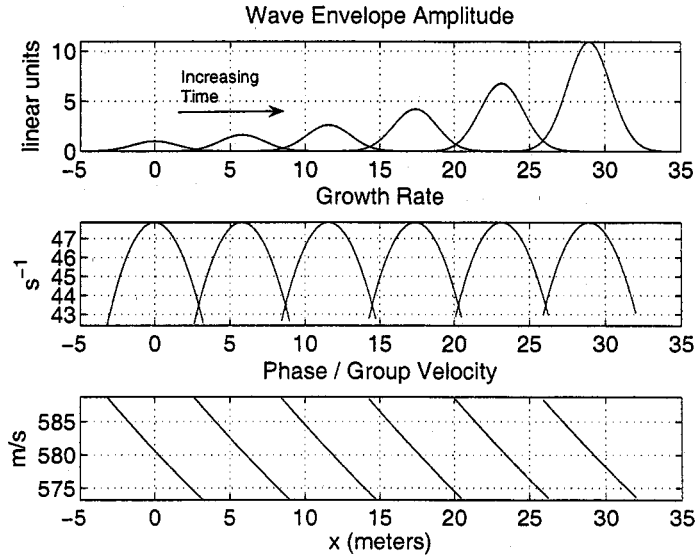

Figure 5.4: A steepening wave packet, plotted vs. position. V_d is above the instability threshold value, and the packet propagation velocity v is set to its "preferred" value, $(1-\psi)V_d$.

velocity is not equal to the group velocity of the wave contained in the envelope.

For completeness we investigate the wave packet behavior versus L and plasma wavelength (or equivalently, k). Figure 5.8 shows plots for several different values of L overlayed; as we expect from theory, the "spatially localized effects" (growth rate parabola, change in phase velocity over packet length) become more pronounced for smaller values of L. The constant portion of the growth rate also increases slightly as L decreases.

In Figure 5.9, L is held constant while the plasma wavelength is varied from 1.5 meters to 5 meters. We chose these values for wavelength based on the scale-length sensitivity of VHF radars: the VHF frequencies extend from 30 MHz to 300 MHz (10 – 1 meters), which means they are sensitive to plasma wavelengths from 5 –

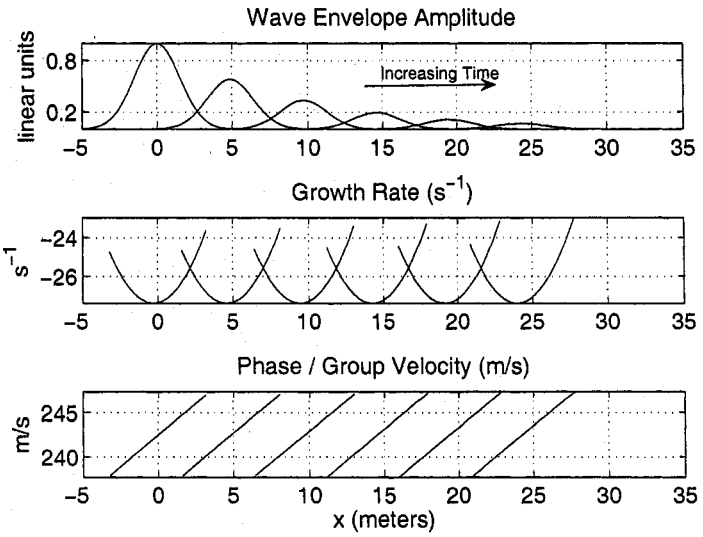

Figure 5.5: A flattening wave packet, plotted vs. position. V_d is below the instability threshold value, and the packet propagation velocity v is set to its "preferred" value, $(1-\psi)V_d$.

0.5 meters. However, at the beginning of Chapter 4 (page 38) we determined that our fluid theory was valid for plasma wavelengths of 1.2 meters and greater, so the smallest λ we consider is 1.5 meters, which is also the plasma structure scale-length to which the MRR is sensitive. As λ increases, k decreases, and $\Gamma \propto k^2$, so this plot does not show any surprising behavior.

5.3.4 Three Dimensional Analysis with Gaussian Envelope

We now extend our analysis to three dimensions, but consider only a Gaussian-shaped (3-D) envelope. We must begin by defining the wave packet itself. A multidimensional Gaussian distribution can be written as the product of the univariate Gaussian functions for each variable, provided the variables are independent. However, if we

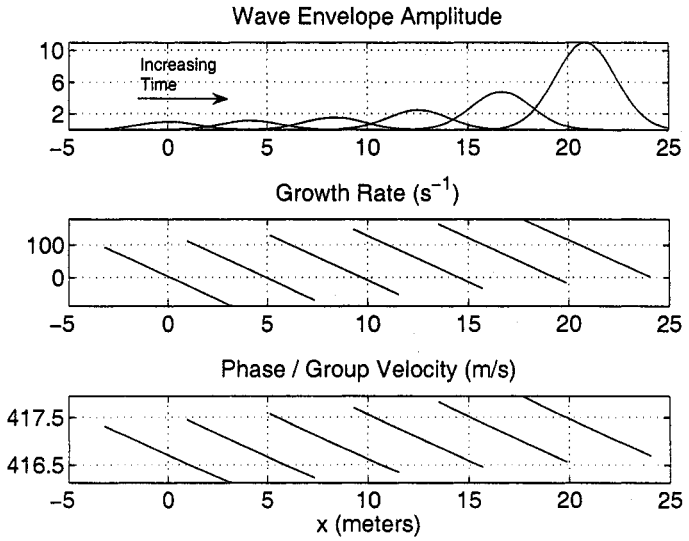

Figure 5.6: The packet propagation velocity v is greater than V_d, and the envelope is outrunning the wave: the phase and group velocities decrease over the length of the packet, as does the growth rate. This steepens the packet from the left. Yet, the wave phase and group velocities are increasing over time. V_d is just above the instability threshold.

wish to include the possibility of more complicated packet shapes in our model – *e. g.*, allow simple, symmetric packets to evolve into asymmetric shapes, or tilt away from the coordinate system axes – we must use the full joint distribution function. A multivariate normal distribution is given by

$$N(\boldsymbol{\mu}, \Sigma) \propto \exp\left(-\frac{1}{2}(\mathbf{x}-\boldsymbol{\mu})^{\mathrm{T}}\Sigma^{-1}(\mathbf{x}-\boldsymbol{\mu})\right) \tag{5.38}$$

(we have left out the constant scaling factors, since we do not intend to use this as an actual probability density function). $\boldsymbol{\mu}$ is the mean vector for $\mathbf{x}$. The covariance matrix Σ is always symmetric and positive semidefinite [19]; an element in the covariance

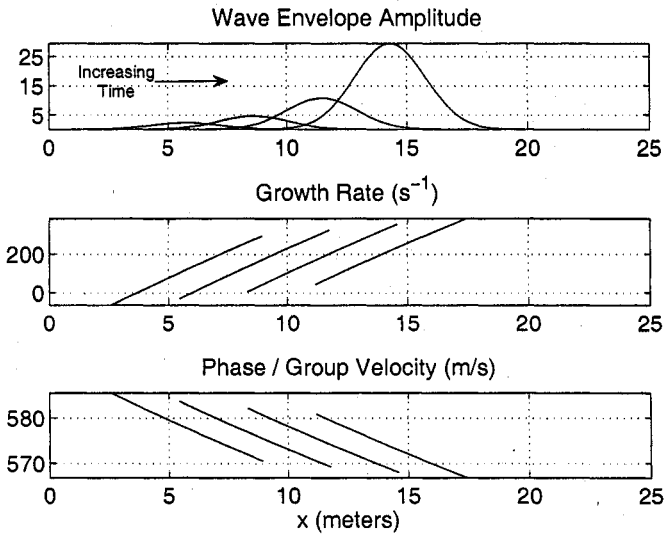

Figure 5.7: In this case the packet propagation velocity v is less than Vd, so the envelope lags behind the propagating wave. The growth rate increases over the length of the packet; however, the phase and group velocities decrease over the length of the packet, and decrease over time as well. In this case, V_d is well above the instability threshold.

matrix is the expected value

$$\Sigma_{ij} = \sigma_{ij}^2 = E[(x_i - \mu_i)(x_j - \mu_j)] \tag{5.39}$$

As in the 1-D case, we will use $\mathbf{v}t$ as the "mean" (*i. e.*, packet center), so

$$\mathbf{x} \equiv \begin{bmatrix} x \\ y \\ z \end{bmatrix} \quad \text{and} \quad \mathbf{v} \equiv \begin{bmatrix} v_x \\ v_y \\ v_z \end{bmatrix} \tag{5.40}$$

The "variance" parameters describe the packet lengths in each dimension (the covariances between spatial variables, if nonzero, indicate orientation of packet symmetry off the main coordinate axes). Thus, Σ is the "packet-shaping matrix." We will

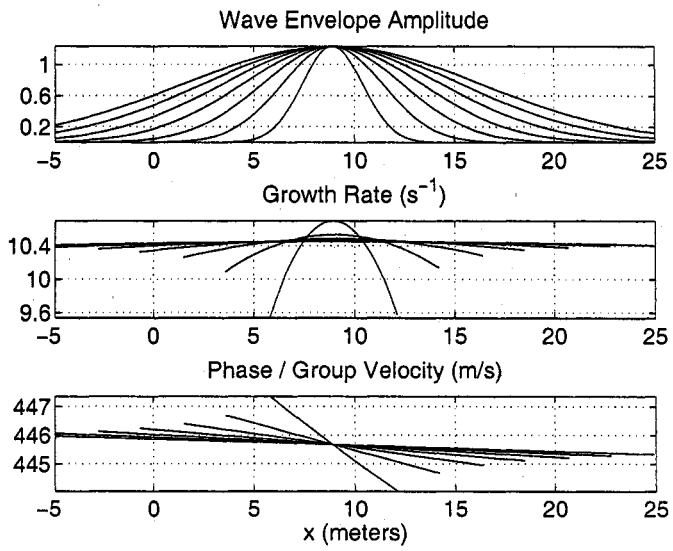

Figure 5.8: Plots versus space (horizontal axis) and packet length L (plot overlays). V_d is set to 500 m/s, λ is fixed at 1.5 meters (the plasma wavelength relevant to MRR), and time is fixed at 0.02 seconds. L varies from 3 meters (2λ) to 15 meters (10λ).

define its contents in terms like L, the intrinsic pulse length (in a certain dimension). We wish to preserve the $L \sim 2\sigma$ convention that we used in the 1-D model, so we modify the normal distribution function accordingly (just as in equation 5.14). We define the three-dimensional Gaussian wave packet as

$$w(t, \mathbf{x}) \equiv e^{-j\omega t} e^{j\mathbf{k}\cdot\mathbf{x}} \exp\left(-2(\mathbf{x} - \mathbf{v}t)^{\mathrm{T}} \Sigma^{-1} (\mathbf{x} - \mathbf{v}t)\right) \tag{5.41}$$

This will be the functional form of perturbations in the medium; for example, $n_1 \sim w$. Here (for equation 5.41), $\mathbf{k}$ is the 3-D wavevector with components k_x, k_y, and k_z. (We will define $\mathbf{k}$ slightly differently below.)

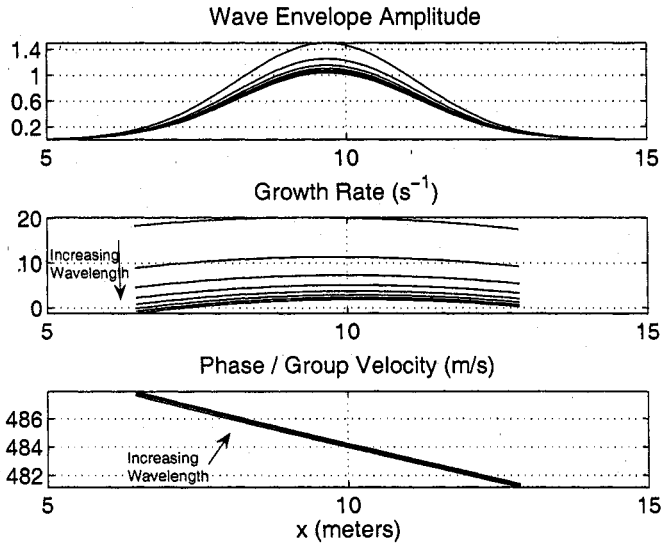

Figure 5.9: Plots versus space (horizontal axis) and plasma wavelength (plot overlays). The wavelength varies from 1.5 m to 5 m, while the packet size L is held constant at 10 meters. Time is also constant, at 0.02 seconds, and $V_d = 500$ m/s.

A Notation Convention

Now, to more easily manipulate and express the voluminous algebra the three-dimensional treatment will involve, we choose to use the Einstein notation convention, in which the last in the following list of equivalent expressions is used:

$$\mathbf{aTb} = \begin{bmatrix} a_1 & a_2 & a_3 \end{bmatrix} \begin{bmatrix} \mathsf{T}_{11} & \mathsf{T}_{12} & \mathsf{T}_{13} \\ \mathsf{T}_{21} & \mathsf{T}_{22} & \mathsf{T}_{23} \\ \mathsf{T}_{31} & \mathsf{T}_{32} & \mathsf{T}_{33} \end{bmatrix} \begin{bmatrix} b_1 \\ b_2 \\ b_3 \end{bmatrix} = \sum_{i=1}^{3} \sum_{j=1}^{3} a_i \mathsf{T}_{ij} b_j = a_i \mathsf{T}_{ij} b_j \quad (5.42)$$

i. e., the repeated appearance of an index in a single term implies summation over that index [66].

Define

$$\mathbf{r} \equiv \begin{bmatrix} t \\ x \\ y \\ z \end{bmatrix}, \quad \mathbf{k} \equiv \begin{bmatrix} -\omega \\ k_x \\ k_y \\ k_z \end{bmatrix}, \quad \text{and} \quad \mathsf{A} \equiv \left[\begin{array}{c|c} \mathbf{v}^{\mathrm{T}}\Sigma^{-1}\mathbf{v} & -\mathbf{v}^{\mathrm{T}}\Sigma^{-1} \\ \hline -\Sigma^{-1}\mathbf{v} & \Sigma^{-1} \end{array}\right] \tag{5.43}$$

Thus, the matrix A is 4×4. The 3-D Gaussian envelope wave packet, exactly the same as equation 5.41, can now be written

$$w(\mathbf{r}) = \exp\left(jk_n r_n\right) \exp\left(-2\mathsf{A}_{nm} r_n r_m\right) \tag{5.44}$$

and its derivatives, in general, are

$$\frac{\partial}{\partial r_l} w(\mathbf{r}) = w(\mathbf{r}) \left[jk_l - 4\mathsf{A}_{lm} r_m\right] \tag{5.45}$$

and

$$\frac{\partial^2}{\partial r_l \partial r_p} w(\mathbf{r}) = w(\mathbf{r}) \left[(jk_l - 4\mathsf{A}_{lm} r_m)(jk_p - 4\mathsf{A}_{pq} r_q) - 4\mathsf{A}_{lp}\right] \tag{5.46}$$

We give a detailed derivation of these Gaussian wave packet derivatives in section A.2.

3-D Gaussian Packet Dispersion Relation

For physical insight, let the indices (1-4) for $\mathbf{r}$, $\mathbf{k}$, and A be t, x, y, and z, and let n be a dummy (summation) index. Then, we derive a dispersion relation by substituting the 3-D wave packet into the ion acoustic differential equation (4.27) and taking appropriate derivatives. We still use the convention $\mathbf{V_d} = V_d\hat{x}$. The multivariate-Gaussian envelope, 3-D dispersion relation is given as follows:

$$\begin{aligned} &\frac{\psi}{\nu_i}\left[(jk_t - 4\mathsf{A}_{tn}r_n)^2 - 4\mathsf{A}_{tt}\right] \\ -\frac{\psi c_s^2}{\nu_i}&\left[(jk_x - 4\mathsf{A}_{xn}r_n)^2 - 4\mathsf{A}_{xx} + (jk_y - 4\mathsf{A}_{yn}r_n)^2 - 4\mathsf{A}_{yy}\right] \\ +(1+\psi)(jk_t - 4\mathsf{A}_{tn}r_n) - \frac{v_{\mathrm{Th,e}}^2}{\nu_e}&\left[(jk_z - 4\mathsf{A}_{zn}r_n)^2 - 4\mathsf{A}_{zz}\right] \\ &+ V_d(jk_x - 4\mathsf{A}_{xn}r_n) = \ 0 \end{aligned} \tag{5.47}$$

In order to solve the dispersion relation and derive expressions for ω_r and Γ, we must specify the packet-shaping matrix Σ. We will show the full treatment for a simple packet, and then briefly discuss other packet shapes.

A Simple Gaussian Packet Shape

The 3-D packet we choose to analyze fully is approximately 2-D and radially symmetric in the $x-y$ plane (the plane perpendicular to $\mathbf{B}$). The "2 standard deviations" packet width L is the same in the $\hat{x}$ and $\hat{y}$ dimensions; for the $\hat{z}$ dimension we add an elongation factor. The packet-shaping matrix is then:

$$\Sigma = \begin{bmatrix} L^2 & 0 & 0 \\ 0 & L^2 & 0 \\ 0 & 0 & (\alpha L)^2 \end{bmatrix}, \quad \text{so} \quad \Sigma^{-1} = \begin{bmatrix} 1/L^2 & 0 & 0 \\ 0 & 1/L^2 & 0 \\ 0 & 0 & 1/(\alpha L)^2 \end{bmatrix} \tag{5.48}$$

(Note that Σ being diagonal implies that Σ^{-1} is diagonal also; this is true in general.)

The parameter $\alpha \gg 1$ so that the instability volume is elongated in the $\hat{z}$ (magnetic field) direction. This is realistic because of the high conductivity along the magnetic field. Substituting this form for Σ^{-1} into the dispersion relation (5.47), we solve for ω in the same way as for the 1-D case: compute a series expansion in ψ of the quadratic formula solution (we only show the marginally damped / growing solution here). Again, we discard terms of 2^{nd} order and higher. Also, as before, we organize our solution in factors of $1/L$, to make explicit the "localized corrections" to plane wave theory. However, there are now factors of $1/\alpha$ in the solution as well, and they represent the degree to which the length of the instability volume along $\mathbf{B}$ is finite. We will begin by presenting the α^0 terms for the ω_r and Γ solutions: in other words, the case for which $\alpha \rightarrow \infty$, and the system is 2-D (no structure in $\hat{z}$ whatsoever). Therefore, we have $k_z = 0$ and $k_\perp = k$. The α^0 solution to the 3-D dispersion relation, with Σ given by (5.48), is:

$$\begin{aligned}
\omega_r &= \mathbf{k}\cdot\mathbf{V_d}(1-\psi) - \\
&\quad \frac{8}{L^2}\frac{\psi}{\nu_i}\left[(\mathbf{k}\cdot\hat{x})(x-v_x t)V_d^2 - \mathbf{k}_\perp\cdot(\mathbf{x}_\perp - \mathbf{v}_\perp t)c_s^2\right] \qquad (5.49)\\
\Gamma &= \frac{\psi}{\nu_i}(k_x^2 V_d^2 - k_\perp^2 c_s^2) + \\
&\quad \frac{4}{L^2}\left[(x-v_x t)V_d(1-\psi) - \mathbf{v}_\perp\cdot(\mathbf{x}_\perp - \mathbf{v}_\perp t) + \frac{\psi}{\nu_i}(v_\perp^2 - 2c_s^2)\right] - \\
&\quad \frac{16}{L^4}\frac{\psi}{\nu_i}\left[(x-v_x t)^2 V_d^2 - (\mathbf{x}_\perp - \mathbf{v}_\perp t)\cdot(\mathbf{x}_\perp - \mathbf{v}_\perp t)c_s^2\right] \qquad (5.50)
\end{aligned}$$

(The perpendicular subscript means a vector with only $\hat{x}$ and $\hat{y}$ components.) We use these expressions to explore the properties of the wave phase and group velocities and instability threshold.

Phase and Group Velocity for 3-D Case

The wave phase velocity is ω_r/k in the $\hat{k}$ direction. Dividing (5.49) by k, we get

$$v_{\rm ph} = (\hat{k}\cdot\hat{x})V_d(1-\psi) - \frac{8}{L^2}\frac{\psi}{\nu_i}\left[(\hat{k}\cdot\hat{x})(x-v_x t)V_d^2 - \hat{k}_\perp\cdot(\mathbf{x}_\perp - \mathbf{v}_\perp t)c_s^2\right] \quad (5.51)$$

We see the familiar $\hat{k}\cdot\mathbf{V_d}$ term, as well as a similar correctional term due to spatially localized effects, proportional to $(V_d^2 - c_s^2)$ and dependent on location. This is essentially exactly like the 1-D phase velocity, except a dependence on c_s in the $\hat{y}$ direction is added.

In 3-D, the phase and group velocities are not necessarily the same. The wave group velocity is

$$\mathbf{v_g} = \hat{x}\frac{\partial\omega_r}{\partial k_x} + \hat{y}\frac{\partial\omega_r}{\partial k_y} + \hat{z}\frac{\omega_r}{\partial k_z} \quad (5.52)$$

where

$$v_{g,x} = \frac{\partial\omega_r}{\partial k_x} = V_d(1-\psi) - \frac{8}{L^2}\frac{\psi}{\nu_i}(x-v_x t)(V_d^2 - c_s^2) \quad (5.53)$$

$$v_{g,y} = \frac{\partial\omega_r}{\partial k_y} = \frac{8}{L^2}\frac{\psi}{\nu_i}(y-v_y t)c_s^2 \quad (5.54)$$

$$v_{g,z} = \frac{\partial\omega_r}{\partial k_z} = 0, \quad \text{since } k_z = 0 \quad (5.55)$$

We have the pleasing result that $v_{g,x}$ is the same as v_g in the $\hat{x}$-1-D case (equation 5.27). The $\hat{y}$ component is exactly the same as the $\hat{x}$ component, except without the V_d contribution. This makes sense since $\mathbf{V_d} = V_d\hat{x}$, but otherwise our choice of Σ makes the $\hat{x}$ and $\hat{y}$ behavior identical. Also, as before, we see that $v_{g,y}$ is a function of v_y; if we set $v_y = v_{g,y}$ and re-solve, we find

$$v_{g,y} = \frac{8}{L^2}\frac{\psi}{\nu_i}yc_s^2 \quad (5.56)$$

which is analogous to equation 5.29 if we set $V_d = 0$. This expression would make more sense if we let $\mathbf{V_d}$ be in an arbitrary direction.

Instability Threshold for 3-D Case

The instability threshold conditions are far more complex in the 3-D case, but we note immediately from equation 5.50 that the $V_d > c_s$ requirement remains the same. Now, the flow angle (k_y/k_x) also comes into play.

Assuming the "preferred packet velocity is the wave group velocity" condition still holds, we let $\mathbf{v} = \mathbf{v_g}$ (equations 5.53–5.55). Interestingly, much of the L^{-2} and L^{-4} terms cancel. We are left with the following terms, all of which are first order in ψ/ν_i:

$$\begin{aligned}\Gamma &= \frac{\psi}{\nu_i}(k_x^2 V_d^2 - k_\perp^2 c_s^2) + \frac{4}{L^2}\frac{\psi}{\nu_i}(v_\perp^2 - 2c_s^2) + \\ &\quad \frac{2}{L^4}\frac{\psi}{\nu_i}\left[(x - v_x t)^2 V_d^2 - (\mathbf{x}_\perp - \mathbf{v}_\perp t)\cdot(\mathbf{x}_\perp - \mathbf{v}_\perp t)c_s^2\right] \qquad (5.57)\end{aligned}$$

The L^{-4} term is again dependent on spatial variables squared, so it will contribute to envelope steepening as before; we discuss this below, after adding corrections to Γ for structure in the $\hat{z}$ direction. Finally, the L^{-2} term makes a small negative contribution unless $v_\perp^2 > 2c_s^2$, or rather $v_x^2 + v_y^2$, which is approximately equal to V_d^2, is greater than $2c_s^2$.

We can also rearrange equation 5.57 into a form that includes the observable quantities of average frequency $\bar{\omega}$ and frequency spread $\Delta\omega$, as Hamza and St.–Maurice do in a nonlinear fluid treatment [45]. Evaluating Γ at the packet center (so that $\mathbf{x} = \mathbf{v}t$), we can write

$$\Gamma \approx \frac{\psi}{\nu_i}(\bar{\omega}^2 + \Delta\omega^2 - k_\perp^2 c_s^2) \qquad (5.58)$$

where

$$\bar{\omega}^2 = k_x^2 V_d^2 \qquad (5.59)$$

$$\Delta\omega^2 = \frac{4}{L^2}(V_d^2 - 2c_s^2) \qquad (5.60)$$

We can now explore the implications of the wave packet "spectral moment" expressions (5.59) and (5.60). Following Hamza and St.–Maurice [45], we note that

observations of primary Farley-Buneman waves (previously referred to as "type 1" in the literature) usually show a narrow spectral width, especially as compared to their average frequency [111, 75]. Then, we expect to find that $\bar{\omega} \gg \Delta\omega$, and this holds true for our wave packet expressions:

$$k_x V_d \gg \frac{2}{L}\sqrt{V_d^2 - 2c_s^2} \tag{5.61}$$

Also, the "spectral width" increases as V_d increases beyond the instability threshold. However, $\Delta\omega$ is not well defined if V_d is less than $\sqrt{2}c_s$, so this expression is not necessarily reliable for use in interpreting spectra.

A Lower Bound for Packet Size

Having found a "preferred" value for the packet propagation velocity model parameter, $\mathbf{v}$, we would also like to determine an intrinsic packet size (a preferred value for the other major packet model parameter). We can use a "marginal stability" argument to put a lower bound on L, the intrinsic packet size in our simplified 2-D Gaussian packet model. Marginal stability implies that the growth rate is positive, but does not exceed zero by too much, so that the medium can support "steady-state turbulence" [45].

Again using equation 5.57 for Γ, evaluated at the packet center, we require $\Gamma \geq 0$ and solve for L:

$$\Gamma \approx k_x^2 V_d^2 - k_\perp^2 c_s^2 + \frac{4}{L^2}(V_d^2 - 2c_s^2) \geq 0 \tag{5.62}$$

$$L^2 \geq \frac{8 - 4\mathcal{M}^2}{k_x^2\mathcal{M}^2 - k_\perp^2} \tag{5.63}$$

$$L^2 \geq \frac{8 - 4\mathcal{M}^2}{k_\perp^2(\mathcal{M}^2\cos^2\theta - 1)} \tag{5.64}$$

We have used $\mathcal{M}$ as the mach number V_d/c_s, and θ as the flow angle (between $\mathbf{V_d}$ and $\mathbf{k}$).

Now we can see that as the electron drift mach number increases, the lower bound on the packet size L decreases (wave packets can be smaller for larger V_d). Therefore, a positive growth rate implies that the plasma is capable of supporting disturbances of finite size. However, $L \rightarrow \infty$ (disturbances are like plane waves) when $\mathcal{M} = 1$ and $\theta = 0$ (*i. e.*, for the marginal stability case, $\Gamma \approx 0$). Also, the lower bound for L is undefined if the growth rate is negative (when waves are damped) or if $\mathcal{M}^2 > 2$ (if $V_d > \sqrt{2}c_s$). This latter case could be interpreted to mean that if V_d greatly exceeds c_s, the plasma can't stabilize until the acoustic speed increases (through nonlinear heating effects) such that $V_d \leq \sqrt{2}c_s$.

Finally, we can use the lower bound on L to make a very rough attempt at explaining why coherent scatter radars measure Doppler shifts which seem to be limited to values near c_s (the discrepancy between theory and experiment discussed on page 75). First, we note that Bragg scatter amplitude is proportional to the size of the disturbance with appropriate scale-size. Therefore, Bragg backscattered power from a wave packet is proportional to L^2, so we would expect the characteristics of radar backscatter from a population of packets to be predominantly determined by the structures with largest L. This is similar to the case for weather radars, in which the backscatter characteristics are dominated by the features of the largest raindrops, since the Rayleigh scattering cross section is proportional to the sixth power of particle radius [56]. From expression 5.64, we see that L can get progressively smaller as V_d exceeds c_s by up to 40% ($c_s < V_d < \sqrt{2}c_s$). We can speculate that the structures with largest L also have V_d closest to c_s; thus, the Doppler shifts measured by radars may remain near the ion acoustic speed. Other authors have determined, through both nonlinear kinetic theory and experiment, that wave phase speeds do not exceed c_s by more than 15% [104, 40].

Corrections for Structure Along $\vec{B}$

We now add small corrections to the solution for ω based on finite α. If the elongation factor α is large but finite, the modeled instability volume changes from a cylinder-like volume that extends indefinitely along the magnetic field to a very elongated ellipsoid (its "two standard deviation length" is αL) that is pinched off at both ends.

To get an idea of an appropriate size for α, we consider first the vertical extent of the Farley-Buneman instability layer itself. The product αL should not be greater than the layer thickness, which is about 25 km. This bound on α depends on what we choose for L, however. If we set L to 3 meters (2λ for the Manastash Ridge Radar, as small a value for L as is reasonable), we find that α should be less than approximately 8500. We would rather define α as an appropriate parallel-to-perpendicular ratio, though, instead of assuming that αL is the entire instability layer thickness. Therefore, we consider the ratio of electron mobility along $\mathbf{B}$ to mobility in the plane perpendicular to $\mathbf{B}$. We use the following formulae from Hysell *et al.* [54]:

$$\mu_{\parallel} = \frac{\Omega_e}{\nu_e B} \tag{5.65}$$

$$\mu_{\perp} = \frac{\nu_e \Omega_e}{B(\Omega_e^2 + \nu_e^2)} \tag{5.66}$$

so

$$\frac{\mu_{\parallel}}{\mu_{\perp}} = \frac{\Omega_e^2}{\nu_e^2} + 1 \tag{5.67}$$

The ratio of parallel and perpendicular electron mobilities is approximately 10^5 in the E region: far larger than our estimate of α using the instability layer thickness. This indicates that individual instability volumes extend vertically throughout the entire unstable region. Alternatively, we could choose the ratio $v_{\mathrm{Th,e}}/c_s$ for α. In the original E region ion acoustic differential equation (4.27), $v_{\mathrm{Th,e}}$ is the speed associated with the direction along the magnetic field, while the acoustic speed c_s is associated with directions perpendicular to $\mathbf{B}$. Since this ratio results in the smallest α (approximately

190), we will use it, to illustrate the greatest possible importance of the magnetic field structure-related terms. Then the factor α^{-2} is on the order of 10^{-5}, and probably smaller.

We will present the α^{-2} corrections to ω_r and Γ here, and also consider terms from the α^{-4} correction when we briefly investigate packet-steepening in the $\hat{z}$ dimension. The L and α dependence continues to $(\alpha L)^{-8}$; however, these terms are not significant. The α^{-2} correction term in the simple 3-D Gaussian packet solution for ω is:

$$\begin{aligned}
\omega_{r,\alpha 2} &= \frac{8}{(\alpha L)^2}\frac{v_{\mathrm{Th,e}}^2}{\nu_e}\left[k_z(1-\psi)(z-v_z t)+\frac{\psi}{\nu_i}k_x V_d\right]+ \\
&\quad \frac{16}{(\alpha L)^2}\frac{\psi}{\nu_i}\frac{v_{\mathrm{Th,e}}^4}{\nu_e^2}k_z^3(z-v_z t)- \\
&\quad \frac{64}{\alpha^2 L^4}\frac{\psi}{\nu_i}\frac{v_{\mathrm{Th,e}}^2}{\nu_e}k_z V_d(x-v_x t)(z-v_z t) \qquad (5.68) \\
\Gamma_{\alpha 2} &= -\frac{4}{(\alpha L)^2}\left[v_z(z-v_z t)+\frac{v_{\mathrm{Th,e}}^2}{\nu_e}(1-\psi)-\right. \\
&\quad \left.\frac{\psi}{\nu_i}\left(v_z^2-2\frac{v_{\mathrm{Th,e}}^4}{\nu_e^2}k_z^2+4\frac{v_{\mathrm{Th,e}}^2}{\nu_e}k_z k_x V_d(z-v_z t)\right)\right]+ \\
&\quad \frac{32}{\alpha^2 L^4}\frac{\psi}{\nu_i}\frac{v_{\mathrm{Th,e}}^2}{\nu_e}V_d(x-v_x t) \qquad (5.69)
\end{aligned}$$

We can use the expression for $\omega_{r,\alpha 2}$ to make slight corrections to the packet phase and group velocities.

To find the additional phase velocity term(s), which will just add to the previous expression for v_{ph} (equation 5.51), we divide expression (5.68) by k:

$$\begin{aligned}
v_{\mathrm{ph},\alpha 2} &= \frac{8}{(\alpha L)^2}\frac{v_{\mathrm{Th,e}}^2}{\nu_e}\left[(\hat{k}\cdot\hat{z})(1-\psi)(z-v_z t)+\frac{\psi}{\nu_i}(\hat{k}\cdot\hat{x})V_d\right]+ \\
&\quad \frac{16}{(\alpha L)^2}\frac{\psi}{\nu_i}\frac{v_{\mathrm{Th,e}}^4}{\nu_e^2}(\hat{k}\cdot\hat{z})k_z^2(z-v_z t)- \\
&\quad \frac{64}{\alpha^2 L^4}\frac{\psi}{\nu_i}\frac{v_{\mathrm{Th,e}}^2}{\nu_e}(\hat{k}\cdot\hat{z})V_d(x-v_x t)(z-v_z t) \qquad (5.70) \\
&\approx \frac{8}{(\alpha L)^2}\frac{\psi}{\nu_i}\frac{v_{\mathrm{Th,e}}^2}{\nu_e}V_d(\hat{k}\cdot\hat{x}) \qquad (5.71)
\end{aligned}$$

On the last line, we assumed that $k_\parallel \ll k_\perp$, so that k_z/k terms in $v_{\mathrm{ph},\alpha 2} \to 0$. This is an appropriate assumption, since we expect the structure in the $\hat{z}$ direction to be very elongated, as discussed above. Therefore, the finite-$\hat{z}$ packet phase velocity is proportional to the electron thermal speed as well as V_d.

Turning to the group velocity, we find the following corrections based on the α^{-2} term:

$$v_{g,x,\alpha 2} = \frac{\partial \omega_{r,\alpha 2}}{\partial k_x} = \frac{8}{(\alpha L)^2}\frac{\psi}{\nu_i}\frac{v_{\mathrm{Th,e}}^2}{\nu_e}V_d \tag{5.72}$$

$$v_{g,y,\alpha 2} = \frac{\partial \omega_{r,\alpha 2}}{\partial k_y} = 0 \qquad \text{(same for all } \alpha \text{ terms)} \tag{5.73}$$

$$v_{g,z,\alpha 2} = \frac{\partial \omega_{r,\alpha 2}}{\partial k_z} = \frac{8}{(\alpha L)^2}\frac{v_{\mathrm{Th,e}}^2}{\nu_e}(1-\psi)(z-v_z t) + \frac{32}{(\alpha L)^2}\frac{\psi}{\nu_i}\frac{v_{\mathrm{Th,e}}^4}{\nu_e^2}(z-v_z t)k_z^2 - \frac{64}{\alpha^2 L^4}\frac{\psi}{\nu_i}\frac{v_{\mathrm{Th,e}}^2}{\nu_e}V_d(x-v_x t)(z-v_z t) \tag{5.74}$$

The $\hat{x}$ component of the group velocity correction now has a contribution from electron thermal velocity: in fact, it is equal to the phase velocity correction if $\mathbf{k} = k_x\hat{x}$. The $\hat{z}$ contribution is interesting just because it shows what happens when we add structure in the $\hat{z}$ dimension. We see that $v_{g,z}$ is proportional to the electron thermal speed (analogous to the "$\hat{z}$-group velocity") and, to a lesser extent, V_d. The 2nd term is a function of k_z; therefore, the wave is dispersive in the $\hat{z}$ direction. Also, as in the other two dimensions, $v_{g,z}$ is dependent on location along the $\hat{z}$ axis (and time). The spatial dependence is slightly stronger in $v_{g,z}$ than in the other two dimensions: the first term, which includes a factor of $(z - v_z t)$, is multiplied by $1/\nu_e$ rather than ψ/ν_i.

We also note that $\mathbf{v_g}$ is independent of $\mathbf{k}$ if $k_\parallel = 0$, as Moorcroft [78] and Drexler *et al.* [18] have shown for the regular plane wave case.

Packet Steepening in 3 Dimensions

To investigate packet steepening ("sharpening" is perhaps a better description for 3-D), we consider second spatial derivatives for the Γ terms with α^0, α^{-2}, and α^{-4} factors (however, $\nabla^2\Gamma = 0$ for all α^{-2} terms). We find:

$$\frac{\partial^2\Gamma}{\partial x^2} = -\frac{32}{L^4}\frac{\psi}{\nu_i}(V_d^2 - c_s^2) \tag{5.75}$$

$$\frac{\partial^2\Gamma}{\partial y^2} = \frac{32}{L^4}\frac{\psi}{\nu_i}c_s^2 \tag{5.76}$$

$$\frac{\partial^2\Gamma}{\partial z^2} = \frac{32}{(\alpha L)^4}\frac{v_{\mathrm{Th,e}}^2}{\nu_e}(1-\psi) + \frac{192}{(\alpha L)^4}\frac{\psi}{\nu_i}\frac{v_{\mathrm{Th,e}}^4}{\nu_e^2}k_z^2 - \frac{256}{\alpha^4 L^6}\frac{\psi}{\nu_i}\frac{v_{\mathrm{Th,e}}^2}{\nu_e}V_d(x - v_x t) \tag{5.77}$$

The x-derivative is the same as in the 1-D case. The y-derivative is the same as the x-derivative, except with $V_d = 0$ (again, if we let V_d be in an arbitrary direction, the $\hat{y}$ effects would make more sense).

It is interesting to note that the first term of $\partial^2\Gamma/\partial z^2$ is potentially very large; it is proportional to $\alpha^{-4}L^{-4}$, ν_e^{-1}, and the square of the electron thermal speed, but not ψ/ν_i, as are all the other growth rate second spatial derivatives. This term is unambiguously positive, which means that the packet is strongly encouraged to flatten in the $\hat{z}$-dimension. Also, from the second term, we see that $\partial^2\Gamma/\partial z^2$ becomes even more positive proportionally to k_z^2; in other words, for shorter wavelengths the flattening effect is more pronounced. Therefore, introducing structure in the $\hat{z}$-dimension seems to be a useful exercise only to show that the model self-consistently eliminates it.

The third term in the second z-derivative could potentially be negative; however, V_d would have to overcome a factor of ψ/ν_i to force $\partial^2\Gamma/\partial z^2$ to become negative, and this is a completely unrealistic requirement.

More Complicated Gaussian Packet Shapes

Now we move on to briefly describe a more general packet-shaping matrix, in which the off-diagonal terms in Σ are nonzero.

The covariance matrix for $\mathbf{x}$ (with $E[\mathbf{x}]$ given by $\mathbf{v}t$), upon which the packet-shaping matrix is based, is defined as

$$\Sigma = E[\mathbf{x}\mathbf{x}^{\mathrm{T}}] - t^2\mathbf{v}\mathbf{v}^{\mathrm{T}} \tag{5.78}$$

We have used the vector outer-product, so Σ is 3×3. If, for example, L is the "two standard deviations length" of a packet in the $\hat{x}$- and $\hat{y}$-dimensions, then $\Sigma_{xx} = \Sigma_{yy} = L^2/4$, but Σ_{xy} is less well defined.

With a diagonal shaping matrix, the resulting packet is symmetric about each of the coordinate axes, x, y, and z. The off-diagonal terms represent asymmetry about the coordinate axes, or rather changing the principal axes of the packet-cloud so that they are no longer aligned with the coordinate system (the new principal axes are, in fact, the eigenvectors of Σ; the eigenvalues specify the packet lengths along these axes [19]). Knowledge of the complete packet-shaping matrix allows us to calculate the size of the packet in any direction or in any subspace. Also, the volume of the packet is directly proportional to $|\Sigma|^{1/2}$ [19].

For example, in a coordinate system in which $\mathbf{B}$ is in the $\hat{z}$ direction, a nonzero Σ_{xy} represents the packet twisting around $\mathbf{B}$; a nonzero Σ_{xz} or Σ_{yz} represents the packet (which is likely elongated along $\mathbf{B}$) tilting away from $\mathbf{B}$ in the x or y direction, respectively.

The packet-shaping matrix parameters could yield insights into the behavior of instability waves. There have been references in the literature to Farley-Buneman waves changing shape and orientation; in particular, St.–Maurice and Hamza describe intermittent "blobs" of turbulence with electric fields and drift velocities that rotate

as the wave electric field becomes large [118]. This nonlinear electric field rotation is also found in numerical simulations of Farley-Buneman turbulence [91, 94, 92]. In the same paper, St.–Maurice and Hamza show that finite size irregularities become elongated during linear growth [118]. Drexler *et al.* describe conditions under which a localized disturbance that is initially perfectly field-aligned tilts so that it develops a nonzero aspect angle and drifts along the magnetic field [18]. Similarly, Janhunen refers to a "tilting wave tower" in a three-dimensional numerical study [57].

It would be interesting to study, analytically, the evolution of the "twist" and "tilt" parameters of the packet-shaping matrix along with the wave vector. This would give us information about the evolution of the packet (and wave) orientation in time and over space, under different conditions. For example, determining how the tilt parameters (Σ_{xz} and Σ_{yz}) and $k_{\parallel}$ change over time if the growth rate is maximized could possibly aid in understanding large aspect angle scatter from irregularities. Letting the twist parameter (Σ_{xy}) and $k_{\perp}$ evolve while the phase velocity is held constant at the ion acoustic speed could shed light on the role of the flow angle in wave phase speed saturation. (Several authors have found evidence that flow angle rotation is a key factor in the apparent phase speed saturation of Farley-Buneman waves at c_s [118, 58, 57].) Here, we very briefly use numeric simulations to investigate the influence of arbitrary packet orientation on wave characteristics; however, we hope to address some of the other ideas listed here in future work.

5.3.5 3-D Model Simulation

We simulate behavior in three dimensions for the Gaussian-shaped wave packet. Similar to the 1-D case, the independent variables are x, y, z, and t; the specified parameters are V_d, Σ (similar to L), v_x, v_y, v_z, and k_x, k_y, k_z; and the solved-for quantities are Γ, v_{ph}, and packet amplitude. V_d is the only ionospheric-related parameter which

we routinely vary. Using equation 5.41, the wave packet amplitude is

$$e^{\Gamma t} \exp\left(-2(\mathbf{x}-\mathbf{v}t)^{\mathrm{T}}\Sigma^{-1}(\mathbf{x}-\mathbf{v}t)\right) \tag{5.79}$$

We obtain the growth rate Γ by solving the 3-D dispersion relation numerically; Σ^{-1} contains whatever values we choose to simulate.

We have two main issues left to explore that we were unable to address in the 1-D simulation: the role of the packet orientation parameters (off-diagonal terms in the packet-shaping matrix Σ), and the influence of the direction of the wave vector with respect to the electron drift. We find that if $\mathbf{k}$ is in any direction other than that of $\mathbf{V_d}$, the wave packets are damped, and flatten. In particular, if $k_{\|}$ is greater than 0.1% of $k_{\perp}$, the damping is strong ($\Gamma < -10$).

With regard to packet orientation, we created a packet with L equal to 2λ in the $\hat{x}$ direction, λ in the $\hat{y}$ direction, and 380λ (*i. e.*, $190L_x$) in the $\hat{z}$ direction. We chose these dimensions both for physical accuracy (see the discussion of quantifying elongation along magnetic field lines on page 97) and so that we can identify the original packet axes of symmetry after it has been rotated. We set the $x-y$ twist parameter Σ_{xy} to 3, resulting in a 62.7° rotation of the 2λ packet axis away from $\hat{x}$; we set the $x-z$ tilt parameter Σ_{xz} to 900, resulting in a 0.16° tilt of the packet's vertical axis away from $\hat{z}$, in the direction of $+\hat{x}$. We then allowed this packet to evolve for 20 milliseconds; the results for packet amplitude, wave growth, and phase velocity are shown in Figures 5.10 ($x-y$ plane, $z=0$ view) and 5.11 ($x-z$ plane, with $y=0$).

In this simulation, $\mathbf{V_d} = 500\hat{x}$ m/s; we set $\mathbf{v}$ equal to $(1-\psi)V_d\hat{x}$ (the appropriate group velocity for the center of the packet); and $\mathbf{k} = (2\pi/\lambda)\hat{x}$ (so that $\mathbf{k}\|\mathbf{V_d}$). We note that the packet axis rotations described above are not flow or aspect angle changes unless we also rotate $\mathbf{k}$ accordingly. Rotating $\mathbf{k}$ in directions corresponding to the packet axis rotation does not result in additionally interesting or insightful behavior;

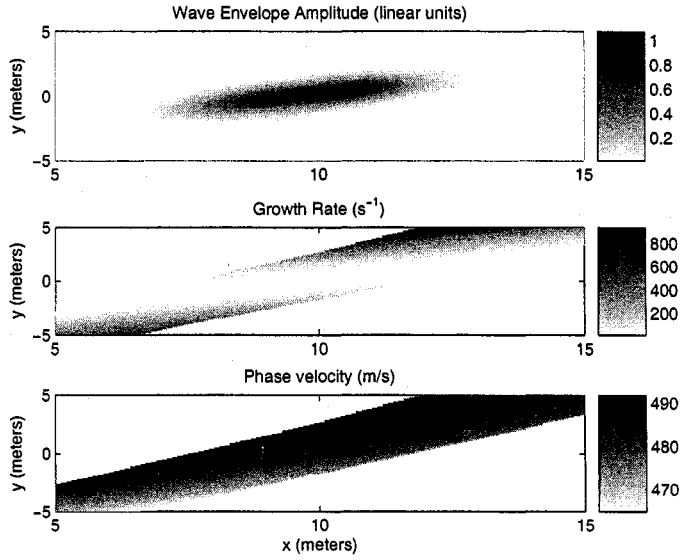

Figure 5.10: A 3-D wave packet with arbitrary spatial orientation. Amplitude, growth rate, and phase velocity are shown in the $x-y$ plane ($z=0$). Time is fixed at 20 ms; $\mathbf{k}$ is parallel to $\mathbf{V_d}$ with $\mathbf{V_d}$ set at $500\hat{x}$ m/s. The packet's lengths along its major axes are 2λ, λ, and 380λ, with $\lambda = 1.5$ meters.

as before, $\mathbf{k} \not\parallel \mathbf{V_d}$ results in wave damping.

Figures 5.10 and 5.11 show that the packet is propagating in the $\hat{x}$ direction at the group velocity $(1-\psi)V_d\hat{x}$. The phase velocity varies over the packet area, but is roughly equal to the group velocity (which we expect, since $\mathbf{k}\|\mathbf{V_d}$ in this case). The packet growth (for example, density fluctuation intensification) is fastest at its edges, as can be seen from the growth rate plots, yet Γ remains positive (the wave is still growing) everywhere.

5.3.6 Implications for Measured Radar Spectra

An important goal of any new theoretical model is that it predict effects that can be measured physically, so that testing of the model is possible. We also hope that

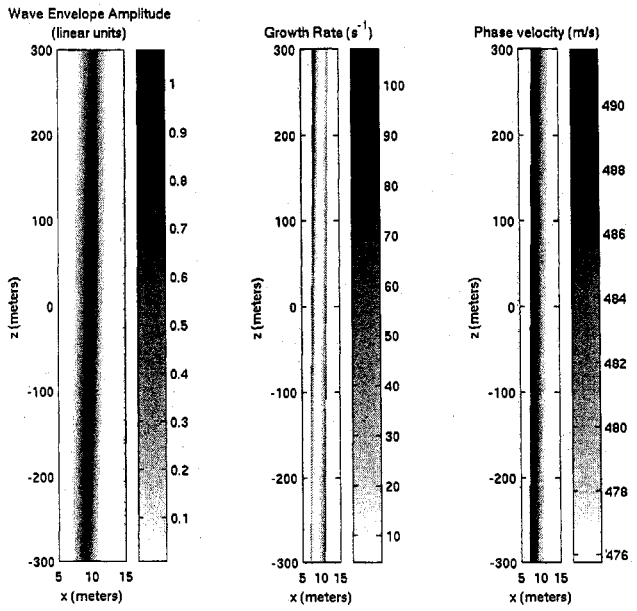

Figure 5.11: The same wave packet as in Figure 5.10, shown in the $x - z$ plane; y is set to zero.

new models will provide additional options for interpreting experimental results. In this chapter we considered the behavior of plasma density irregularities modeled as spatially localized wave packets in a medium subject to the ionospheric two-stream instability. We determined the phase velocity and growth rate of localized waves under various conditions. These two characteristics are important because phase velocity is readily measured by radars as a Doppler shift, and radar backscatter features are dominated by the signatures of the largest waves, which the growth rate can help us identify. We also determined reasonable bounds for the new model parameters we introduced (packet size and propagation velocity), and provided a rough link between spatial packet size and irregularity spectral width, which can be measured with radar.

The most important feature of this model for understanding radar spectra is ac-

tually one we did not explore in detail here: that spatially localized wave packets can produce Bragg backscatter in any direction, rather than only a single, well-defined direction, as in the plane wave model. We discussed this idea, and mentioned experimental results that a localized wave model might help explain, in section 5.1.1. A more detailed analysis requires a method for estimating wave packet radar cross section from theory, which has been covered by Moorcroft [79].

Another important implication of the wave packet model is the spreading of energy in the k-spectrum (the coupling of wave energy into adjacent wavenumbers, which could affect Doppler features measured by radars). A thorough treatment of this topic also requires us to estimate radar cross section, or backscatter intensity from irregularities, which we did not address here. However, we did determine the range of wavenumbers introduced by finite packet size for the 1-D case (page 75). Finally, we offered one possible explanation for why radar phase velocity measurements seem to saturate at or near the ion acoustic speed.

5.4 Suggestions for Further Work

For the material presented here, we are satisfied with the single wave-packet model which grows and decays in the same way as the traditional plane wave theory (with the growth rate being the imaginary part of ω). However, one could also model growth as the number of wave packets increasing (for example, when modeling radar backscatter from a volume much greater than that of an individual wave packet), or let both k and ω be complex (which could introduce an extra degree of freedom in solving the dispersion relation).

Although we claim that the Gaussian-shaped wave envelope is about as mathematically convenient and physically appropriate as possible, it would be interesting to investigate non-Gaussian packet envelopes. Most likely a 1-D treatment would

suffice to determine the new model's usefulness (the arbitrary-disturbance-model 1-D dispersion relation in equation 5.13 could be used).

It would almost certainly be instructive to determine the importance and roles of nonlinear terms in the ion acoustic differential equation when using the wave packet disturbance model. For example, the nonlinear effect of wave-wave interaction would be modified by the finite spatial extent of the waves. This analysis would need to be done in three dimensions, as the simplification to 1-D gets rid of all the nonlinear terms.

A limitation of the analysis we present here is that there is no means for the packet envelope to evolve in shape. An analysis which provided a differential equation for the packet envelope itself, so changes in packet shape over time could be expressed, would be a better tool for visualizing and understanding irregularity behavior.

As we discussed above, it could be useful to investigate the effects of off-diagonal packet-shaping matrix elements (the "twist" and "tilt" parameters) on the wave velocity and growth rate expressions. Inverting those expressions to find a "packet orientation evolution equation" could also be interesting. Equivalently, one could rederive the results given here for background magnetic and electric fields in arbitrary directions.

A more sophisticated version of our simulation in section 5.3.5 would let V_d be a function of space and have an arbitrary direction, as well as other generalizations, such as allowing $\mathbf{k}$ and the packet shaping-matrix parameters to be functions of time.

Finally, our wave packet model for ionospheric two-stream irregularities could be a useful tool for modelers in E region aeronomy. Modeling turbulent regions with wave packets rather than plane waves might allow the use of a smaller computation grid, or instead of a grid, simply a population of packets, each described by a certain number of parameters (*e. g.*, shaping-matrix parameters, etc.).

Chapter 6

MULTISTATIC PASSIVE RADAR

We have developed the Manastash Ridge Radar into a multistatic system and applied new experimental techniques to passive radar. In this chapter, we describe additions and changes we have made to the MRR and the new experiments we can perform with the enhanced system. The addition of a third receiver node is a first step toward the larger goal of developing distributed arrays of simple instruments (such as the DASI initiative discussed in section 3.3).

6.1 The Three-Receiver MRR System

In July 2005, we added a third receiver to the MRR network, making the radar multistatic. The new radar configuration is shown (as a cartoon) in Figure 6.1. With this system, we can use the "western" and "eastern" bistatic links separately, and also perform true multistatic experiments. The third receiver, initially intended to record new reference FM signals, is located near Spokane, Washington (the precise location is actually the Eastern Washington University (EWU) Physics Department in Cheney, WA, but we will frequently refer to "the Spokane receiver" or "the eastern receiver"). Many of the transmitters we monitor with this receiver serve the Spokane area. Figure 6.2 shows a map of the MRR field of view marking the locations of frequently used transmitters in the Seattle and Spokane areas as well as the scatter receiver at Manastash Ridge Observatory (MRO).

The Spokane receiver itself is almost identical to the others at the University of Washington (UW) and MRO: the new receiver uses a different GPS time/frequency

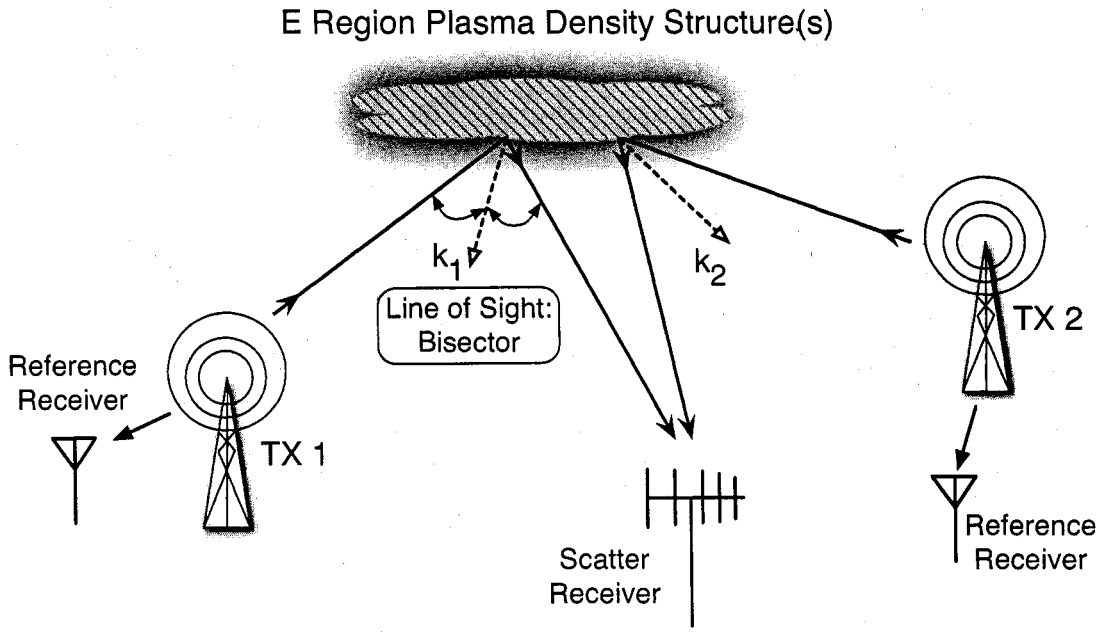

Figure 6.1: A cartoon illustration of the 3-receiver MRR system. The reference receivers (located in Seattle and Spokane) record copies of broadcasts from area transmitters, while the scatter receiver (located on Manastash Ridge in Central Washington) records the broadcasts after they have scattered from targets. Bistatic radar lines of sight bisect the transmitter-to-target and target-to-receiver ray paths.

reference module and has an 80 MHz analog-to-digital converter, while the other two can operate only as fast as 65 MHz. These differences do not affect the performance of the system as a whole, and we may treat the MRR on a high level as if it were composed of three identical receiver nodes. (An important exception is the quality of the GPS and receiver antennas and their mounts at each location; so far we have had to tolerate a dipole receiver antenna duct-taped to the window of the Physics Student Lounge at Eastern Washington University, which certainly has an impact on its effectiveness.)

With the addition of the Eastern receiver, we now routinely record commercial FM broadcasts from two to three stations in both Seattle and Spokane. As before, scattered signals from plasma density irregularities (and other targets) are received at MRO in central Washington State. By using different bistatic combinations of the three MRR receivers, we can simultaneously monitor slightly different fields of view in the sub-auroral latitudes of southwestern Canada. Figure 6.2 also shows contours of constant range and aspect angle overlayed for two different bistatic links (one western and one eastern).

In principle, we can run the passive radar "backwards" with the MRO receiver recording a reference FM broadcast in Central Washington and the Seattle or Spokane receiver listening for scattered signals. We can also compute cross-ambiguities between the Seattle and Spokane receivers, which are further apart but again in principle should yield detectable correlations. So far, none of these options has produced useful results; we cannot detect ground clutter from the Cascade mountain range (our default "radar Turing test"). This may be due to multipath and interference complications in the urban, low-elevation, and radio-loud environments of Seattle and Spokane. We also have significantly less sophisticated antennas for the reference receivers, since local FM transmitter signals are easy to detect.

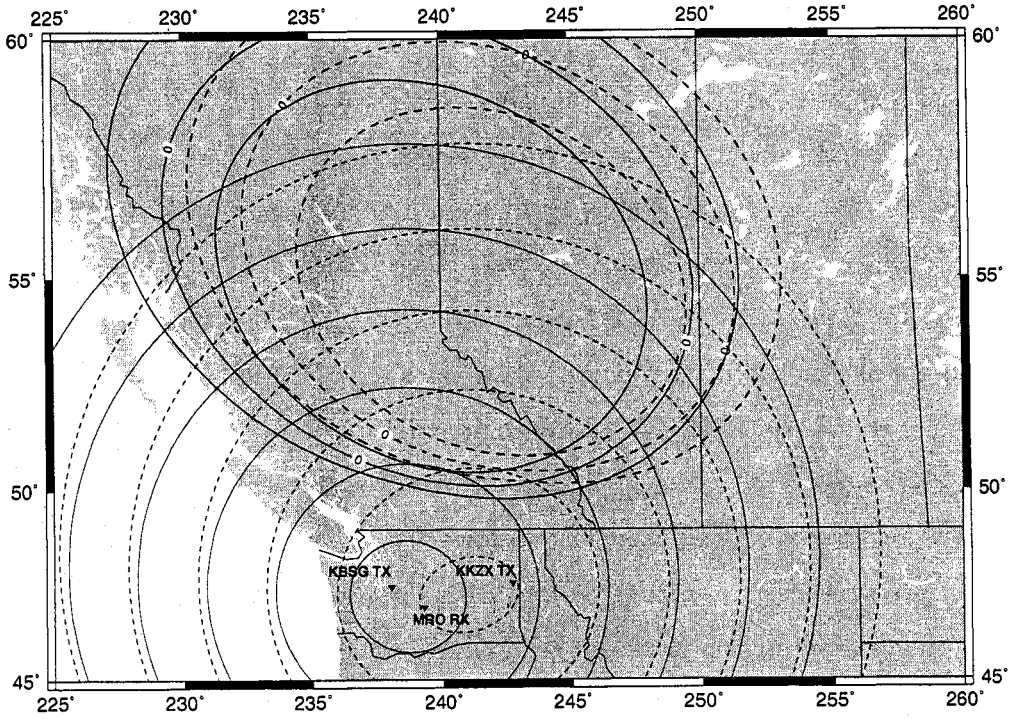

Figure 6.2: The MRR field of view with two separate observing links identified. Contours of constant range are marked every 200 km; contours of perpendicular magnetic aspect angle are shown along with $\pm 1°$ as calculated for an altitude of 100 km. The dashed contours represent an eastern transmitter (KKZX)-MRO link, while the solid lines represent a western transmitter (KBSG)-MRO link.

Therefore, we have identified 8 useful combinations of reference- and scattered-signal. With the reference receivers (Seattle/UW and Spokane/EWU), we record channels 97.3 MHz (KBSG in the Seattle area; KKRS in the Spokane area) and 98.9 MHz (KWJZ in Seattle; KKZX in Spokane)[1]. At MRO, which we use strictly to record scattered signals, we record both of these channels on each of two antennas. This uses all four available receiver channels at MRO, but enables us to use interferometric techniques with both frequencies (97.3, 98.9 MHz) on both the UW-MRO and EWU-MRO bistatic links. This means we are correlating time series measured on one channel at MRO with the same channel from both Seattle and Spokane transmitters. Clearly the transmitter time series are independent, but it is reasonable to wonder if system performance will suffer due to in-band signal from other locations. However, we expect matched filtering to mitigate most loss of dynamic range due to co-channel transmitters, based on a study by Morabito [unpublished, 2004] on simulated co-channel interference effects on aircraft tracking with the three-receiver MRR topology.

We also find the 96.5 MHz Seattle station (KJAQ) to be very useful, but we often do not record on that channel since 96.5 MHz is an unused channel in Spokane, and we wish to make the most of our 4 available MRO receiver channels for interferometry. When investigating TDOA (time difference of arrival) techniques for point targets such as aircraft and meteors, however, three separate frequencies with one recorded on a second antenna for interferometric purposes is a very effective use of the MRO receiver capacity.

It is clear that the allocation of receiver channels for various experiments and the optimal choice of transmitters of opportunity are complicated and currently problems which require case-by-case, detailed attention. The automation of this process (at least the identification of suitable transmit-receive channels) should be possible and

[1]For an up-to-date database of licensed operating transmitters, we use the "FM Query" feature on the FCC.gov website.

we expect to implement a "frequency sweep diagnostic" sometime in the future.

6.2 *Multistatic Remote Sensing Experiments*

New instrument designs frequently enable new scientific inquiries. In this section we will describe several experiments relevant to the study of E region plasma density irregularities that we were previously unable to do with the two-receiver MRR system. Many similar experiments have been performed with active radars with mobile antennas and/or multiple radars observing the same view volume (*e. g.*, EISCAT work done by Williams *et al.* [131]); this will be the first time these experiments have been performed with a completely passive radar system. The proof of concept for geophysical experiment techniques with distributed passive radar is very important. The aeronomy community is moving away from large, expensive "class 1 facilities" and placing a new emphasis on "Distributed Arrays of Small Instruments" (codenamed DASI by proponents [90, 67]), of which the MRR is an early example.

A common theme in most of these experiments is the availability of multiple independent observations of an event or target, as well as larger and more diverse (e.g., different lines-of-sight) spatial coverage. Greater coverage lets us monitor mesoscale phenomena and observe large-scale structures moving through the radar view volume by comparing the evolution in time of observations on the various MRR links. The slightly different areas of sensitivity for a UW-MRO link and an EWU-MRO link can be seen in Figure 6.2. Finally, to a limited extent, we should be able to validate observations on one link with those of another. We now discuss some specific new scientific opportunities the multistatic MRR architecture affords.

6.2.1 Detection of Space Weather "Fronts"

By space weather fronts, we mean evidence of a disturbance in the geomagnetic system that can be observed to be propagating from one area to another. The analogy with tropospheric weather fronts is appropriate and intended. The Millstone Hill Observatory (MIT Haystack) group has been using the term "space weather front" for several years to describe the temporal and spatial evolution of observations of storm-enhanced plasma density (SED), sub-auroral electric field structures, steep total electron content (TEC) gradients, plasma convection patterns over the poles, and more [31, 32, 29, 33]. Specifying and understanding these phenomena in the context of the coupled magnetosphere-ionosphere system, particularly during geomagnetic disturbances and storms, defines a very important and active area of aeronomy research today.

For example, large-scale plasma density redistribution can occur during magnetic storms. Electric fields form, sometimes subject to feedback instabilities, eroding the low latitude plasmasphere density and sweeping it toward the cusp region of the ionosphere in highly localized plumes with steep gradients [31, 13]. These plumes can reach densities as high as 100 TEC units (one TECu, or unit of altitude-integrated total electron content, is 10^{16} electrons per square meter). The entire plasma redistribution process can be observed by a multitude of instruments at different geographical locations as the event develops (*e. g.*, widely distributed GPS receivers measuring TEC; incoherent scatter radars measuring plasma density versus altitude; satellites imaging the auroral oval and plasmasphere, and others). This particular space weather phenomenon – storm-time sub-auroral redistribution of ionospheric plasma – is of interest to us because the MRR can contribute useful measurements; however, many other storm-time system reactions could be studied over an extensive geographic area as space weather fronts.

The newly enhanced MRR system (with its second reference receiver, and thus additional view geometry) is well suited to provide observations for the study of space weather fronts and other large-scale ionospheric phenomena. As we mentioned in Section 4.3, much can be learned from simply considering the time and location of coherent backscatter occurrence (indicating irregularities and thus elevated electric field strength), along with background space weather conditions, in the context of large-scale models of ionospheric behavior. Using multiple bistatic links, we can simultaneously focus on small-scale, local events (individual plasma instabilities), observe meso-scale effects (say, the size of the entire field of view for one bistatic link), and contribute to the monitoring of global-scale events with all the bistatic links and spatial coverage we have available. By taking into account Doppler shifts and aspect angle sensitivity, we can infer the meso-scale convection of electric field structures through the MRR field of view. The goal of this type of study is to evaluate meso- and global-scale models of plasma behavior (such as the SAPS and magnetospheric convection) in the midlatitude ionosphere. Relevant space weather conditions, such as the extent of auroral oval expansion into the MRR field of view, can be obtained from various satellite and/or magnetometer data available via the internet.

The utility of multistatic passive radar networks will only increase as more receivers are installed. Add to this the passive radar potential for year-round (inexpensive) continuous time coverage, excellent resolution, and lack of range/Doppler ambiguities, and we have a superb network-instrument for distributed space weather monitoring. Of course, as receivers are added, the complexity of the system also vastly increases. The larger amounts of data and network traffic could cause "data logistics" issues to become crippling. As the MRR and ISIS grow, it will be a significant challenge to keep up with controlling software infrastructure requirements. An increment of one receiver is a start, and a useful testbed for the development of more

extensive systems.

Example Front Observation: SAPS

The sub-auroral polarization stream (SAPS) is a midlatitude electric field that plays an important part in the above-mentioned storm-time plasma redistribution. It is integral to several magnetosphere-ionosphere coupling processes (we discussed some in Section 2.3.1, page 20), and the current MRR system, located in the northwest United States, is in an excellent position to contribute to SAPS-related observations. On 17 July 2004, we recorded three hours of MRR backscatter which we believe is due to a SAPS electric field. Unfortunately, this event occurred before the third (Eastern Washington) receiver was installed, so we have only observed it with a single view geometry (however, we do have two independent FM channels).

Figure 6.3 shows MRR backscatter power versus range and time for the Seattle KBSG transmitter – MRO bistatic link. This plot is very similar to one reported by the Millstone group [32] and is believed to be indicative of fine-scale electric field structure within a SAPS channel which is itself moving (more slowly) equatorward. We can treat the coherent backscatter structure as if it were electric field structure since enhanced electric fields must be present to generate the plasma density irregularities that cause coherent radar backscatter. Also, Foster and Erickson performed an experiment with the Millstone Hill incoherent scatter radar that indicated a linear relationship between electric field strength and the log of coherent backscatter power [30], although this (linear relationship) result may only be valid at UHF frequencies.

Satellite measurements indicate that the auroral precipitation region did not extend far enough equatorward to influence MRR backscatter during the period shown in Figure 6.3. Furthermore, we find SAPS signatures in density and plasma drift measurements by other instruments on this date. Therefore, we believe the equatorward-

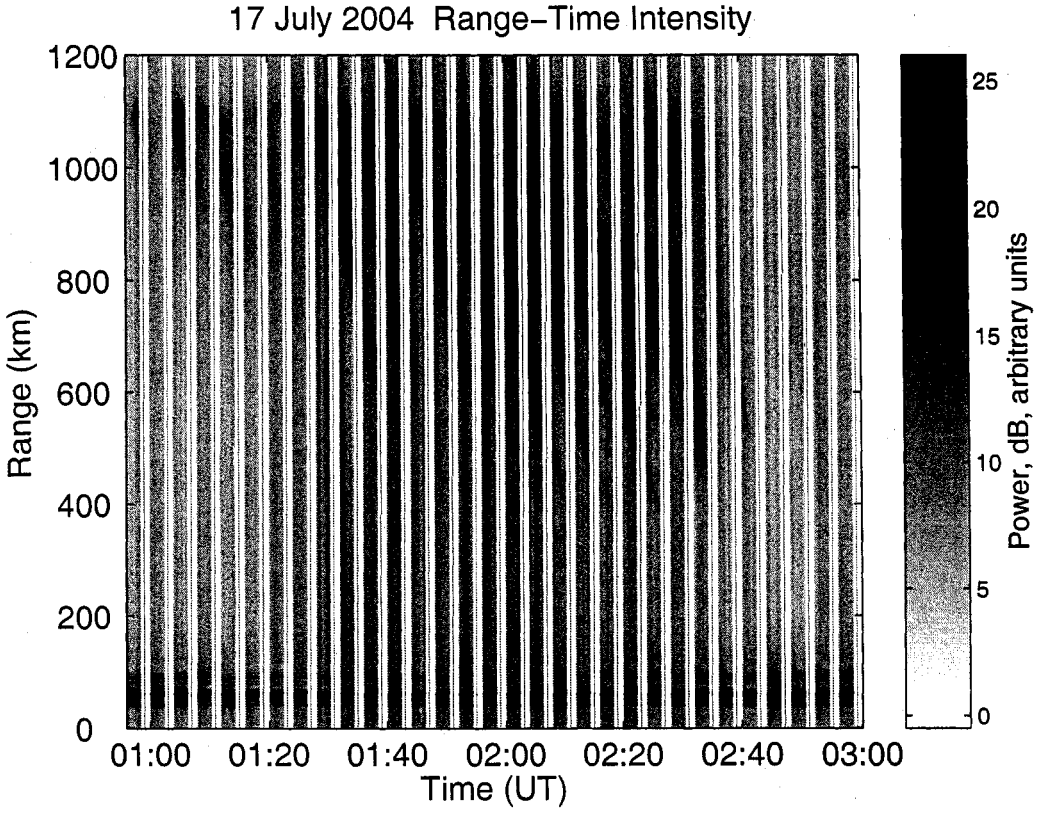

Figure 6.3: A range-time intensity diagram from the MRR observations on 17 July 2004. (The white areas represent gaps in the data.) The transmitter used is KBSG (Seattle, 97.3 MHz). The usual ground clutter can be seen along the bottom edge at approximately 70 km range; above, electric field structures possibly due to SAPS convect equatorward through the radar field of view.

traveling "space weather front" in Figure 6.3 is caused by the sub-auroral polarization stream. We show more detailed SAPS observations, supporting satellite data, and potential irregularity mappings for the 17 July 2004 event in Chapter 7, section 7.2.2.

6.2.2 3-D Velocity Measurements

Three or more spatially diverse radar lines of sight enable (in most cases) the estimation of full 3-D vector velocities for plasma drifts and waves. With the addition of the third MRR receiver, we can now estimate the relative electron-ion drift, $\mathbf{V_d}$. $\mathbf{V_d}$ is the source of free energy for the ionospheric two stream instability, and therefore is very important in the interpretation of radar backscatter and in understanding the unstable plasma in general. We can use the full vector velocity $\mathbf{V_d}$ to obtain the flow angle ($\theta = \cos^{-1}(\hat{k} \cdot \hat{V_d})$), approximate the applied electric field (through equation 4.15), and to determine an upper bound for the acoustic speed, and thus the plasma temperature ($c_s^2 \equiv \frac{k_B}{m_i}(T_i + \gamma T_e)$).

This new capability to estimate plasma velocities in 3-D is enabled by probing scattering regions from substantially diverse directions; the Seattle and Spokane radar links make measurements projected onto directions that span the three spatial dimensions. For example, in Figure 6.4, we have determined for an arbitrary scattering region (labeled "target") the wave k-vectors to which the MRR is sensitive for four different bistatic links. In each case, the target is illuminated by a commercial FM transmitter and the resulting scatter is received at MRO. Thus, each hypothetical irregularity k-vector points from the scattering region along the bisector of the angle between the ray paths to the appropriate transmitter and MRO. The k-vector magnitudes shown in Figure 6.4 are not to scale; we expect them to correspond to a wavelength of roughly 1.5 m due to the condition for Bragg scatter. We have elongated the k-vector lengths to illustrate the different directions probed in the scattering

volume.

In the past, we have attempted to estimate the full vector velocity of the plasma by different methods. Previously Meyer and Sahr [74] approximated plasma drift velocity vectors with the MRR by using both range rate and azimuth interferometer phase rate (transverse drift through the radar beam). This gave two independent, orthogonal velocity estimates; they assumed the plasma velocity parallel to B was negligible to complete the three-dimensional vector. However, "range rate" drift velocities may represent other effects separate from electron drift or irregularity phase velocity. These velocity measurements are important, but they are not necessarily proportional to electric field. For example, meteors ionize columns of gas during their ablation at mesospheric heights; the resulting "meteor tubes" of plasma are pushed around by neutral winds. Scientists use range rates of density irregularities arising in the meteor tube plasma as tracers in order to study neutral winds and wind shears with radar [103].

In the case of a large scattering volume excited by electric field(s), a range rate velocity estimate may "spoof" motion by capturing the radar-geometrical solution as it shifts around, or the plasma becoming unstable in different regions independently (which can cause grossly overestimated velocities).

Therefore, we are enthusiastic about using a well-defined method to estimate the fully 3-D relative electron-ion drift now that the MRR has multiple bistatic links with large spatial separations. The technique is as follows: from the Farley-Buneman dispersion relation, the measured Doppler velocity (or wave phase velocity) $v_{D,i}$ on a bistatic link i is equal to $\hat{k}_i \cdot \mathbf{V_d}$. The unit wavevector $\hat{k}_i$ is defined by the angle bisector between the ray paths from target to transmitter and target to receiver ($\hat{k}_i$

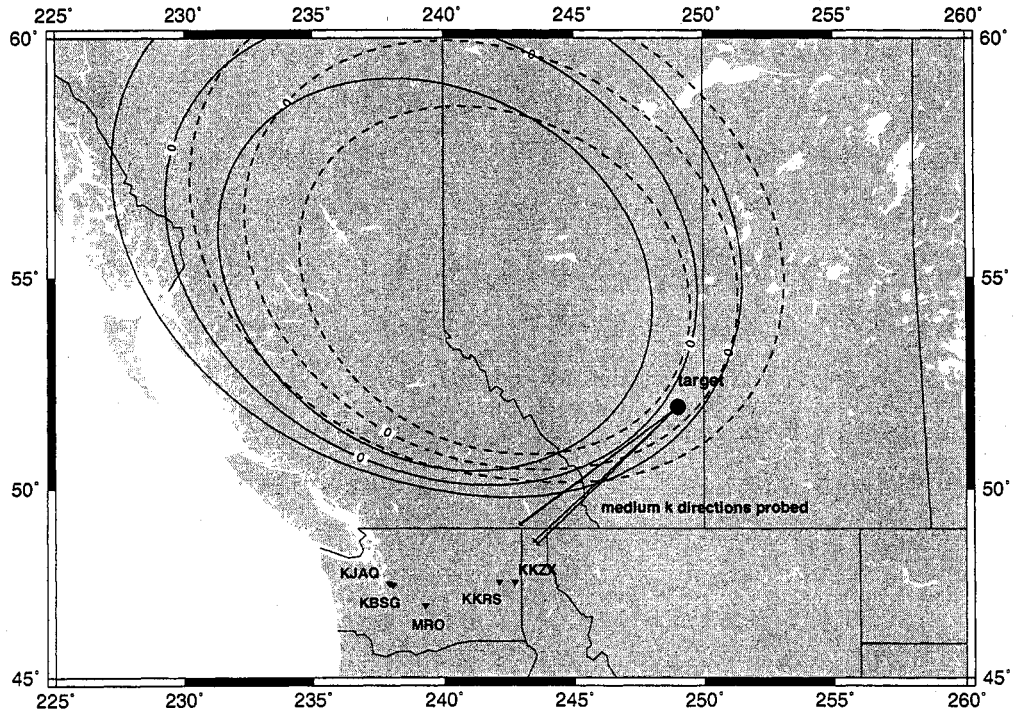

Figure 6.4: Wave k-vectors in a target scattering volume to which the MRR is sensitive for four different bistatic links. The illuminating transmitters are labeled; all scatter is received at MRO. The magnitude of the simulated k-vectors has been artificially increased. Contours of constant aspect angle within 1° of perpendicular are also overlayed for two of the bistatic links (one west link and one east link).

points in the opposite direction of the radar line of sight for bistatic link i). Thus,

$$\mathsf{K}\mathbf{V_d} = \mathbf{v_D}, \quad \text{where} \quad \mathsf{K} = \begin{pmatrix} k_{1x} & k_{1y} & k_{1z} \\ k_{2x} & k_{2y} & k_{2z} \\ & \vdots & \\ k_{nx} & k_{ny} & k_{nz} \end{pmatrix} \tag{6.1}$$

$\mathbf{v_D}$ is a vector of n independently measured Doppler velocities and K is a matrix containing the unit wavevectors probed by the n different bistatic radar links (such as those shown in Figure 6.4). (We have assumed that the ionospheric parameter ψ is negligible, which is reasonable in the E region). We can invert the matrix K to solve for $\mathbf{V_d}$ provided that it is not singular. Ideally, three of the n bistatic lines of sight (and therefore the probed medium k-vectors) should be orthogonal; however, this is difficult to achieve, especially when using transmitters of opportunity for illumination. Instead, we hope that the available lines of sight are sufficiently independent to span the three spatial dimensions, and with multi-channel receiver infrastructure we are often able to obtain more than three k-vectors so that the problem becomes overdetermined, and we can use a least squares method to solve for $\mathbf{V_d}$.

Once we know $\mathbf{V_d}$, we can determine the flow angle for each bistatic radar link, an important parameter in the study of the "microphysics" of the Farley-Buneman instability. We can also obtain the electric field if we make the assumption that $\mathbf{V_d} = \mathbf{E}\times\mathbf{B}/B^2$. This is a decent assumption in the E region; it is a better assumption in the F region and most radar experiments that claim to measure $\mathbf{E}$ and/or the $\mathbf{E}\times\mathbf{B}$ drift are observing the F region.

The condition for meter-scale instability from the Farley-Buneman dispersion relation is $V_d > c_s(1+\psi)$ (true along the direction parallel to $\mathbf{V_d}$). Therefore, $|\mathbf{V_d}|$ is

an upper bound on the acoustic speed c_s, and

$$T_i + \frac{5}{3}T_e = \frac{c_s^2 m_i}{k_B} \leq \frac{V_d^2 m_i}{k_B} \tag{6.2}$$

is an upper bound on the plasma temperature (in Kelvin). Equation 6.2 assumes isothermic ions and adiabatic electrons; k_B is the Boltzmann constant; and the ion mass m_i is the proton mass times an average molecular weight of 31 for the E region.

Receiver Channel Allocation and Geometric Dilution of Precision

More diversity in the radar lines of sight for the multiple bistatic links means our experimental velocity estimates can be more reliable and complete. As we mentioned above, ideally we would use three orthogonal lines of sight. However, for high latitude coherent scatter, this is impossible no matter how conveniently placed the transmitters are, since perpendicular aspect angles cannot be achieved for zenith observations. Fortunately, three of the most useful transmitters in our area (KBSG – Seattle 97.3, KJAQ – Seattle 96.5, and KKZX – Spokane 98.9) provide sufficient diversity to span the three spatial dimensions.

Another useful transmitter is KWJZ, the Seattle 98.9 MHz channel (52 kW ERP), which has the added advantage of sharing its frequency with KKZX on the Eastern Washington side (so that a single scatter-receiving channel at MRO can be used for both). KWJZ would be an excellent choice – since receiver channels at MRO are an important, limited resource – but for the fact that the transmitter is mounted on the same tower as KBSG, the Seattle 97.3 station, giving us no additional line-of-sight information. We prefer to keep using KBSG because it currently provides the cleanest, strongest radar data of all the transmitters (most likely through a lack of interference at MRO); therefore, we cannot use the KWJZ transmitter. (In the future, we plan to implement interference-mitigating signal processing, which should allow us to use other stations without suffering a performance penalty. Zhou has provided

a start toward this goal in his PhD thesis [133].) The shared location for the KBSG and KWJZ transmitters is an unfortunate coincidence, since it limits our ability to perform interferometry and multistatic experiments simultaneously in the following way. There are four digital receiver channels (with two analog inputs) available for collecting scattered signals at MRO. We use one analog input for each interferometer antenna, leaving two possible digital channels per antenna (or three and one, or four and zero). If we wish to use the interferometer, we must allocate one digital channel on each antenna to the same frequency. If we wish to obtain interferometric measurements for two separate frequencies (as is required for the azimuth de-aliasing technique described in Section 6.2.3), we require all four digital receiver channels, and we can only monitor two frequencies (both frequencies on both antennas). Next, the most (only, really) useful transmitters in Seattle are 97.3, 96.5, and 98.9 MHz (with 97.3 and 98.9 on the same tower). The useful transmitters in Spokane are 98.9 and 97.3 MHz; there is no 96.5 MHz station in the Eastern Washington area. Therefore, our optimal choices for receiver channel allocation at MRO are the following:

1. Antenna 1: 97.3, 98.9 MHz. Antenna 2: 97.3, 98.9 MHz. This configuration enables interferometry on the 97.3 and 98.9 channels for both the eastern and western bistatic links (the eastern 97.3 channel is only 5.1 kW and often not useful, however). There are potentially three independent lines of sight.

2. Antenna 1: 97.3, 98.9, 96.5 MHz. Antenna 2: 98.9 MHz. This configuration enables interferometry on the 98.9 channel for both the eastern and western bistatic links. It also provides three independent lines of sight. This configuration is best for multistatic experiments.

3. Antenna 1: 97.3, 96.5 MHz. Antenna 2: 97.3, 96.5 MHz. This configuration enables interferometry on the 97.3 and 96.5 channels for the western bistatic link

(and potentially 97.3 interferometry for the eastern link, although that channel does not often work very well for us). This configuration is best for attempting experiments which require interferometer data on two channels; however, it does not provide any reliable data for the eastern bistatic link.

We are not currently limited by available receiver channels at the reference receivers in Seattle and Spokane.

We can see that when allocating the MRO receiver channels, we must often choose between multistatic experiments and interferometer information. However, the reality of the situation is somewhat worse; another choice we must make is between reliable, "strong" radar data and weak links which may disappoint with empty or noisy datasets if we attempt to use them during (the relatively infrequent, and precious for those trying to graduate) magnetic storms. The only channels we have found that currently provide reliable radar data are 97.3 and 96.5 MHz in Seattle and 98.9 in Spokane. Thus, to maximize our "good data," we use configuration (2) most often, and always when geomagnetic disturbances are predicted, unless there is a specific alternate experiment we wish to perform.

We are fortunate that the lines of sight for the bistatic links using 97.3, 96.5 (Seattle) and 98.9 (Spokane) satisfactorily span the three spatial dimensions. As the MRR and ISIS passive radar networks expand, view geometry diversity will become an important consideration when placing receivers and choosing illuminating transmitters. If transmitters are located in sufficiently similar positions, our spatial resolving power is weakened due to the "stiffness" of the K matrix (radar lines of sight matrix). Inverting a very stiff matrix can be difficult to do with guaranteed accuracy. In a worst case scenario, we might be unable to achieve three independent lines of sight for a radar field of view. This effect is called geometric dilution of precision (GDOP) and is often a topic seen in relation to GPS receivers [132]. If a GPS device detects only

satellites spaced closely together, the quality of its location estimate suffers. Passive radar networks may have a similar problem, except many transmitters of opportunity do not move (as the GPS satellites do), so passive receiver nodes must be placed carefully.

We suggest that a metric by which to rank possible locations for passive radar nodes can be obtained by investigating the range of the GDOP values and condition numbers of the K matrix computed along the perpendicular aspect contours of the area. These GDOP values / condition numbers will be dependent on the locations of transmitters in the area; the location (to be chosen) of passive radar receiver(s) in the area; and the local magnetic field geometry. The maximum or minimum of (or some statistic of) the GDOP values or K-condition numbers could be used to make recommendations for optimal placing of receiver nodes in a region, as well as the optimal density of receiver nodes. We show some example calculations of K-condition numbers and GDOP values for the MRR in Chapter 7, page 201.

An Inverse Problem

A significant assumption inherent in the $\mathbf{V_d}$ estimation technique given in Section 6.2.2 is that we will be able to associate multiple independent Doppler velocity measurements, from multiple bistatic radar links, with each other to form a vector of related measurements with which to determine a single electron drift velocity. As it turns out, it is nearly impossible to say with any confidence that two irregularity spectra, one observed on a western MRR bistatic link and the other on an eastern link, originated from the same scattering volume. Two western links are often similar enough to match data, however. (We show radar data from multiple bistatic links in Chapter 7; for example, see Figures 7.9 and 7.11.) Making the assumption that all bistatic links are observing the same scatterer would be like assuming the configura-

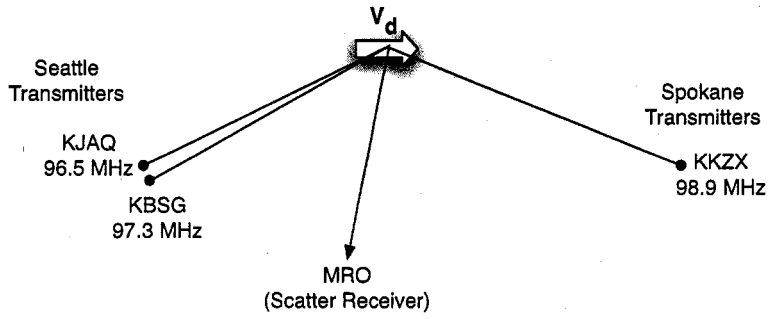

Figure 6.5: A hypothetical illustration of three MRR bistatic links observing the same scattering region.

tion shown in Figure 6.5, which is unreasonably strict. In fact, the individual plasma instabilities causing the backscatter are almost certainly independent events (they are short-lived and probably too spatially compact to span the $\approx$ 120 km between equivalent aspect angle contours on an eastern and western bistatic link). Furthermore, depending on the level of aspect angle sensitivity, there are limited near-zero aspect angle intersections between the western and eastern link view volumes, and intersections do not exist for every range (see, for example, Figure 6.2). Another complicating factor is that aspect angle depends on the scatterer altitude, which is also unknown.

Therefore, a more appropriate question is, are the irregularities observed on different radar links all within a spatially homogeneous medium? Did they originate due to the same external electric field? If so, Figure 6.6 shows an illustration of the situation; if not, our scattering situation looks more like the scenario in Figure 6.7.

Geophysical inverse theory offers a formal way to pose this question. Before we describe an inverse theoretical approach to our problem, we state the related forward problem: given a value for the electron drift $\mathbf{V_d}$ (or its statistical distribution information), what Doppler shift will the radar measure (how probable is this mea-

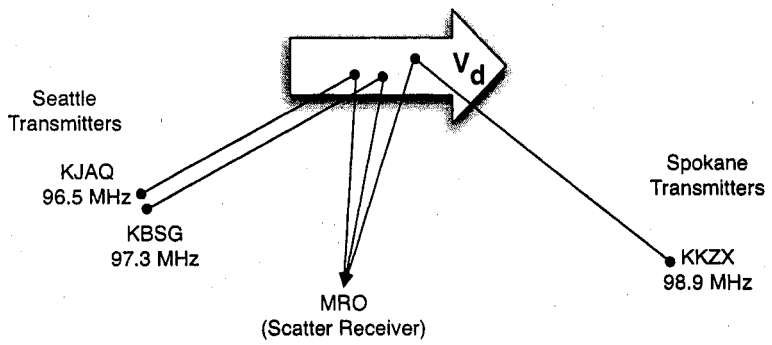

Figure 6.6: A hypothetical illustration of three MRR bistatic links observing different scattering regions within a homogeneous medium. The instability driver (electron drift, or electric field) is the same in all three measurements.

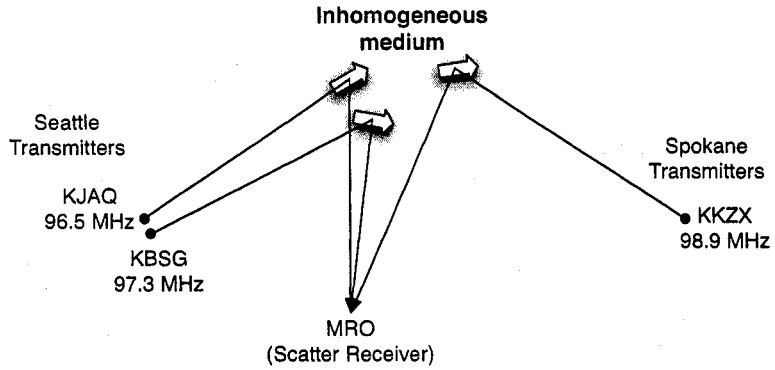

Figure 6.7: A hypothetical illustration of three MRR bistatic links observing different scattering regions within an inhomogeneous medium. We cannot assume that plasma parameters measured on the three radar links are related.

surement)? Essentially, the forward problem is that of understanding the statistics of our instrument and the underlying theory of the phenomenon being measured. The inverse problem, then, can be posed: given a set of Doppler velocity measurements (with corresponding measurement error statistics) at the following locations (within error contours, for example), what is the probability that $\mathbf{V_d}$ was equal to a certain value? Most estimators seek to determine the maximum likelihood value for the sought parameter (in this case, $\mathbf{V_d}$), but a full inverse theory treatment seeks to determine the probability density function of the parameter [126].

To attempt to solve the inverse problem requires a complete understanding of the forward problem, and the current knowledge of nonlinear plasma instability theory is insufficient to specify the forward-relationship between irregularity parameters and radar spectral features. However, it is possible to use an "inverse theory informed" attitude when estimating parameters. For example, after making assumptions about scatterers (such as perfectly perpendicular aspect angle, or 100 km altitude) and treating measurements as error-free (Doppler shift, for example), we may produce inconsistent or unrealistic results (for example, electron drifts that are far too large, or extremely steep velocity shears over a small space). When we encounter these inconsistencies in our results, we know that we must adjust our underlying assumptions, increase the error bars on our instrument measurements, or some combination of both.

In practice, we imitate the homogeneous medium assumption (as in Figure 6.6) used by many incoherent scatter radars to estimate electron drift velocity and electric field strength. For example, the Arecibo Observatory measures ionospheric electric fields by pointing its transmitter in three orthogonal directions, dwelling on each momentarily [114]. Thus, the accuracy of their measurement depends on both spatial homogeneity and temporal stationarity (over the three dwelling periods). Only the

European Incoherent Scatter radar (EISCAT), with its multiple receiver configuration and tight antenna beams, can truly estimate a vector electric field without using this assumption. In Chapter 7, Section 7.2.3, we show an example of using the multiple k-vector technique described here to estimate $\mathbf{V_d}$ with MRR data.

6.2.3 Reducing Interferometer Azimuth Ambiguity

In order to do the 3-D, multistatic experiments described above, we need information about scatterer locations to determine the required k-vectors for each bistatic link. A straightforward but oversimplified method (which we nevertheless use, for lack of a better option, in Section 7.2.1) is to assume an altitude and perfectly perpendicular aspect angle, then find the intersection(s) of the target range and zero degree aspect angle contours.

Alternatively, we can use interferometry, which has been implemented for the MRR by Meyer and Sahr [76, 74]. However, in its current state the MRR interferometer is badly aliased in angle of arrival (θ). It has a long baseline ($\approx 16\lambda$), enabling it to perform high resolution transverse imaging [76], but crippling it as an absolute direction-finder for the entire radar field of view, since phase differences between the antennas do not uniquely map to angles of arrival.

Here, we present a technique for overcoming the azimuth angle aliasing which uses multiple frequency channels. By the same principle that enables frequency domain interferometry to work [65], we can obtain independent phase differences between two antennas (ϕ) by listening to two different frequencies on both antennas. We can then use the two independent interferometer measurements to obtain an estimate for the absolute angle of arrival. (However, performing this technique is costly in terms of the number of receiver channels that must be exclusively allocated to the experiment, as we note above on page 122.)

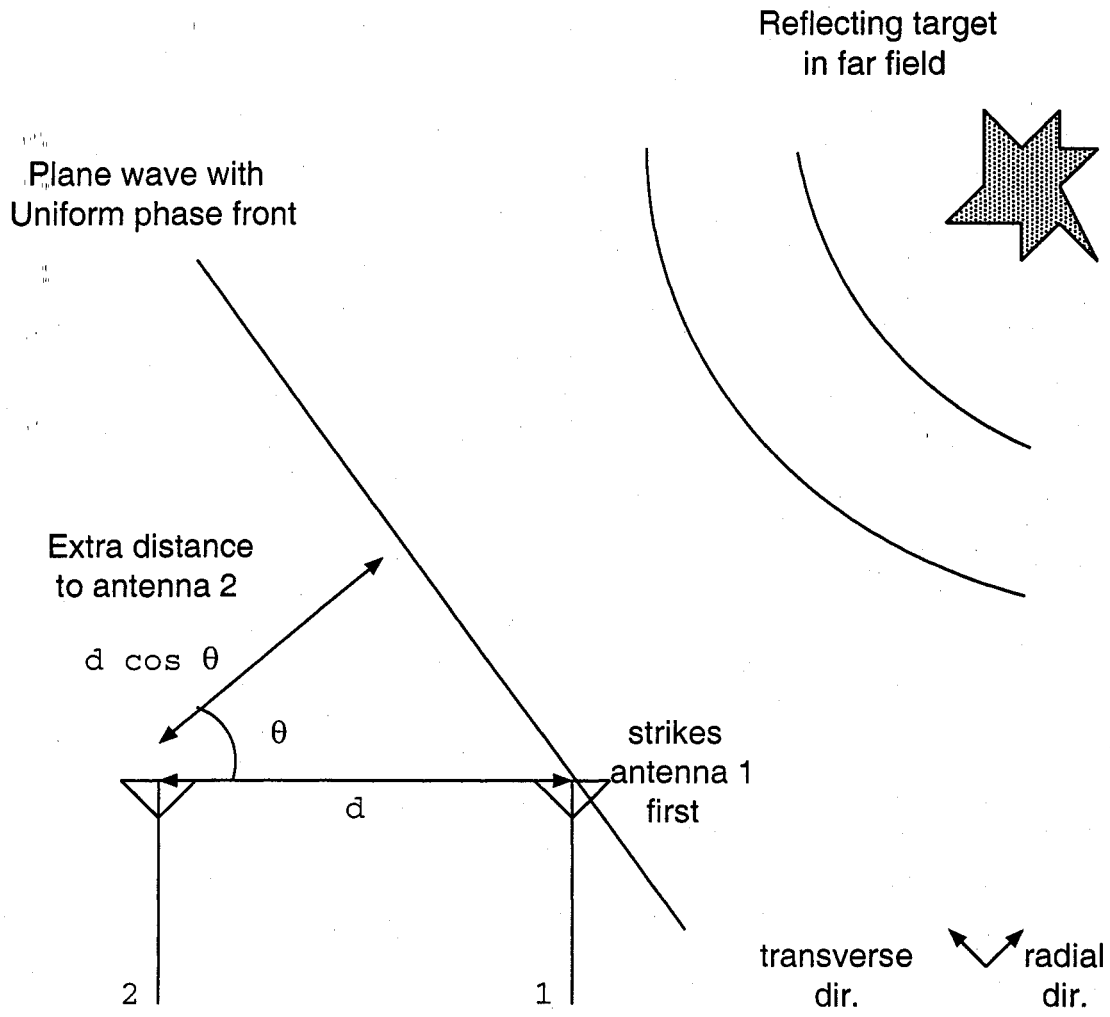

Figure 6.8: An illustration of basic radar interferometer geometry. The extra distance traveled by the plane wave to antenna 2 can be converted to a phase value by multiplying by k (the transmitter wavenumber, which has units of m^{-1}).

The problem is formulated in the following way. The basic horizontal interferometer relation is

$$kd\cos\theta = \phi + n2\pi \tag{6.3}$$

where the transmitter wavenumber (k) and the antenna baseline (d) are known, and the phase difference ϕ is measured via the interferometric technique. (See Figure 6.8 for an illustration of the basic interferometry concept.) However, we can only determine the principal angle for ϕ. To determine the alias number n, we take advantage of a second pair of phase measurements at a different frequency so that we have

$$d\cos\theta = \frac{\phi_1 + n_1 2\pi}{k_1} = \frac{\phi_2 + n_2 2\pi}{k_2} \tag{6.4}$$

$\Delta kd < 2\pi$ is the condition for the two alias numbers, n_1 and n_2, to be equal (or adjacent; but we ignore this possibility at the risk of a statistically small number of mis-estimates). Plus, we can use the magnetic aspect angle criterion to alert us to grossly inaccurate location estimates. For the FM channels 97.3 and 96.5 MHz, $\Delta kd \approx 0.84$ radians. Therefore, we assume $n_1 = n_2$ and then invert one of the equations to find θ:

$$n_1 = n_2 = \frac{\lambda_2\phi_2 - \lambda_1\phi_1}{2\pi(\lambda_1 - \lambda_2)} \tag{6.5}$$

$$\theta = \cos^{-1}\left[\frac{\lambda_1}{2\pi d}\left(\phi_1 + \frac{\lambda_2\phi_2 - \lambda_1\phi_1}{\lambda_1 - \lambda_2}\right)\right] \tag{6.6}$$

To calibrate the interferometer for absolute (instead of relative) positioning, we must also estimate an additional phase shift (denoted ϕ_0) between the two antennas due to system effects (such as a difference in antenna cable lengths, phase effects in amplifiers and filters, etc.). This phase shift must be estimated and subtracted from the interferometer ϕ estimates, resulting in the following adjusted equations:

$$\phi_{\text{measured}} = \phi_{\text{true}} + \phi_0 \tag{6.7}$$

$$kd\cos\theta = \phi_{\text{measured}} - \phi_0 + n2\pi \tag{6.8}$$

A possible method for determining ϕ_0 is to observe an area FM transmitter in a known location and average for a long time to get a reliable estimate for ϕ. This is possible since the known transmitter signal can be assumed stationary (in both the physical and statistical senses). Then, θ and n are known quantities, and we can obtain the interferometer calibration ϕ_0. We write the solution for azimuth angle using four channels to de-alias the interferometer below.

$$\theta = \cos^{-1}\left[\frac{\lambda_1}{2\pi d}\left(\phi_1 - \phi_0 + \frac{\lambda_2(\phi_2 - \phi_0) - \lambda_1(\phi_1 - \phi_0)}{\lambda_1 - \lambda_2}\right)\right] \tag{6.9}$$

Unfortunately, the inherent interferometer phase offset is frequency dependent due to the contribution from cable length differences. If the above-described FM transmitter calibration method is used for estimating ϕ_0, a transmitter should be chosen that is very close in frequency to the two channels being used for interferometry (also, the two channels should ideally be as close as possible). Another concern is that the observed FM transmitter be located within the main beams of both interferometer antennas (assuming most targets we observe are also in the antenna main beams). We would also like the transmitter we choose for calibration to be relatively high power, so that co-channel interference does not confuse the estimate. Finally, the received signal should be checked for evidence of significant multipath (*e. g.* autocorrelation peaks at nonzero lags), which will also make a phase offset estimate less reliable. Often, all of these conditions cannot be met when one is relying on transmitters of opportunity in the area.

We can take steps to avoid some of the constraints on the choice of calibration transmitter. We can physically measure the coax cables connecting the interferometer antennas to the receiver (often it is surprisingly difficult to achieve an accurate measurement, especially when very long cables, conduits, and coils of cable are involved); always record the exact physical length of cables when installing new antennas; test amplifiers, filters and other receiver equipment while they are isolated from the system

to determine their phase contributions; manually correct for antenna phase shifts if the transmitter being used for calibration is outside the main beam(s) (requires knowing antenna gain patterns in detail); and manually remove any multipath echoes in the signal from the chosen transmitter. Alternatively, briefly operating our own transmitter would allow us to control most of the calibration parameters (of course, this requires a transmitter and license).

Interferometer Calibration Example

On 17 July 2004, we recorded the amount and type of data we need to attempt the above technique for gleaning true angle of arrival (AOA) information from the interferometer. For three hours (using a data-taking scheme that recorded signals for 2 minutes and 40 seconds out of every 4 minutes), the MRR received irregularity scatter from 2 different channels on each of 2 antennas at MRO (thus utilizing all available analog and digital receiver channels on the remote receiver). We recorded reference signals for those two channels (97.3 MHz KBSG and 96.5 MHz KJAQ) with the Seattle receiver. Both scatter-receiving antennas had a clear enough view of the irregularities to perform interferometry on both channels.

To de-alias the interferometer and determine the angle of arrival for these irregularities, we must first calibrate the instrument by estimating the instrument-inherent phase shift ϕ_0. We will use the method outlined above: measuring the interferometer phase for the signal from a known transmitter, calculating what ϕ_{true} should be from the location of the transmitter, then determining ϕ_0 using the following relationship:

$$\phi_{\text{measured}} - \phi_{\text{true}} = \phi_0 \tag{6.10}$$

Our first task is to choose an appropriate transmitter for the calibration. After investigating FCC records, we found three potential transmitters for the calibration (see Figure 6.9): KXLE in Ellensburg (47.2° N, 239.2° E), at 95.3 MHz and 51 kW

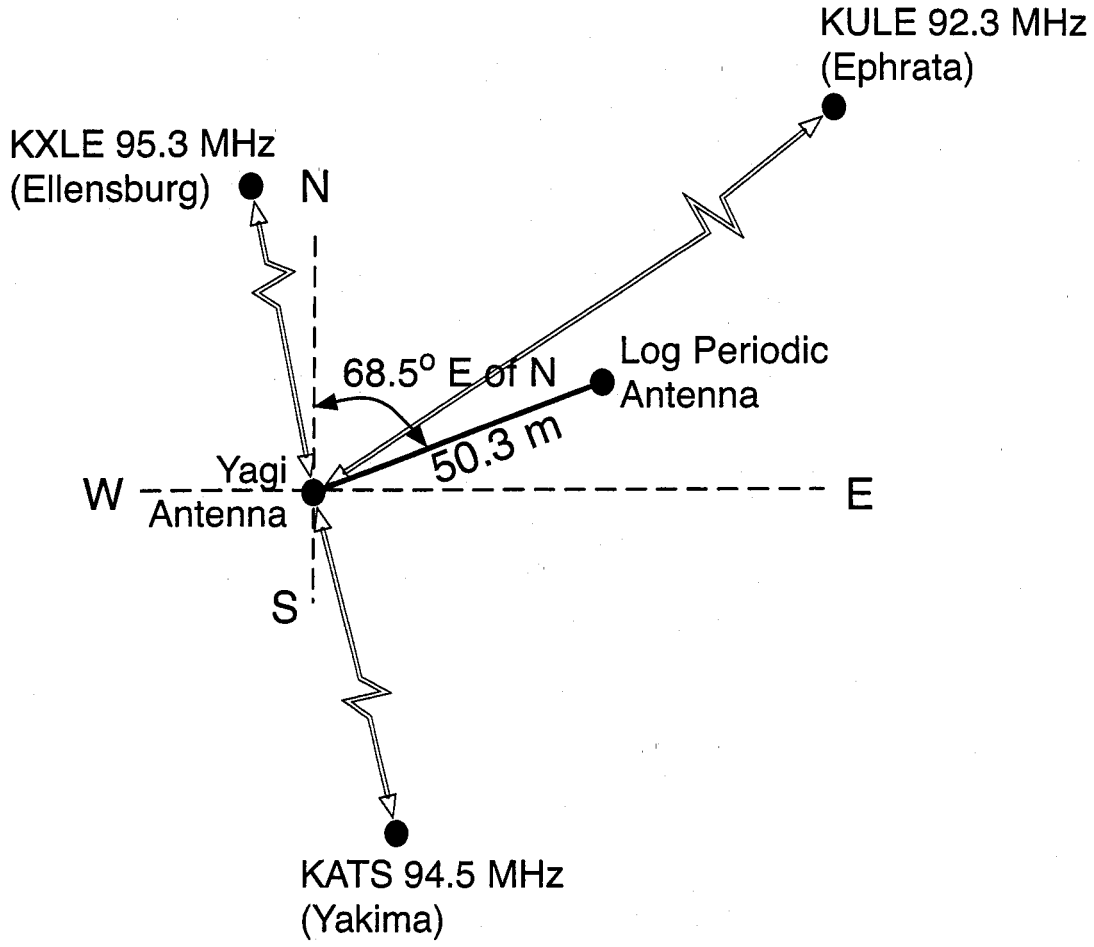

Figure 6.9: A diagram of the scatter-receiving antenna baseline at MRO. The Yagi and log-periodic antennas are the two most often used for interferometry; their baseline is about 21° off horizontal (East-West). Three transmitters considered for the interferometer calibration are also shown. The figure is not to scale, but the relative positions of the antennas and transmitters are accurate.

ERP; KULE in Ephrata (47.3° N, 240.4° E), at 92.3 MHz and 26 kW ERP; and KATS in Yakima (46.5° N, 239.5° E), at 94.5 MHz and 100 kW ERP. The MRO receiver is located at 47.0° N and 239.3° E. Using a handheld GPS device, we measured our antenna baseline at MRO to be 50.3 meters, oriented in a bearing 68.5° east of north, as shown in Figure 6.9. This figure is not to scale, but it shows the relative locations of the relevant antennas and transmitters.

The Ellensburg and Ephrata transmitters are most promising, since the Yakima transmitter is to the south of the antenna baseline and the Yagi antenna has a decent front-to-back ratio (causing phase shift and attenuation of the Yakima signal). We took 150 seconds of 100kHz data on both interferometer antennas for each of the two transmitters to the north of the baseline (KXLE and KULE). The resulting time series are complex-valued and 15 million samples long. (We wish to average for a long time; this is unequivocally to our advantage since the transmitter signals are stationary.) Since FM signals are ideally constant modulus, we can ignore the sample magnitudes and focus on the phase difference between the transmitter signals arriving at the log periodic antenna (y_1) and the Yagi antenna (y_2):

$$\arg(y_1 y_2^*) = \arg\left(e^{j\beta_1} e^{-j\beta_2}\right) = \beta_1 - \beta_2 = \phi_{\text{measured}} \tag{6.11}$$

This phase difference can be calculated for each sample (care must be taken to keep track of which antenna's signal is conjugated). Averaging over the entire 150 seconds, we find $\langle\phi_{\text{measured}}\rangle$ is approximately -2.504 radians for KXLE (the Ellensburg station), with a variance of 0.05 rad^2; for KULE (the Ephrata station), $\langle\phi_{\text{measured}}\rangle$ is 0.760 radians with a variance of 3.88 rad^2. Figure 6.10 shows a 0.1-second slice of the KXLE ϕ-measurements. They seem (at least throughout the 150-second sample) to follow a roughly periodic trend; the period is about 10 milliseconds (corresponding to 100 Hz). This apparent periodic behavior should be investigated further.

We choose to use the KXLE data to estimate ϕ_0 because of the very large variance

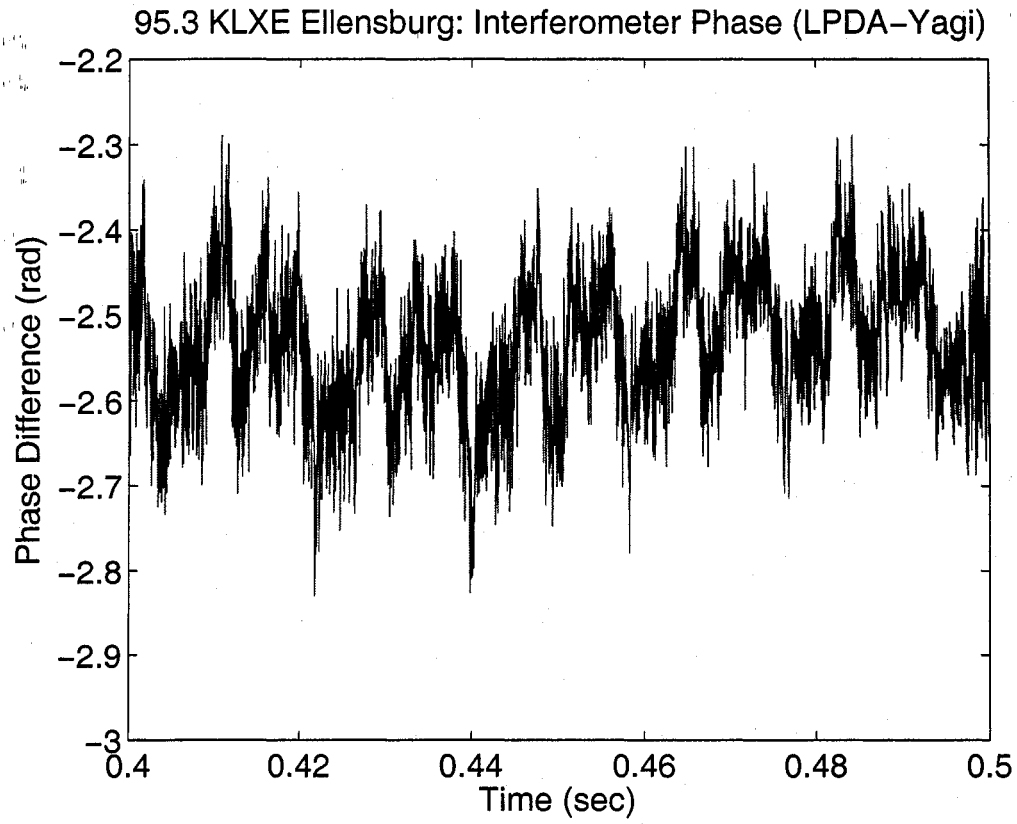

Figure 6.10: Interferometer phase vs. time for 95.3 MHz transmitter in Ellensburg, WA (MRO area). These samples are part of a 150 second-long time series. The low frequency, semi-periodic trend should be investigated.

in the interferometer phase measured for KULE; this large variance may be due to that station's lower power (26 kW as compared to 51 kW for KXLE) or possibly interference. Also, KXLE, at 95.3 MHz, is closer in frequency to the channels we use for the radar (96.5, 97.3 MHz). Finally, it turns out that the KULE transmitter is in a very inconvenient spot with respect to our interferometer baseline for estimating ϕ_0: the true value for the angle of arrival θ is zero or potentially negative (in the interferometer's "southern hemisphere") within the error bars of the handheld GPS baseline measurements. For the KXLE transmitter, we calculate a value of 85.8° for the signal's AOA, θ (see Figure 6.19 for a diagram of the system geometry). Thus, $kd\cos\theta = 7.3$ radians and we have $n = 1$ and $\phi_{\text{true}} = 1.01$ radians. This leads to an estimate of -3.5 radians for ϕ_0. (Calculating the estimate with the KULE data, despite its large variance, results in $\hat{\phi}_0 = -3.2$, which is encouragingly close. We expect the ϕ_0 estimates to be slightly different due to the frequency dependence of ϕ_0.) A summary of relevant values and intermediate calculations for the interferometer calibration is shown in Table 6.1.

Now that we have an estimate for the phase offset due to the instrument itself, we can use equation 6.9 to find the interferometer angle of arrival, θ, for targets at each range and time in our 17 July 2004 dataset. We require the interferometer phase for each target on two different channels (96.5 and 97.3 MHz) to use equation 6.9. We find these phase values by computing the cross spectrum between the two scatter-receiving antennas at MRO [74]: the cross spectrum phase is the desired interferometer phase ϕ_{measured} and the cross spectrum magnitude, or coherence, is the correlation coefficient between the two antenna signals. (The coherence is useful as a measure of how "strong" or compact the target is – a coherence of 0.25 or greater is statistically 95% likely to come from a coherent target [76] – and can also be used for interferometric imaging with two or more antennas [25].) We show examples of

Table 6.1: A table of parameters relevant to calibrating the interferometer phase shift ϕ_0 using transmitters of opportunity.

Parameter	KXLE	KULE
TX Frequency	95.3 MHz	92.3 MHz
ERP	51 kW	26 kW
$\langle\phi_{\text{meas}}\rangle$ (Measured interferometer phase)	-2.5 rad	0.76 rad
VAR[ϕ_{meas}] (Interferometer phase variance)	0.053 rad^2	3.9 rad^2
Latitude, Longitude	47.2° N, 239.2° E	47.3° N, 240.4° E
θ (Interferometer AOA)	85.8°	$\approx 0°$
n (Alias number)	1	15
ϕ_{true} (Interferometer phase due to AOA)	1.0 rad	4.0 rad
$\hat{\phi}_0$ (Estimated calibration phase)	-3.5 rad	-3.2 rad

interferometer cross-spectra in Figures 6.11 – 6.14.

Figures 6.11 and 6.12 show interferometer data for two different ranges (855 and 862.5 km) for the KBSG (97.3 MHz) Seattle transmitter – MRO bistatic link. The top panels are interferometer phase; the middle panels are coherence (with the 95% significance level overlayed); and the bottom panels show power spectral densities for both interferometer antennas individually. In Figures 6.13 and 6.14, we show interferometer data at the same date, time, and two ranges, but for the KJAQ (96.5 MHz) Seattle transmitter – MRO bistatic link.

However, now we have phase and coherence values for an entire spectrum of frequencies (Doppler shifts) for each target. Doppler-broadening of the illuminating signal is one of the challenges that the plasma irregularity target presents to radar experimentalists. We must determine how to estimate a single value for ϕ from each target's cross spectrum. We choose to simply use the cross spectrum value for the

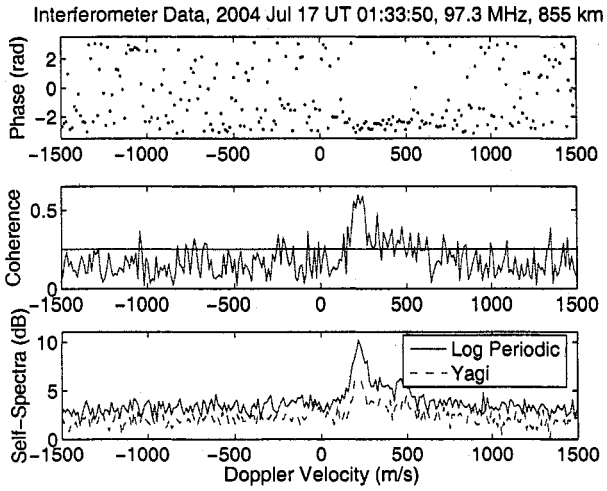

Figure 6.11: Interferometer data vs. Doppler shift for a single time, range, and frequency channel. The 95% significance level for coherence is overlayed in the middle panel.

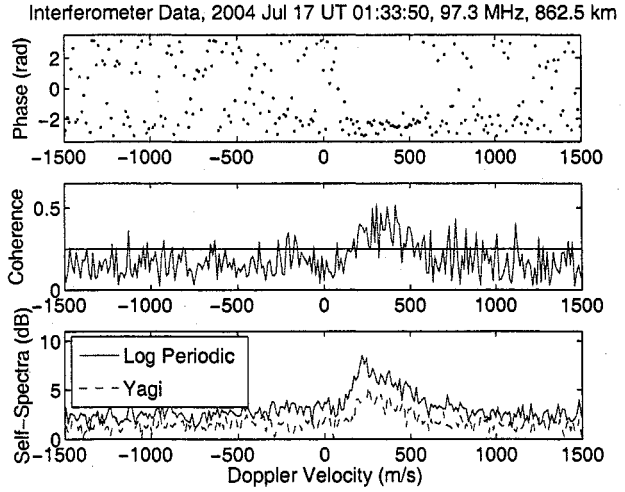

Figure 6.12: Interferometer data vs. Doppler shift for the same time and frequency channel as Figure 6.11; a different range is shown.

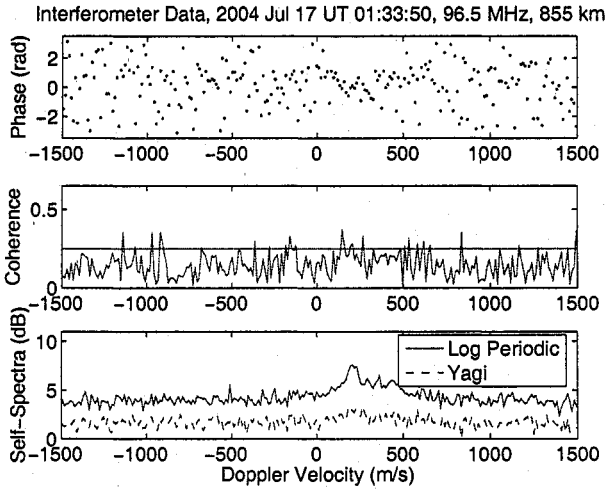

Figure 6.13: Interferometer data vs. Doppler shift for the same time and range as Figure 6.11; a different frequency channel is shown.

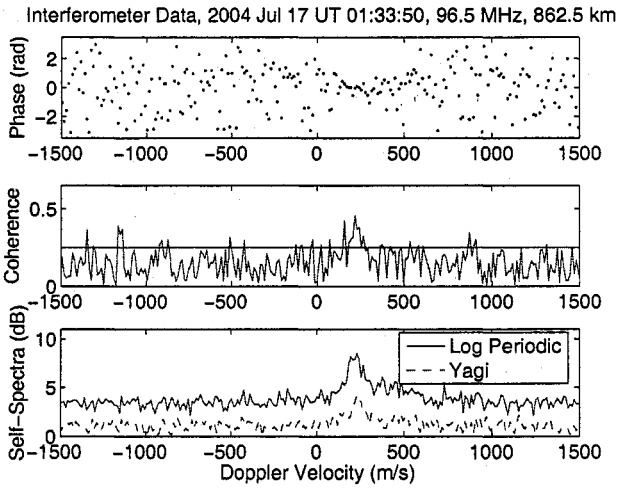

Figure 6.14: Interferometer data vs. Doppler shift for the same time and range as Figure 6.12; a different frequency channel is shown.

Doppler bin where the log periodic antenna power spectral density is maximum (finding the maximum coherence is not always a reliable indicator, as can be seen from Figure 6.13). More complicated estimators can be devised, but these do not always yield satisfying results, and often require estimating other spectral quantities, such as a target's Doppler width [76].

Using the maximum-power Doppler bin approach, we now look at estimated target parameters over several ranges at once. Figures 6.15 and 6.16 show interferometer phase and coherence respectively for both 97.3 and 96.5 MHz. Figure 6.17 shows target mean Doppler shifts and SNRs over ranges 750–1150 km for the 97.3 MHz channel. All of these estimates are for UT 01:33:50 on 17 July 2004 (the same time and date as that shown in Figures 6.11 – 6.14). We can clearly tell which ranges contain strong scattering regions by observing the larger SNRs, the most significant coherences, and the organization – or compactness – of the Doppler velocities and interferometer phases. These all occur mostly between ranges 800 and 900 km (the coherence of the 96.5 MHz signal is lower than 97.3 MHz in general). An interferometer image for the same date and time (Figure 6.18) confirms that the strongest backscattered signal occurs over 800–900 km. (The procedure for creating 2-D interferometer images as in Figure 6.18 is given by Meyer and Sahr, 2004 [74].)

With interferometer phase estimates on two independent channels for targets at each range and time, we are able to estimate θ, the target signal's angle of arrival to the interferometer baseline. To prevent confusion by high-variance noise and low-coherence targets, we exclude all targets with SNR lower than 2 dB or coherence below the 85^{th} percentile on either interferometer channel. This excludes 90% of the 17 July 2004 spectra (a more robust interferometer, including carefully placed and spaced antennas, will surely be the subject of future work). We now need to relate our θ values to geographic bearing; we can use that along with range to determine each

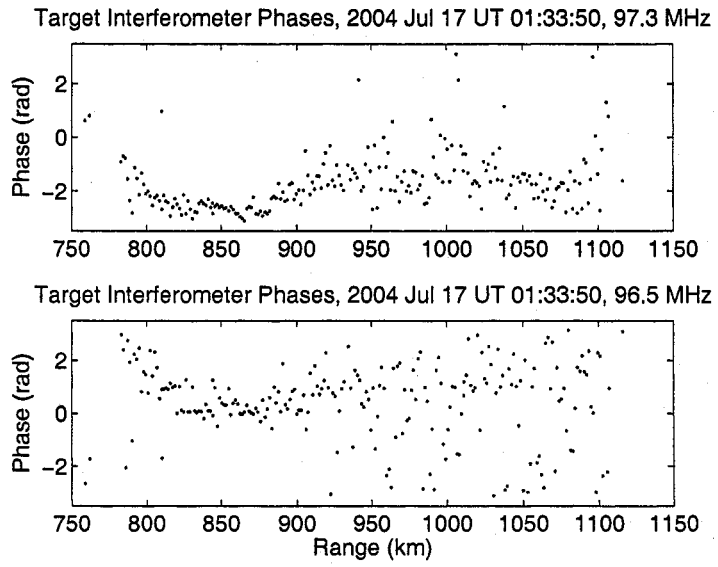

Figure 6.15: Interferometer phase estimates over several ranges for channels 97.3 MHz (top panel) and 96.5 MHz (bottom panel). Same date and time as Figures 6.11–6.14.

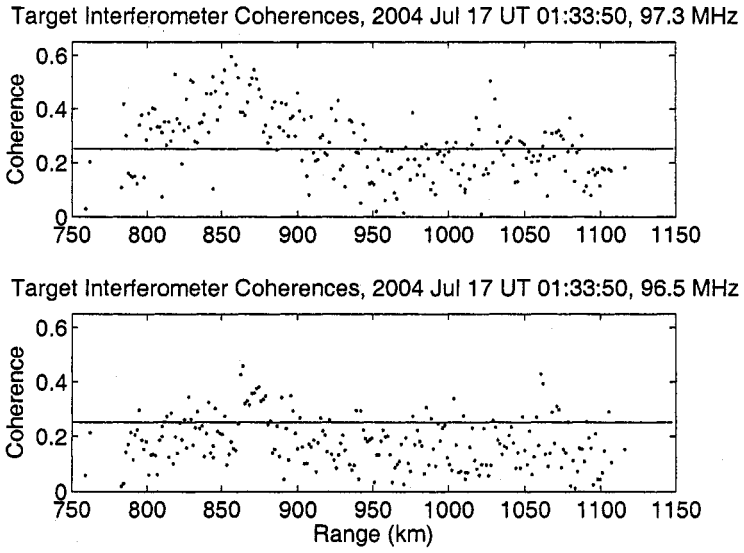

Figure 6.16: Interferometer coherence values over several ranges for channels 97.3 MHz (top) and 96.5 MHz (bottom). Same date and time as Figures 6.11–6.15.

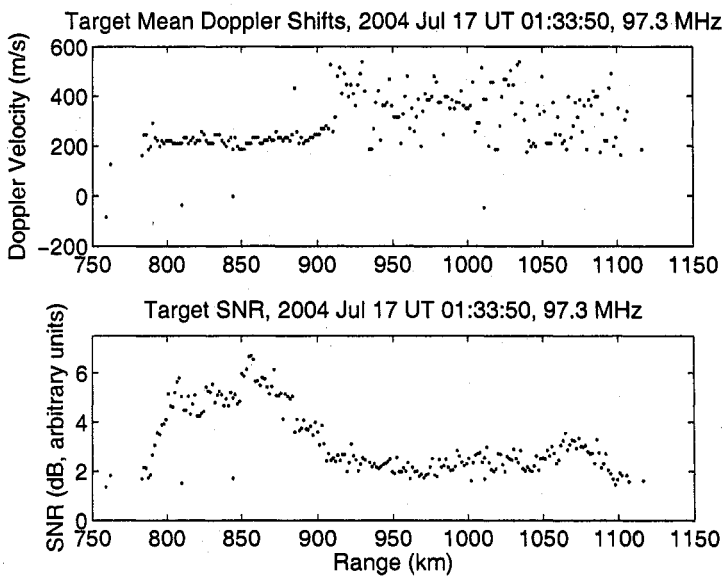

Figure 6.17: Estimated target Doppler velocity and signal-to-noise ratio over several ranges for 97.3 MHz. Same date and time as Figures 6.11–6.16.

target's location in latitude / longitude format, which is our ultimate goal. (Actually, our ultimate goal is to determine target altitude using vertical interferometry as well, but that is beyond the scope of this work.) The geometric relationship of θ to the antenna baseline and the baseline geographic orientation are shown in Figure 6.19. The target bearing is $(68.5 - \theta)°$ east of north.

The final task in de-aliasing the MRR interferometer is to determine an expression for the distance "b" in Figure 6.19. With the value for b we will know a target's distance and bearing from a known location (in this case, the Yagi antenna tower), and thus can solve for the location of the target itself. The known quantities in Figure 6.19 are the distance c (given a certain Seattle-area transmitter) and the angle A (which also depends on θ). These values are given in Table 6.2 for two commonly used Seattle-area transmitters (97.3 and 96.5 MHz). We also know the target bistatic

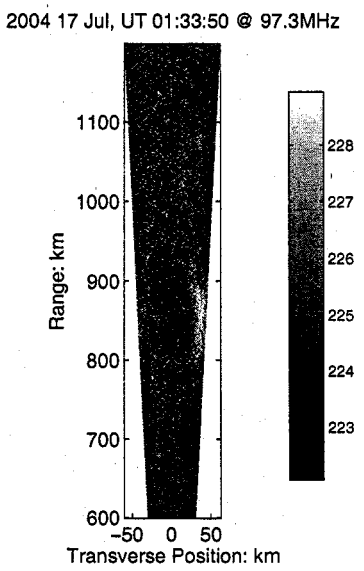

Figure 6.18: Interferometer image for 17 Jul 2004, UT 01:33:50 (same date and time as above figures). The greyscale represents backscattered power, in dB (arbitrary units).

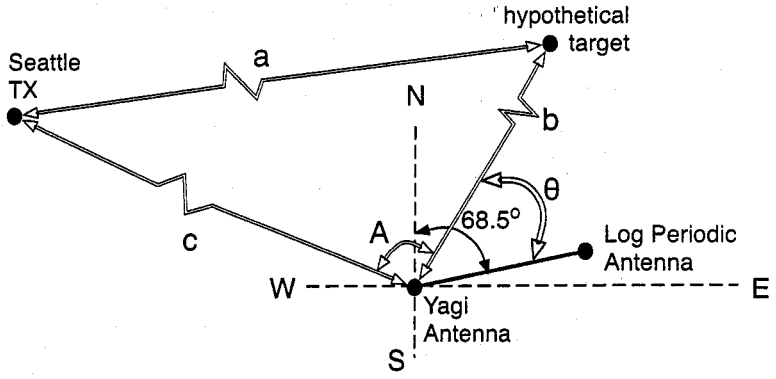

Figure 6.19: A diagram of the interferometer baseline at MRO and its geometric relationship to a target and transmitter. (See the text for an explanation of the symbols used in this figure.)

Table 6.2: A table of useful parameters for using interferometer bearing and bistatic range to locate a target. Refers to Figure 6.19.

Parameter	KBSG	KJAQ
TX Frequency	97.3 MHz	96.5 MHz
Latitude, Longitude	47.5° N, 238.0° E	47.5° N, 237.9° E
Distance to UW RX	30.54 km	20.06 km
Distance to Yagi antenna tower (c)	112.57 km	123.45 km
Target → TX bearing (angle A)	$124.96° - \theta$	$125.73° - \theta$

range r, which equals the sum of the distances a and b. Using the Law of Cosines, we find the desired expression for b in terms of known quantities:

$$b = \frac{c^2 - r^2}{2c\cos A - 2r} \tag{6.12}$$

We note that when determining target bistatic ranges, one should double the monostatic approximation range (currently the default value reported by the MRR software) and then add the distance from the transmitter to the reference receiver (currently neglected by the MRR software). Distances to the UW reference receiver for the 97.3 and 96.5 MHz Seattle transmitters are also given in Table 6.2.

De-aliased Interferometer Data

We used all of the above techniques on the 17 July 2004 three-hour dataset. Unfortunately, the many measurement uncertainties were too much for the admittedly stiff solution for the alias number n. The estimates for n were frequently much larger than the number of wavelengths separating the interferometer antennas (a nonsense result). This led to $\cos^{-1}$ arguments greater than 1, which in turn meant unphysical and nonsensical bearing and location results.

We could hardly ask for a better dataset (in terms of higher SNR and more data diversity) than the one from 17 July 2004, so the conclusion from this dealiasing experiment is that we should erect better antennas (in terms of front-to-back ratio and mount reliability, for example) and place them in useful patterns rather than attempting to use multiple measurements and signal processing to eliminate ambiguities.

In the meantime, we use a "brute force" method in which we try all possible values for n ($-16 \leq n \leq 16$ for our 50.3 meter interferometer baseline and FM band frequencies) and choose the value which results in the location closest to the intersection of the target range contour and the contour for perpendicular magnetic aspect angle at 100 km altitude. We performed this test for several targets in the 17 July 2004 dataset, then used the resulting value for n on the entire 3 hours of data. We show the resulting irregularity mappings using interferometer information in Chapter 7, on page 184.

6.3 Implementation Issues and Future Steps for Multistatic Systems

We now present an overview of the challenges ahead for the development of multistatic, distributed passive radar systems. Some of the problems are technical; many are related to logistics and resource organization.

6.3.1 Data Transfer and Organization

The amount of processing power, network traffic, and data storage required in distributed passive radar systems grows combinatorially if one wishes to observe with each pair of receivers. We find it easy to become overwhelmed with only 8 channels of simultaneous data in well-defined reference-scatter pairs: two frequencies each from the reference receivers in Seattle and Spokane, and two frequencies on each of

two antennas collecting scatter at MRO. We could double the number of channels immediately by adding one more digital receiver at MRO. However, we would be hard-pressed to handle the increase in complexity at this time.

The optimal organization and "data flow" of distributed instrument arrays such as MRR and ISIS require careful, generalized design and sophisticated software infrastructure. System resources such as network bandwidth and computational power will need to be managed and allocated appropriately, and this must all happen automatically for the instrument to be sustainable and scalable. Essentially, we need to design an operating system for the passive radar network. Many scientists in the community, particularly several with the Millstone Hill Radar group, have been thinking seriously about the design of common data protocols and standard, automatable ways to organize and share data resources [Lind, personal communication, 2004]. This is a lead we hope to follow as we make the transition into bigger and more complex systems with multiple receivers and illuminators.

6.3.2 System Autonomy and Robustness

Autonomy and robustness are two more important features we must develop for the passive radar system as it grows larger and becomes more distributed geographically. Ideally, the system should have a "scientific" interface: users should be able to specify experiments to perform, not required to determine detailed radar parameters. This means developing algorithms for automatic transmitter-receiver pair selection and signal processing configuration (based on, for example, a desired field of view, required resolution, expected target scattering cross section, etc). Once the network of receivers grows large enough, even expert users will find selecting from thousands of possible parameters difficult.

Also, larger spatial coverage means less physical access to the radar hardware.

Therefore, we need to develop and streamline remote access and control, both for convenience and – once the system grows too large to feasibly travel to each node regularly – out of necessity.

Eventually, for deploying new receiver nodes, we would like to develop a system which identifies and selects optimal transmitters of opportunity. This system should be aware of different kinds of transmitters at many operating frequencies.

6.3.3 Scientific Use of Data

Once we have sets of data to analyze from N different fields of view, we will need to completely understand the system geometry to take advantage of spatial diversity and make sense of the passive radar network's observations in terms of global physical models. There will be significant instrument deconvolution problems to solve (for example, backscattered power calibration, antenna beam pattern determination, mitigation of co-channel interference and multipath effects). All of these challenges exist in the current MRR system, but they will be exacerbated with many receiver nodes. There will be opportunities to apply data fusion techniques toward combining observations from diverse locations, view geometries, and illuminating transmitters.

Spectral Moment Estimator

Phase velocity measurements on each radar channel are required for most of the experimental techniques described in this chapter. Therefore, as a practical matter, we need a reliable model and automatic spectral-fitter to determine the mean Doppler velocity and/or spectral width for targets at each range and time. Creating a reliable estimator for radar spectral features is a mundane but very necessary task – we can gather potentially hundreds of thousands of spectra with the MRR over the course of a magnetic storm. The selection of a "best" estimator is also somewhat controversial

(primarily because the exact stochastic nature of the fluctuating ionospheric target is unknown); Meyer *et al.* discuss several different spectral moment estimators used in E region irregularity experiments in a 2004 statistical study of MRR observations [75].

Currently we use the Levenburg-Marquardt nonlinear least squares data fitting algorithm [98] to fit spectral models to radar data once they are in Doppler power spectrum form. However, the speed of the fitting algorithm could be improved (most readily by implementing it in a compiled, rather than interpreted, language). Two basic models are fitted to spectra (and ranked in goodness-of-fit): Gaussian and Lorentzian, as well as binary combinations thereof.

$$G(f) = N + A\exp(-\frac{(f-b)^2}{c^2}) \quad \text{(Gaussian)} \tag{6.13}$$

$$L(f) = N + A/(1+\frac{(f-b)^2}{c^2}) \quad \text{(Lorentzian)} \tag{6.14}$$

The fitted parameters are noise power (N), amplitude (A), mean Doppler shift (b), and spectral width (c). A white noise model is also fitted to each spectrum; this serves as an irregularity detector.

The MRR has been operating continuously since January 2002 with few interruptions (this capability is a significant advantage of passive remote sensing). To date, we have compiled over 575,000 independent E-region irregularity observations – and that number only represents a single FM channel. We often record events on multiple frequencies and with multiple antennas. By independent observations, we mean that each irregularity spectrum is separated from others by at least 1.5 km in range and/or 10 seconds in time. We have used detectors and fitters on each of these spectra, estimating irregularity characteristics including SNR, location, and Doppler spectral moments, and recording additional information such as date, time, and background space weather parameters. In 2004 we published the first compilation of passive radar

E region irregularity statistics [75]. This was also the first substantial data set near 100 MHz: our FM-band carrier frequency partially fills the gap between existing VHF auroral radar observations near 50 MHz (Saskatoon [129] and CUPRI [108]), 140 MHz (STARE [89]), and 150 MHz (SABRE [115]). Previous auroral backscatter studies have been done at 93 MHz [130, 127]; however, these do not address Doppler spectral issues. We also compared our statistical distributions with those reported from other HF and VHF coherent radar experiments [75].

Chapter 7

ANALYSIS OF PASSIVE RADAR OBSERVATIONS

After spending Chapters 5 and 6 describing a new model for plasma density irregularities and outlining several new types of experiments that can be performed with multistatic passive radar, we now show some examples using actual data from the Manastash Ridge Radar.

The chapter is organized as follows: in Section 7.1, we discuss whether real data from the MRR supports the new "spatially localized" irregularity model we presented in Chapter 5. In Section 7.2 we show examples of each of the new (for passive FM radar) experimental techniques we described in Chapter 6.

7.1 Evaluation of the Localized Irregularity Model with MRR Data

Here, we describe two experiments using MRR data in which we evaluate the feasibility of the localized wave packet model from Chapter 5. In the first, we vary the resolution of the MRR to determine if there is any change in total backscattered power. In the second experiment, we use frequency-domain interferometry to achieve very fine range resolution, and look for coherence at very small scale sizes.

7.1.1 Irregularity Scale Size versus MRR Resolution

The MRR inherent range resolution is 1.5 km, finer than any other coherent auroral radar experiment. This is the resolution available from FM radio, which is currently the only source of illumination we use. (The average FM waveform correlation time is 10μs, corresponding to a receiver bandwidth of 100 kHz and radar range resolution

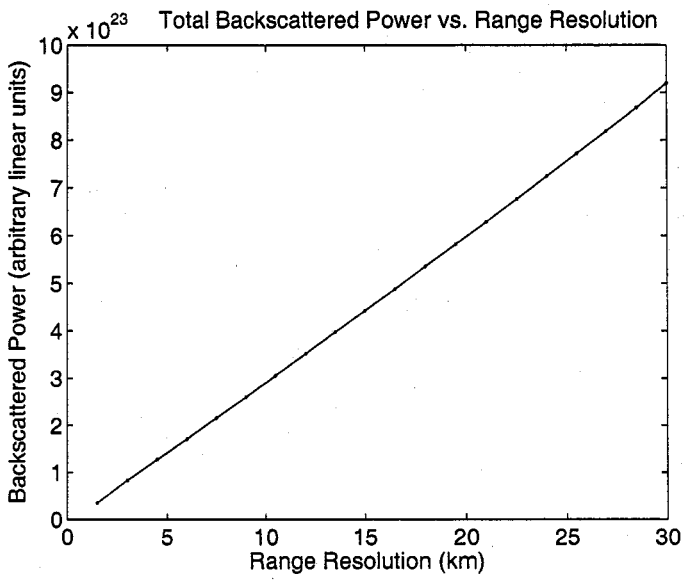

Figure 7.1: Manastash Ridge Radar E region irregularity backscattered power versus range resolution. The power scales linearly with resolution. The number of independent data represented in the power estimate for each resolution is no less than 7,000; for the native MRR resolution of 1.5 km there are over 370,000 independent measurements. (Achieving lower spatial resolution requires summing over independent, higher resolution measurements.)

of 1.5 km [110, 76].) We summed up to 20 independent 1.5 km range cells to achieve resolutions as coarse as 30 km, then plotted irregularity backscattered power as a function of resolution in Figure 7.1.

Bragg scatter amplitude is proportional to the distance traveled through the scattering volume by the transmitter wave (or the irregularity wave packet length L, to allude to our model from Chapter 5). Therefore, Bragg scattered power is proportional to the scattering medium size, squared. If the radar field of view contained a single, coherent plane wave (the "traditional" model), we would expect the backscattered power to scale quadratically with range resolution. In fact, the power scales

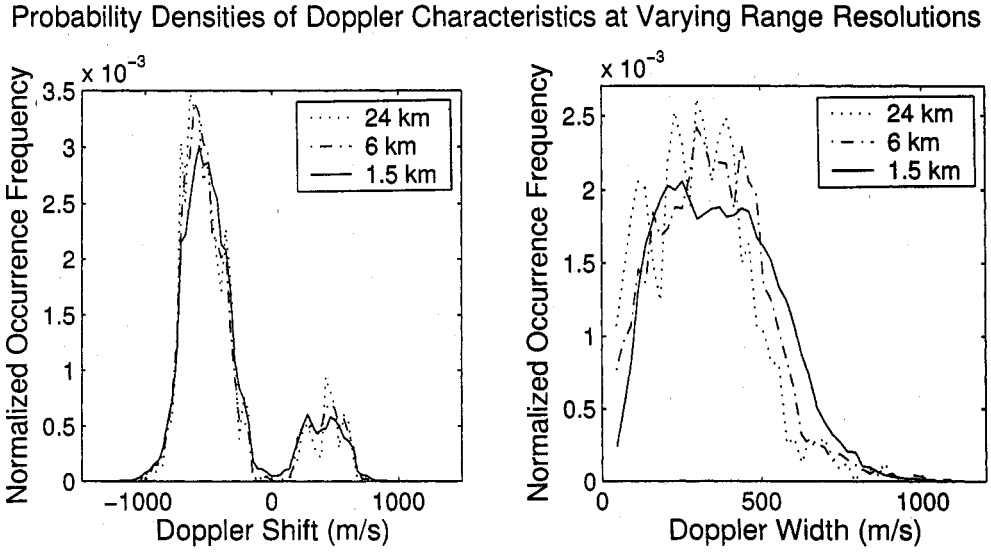

Figure 7.2: Normalized occurrence histograms for mean Doppler shift (left) and spectral width (right) for data from the 20 November 2003 storm (approximately 4000 samples). The spectral features have been estimated at three different range resolutions: 1.5 km, 6 km, and 24 km. In all cases, the histogram bin width is 23 m/s.

linearly as a function of range resolution, as shown by Figure 7.1. This indicates, unsurprisingly, that the entities causing coherent backscatter are not infinite plane waves, but instead are individual scattering region(s) whose size is smaller than a single 1.5 km MRR range cell. This experiment will be interesting to repeat once we bring HDTV passive remote sensing online; the HDTV signals at 600 MHz can potentially provide range resolution as fine as 30 meters, and we may then begin to see evidence of "large" (with respect to instrument resolution) scattering regions.

To show the effect of range-averaging on Doppler moments, in Figure 7.2 we present the Doppler shift and width distributions for a subset of the MRR irregularity data obtained with three different range resolutions: 1.5 km, 6 km, and 24 km. The intrinsic range resolution of the MRR is 1.5 km, and we have chosen the other

two resolutions to roughly mimic that of CUPRI (5–6 km) [108] and SABRE (20 km) [115], two other VHF high latitude coherent radar experiments. This demonstrates the MRR's unique capacity to provide data that may be readily and directly compared to other auroral radars through "resolution-matched comparison." The subset of data we used in this figure was obtained during a 15 hour period on 20 November 2003 (a severe geomagnetic storm occurred on this day, associated with the famous "Halloween Storm" of 2003; Kp values ranged from 7.0 to 9.0 over the period of observation). For the cases with more coarse range resolution, fewer measurements are available; thus, the lower resolution histograms in Figure 7.2 are more jagged in appearance. Nevertheless, the different-resolution data clearly agree, even in subtle trends (particularly in the Doppler shift case). This provides further evidence that whatever features the MRR observes are smaller in size than our finest 1.5 km resolution.

7.1.2 Frequency Domain Interferometry

Frequency domain interferometry (FDI) provides high resolution in the radial dimension by subdividing range gates [65]. It works by exploiting the phase difference between signals at slightly different frequencies: the signal arrival phase for a target detected at frequency ω_1 is equal to the time of flight $2r/c$ times ω_1 (assuming a starting phase of zero radians). If the target is detected with two different carrier frequencies, there will be a phase difference between the two signals arriving at a single antenna:

$$\phi_{\mathrm{FDI}} = 2r\Delta\omega/c \tag{7.1}$$

Then, we can choose two transmitters with a difference in carrier frequency such that a single range gate distance corresponds to a phase difference of 2π. This should enable the resolution of targets whose spatial extent is smaller than the radar range

resolution. Larger differences in carrier frequency correspond to finer subdivisions of each range gate (and multiple frequency-domain interferometer lobes). In the case of MRR, the single FDI-lobe frequency difference is 100 kHz. Since FM stations have a bandwidth of 200 kHz, we must either split the bandwidth of an individual FM station, as Sahr has done for meteor observations [unpublished work, 2005], or accept a finer range resolution (but aliased target position within the range gate).

We attempted to resolve plasma irregularities using the FDI technique with transmitters at 97.3 MHz and 96.5 MHz ($\Delta f = 800$ kHz). In this case, there are 8 multiples of 2π phase within one 1.5 km range gate; thus, targets of size less than $\approx$200 meters can be detected coherently. If the wave packet model introduced in Chapter 5 is accurate, and if the wave packets are very compact (L less than 200 meters), then there could conceivably be some correlation of irregularity scatter at these two frequencies, on the same antenna. However, after testing a substantial number of spectra, we did not find any FDI correlation. This is not surprising, given that we are integrating in time (10 seconds) and space (200 meters), and we expect multiple wave packets to be present in a turbulent scattering volume, reducing the coherency of any received scatter. On the other hand, we would not expect an FDI correlation to appear in the case of a very large plane wave, either; so we have not learned anything about the spatial extent of irregularities from this experiment. However, as we mentioned above, HDTV passive radar provides an exciting prospect for future fine-resolution experiments.

7.2 Three-Receiver Observations

As we have entered solar minimum in recent years (2004–2005), we were lucky to obtain any irregularity data with the new Eastern receiver at all. However, since installing the third MRR receiver in July of 2005, significant geomagnetic events

have occurred on two separate occasions. On 11 September 2005, the MRR observed irregularities on 4 different bistatic links for several hours. We recorded 3 channels in Seattle, but only one channel on the Spokane receiver. Also, at MRO, we only used one receiver channel for the Yagi antenna, and recorded three different frequencies with the log periodic. Therefore, we only have the possibility of using the interferometer on one channel. After assessing the usefulness of the data we recorded on 11 September, we decided to re-allocate some of the receiver channels. When another magnetic substorm occurred on 8 October 2005, we recorded two separate frequencies in both Seattle and Spokane, and used the four MRO receiver channels to record those two frequencies on both interferometer antennas. (Fortunately Seattle and Spokane have two stations that are "good for radar" at the same frequencies. Otherwise it would be difficult to determine the optimal use of the four MRO receiver channels.) With this configuration, we hoped to have measurements from four independent bistatic links (two eastern and two western) and also to be able to perform de-aliased interferometry on both an eastern and western link.

On each of these days (11 September and 8 October 2005), we put the MRR into a "super data-taking mode", recording $2\frac{1}{2}$ minutes out of every 4 minutes on each receiver channel, plus regular 10 second bursts for immediate processing and posting to the web. In July of 2004 (before the third MRR receiver was installed), we also recorded long bursts of data during a severe magnetic storm which lasted for nearly 10 days. This data has proven to be very useful, mainly because it was the first large storm during which we recorded more continuous data (previously we had only been saving 10 seconds out of every 4 minutes), but also because it is an excellent example of the SAPS in the MRR field of view. In Section 7.2.2, we discuss the SAPS observation of 17 July 2004 in detail. We also saved the appropriate channels on this day to attempt to de-alias the interferometer, which we demonstrated in Chapter 6,

Table 7.1: A summary of the long and multi-channel MRR datasets described in Section 7.2. The UW–MRO (western) bistatic links use Seattle transmitters; the EWU–MRO (eastern) links use Spokane-area transmitters. The channels are identified by frequency (in MHz), and the super-scripted "L" and "Y" indicate the antenna(s) used at MRO: either the log periodic (L), Yagi (Y), or both.

Storm Date	UW–MRO Channels	EWU–MRO Channels
17 July 2004	$97.3^{(L,Y)}, 96.5^{(L,Y)}$	None
Possible experiments:	De-aliased interferometry; SAPS Observations	
11 September 2005	$97.3^{L}, 96.5^{L}, 98.9^{(L,Y)}$	$98.9^{(L,Y)}$
Possible experiments:	3-D estimation	
8 October 2005	$97.3^{(L,Y)}, 98.9^{(L,Y)}$	$97.3^{(L,Y)}, 98.9^{(L,Y)}$
Possible experiments:	~~De-aliased interferometry~~; 3-D estimation	

on page 133.

Unfortunately, on 8 October 2005 one of our interferometer antennas was not pointing in the direction we intended (the strong winds atop Manastash Ridge frequently rotate it), and it missed all of the irregularities that the other antenna detected. So, we cannot use the interferometer on this date, and the general SNR quality of the observations is lower as well. Therefore, we will use the 11 September 2005 data to demonstrate multistatic experiments and the 17 July 2004 data to discuss the MRR SAPS observations. Another unfortunate circumstance that we didn't notice until too late is that two of the three Seattle transmitters we regularly use are co-located on a tower. We lost one independent bistatic link out of four possible on both 11 September and 8 October 2005 before we noticed this. Table 7.1 summarizes each of the long datasets we have.

7.2.1 Space Weather Fronts

As we described in Chapter 6, Section 6.2.1, multistatic passive radars can achieve greater and more diverse spatial coverage, thus making them attractive for observing meso-scale phenomena, or as part of a network of instruments observing global-scale phenomena. In this section and the next, we show observations over the entire MRR field of view, sometimes from multiple bistatic links, that allow us to speculate about the details of larger-scale events causing the coherent scatter.

Scattering Volume Mapping

Determining scatterer locations within the radar field of view is an important task for many radar applications. Clearly, target location is of utmost importance in military and many civilian applications, and for tracking. Knowing the exact locations of scattering volumes is also very useful in geophysical studies, if not absolutely necessary for some types of experiments. For example, if we know the latitude, longitude, and altitude of a plasma density irregularity, we can determine its magnetic aspect angle. Coherent scatter position maps are also useful for studying larger-scale phenomena, such as the onset of a magnetic storm, or the propagation and time-evolution of a SAPS electric field.

A straightforward method for determining the location of a scattering region would be to combine range and interferometer azimuth information. However, the MRR interferometer in its current state has severe limitations as an instrument for locating scatterers, and the de-aliasing process (discussed in Section 6.2.3) requires 4 separate, specific channels of data to be both present and "clean" (not suffering from interference, bad ambiguity, etc). This is rather a tall order and we cannot assume that it will be possible to unambiguously determine the azimuth of most scatterers. In fact, the 17 July 2004 dataset we use to demonstrate the de-aliasing technique (on page

133, with results below in Section 7.2.2) is the only one (with plasma irregularities) we have so far for which this is even possible to try. Therefore, we propose to make inferences about location by assuming an altitude (100 km) and aspect angle (0°, perfectly perpendicular) for each target, and then finding the intersection of the target range contour and the 0° aspect angle contour at 100 km altitude.

This generally gives us two choices – a western and an eastern intersection of the range and aspect contours (see, for example, Figure 6.2) – and our default choice is the eastern solution, for two reasons. First, the Yagi antenna, with a narrower gain pattern ($\approx 45°$), points approximately 20° east of north[1]. Second, the eastern scatterer locations are closer to the magnetic pole. This criterion is valid for auroral precipitation-related irregularities, but not necessarily meaningful for other irregularity-generating phenomena, such as the sub-auroral polarization stream (SAPS).

In Figures 7.3 – 7.5, we show field of view irregularity mappings using this "0° aspect" technique for 15 consecutive 10-second time periods (UT 09:24:00 – 09:26:20) on 11 September 2005. (These are the same 15 data periods we use to estimate 3-D electron velocity vectors in Section 7.2.3.) Irregularities detected on three different bistatic links are overlayed on each map: 97.3 KBSG–MRO and 96.5 KJAQ–MRO (western links) and 98.9 KKZX–MRO (an eastern link). The KBSG data are represented by squares, KJAQ by diamonds, and KKZX by circles. Irregularities with positive (toward the radar) Doppler shifts are black, while negative (away from the radar) Doppler shifts are white. The aspect and range contours for the two western links are very close together. It is difficult to tell their irregularities (squares and diamonds) apart on these maps, but it turns out that their detections and mappings are extremely similar.

We can bound the scale size of ionospheric electric field features by noting that

[1]We have found this antenna bearing to be quite unreliable due to inadvertent rotation of the Yagi antenna on its mount on Manastash Ridge.

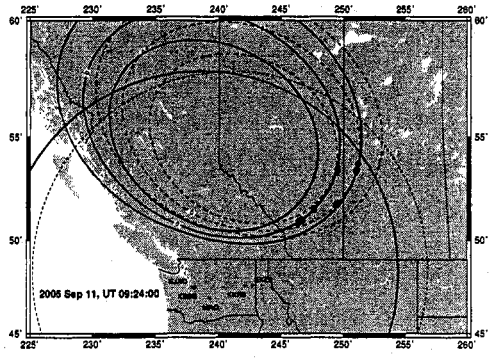

(09:24:00)

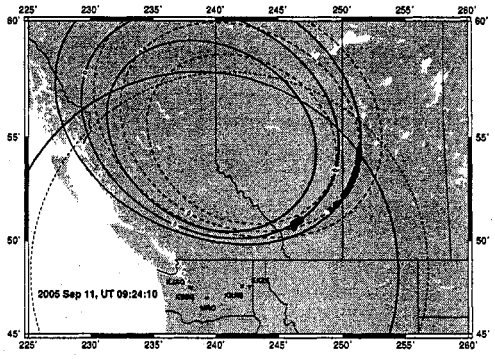

(09:24:10)

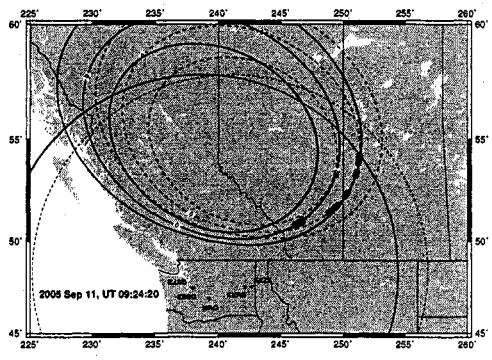

(09:24:20)

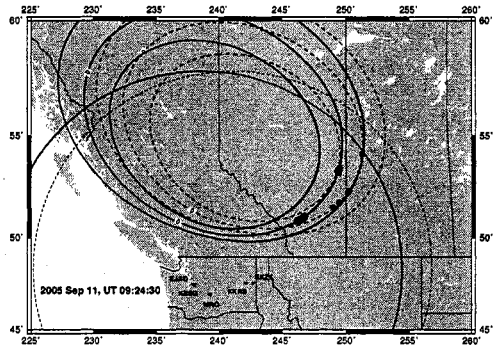

(09:24:30)

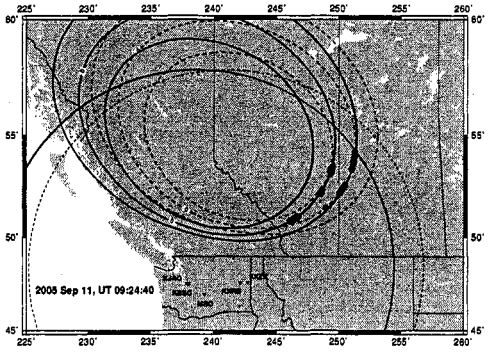

(09:24:40)

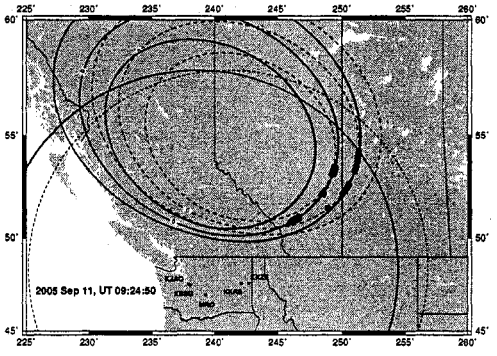

(09:24:50)

Figure 7.3: 0° aspect irregularity mappings; 2005 Sept 11, UT 09:24:00–09:24:50

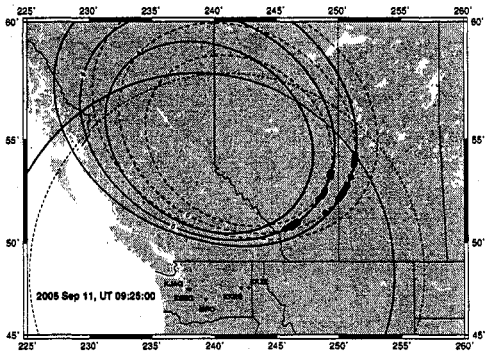

(09:25:00)

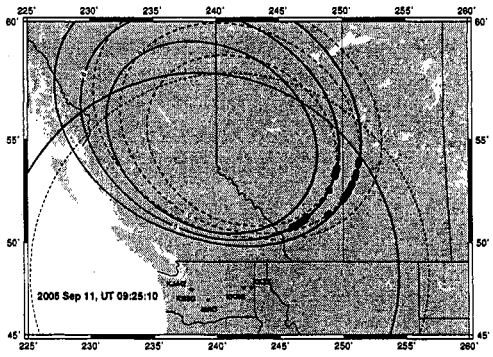

(09:25:10)

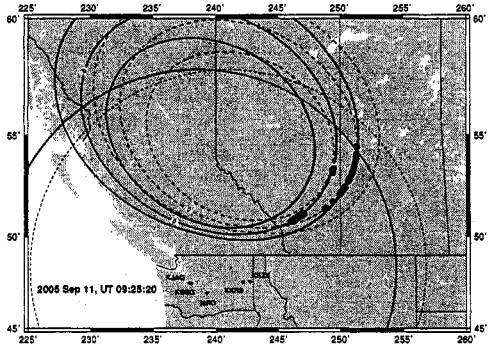

(09:25:20)

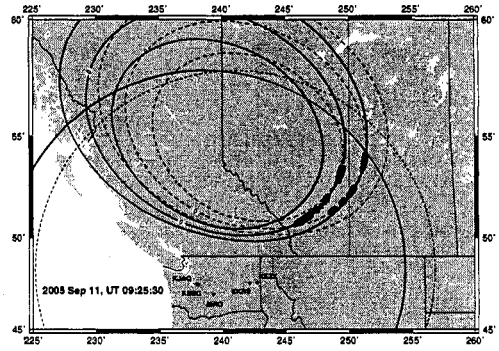

(09:25:30)

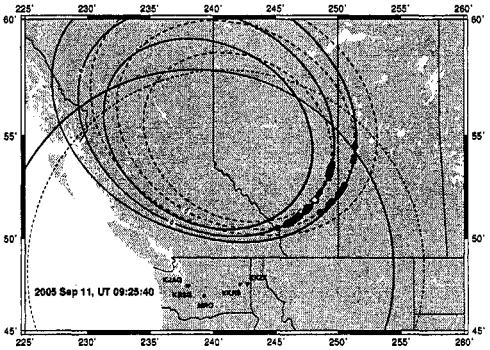

(09:25:40)

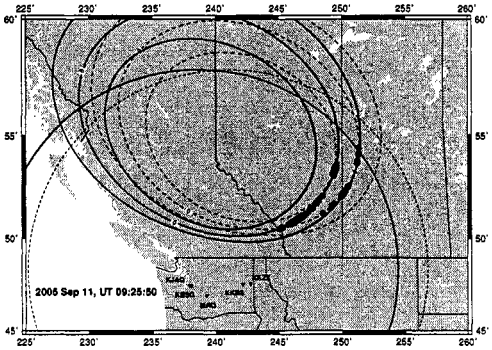

(09:25:50)

Figure 7.4: 0° aspect irregularity mappings; 2005 Sept 11, UT 09:25:00–09:25:50

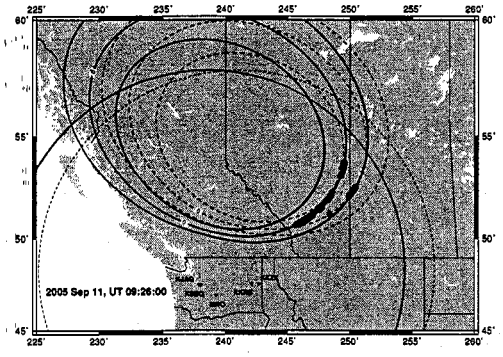

(09:26:00)

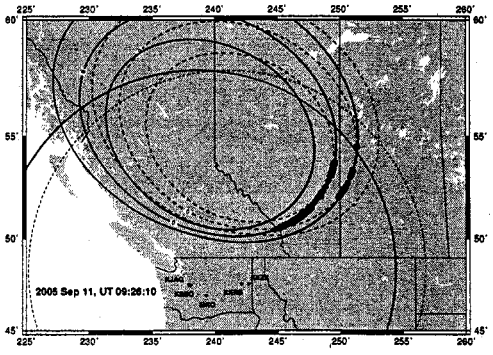

(09:26:10)

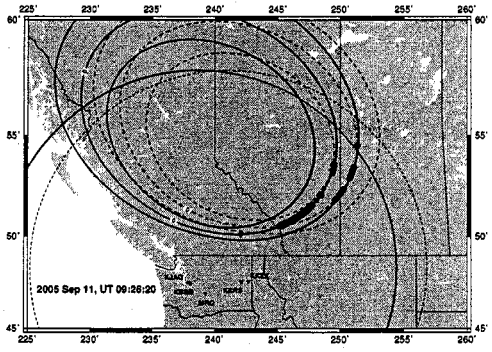

(09:26:20)

Figure 7.5: 0° aspect irregularity mappings; 2005 Sept 11, UT 09:26:00–09:26:20

the two western links have 0° aspect angle contours approximately 10 km apart (for relevant ranges and eastern irregularity mappings) and usually exhibit similar irregularity structures. This indicates probable correlation of the causative electric fields for distances of 10 km and smaller.

On the other hand, the eastern and western bistatic view volumes, while still relatively close (their 0° aspect angle contours are roughly 60 km apart for relevant ranges), nevertheless often exhibit vastly different irregularity structure over range (*cf.* Figure 7.5 at UT 09:26:00). There can also be steep phase velocity shears (as in Figure 7.12, shown along with corresponding range-Doppler diagrams below). This tells us that better passive radar receiver coverage is justified, so that we can resolve fine (less than 60 km wide) electric field structures.

We can also make inferences about the shape and orientation of the unstable volume (or electric field structure) by observing the "band thickness" (number of ranges with irregularities) in combination with the relative location of the "active bands" on different radar links. For example, Figure 7.6 shows four hypothetical electric field structures, with different thicknesses and geographic orientations, along with their corresponding probable zero-aspect irregularity mappings on both an eastern (EWU–MRO) and western (UW–MRO) bistatic link. In the 11 September 2005 data, at UT 09:24:40 and 09:24:50 (Figure 7.3), we see an east-west striping effect which indicates narrow electric field structures stratified in the north-south direction. Of course, in many cases the electric field structures are not so easily determined; multiple passive radar links and view geometries will help us specify ionospheric structures more accurately.

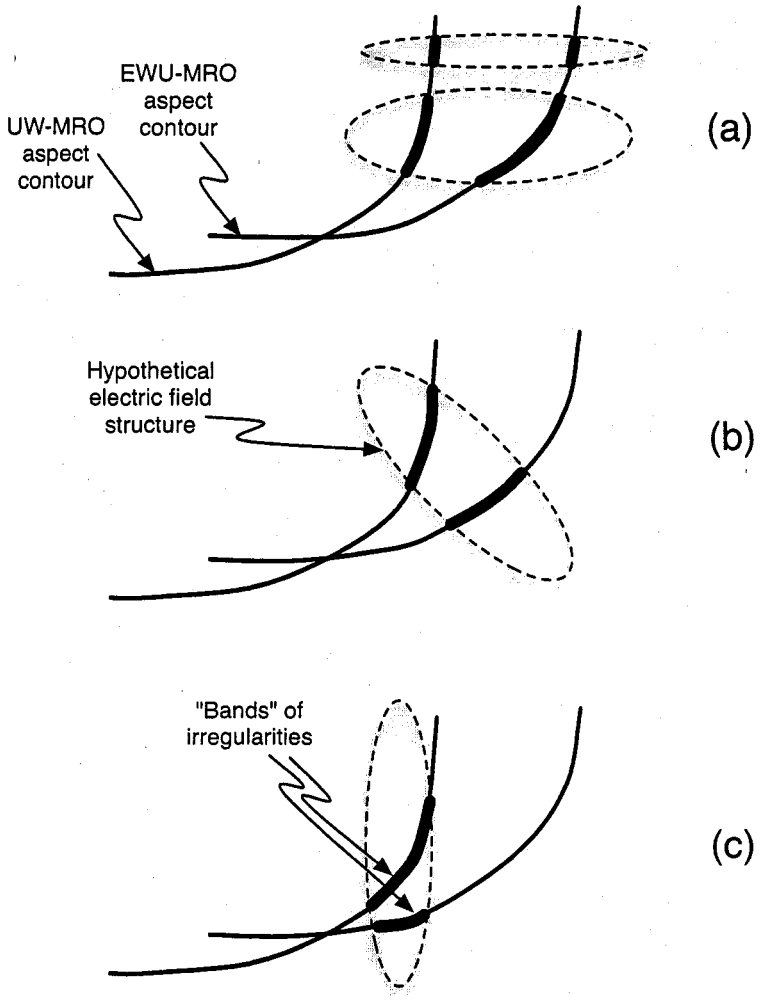

Figure 7.6: Hypothetical ionospheric electric field structures and expected resulting irregularities on an eastern (EWU–MRO) and western (UW–MRO) bistatic link. Four different electric field structures are shown: horizontal orientation (east-west), with two different thicknesses (a), oblique orientation (b), and vertical (north-south) orientation (c).

Timing Differences

In addition to electric field structures in space, there may also be structures in time that we can detect with multiple passive radar bistatic links. For example, if a space weather front is moving through the MRR field of view, it may be detected first on one link and then later on another by some measurable and/or predictable amount of time.

With the compiled irregularity statistics discussed at the end of Chapter 6, we can make two-dimensional histograms such as those shown in Figures 7.7 and 7.8. These allow us to monitor general trends in irregularity occurrence versus various parameters, such as time, phase velocity (mean Doppler shift), and range. To detect possible correlations in irregularity occurrence delayed in time between eastern and western MRR bistatic links, we created Figure 7.7, which shows the number of irregularity occurrences (indicated with the greyscale) versus local time and mean Doppler shift. The data represented cover a $4\frac{1}{2}$ hour period (UT 08:00 – 12:30) on 11 September 2005.

In this particular example, we do not detect any features clearly "following each other" from the eastern view volume to the western view volume (or vice versa). A large number of irregularities are detected on the eastern bistatic link just before time (a) (marked with a vertical dotted line in Figure 7.7), while the same number of detections seem to be more spread out in time on the western link. At time (b), both the eastern and western links detect groups of irregularities, but the eastern link observes positive Doppler velocities while the western link observes negative Doppler velocities. At time (c), it is possible that a phenomenon causing irregularities is just moving from the western view volume to the eastern view volume, since groups of irregularities occur just before (c) on the western link and just after (c) on the eastern link. We cannot accurately determine yet whether any of these groups of irregularities

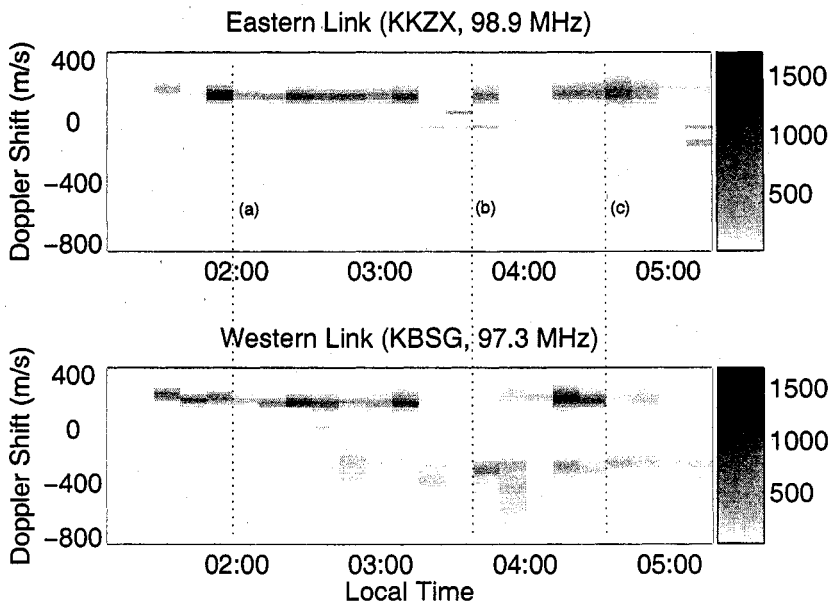

Figure 7.7: 2-D histograms of irregularity occurrences on 11 September 2005, versus Doppler shift and local time, for an eastern and western bistatic link. The greyscale indicates number of occurrences. The (a), (b), and (c) labels mark specific times discussed in the text.

are associated with one another, or the same external electric field, however.

Figure 7.8 also shows two-dimensional histograms for the eastern and western links (over the same $4\frac{1}{2}$ hour time period), this time with irregularity Doppler shift versus range. We see that the irregularities observed by the western link are more structured over range than those detected with the eastern link, which appear in a roughly contiguous band of ranges. Also, it is clear from both figures that the western link sees far more negative Doppler shifts than does the eastern link (at least between UT 08:00 and 12:30 on 11 September 2005).

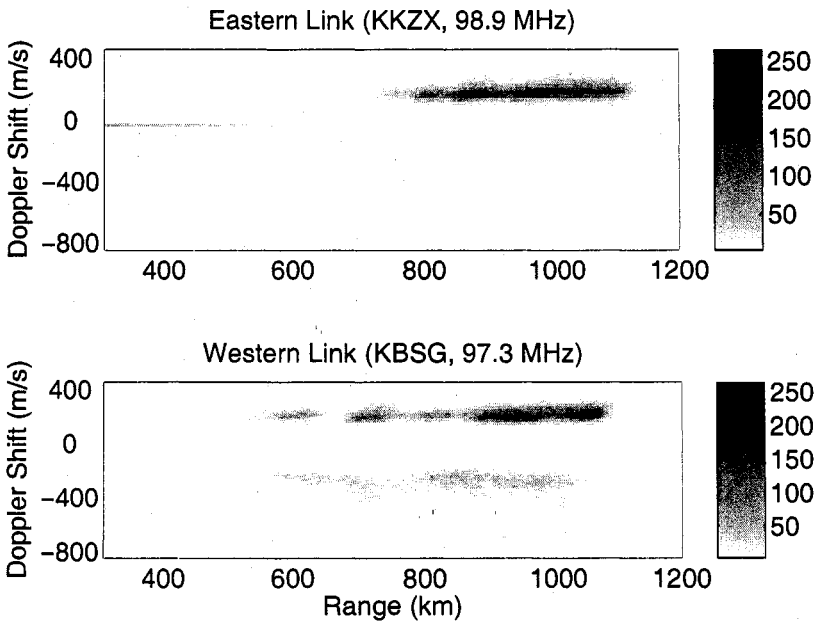

Figure 7.8: 2-D histograms of irregularity occurrences on 11 September 2005, versus Doppler shift and range, for an eastern and western bistatic link. The greyscale indicates number of occurrences.

Doppler Feature Variation Between Bistatic Links

In some of the data from 11 September 2005 (for example, see the range-Doppler spectra in Figures 7.9 and 7.11), there is a marked Doppler polarity (positive/negative velocity) difference between the bistatic links. Often, one link will see bi-modal spectra (peaks at both positive and negative Doppler shifts) while the other link observes only a single direction of convection. The Doppler shifts also depend on range in a complex manner: in Figure 7.9, the western links see a single patch of range with negative Doppler shifts while the rest are positive. This may be due to a large-scale, oscillating electric field in space whose polarity changes from positive to negative over several MRR ranges. The differences between the western and eastern link irregularity features indicate an upper bound on the size of the electric field, as we discussed above. We also see clear boundaries between wide Doppler spectra and very narrow spectra in range and Doppler polarity as well as between the western and eastern bistatic links.

In Figures 7.10 and 7.12, we present the 0° aspect mappings corresponding to the range-Doppler spectra shown in Figures 7.9 and 7.11. Irregularities from all three bistatic links are presented on each mapping. Doppler shift is indicated as before with black (positive) and white (negative). However, Doppler spectral width is not encoded on the irregularity location mappings. The intriguing differences in range structure, Doppler polarity, and Doppler width between the eastern and western links may suggest a larger-scale trend, or provide clues about the anisotropy of the scattering medium, but so far the causes for Doppler discrepancy are not clearly visible. An interesting and challenging task for future work will be to synthesize all of this information and use it to devise a self consistent, meso-scale model (based on either SAPS, the auroral electrojet, or magnetospheric convection) for electric fields and drifting plasma that can explain these complex range, phase velocity, and spectral

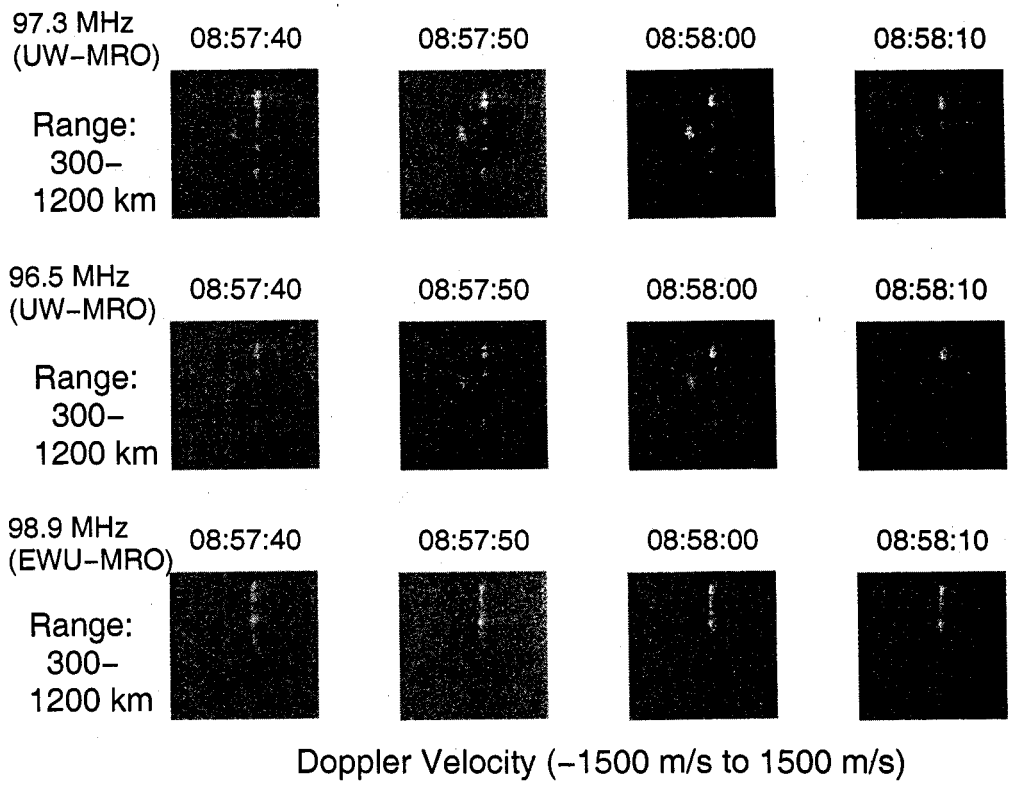

Figure 7.9: Range-Doppler diagrams for four 10-second periods (UT 08:57:40–08:58:10) on three different bistatic links: 97.3 and 96.5 (western) and 98.9 (eastern). Each plot shows Doppler velocities from -1500 m/s to 1500 m/s (horizontal axis) and ranges from 300 to 1200 km (vertical axis). The greyscale is backscattered power, ranging over 4 dB.

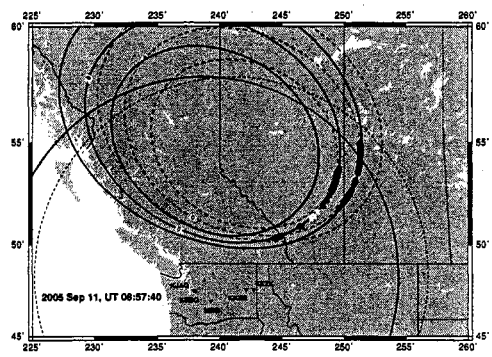

(08:57:40)

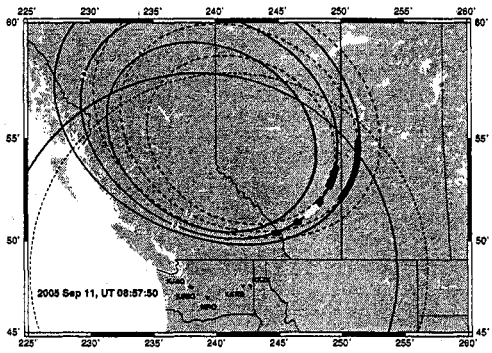

(08:57:50)

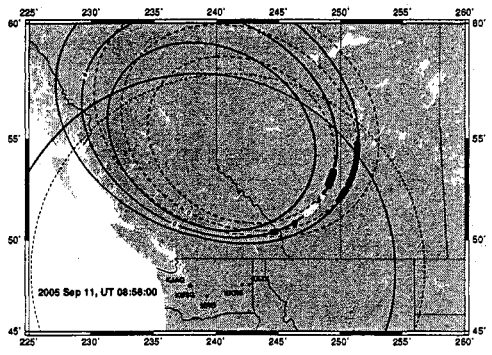

(08:58:00)

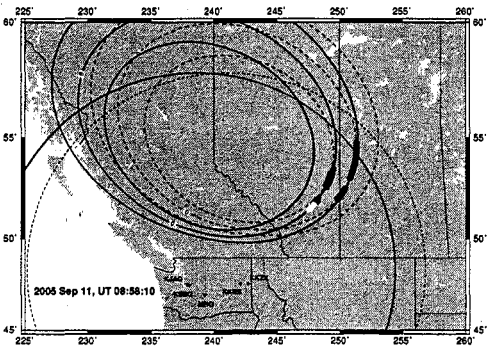

(08:58:10)

Figure 7.10: 0° aspect irregularity mappings; 2005 Sept 11, UT 08:57:40–08:58:10. These 4 figures correspond to the range-Doppler diagrams in Figure 7.9.

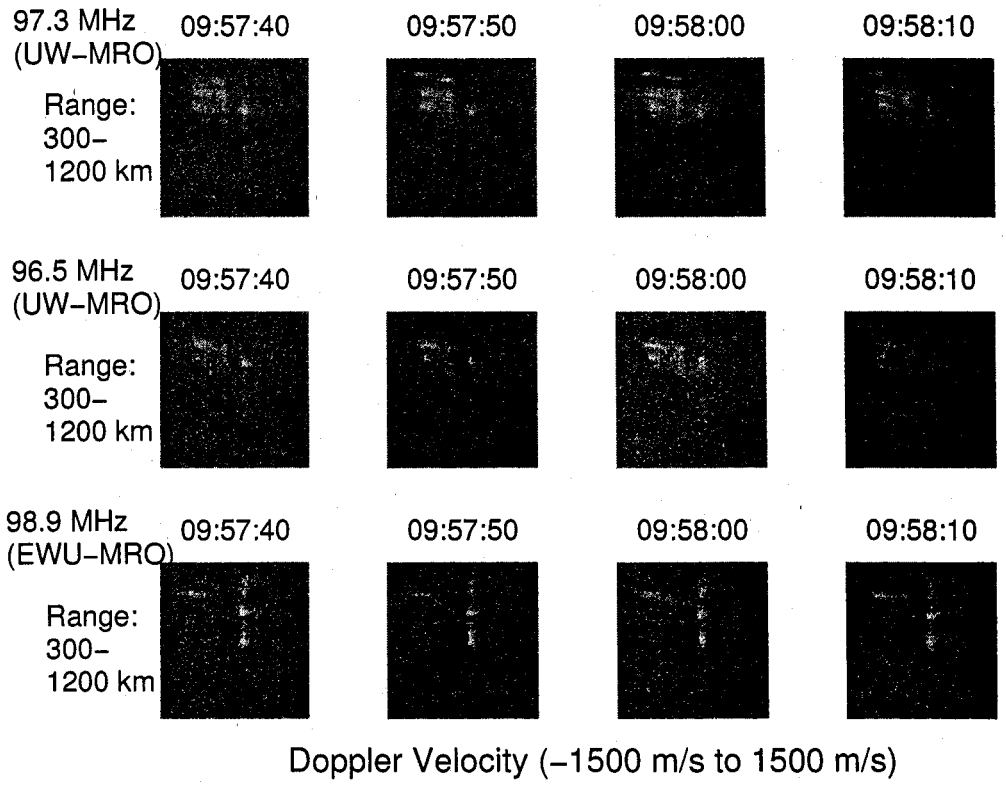

Figure 7.11: More range-Doppler diagrams, an hour later (UT 09:57:40–09:58:10) on three different bistatic links: 97.3 and 96.5 (western) and 98.9 (eastern).

width differences between slightly different fields of view.

Uncertainties in Scattering Volume Mappings

Finally, we discuss sources of uncertainty in the 0° aspect irregularity mappings. One factor that can possibly affect the apparent location of a scatterer is refraction of the radar wave. This is a particularly important effect for HF radars. We do not expect ionospheric refraction to be a significant effect for MRR signals at 100 MHz; however,

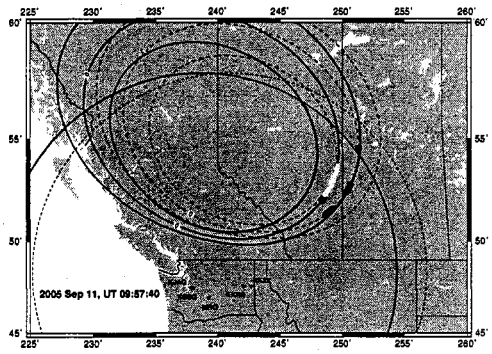

(09:57:40)

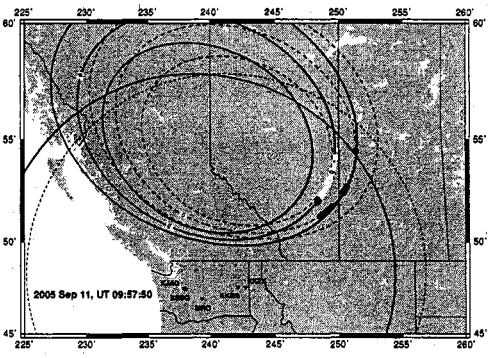

(09:57:50)

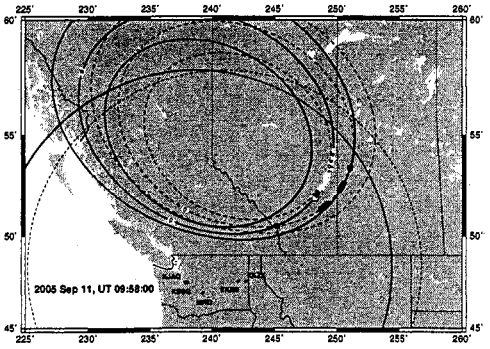

(09:58:00)

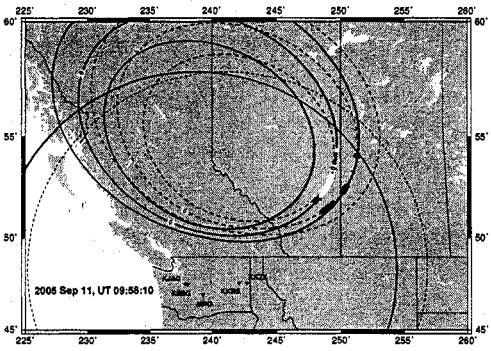

(09:58:10)

Figure 7.12: 0° aspect irregularity mappings; 2005 Sept 11, UT 09:57:40–09:58:10. These 4 figures correspond to the range-Doppler diagrams in Figure 7.11.

the effect should be measured and it would be a worthwhile simulation to carry out in future work.

Most importantly, though, the aspect contours used to map the 11 September 2005 irregularity data were computed for a specific altitude of 100 km. We can limit the altitudes of interest to the E region (90-180 km), but the aspect contour positions do vary significantly over these altitudes, as shown in Figure 7.13. Mitigating this source of error in our irregularity position estimates will require information about the altitudes of scattering regions; this can be achieved with vertical interferometry [111], for example.

However, we can also turn this uncertainty into an opportunity for estimating scattering volume characteristics. Using horizontal interferometer measurements of the transverse (cross-beam, roughly East-West) extent of a scattering region, we can estimate the altitude thickness of the scattering layer, or alternatively, the magnetic aspect angle sensitivity. This is because scattering volume transverse extent must be due either to aspect angle variation at a fixed altitude, altitude variation at a fixed aspect angle, or a mixture of these effects. We can make these claims because of the extremely high magnetic aspect sensitivity of coherent scatter.

For example, MRR interferometer data (such as that shown in Figure 7.14, for example) typically show scattering volume widths of 20–30 km down to as narrow as 5 km in the transverse beam dimension. Magnetic aspect angles (in the MRR field of view) vary by roughly 0.5° per 10 km altitude. On the other hand, a 10 km altitude variation while maintaining a perfectly perpendicular aspect angle (0°) is roughly equivalent to 60 km displacement in the East-West direction. Therefore, a 30 kilometer east-west span corresponds to an altitude range of 5 km assuming an aspect angle of 0°, or an aspect angle span of zero to 0.25° at a fixed altitude of 100 km. (Aspect angles of 2° or more are considered "large" [82].) A scattering

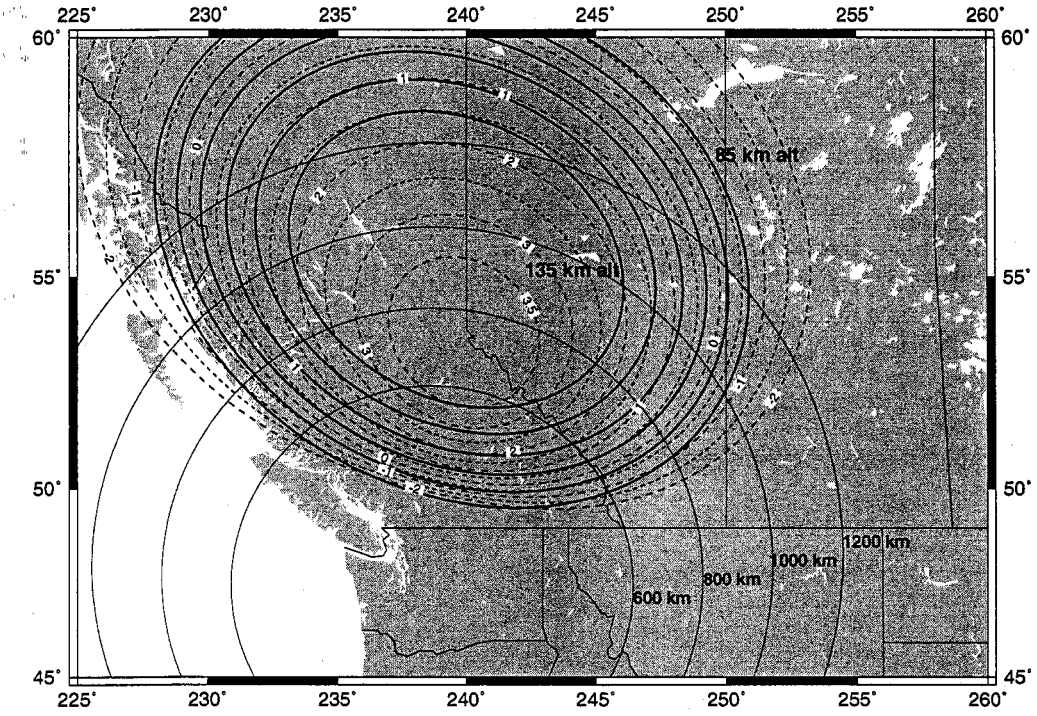

Figure 7.13: Aspect angle variation with altitude and latitude. The heavy black contours are 0° aspect angle contours for 6 different altitudes: 85 – 135 km in steps of 10 km. The dashed contours are aspect angle contours for values between 3.5° and −2°, all computed for an altitude of 100 km. Bistatic radar range contours for 600 – 1200 km are also overlaid.

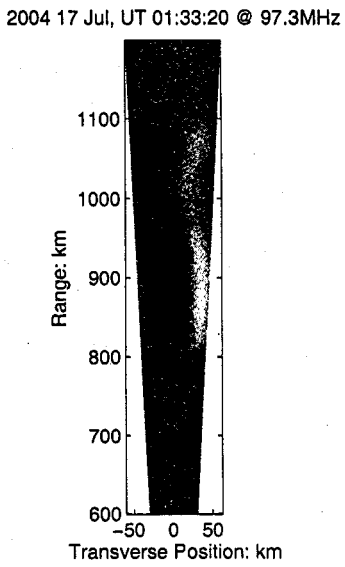

Figure 7.14: Interferometer 2-D image for 17 Jul 2004, UT 01:33:20.

volume which covers 5 km in transverse width corresponds to an altitude range of 800 meters (with perpendicular aspect angle) or 0.04° in aspect variation at 100 km altitude. This is a very rough analysis. Aspect angle variation with altitude actually depends on radar range and geographic location; the values we give above are appropriate for the MRR field of view at ranges close to 1000 km. Changes in longitudinal position due to altitude variation also depend weakly on altitude; we assume all altitudes are near 100 km. We also assumed that the transverse width measured by our interferometer data is purely in the east-west direction. In reality, we expect that scattering volumes vary over both altitude and aspect angle; however, these calculations give us an understanding of how much variation we can expect in our data.

7.2.2 Meso-Scale Observation Example: SAPS

As we mentioned in the discussion of space weather "fronts" in Section 6.2.1, the MRR is in a very useful position to contribute to the study of the SAPS, or sub-auroral polarization stream. The SAPS is a large-scale electric field which can cause plasma density irregularities to erupt in its path, acting as tracers for coherent scatter radars observing area. Here, we present detailed data for a SAPS event which occurred over three hours on 17 July 2004. This particular event occurred before the eastern (Spokane) MRR receiver was installed; however, studies of SAPS could greatly benefit from simultaneous observation by multiple bistatic links.

Over the 3-hour period on 17 July 2004, we recorded 2.5 minutes plus 10 seconds of 100 kHz data every 4 minutes, on 4 channels: two different frequencies (both Seattle area transmitters) on both interferometer antennas. Therefore, we are able to perform interferometry on two channels. A summary of the complete dataset, in the form of a range-time intensity (RTI) diagram, is shown in Figure 6.3 (page 117). This figure shows the entire SAPS channel drifting equatorward through the MRR field of view, with semi-periodic electric field structures propagating (faster) through the channel itself.

In Figures 7.15 and 7.16, we show individual interferometer images (on the 97.3 KBSG channel) with 10 second time resolution. These images are two-dimensional views of the scattering volume, roughly parallel to the Earth's surface. They cover the radar ranges 600–1200 km (vertical axis). We note that the time-consecutive plots also show the equatorward motion seen in the RTI. As individual scattering regions move equatorward, they also move toward the center of the interferometer beam. This indicates that the MRR detects scatter very close to perpendicular aspect angle even as the scattering regions themselves propagate (the perpendicular aspect contour curves inward as range decreases).

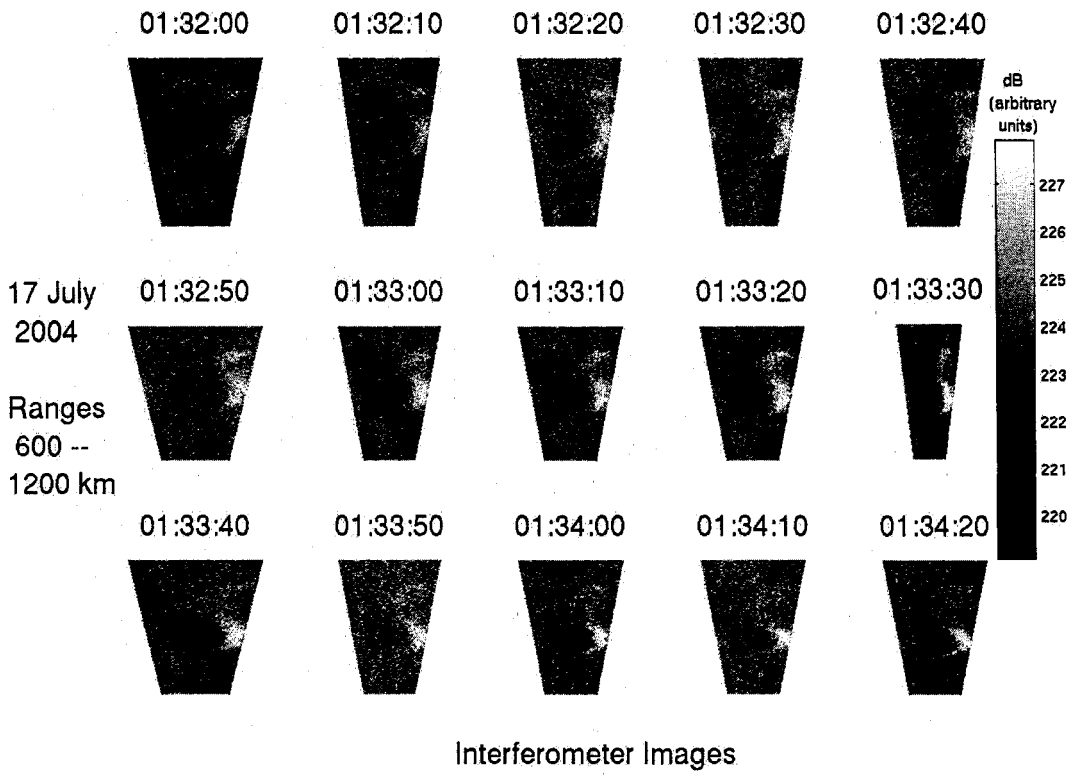

Figure 7.15: Consecutive interferometer images for 17 July 2004, UT 01:32:00–01:34:20, ranges 600–1200 km. The 97.3 MHz FM channel is used. Each image is approximately 50 km wide at the bottom; 100 km wide at the top.

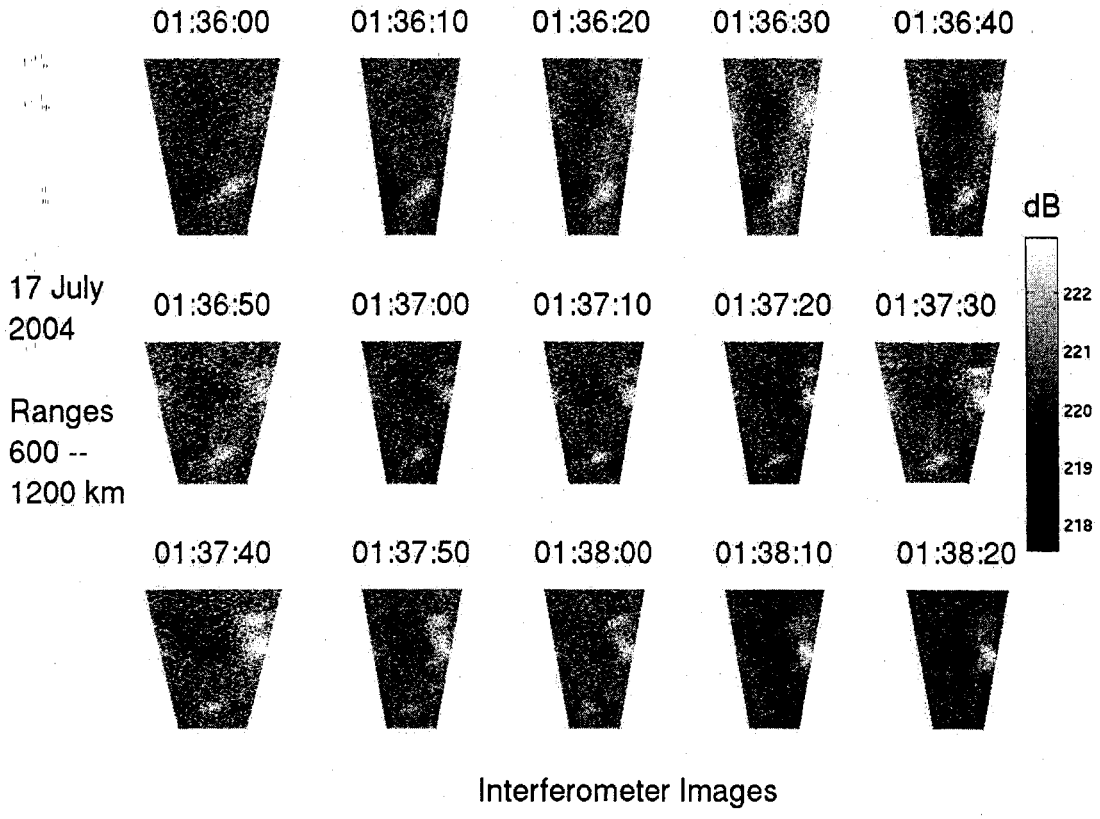

Figure 7.16: Continuing from Figure 7.15: consecutive interferometer images for 17 July 2004, UT 01:36:00–01:38:20, ranges 600–1200 km. The 97.3 MHz FM channel is used. Each image is approximately 50 km wide at the bottom; 100 km wide at the top.

In Figures 7.17 and 7.18, we show range-Doppler diagrams for the same 10 second time periods presented in the interferometer images. The vertical axis of each plot is radar range (600-1200 km), and the horizontal axis shows Doppler velocity from -1500 m/s (left) to +1500 m/s (right). These plots, too, show the irregularity features periodically moving equatorward. All the spectra have positive (toward radar) Doppler shifts. In some of the range-Doppler plots, very fine (10 km scale), semi-periodic structures in range can be seen; we speculate that this SAPS channel is modulated by wavelike disturbances of many different scale sizes.

Evidence of a SAPS Channel

We are fairly confident that a SAPS electric field, rather than another phenomenon, caused these irregularities. Using energetic electron precipitation measurements made by the Defense Meteorological Satellite Program (DMSP) satellites [F. Rich and J. Foster, personal communication, 2005] during their 17 July overflights of the MRR field of view, we can show that the equatorward boundary of the auroral oval was north of the MRR irregularity scatter on this date.

Figure 7.19 shows the DMSP F13 satellite flight path over the MRR field of view for two consecutive passes at approximately 00:30 UT and 02:10 UT. MRR irregularity observations which occurred during the overflights are overlayed on the map (inverted triangles). These mappings were made by assuming a western interferometer alias number (see the section discussing interferometer-informed irregularity mappings below). The auroral oval boundary, inferred from the equatorward boundaries of energetic electron precipitation measured by DMSP satellite F13 (and marked on Figure 7.19 with "+"), is significantly poleward of the irregularities detected by the MRR. From this we infer that the irregularities are due to a SAPS electric field.

Inspecting the plasma density and velocity measured by DMSP F13, we find

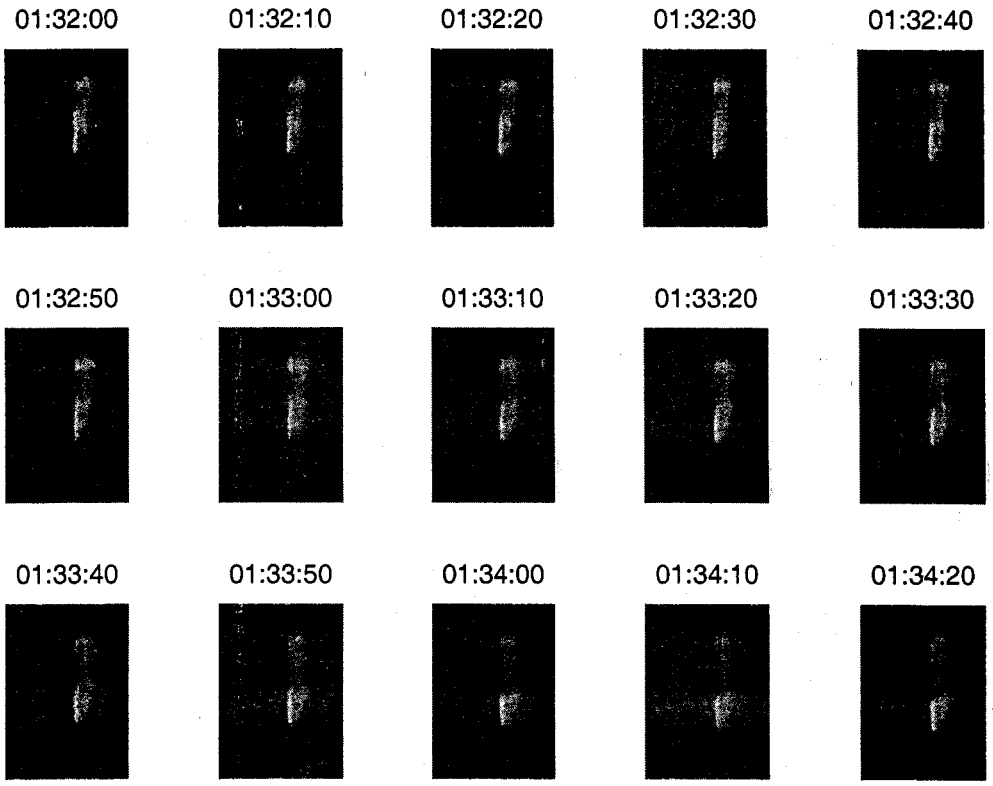

Figure 7.17: Consecutive range-Doppler diagrams for 17 July 2004, UT 01:32:00–01:34:20. The 97.3 MHz FM channel and log periodic antenna are used. The horizontal axis shows Doppler velocity from -1500 – +1500 m/s; the vertical axis shows ranges from 600–1200 km. The greyscale is backscattered power which ranges over 8 dB (arbitrary power units).

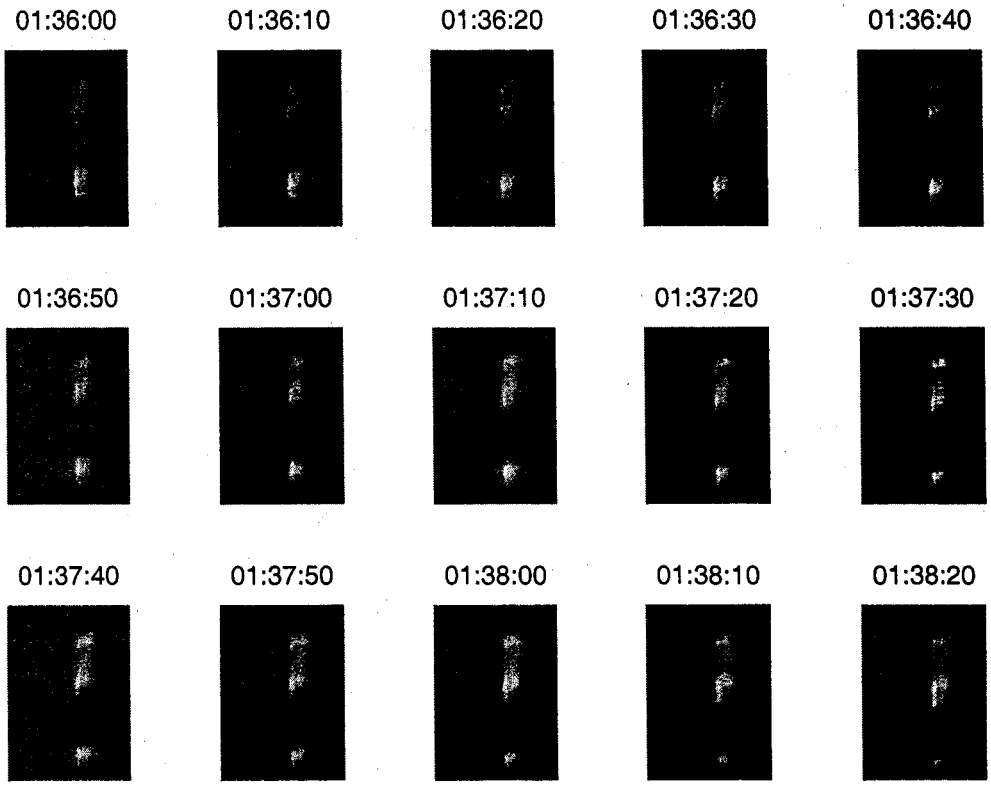

Figure 7.18: Continuing from Figure 7.17: consecutive range-Doppler images for 17 July 2004, UT 01:36:00–01:38:20. The 97.3 MHz FM channel and log periodic antenna are used. The horizontal axis shows Doppler velocity from -1500 – +1500 m/s; the vertical axis shows ranges from 600–1200 km. The greyscale is backscattered power which ranges over 8 dB (arbitrary power units).

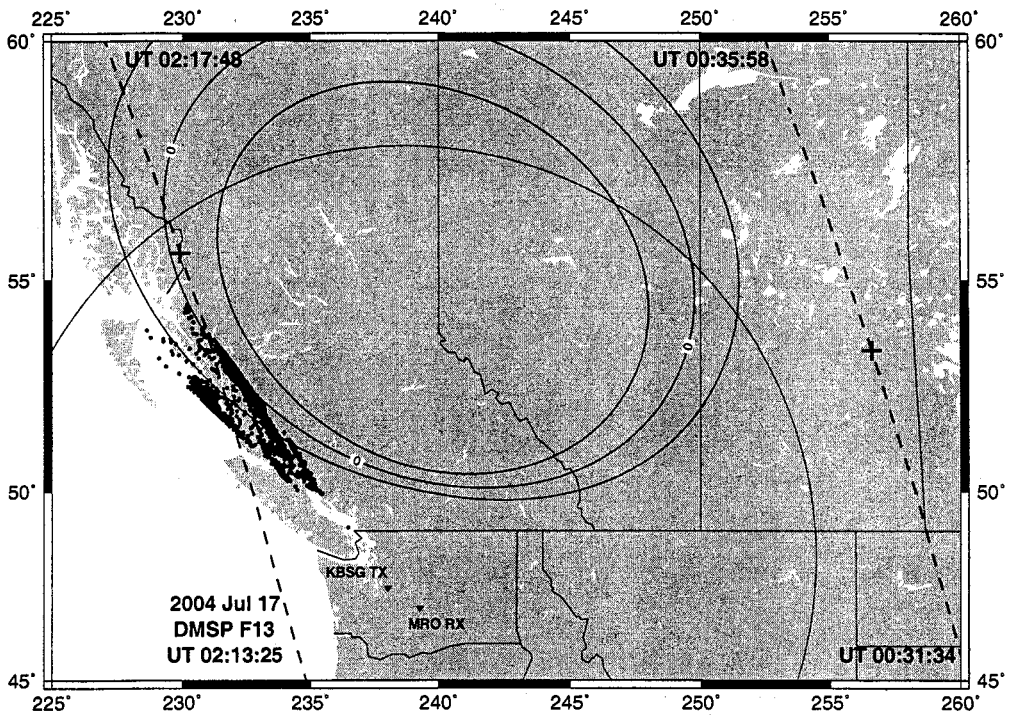

Figure 7.19: DMSP F13 passes (heavy dashed lines) over the MRR field of view on 17 July 2004. In both passes (beginning UT 00:31:34 and 02:13:25) the satellite is traveling northward. The pluses ("+") mark the equatorward boundary of energetic electron precipitation for each pass. Irregularities observed by the MRR during the overpass time periods are overlayed (circles).

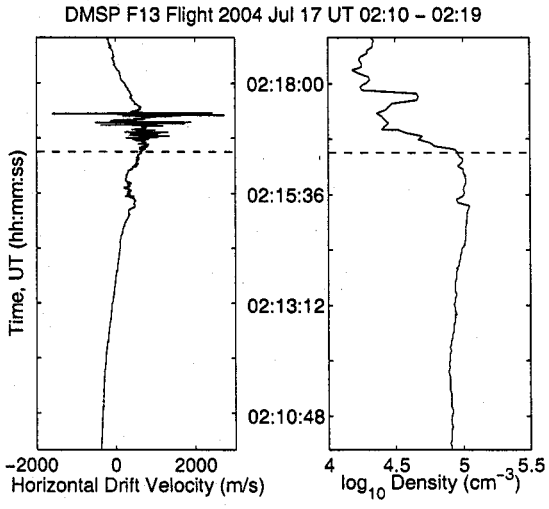

Figure 7.20: Plasma velocity and density during DMSP F13 pass on 2004 July 17, UT 02:10–02:19 (western track in Figure 7.19). The dashed lines mark the auroral precipitation region boundary.

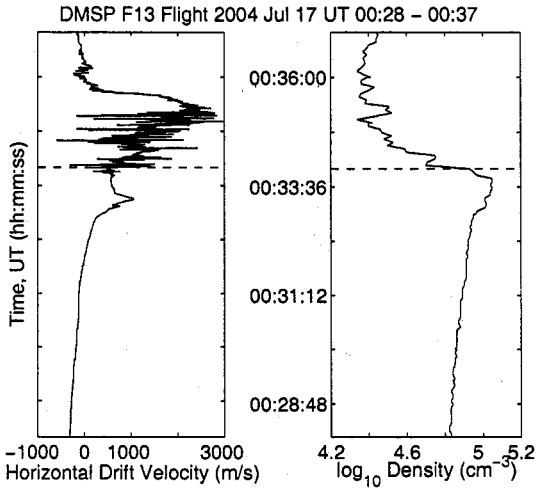

Figure 7.21: Plasma velocity and density during DMSP F13 pass on 2004 July 17, UT 00:28–00:37 (eastern track in Figure 7.19). The dashed lines mark the auroral precipitation region boundary.

further evidence of a SAPS channel: a density depletion in combination with enhanced sunward plasma drift [35]. Figures 7.20 and 7.21 show plasma horizontal drift velocity and density measured during the DMSP F13 passes on 2004 July 17, UT 02:10–02:19 and 00:28–00:37 (western and eastern F13 passes in Figure 7.19, respectively). Sunward plasma drift has positive velocity. Geodetic latitude increases in the same direction as time; the dashed lines mark the auroral precipitation region boundary.

Interferometer-Informed Irregularity Mappings

Finally, we present irregularity location mappings for the 17 July 2004 SAPS observations. As we showed in Chapter 6, Section 6.2.3, it is possible to de-alias the interferometer using the type of data we have available in the 17 July 2004 dataset. However, the de-aliasing procedure turned out to be rather brittle, and most of the de-aliased mappings were nonsensical. Therefore, we chose a few specific targets for which to try each of the 32 possible values for the alias number n, and determined the values of n which resulted in the irregularity mappings closest to the intersection of each target's range contour and the 0° aspect contour at 100 km altitude. We also performed these mapping tests both with and without our estimate for ϕ_0, the frequency-dependent interferometer calibration phase. Essentially, this means we tested cases for which ϕ_0 equaled -3.5 radians and 0 radians. Figure 7.22 (a nice illustration of the MRR interferometer ambiguity) shows all the potential mappings for two test targets. One target is denoted by black symbols; the other by white symbols. Mappings with ϕ_0 equal to -3.5 radians are marked by stars, and mappings that did not take ϕ_0 into account are marked by circles. The perpendicular aspect angle contour (for 100 km altitude) and the two target range contours are overlaid on the map as well. In this way we determined values for n and ϕ_0 to use on the entire 17 July SAPS dataset.

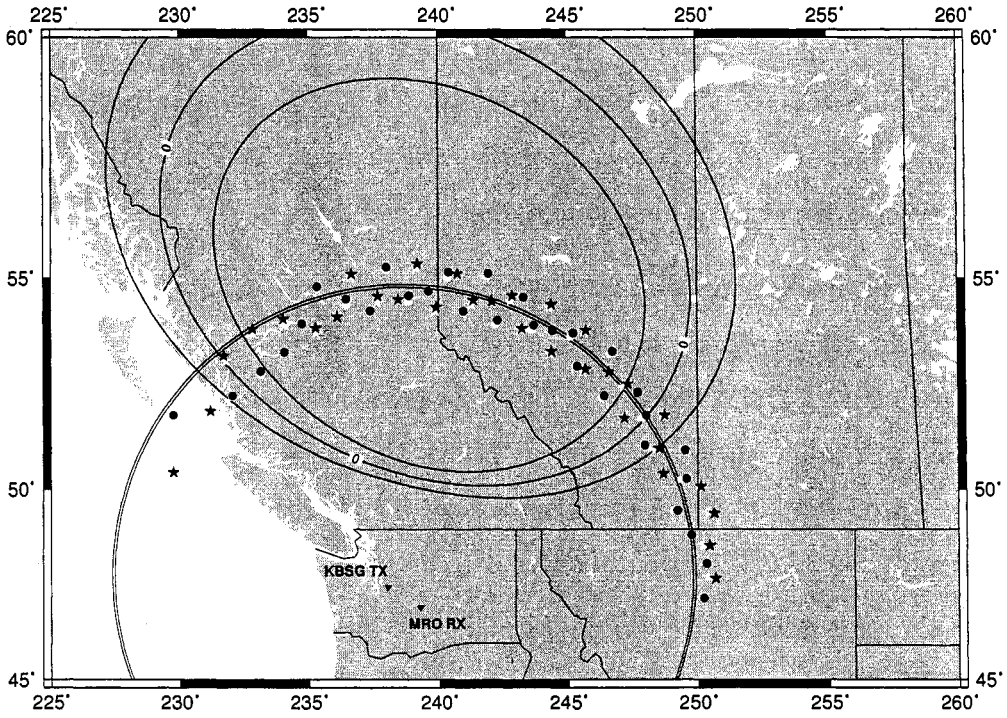

Figure 7.22: An illustration of interferometer azimuth ambiguity for two real targets at ranges 855 and 862.5 km (contours are overlaid, along with constant magnetic aspect angle contours for -1, 0, and 1 degrees). Potential mappings for the target at 855 km are white; 862.5 km mappings are black. Circles denote location estimates that do not include the arbitrary phase correction ϕ_0; stars are with $\hat{\phi}_0 = -3.5$ radians. Assuming the correct altitude is 100 km, the settings yielding target positions closest to perpendicular aspect angle (at the respective target ranges) are $n = 14, \phi_0 = -3.5$ rad (western solution) and $n = -7$, no ϕ_0 correction (eastern solution).

Using the "brute force" technique, we arrived at two possible range/aspect contour intersections for the irregularity mappings: a western solution ($n = 14, \phi_0 = -3.5$rad) and an eastern solution ($n = -7$, no ϕ_0 correction). Interestingly, the western, rather than the eastern, mappings seem to be correct in this particular case. We say more about this below. The resulting "interferometer informed," western irregularity mappings (for UT 01:32:00 – 01:34:20 and 01:36:00 – 01:38:20) are shown in Figures 7.23 – 7.27. Each irregularity occurrence is marked with an inverted triangle (symbolizing the toward-radar Doppler shifts of these echoes).

In the mappings we can identify cases where an adjacent alias number should have been used by noting secondary concentrations of irregularities (*e. g.*, at UT 01:36:50 and 01:37:10 in Figure 7.26). The 2-D interferometer images (in Figure 7.16) for these two times show that the scatter happens to be split across two interferometer lobes, so a single alias number will not suffice to correctly map all the irregularities. Also, not surprisingly, we see the same "pushing equatorward" behavior for the mapped irregularities. The interferometer-informed irregularity maps are more interesting than the zero-aspect maps, because we can actually see scattering volume structure, even with only the single bistatic link shown here.

Another feature to note in Figures 7.23 – 7.27 is that the irregularities begin to stray away from the perpendicular aspect contour as range decreases. We speculate that this is because the scattering layer altitude is lower at the nearer ranges. From Figure 7.13, we can see that the perpendicular aspect contours for lower altitudes are wider curves than those for higher altitudes (the contours are concentric, with the higher altitude contours inside the lower altitude ones). The aspect contours in the July 2004 mappings (Figures 7.23 – 7.27) have all been computed for an altitude of 100 km. Therefore, we believe the irregularity mappings which fall on the outside of the 100 km aspect contour actually belong at lower altitudes. Observations such as

this are useful ways to obtain altitude information about scattering volumes, as long as one can assume that the irregularities are strongly field-aligned.

For completeness, we show two examples of the "eastern solutions" for the 17 July irregularity mappings in Figure 7.28. For comparison, the western solutions at the same times are in Figures 7.23 (01:32:50) and 7.26 (01:37:00). We have several reasons for choosing the western mappings over these. First, in the eastern solutions, there are far more outliers: irregularities located further away from the main group of (presumed) correct mappings. Second, there are many complex-valued estimates (which cannot be displayed on the map). This occurs when the argument of $\cos^{-1}$, which includes interferometer phase, $2\pi\times$ the alias number, and the phase offset ϕ_0, becomes greater than unity, a situation which should not happen if n (and ϕ_0) have appropriate values. There are no complex-valued estimates in the western solutions. Third, features such as the "S"-shape over range (evident in the interferometer images of Figures 7.15 and 7.16; akin to an auroral curtain) can be identified in the western mappings, but not in the eastern ones. Also, a more subjective, but still important [126] observation is that the eastern mappings just don't seem to fit, qualitatively, as well along the aspect angle contours as the western mappings do.

7.2.3 Estimation of 3-D Vector Electron Drift Velocity

Now we move on to demonstrate the electron drift velocity estimation procedure described in Chapter 6, Section 6.2.2. We use 15 example cases: 10 second-long time samples between UT 09:24:00 and 09:26:20 on 11 September 2005 (irregularity mappings are shown in Figures 7.3 – 7.5). For this day, we have three independent measurements of irregularities available on bistatic links 97.3 UW-MRO, 96.5 UW-MRO, and 98.9 EWU-MRO. This is just enough information to attempt to estimate the velocity vectors in three dimensions.

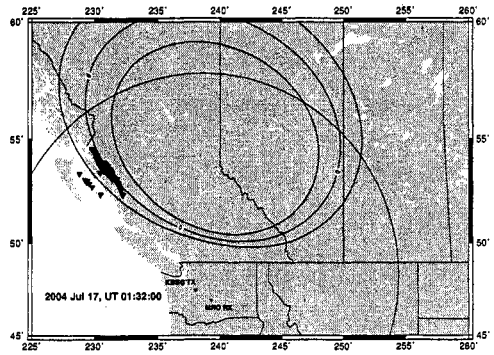

(01:32:00)

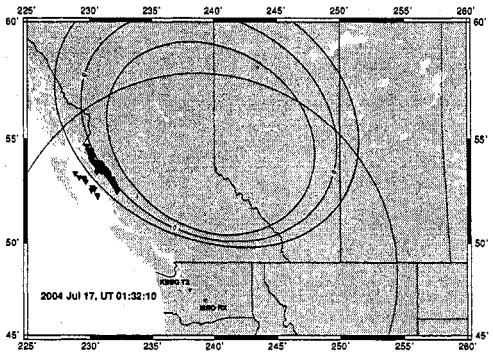

(01:32:10)

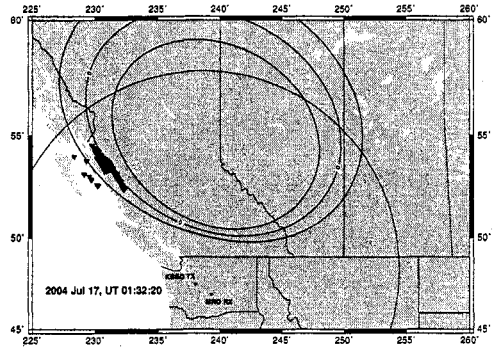

(01:32:20)

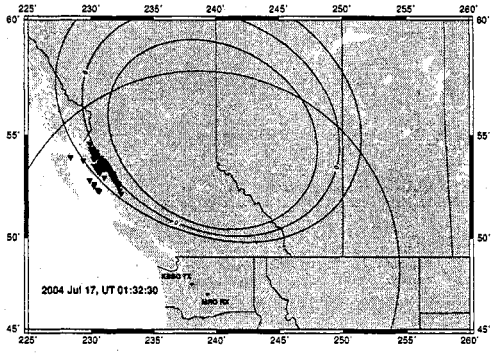

(01:32:30)

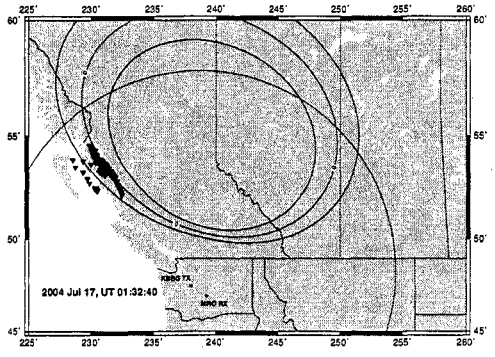

(01:32:40)

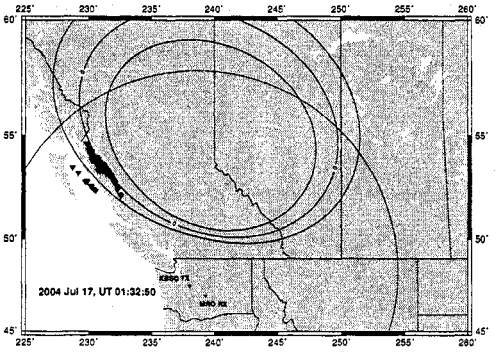

(01:32:50)

Figure 7.23: Interferometer informed irregularity mappings; 2004 Jul 17, UT 01:32:00–01:32:50

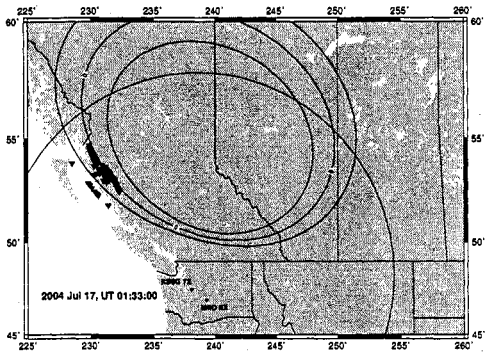

(01:33:00)

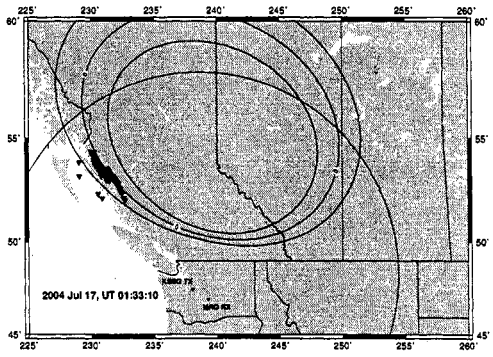

(01:33:10)

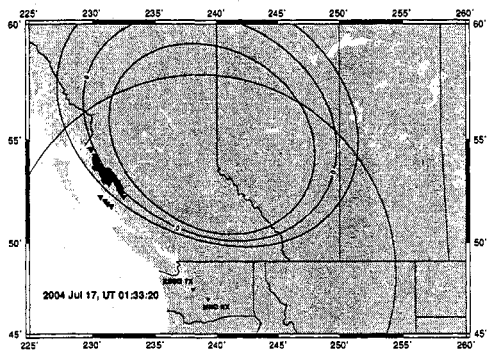

(01:33:20)

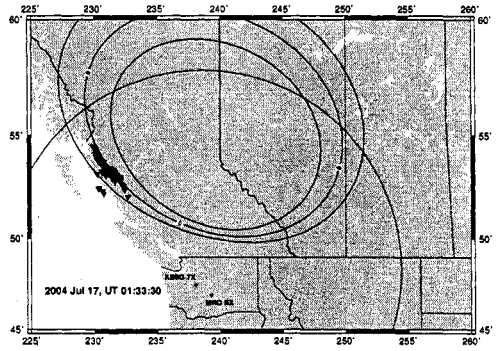

(01:33:30)

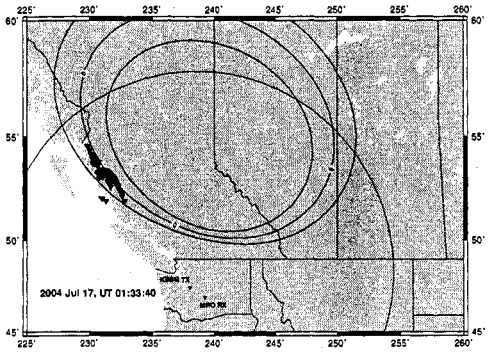

(01:33:40)

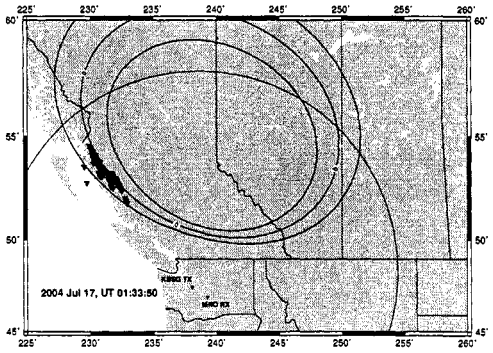

(01:33:50)

Figure 7.24: Interferometer informed irregularity mappings; 2004 Jul 17, UT 01:33:00–01:33:50

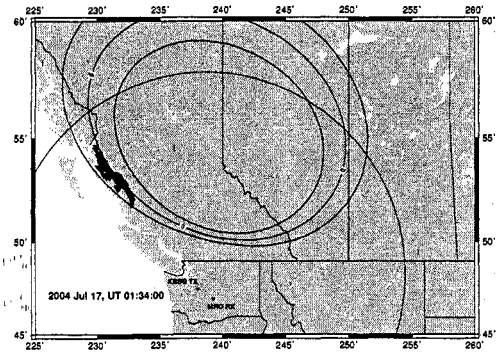

(01:34:00)

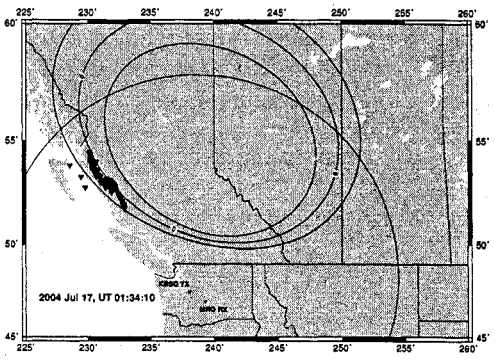

(01:34:10)

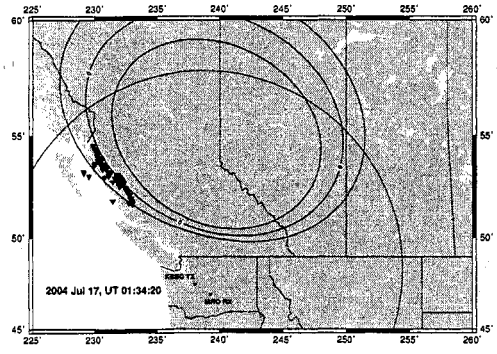

(01:34:20)

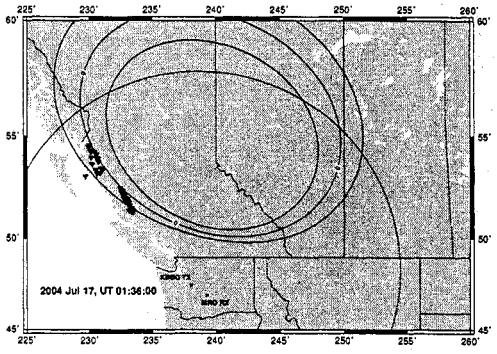

(01:36:00)

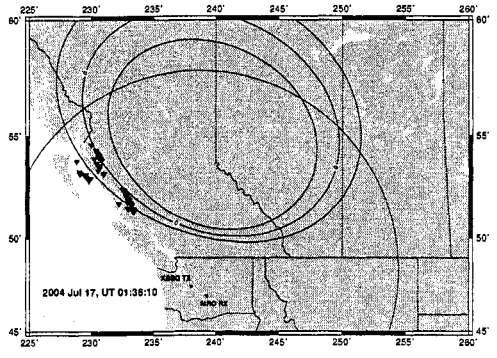

(01:36:10)

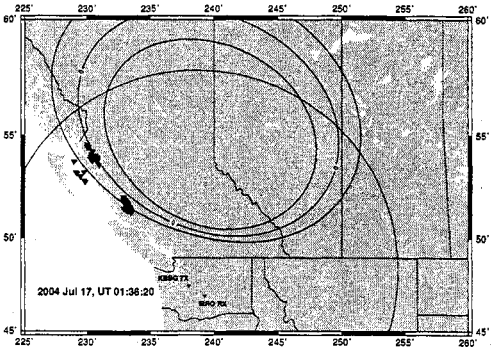

(01:36:20)

Figure 7.25: Interferometer informed irregularity mappings; 2004 Jul 17, UT 01:34:00–01:34:20 and 01:36:00–01:36:20

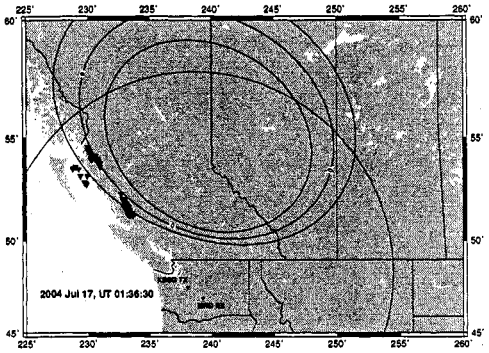

(01:36:30)

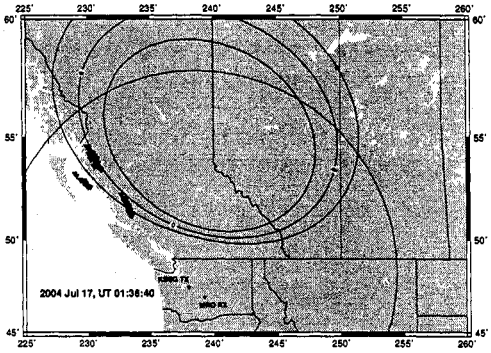

(01:36:40)

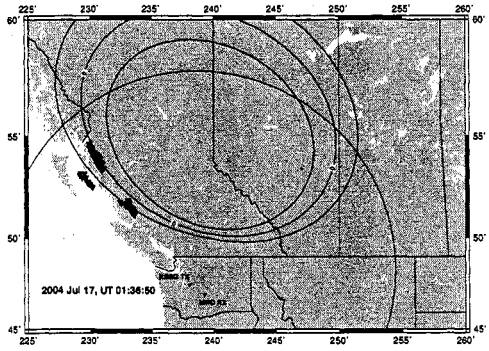

(01:36:50)

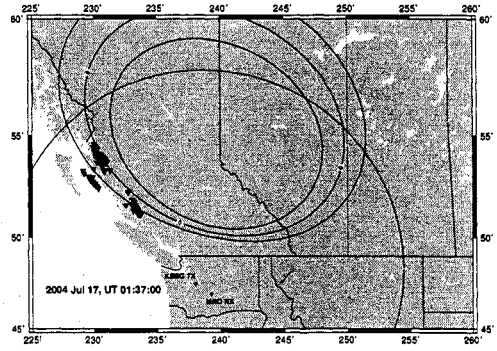

(01:37:00)

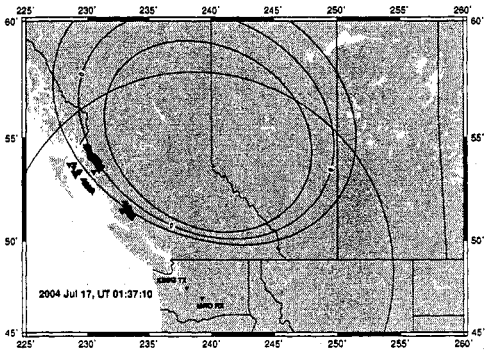

(01:37:10)

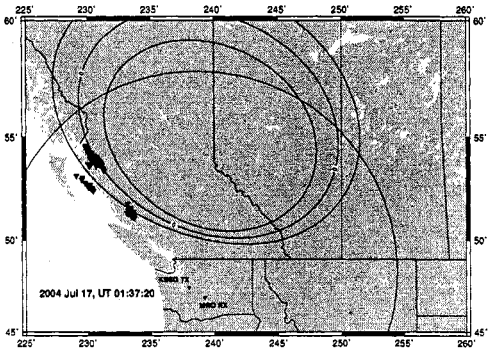

(01:37:20)

Figure 7.26: Interferometer informed irregularity mappings; 2004 Jul 17, UT 01:36:30–01:37:20

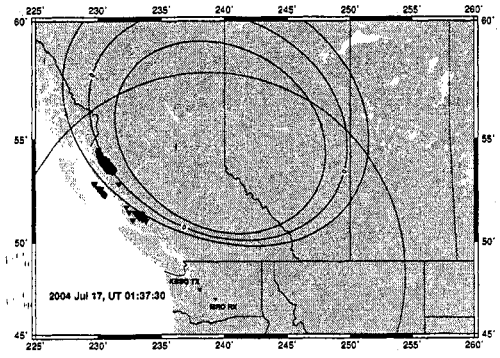

(01:37:30)

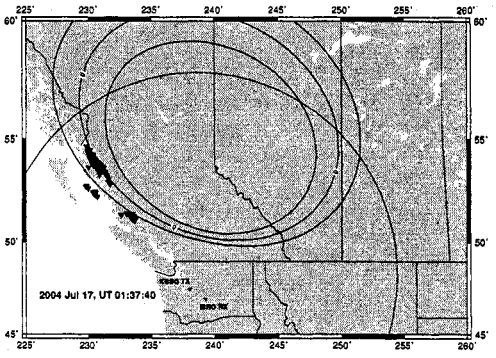

(01:37:40)

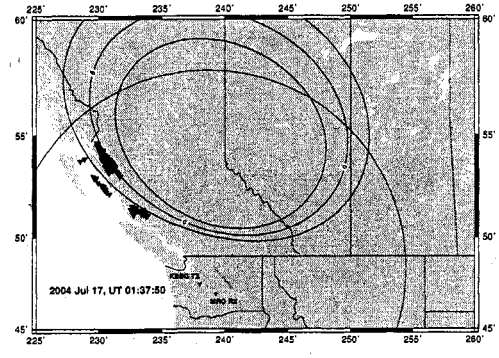

(01:37:50)

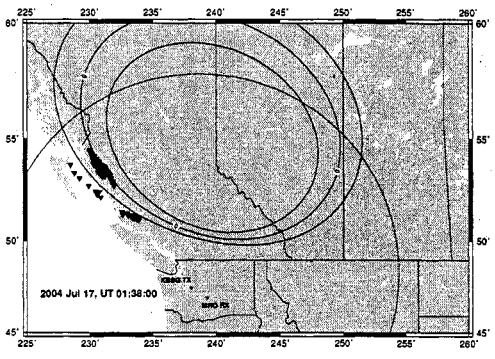

(01:38:00)

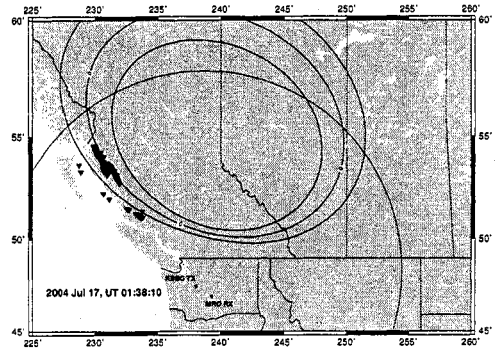

(01:38:10)

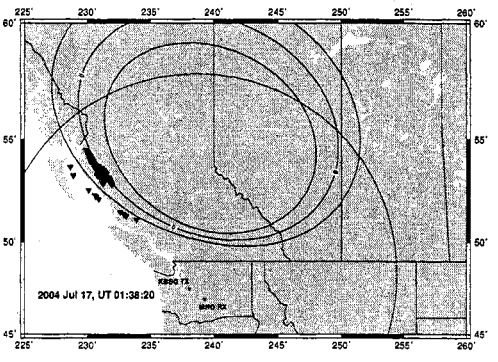

(01:38:20)

Figure 7.27: Interferometer informed irregularity mappings; 2004 Jul 17, UT 01:37:00–01:38:20

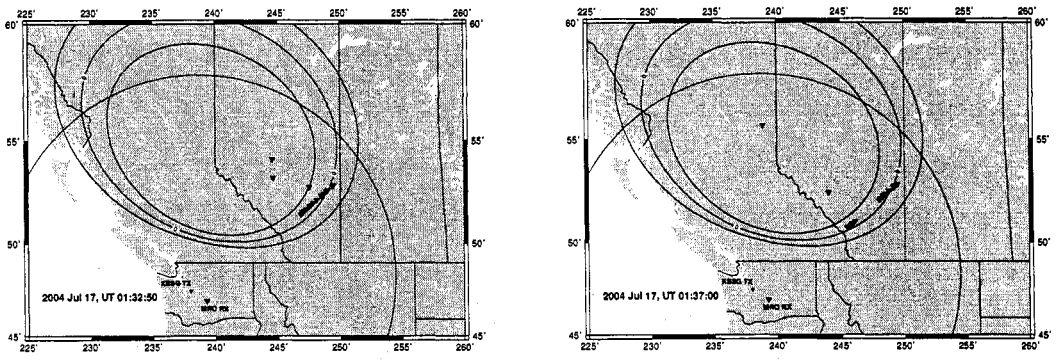

(01:32:50) (01:37:00)

Figure 7.28: Interferometer informed irregularity mappings for 2004 July 17, UT 01:32:50 and 01:37:00 – eastern solutions (believed to be incorrect).

To get the k-vectors (irregularity wavevectors) for each target (required to form the K-matrix in equation 6.1), we need to estimate the locations of scatterers. However, we are unable to use interferometer measurements to estimate irregularity locations because we only had the Yagi antenna recording a single channel during the 11 September 2005 event (we recorded three channels on the log periodic antenna). We cannot obtain the two independent interferometer measurements required to de-alias the azimuth angles of arrival with equation 6.9. Therefore, we estimate the scatterer locations with the 0°-aspect angle technique described above (Section 7.2.1).

Once we have locations associated with all irregularity spectra, we need to match groups of three (one for each bistatic link) to obtain the vector of Doppler velocity measurements in equation 6.1. However, we cannot directly match spectra from different bistatic links by range, as the ranges with activity and even general structures in range are often very different between the Eastern and Western links (for example, see Figures 7.9 and 7.11). Our solution is to whole-heartedly accept the spatial

homogeneity assumption (*i. e.* Figure 6.6), ignore range information (align scattering volumes from different radar links only in time), and pick trios of observations in which the irregularity phase velocities (mean Doppler shifts) are similar across large swaths of range. For our initial group of test cases, we chose times for which the mean Doppler velocities remain fairly constant over most ranges so that we could estimate a single Doppler velocity for each 10-second period in a straightforward manner. Figures 7.29, 7.31, and 7.33 illustrate this method for obtaining the vector of three Doppler velocities ($\mathbf{v_D}$ in equation 6.1) for three of the fifteen test cases. In each of these figures, the organization of ranges with irregularity activity is different between bistatic links (particularly between the Western (top two panels) and Eastern (bottom panel) links), yet on all three links the Doppler velocities remain roughly constant. For reference, we show the range-Doppler diagrams corresponding to Figures 7.29, 7.31, and 7.33 in Figures 7.30, 7.32, and 7.34, respectively. We use a similar method for obtaining the K-matrix (selecting a trio of k-vectors, one from each bistatic link).

The resulting 15 estimates for $\mathbf{V_d}$ are shown in Figure 7.35. It will be important to refine our estimation technique and test it on a larger dataset, but these first results are mostly consistent with each other (particularly in their direction), which is satisfying.

Although using $\mathbf{V_d} = \mathbf{E} \times \mathbf{B}/B^2$ to estimate the E region electric field is an approximation (see equation 4.15), we try it anyway; by inspecting Figure 7.35, the electric field direction points roughly East/Southeast ($\mathbf{B}$ points mostly downward at MRR latitude). Using $E = BV_d$, we estimate the electric field magnitude to be between 30 mV/m (completely believable) and 6 V/m (unrealistically high).

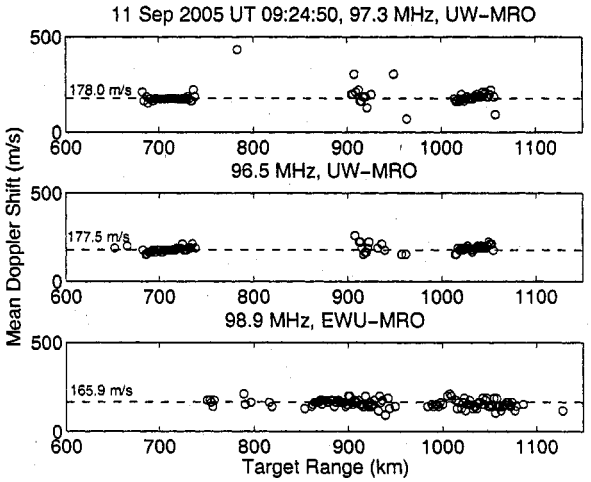

Figure 7.29: Mean Doppler velocities for irregularity spectra over several ranges for the 10 second period starting at UT 09:24:50. The corresponding range-Doppler diagrams for the three bistatic links are shown in Figure 7.30. For this 10 second time period, we estimate $\mathbf{v_D} = [178.0\ 177.5\ 165.9]$ m/s.

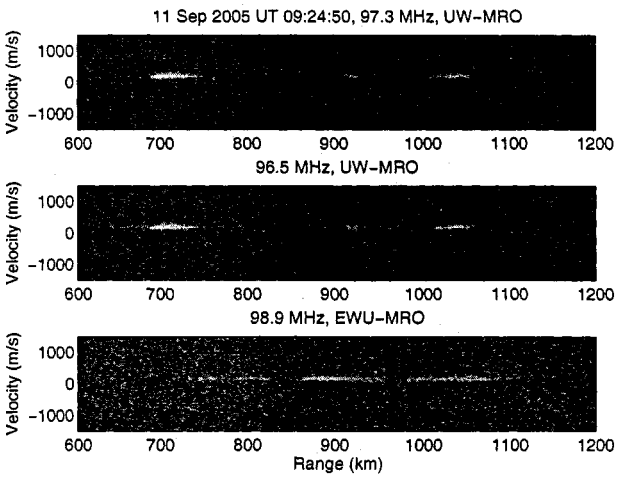

Figure 7.30: Range-Doppler diagrams for three separate bistatic links (greyscales are backscattered power in dB). These correspond to the mean Doppler data shown in Figure 7.29.

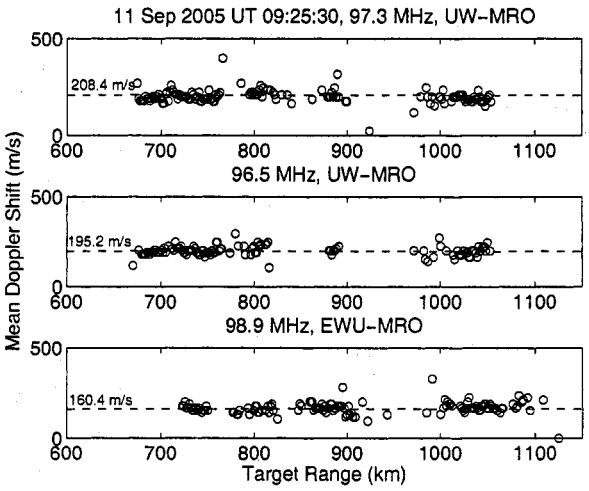

Figure 7.31: Mean Doppler velocities for irregularity spectra over several ranges for the 10 second period starting at UT 09:25:30. The corresponding range-Doppler diagrams for the three bistatic links are shown in Figure 7.32. We estimate $\mathbf{v_D} =$ [208.4 195.2 160.4] m/s.

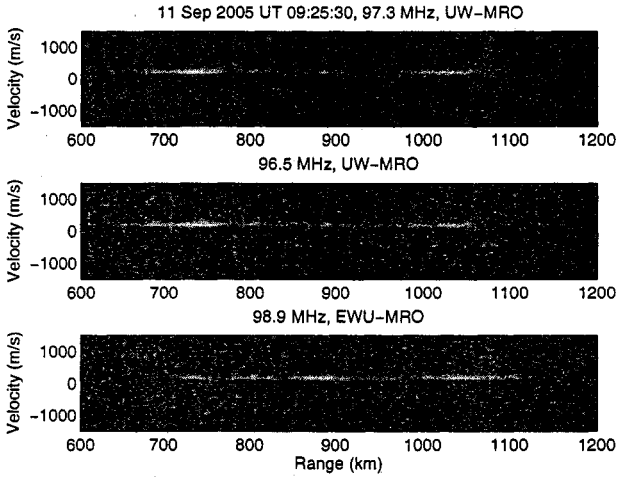

Figure 7.32: Range-Doppler diagrams for three separate bistatic links (greyscales are backscattered power in dB). These correspond to the mean Doppler data shown in Figure 7.31.

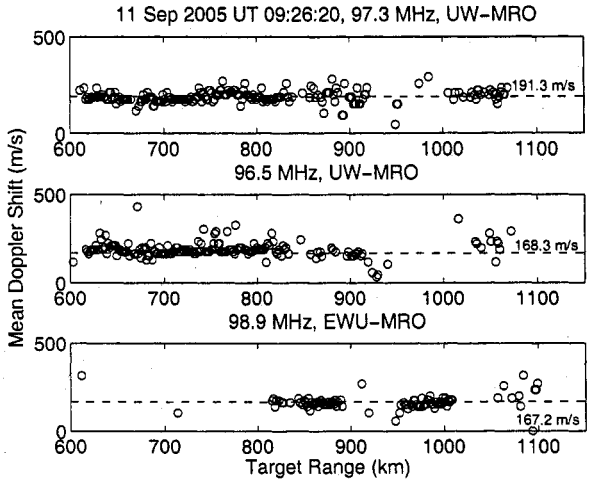

Figure 7.33: Mean Doppler velocities for irregularity spectra over several ranges for the 10 second period starting at UT 09:26:20. The corresponding range-Doppler diagrams for the three bistatic links are shown in Figure 7.34. We estimate $\mathbf{v_D} =$ [191.3 168.3 167.2] m/s.

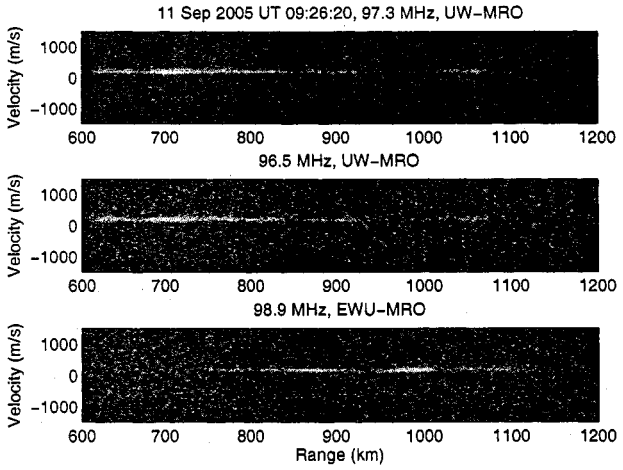

Figure 7.34: Range-Doppler diagrams for three separate bistatic links (greyscales are backscattered power in dB). These correspond to the mean Doppler data shown in Figure 7.33.

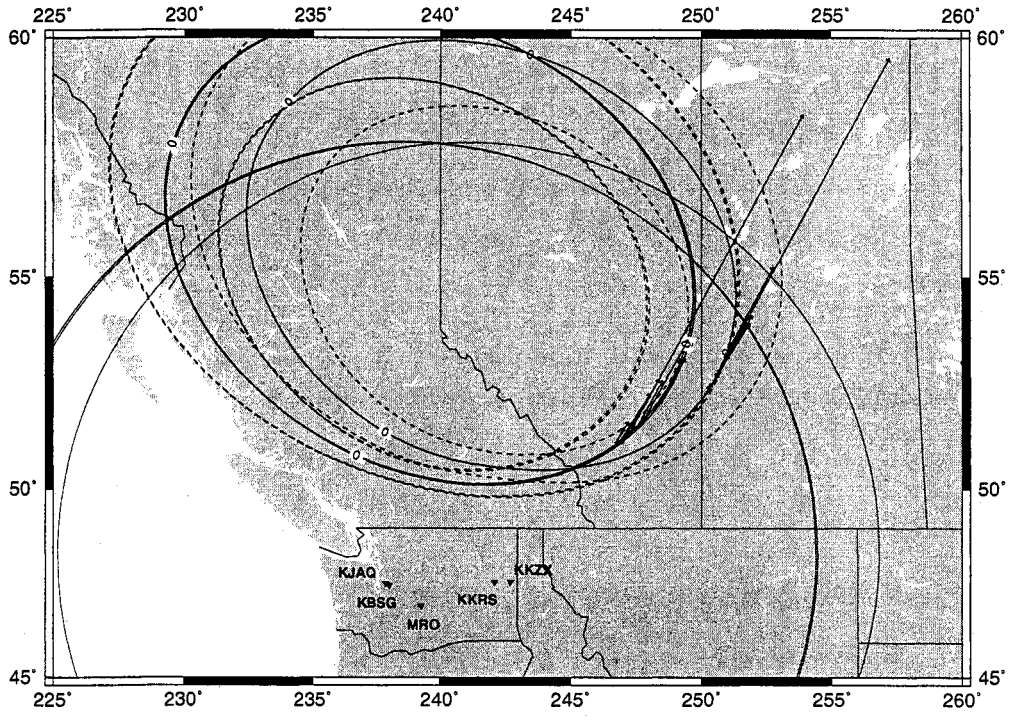

Figure 7.35: 15 estimates for vector electron drift velocity between UT 09:24:00 and 09:26:20 on 11 September 2005. These estimates use three bistatic links: KBSG–MRO, KJAQ–MRO, and KKZX–MRO, and employ target locations which assume perfectly perpendicular aspect angle and 100 km altitude. The vector magnitudes are to scale (we believe some of them to be unrealistically large). This plot only shows two of the three estimated dimensions for $\mathbf{V_d}$.

Upper Bounds for Acoustic Speed and Temperature

For each of the 15 test cases, we can estimate an upper bound for the ion acoustic speed c_s by taking the magnitude of the relative electron-ion drift, $|\mathbf{V_d}|$. We find c_s to be between 630 m/s and 140 km/s, with a mean of 20 km/s. Several of these values are too large, but at least the minimum is feasible. The 630 m/s electron drift corresponds to an electric field with magnitude approximately 30 mV/m.

Next, by squaring the acoustic speed upper bound and multiplying by m_i/k_B, we obtain a temperature upper bound ($\gamma_e T_e + \gamma_i T_i$, with $\gamma_e = 5/3$ and $\gamma_i = 1$). The plasma temperatures fall between 1500 K and 7×10^7 K and have an average value of 6×10^6 K. As before, most of these values are unreasonably large. Consulting typical E region parameters used in a 1983 modeling study by St.-Maurice and Schlegel [119], T_e equals 1130 K and T_i equals 600 K under conditions with a very large $\mathbf{E} \times \mathbf{B}$ drift (2000 m/s). This puts the temperature estimate $\gamma_e T_e + \gamma_i T_i$ at 2480 K, which implies that our minimum value is reasonable (though quite elevated), but our mean and maximum values are far too high to be believable.

Flow Angle Estimates

Very large flow angles may be one reason our $|\mathbf{V_d}|$ estimates are so high. We can determine the irregularity flow angles for our test cases using both $\mathbf{k}$ and $\mathbf{V_d}$. Since we obtain a k-vector for each bistatic link, we have three possible estimates. If our spatial homogeneity assumption is reasonable, each channel should have a similar flow angle. As we can see from the results given in Table 7.2, the flow angles for each channel are very similar (supporting the homogeneous medium assumption), but all the flow angles seem too large.

If these estimates are close to the true values, traditional linear fluid theory indi-

Table 7.2: Statistics of estimated flow angles for the three independent bistatic links.

	97.3 MHz UW–MRO	96.5 MHz UW–MRO	98.9 MHz EWU–MRO
minimum flow angle	72°	72°	75°
corresponding phase velocity	200 m/s	200 m/s	170 m/s
maximum flow angle	$\approx 90°$	$\approx 90°$	$\approx 90°$
corresponding phase velocity	190 m/s	130 m/s	160 m/s
mean flow angle	87°	87°	87°
mean phase velocity	190 m/s	180 m/s	150 m/s

cates that $\mathbf{V_d}$ must be extremely large to drive instabilities at such flow angles:

$$v_{\text{Dopp}} = V_d \cos\theta \tag{7.2}$$

(In this equation, θ is the flow angle.) The irregularity phase (Doppler) velocities corresponding to the minimum and maximum flow angles are also given in Table 7.2, along with the average of the Doppler velocities in the 15-point dataset for each channel.

The corresponding $\mathbf{V_d}$ magnitudes are indeed very large and this can be seen from the electric field magnitude, acoustic speed, and temperature upper bounds given above. The example cases with the largest $|\mathbf{V_d}|$ values also have the flow angles nearest 90°, as we expect. Also, the vertical (altitude) component of the $\mathbf{V_d}$ estimates is negligible compared to the latitudinal and longitudinal components in all 15 test cases. We conclude that either the flow angle estimates are incorrect (through errors in the $\mathbf{V_d}$ directions, which drive our $\mathbf{V_d}$ magnitudes too high), or the unreasonably large linear plane wave-theory predictions for electron drift velocity support the idea

that the radar is observing specular-like line-of-sight reflections from a target moving in the $\hat{V}_d$ direction (rather than scatter from a wave propagating in the $\hat{k}$ direction).

Geometric Precision

If errors in our $\mathbf{V_d}$-direction estimates are to blame for the unrealistically high $\mathbf{V_d}$ magnitudes, it may be because we are unable to glean enough geometric precision from the current 3-receiver MRR configuration. To determine how accurate we can expect our velocity vector measurements to be, we also computed the geometric dilution of precision (GDOP) values and K-matrix condition numbers for our test data.

The GDOP is determined by computing the ratio of the largest to the smallest eigenvalue of the line-of-sight (K) matrix. If one of the eigenvalues is zero (for example, if two of three transmitters are mounted at the same location), then the matrix cannot be inverted (the condition number is infinite) and the GDOP is also infinite. All this means is that we cannot locate the target in three dimensions; we can reduce our resolving space to two dimensions (*i. e.*, assume an altitude for the target), and the 2-D GDOP becomes the ratio of the largest to the second-smallest eigenvalue.

In the case of an overdetermined system (3-D location with 4 or more independent lines of sight), the matrix is not directly invertible and so the concept of a condition number does not make sense. The singular value decomposition can be used on the non-square K-matrix, though, and the GDOP value becomes the ratio of the largest to the smallest singular value. Because two of the four transmitters we recorded during the 11 September 2005 event turned out to be mounted on the same tower, we only have three independent lines of sight, so our K-matrix is 3×3 and the system is not overdetermined.

The K-matrix condition numbers, 3-D GDOP values, and 2-D GDOP values for our example data are shown in Table 7.3. These values are reasonable. Condition

Table 7.3: Statistics of estimated GDOP values and corresponding condition numbers for 15 line-of-sight matrices.

	K condition number	3-D GDOP	2-D GDOP
minimum	630	120	25
maximum	6500	1150	65
mean	3000	530	40

numbers in the millions are considered "high." On the other hand, a GDOP value of 10 might be considered large. While the line-of-sight matrix condition number is a measure of how difficult the matrix is to invert accurately, the GDOP value is actually a resolution dilution factor; *i. e.*, if the native instrument resolution is 1.5 km and the GDOP is 10, then the working resolution is 15 km. The current three-receiver MRR geometric precision is limited by the fact that the Seattle area transmitters are very close to each other, especially with respect to the locations of our irregularity targets. Therefore, we cannot expect a great amount of precision in our velocity direction estimates. Fortunately, this situation will get better as more receivers are added to the system.

Our geometric precision should improve if we only try to estimate 2-D information, since two out of the three bistatic links are at least as far apart as Seattle and Spokane. The third bistatic link must be added on either the western or the eastern side of the MRR system, and does not add much to the line-of-sight diversity. As we expect, the 2-D GDOP values look much better, with a mean value of 40, as opposed to 530 in the 3-D case.

Technique Critique

Although it will be important to perform further tests to learn more, our current verdict is that this technique is not yet reliable. The magnitude of $\mathbf{V_d}$ is getting overestimated; this is probably due to errors in the $\mathbf{V_d}$ direction estimate, which sometimes causes flow angles close to perpendicular. When used with linear fluid theory, the large flow angles result in vastly overestimated electron drift speeds.

Adding more receivers (to obtain better view geometry diversity) will help the situation; the GDOP values in this example are very large. However, more development of the experimental procedure and the estimators we use will be beneficial as well. The most suspect part of the procedure presented here is the estimation of a single Doppler shift and k-vector from many spectra at different ranges.

We chose to distill a single v_D and $\mathbf{k}$ from 10 seconds and 1000 kilometers of data because we are unable to find correlations between the range structures on different bistatic links at similar times. We use a least squares spectral fitter to estimate mean Doppler shifts for each range. However, now we need a more sophisticated method to determine the "primary ranges" of a large scattering volume, so we can use the Doppler shift from that range, or an average of those ranges, to represent the entire scattering volume. Averaging over all the ranges for a certain time is not a reliable method, as there are usually too many outlier-spectral features. Here, we used the median of the mean Doppler shifts over all the ranges (for each 10 seconds of data), and the k-vector corresponding to that particular irregularity spectrum.

We estimated an error range for our $\mathbf{V_d}$ estimates by re-computing the values using different k-vectors within the ranges with appropriate Doppler shift. We found, on average, that the estimated magnitude of $\mathbf{V_d}$ could be six to ten times larger or smaller than those values estimated using the method outlined above for choosing a k-vector given a certain Doppler shift. (The 12 m/s uncertainty in the radar Doppler

velocity measurements was comparatively insignificant with respect to its impact on the final $\mathbf{V_d}$ estimate.) Interestingly, error factors between 6 and 10 agree rather well with the cube roots of the 3-D GDOP values given above.

Another step which likely introduces a lot of error into our estimates is determining the scattering volume locations. If our assumptions leading to the position estimate (100 km altitude, 0° aspect angle, and eastern intersection of aspect angle and range contours) are incorrect, there will be large errors in the k-vectors themselves, and this will render our estimate of $\mathbf{V_d}$ useless.

Finally, our assumption of spatial homogeneity could be wrong (discussed on page 127); also, the time difference between related phenomena observed on different bistatic links could be greater than 10 seconds (our current time resolution). This might be the case if the MRR were observing a spatially compact, rapidly propagating ionospheric electric field disturbance, such as a SAID (sub-auroral ion drift) event [3, 22]. If we cannot use time to match scattering volume features from different bistatic links, we will need to devise a new method for this task as well.

Alternatively, our near-perpendicular flow angle estimates could be correct, and the resulting unrealistic values for V_d might indicate that the radar aurora model of Bragg scatter from irregularity plane waves is inaccurate. Only further experimentation will tell.

Chapter 8

SUMMARY AND SUGGESTIONS FOR FUTURE WORK

We have developed a linear fluid theory of E region plasma density irregularities as well as new experimental techniques for radar remote sensing of these irregularities.

We derived a new form of the ionospheric two-stream instability dispersion relation based on a model of disturbances as spatially localized plane wave packets. Our main goal was to understand the instability behavior and resulting radar scatter in a new theoretical framework that is sensitive to disturbance spatial size. To do this, we modeled the behavior of spatially localized plasma density wave packets in a medium subject to the ionospheric two-stream instability. We determined the phase velocity and growth rate of localized waves under various conditions. These two characteristics are particularly important because phase velocity is readily measured by radars as a Doppler shift, and radar backscatter features are dominated by the signatures of the largest waves, which the growth rate can help us identify. We also determined reasonable bounds for the new model parameters we introduced (packet size and propagation velocity), and provided a rough link between spatial packet size and irregularity spectral width, which can also be measured with radar.

We further showed that spatially limited irregularity wave packets allow the coupling of energy into spatial Fourier components and propagation directions other than those of the instability primary waves themselves. Therefore, this model may be a useful interpretive device for coherent radar backscatter at large flow or aspect angles, since it supports the idea that radars detect line-of-sight scatter from irregularities that appear to the radar as hard targets moving in one specific direction.

We also described our development of a passive VHF radar used to observe plasma irregularities into a multistatic, distributed system capable of performing new experiments. The experiments we describe are "spatially diverse," incorporating multiple view geometries, and are the first of their kind with passive radar. Our work provides an important proof of concept for other scientists in the aeronomy community who hope to implement large-scale versions of distributed, passive radio remote sensing instruments. The experimental techniques we described and demonstrated here will only get better as more receivers are installed and more transmitters are used for spatially diverse illumination.

We close by suggesting several projects for the improvement of the Manastash Ridge Radar and future passive receiver networks that would make them even better tools for aeronomy and space physics.

8.1 Suggested Improvements to the MRR

The following is a "laundry list" of potential projects that would benefit the MRR. An "off the shelf" improvement – rather expensive, yet one that would immediately be extremely useful – would be to replace the 500 kbps microwave link, currently used to connect the scatter receivers at MRO to the internet, with a faster connection. Faster data transfer from MRO ultimately means more continuous data available from the radar. The current controlling scripts for the radar's daily operation "tiptoe" around the slow and unreliable MRO connection; if this were not an issue, MRR operation would be more robust, and it would be easier to write straightforward, standardized controlling software for the radar. Plus, observation latency would be vastly reduced.

Regardless of whether the MRO connection speed is improved, the radar controlling software should be updated. A new, standard suite of software (preferably all written in the same programming language!) should be developed which automates

the default control of the three MRR receivers. Scalable software that can handle an arbitrary number of receivers and channels would be ideal. The software should easily allow temporary changes in the default receiver operation; have a user-friendly interface (an online, graphical interface would be ideal); offer regular, easily accessible reports of system diagnostics (the diagnostics will also need to be designed); and be well documented for academic posterity. Designing such software will take significant forethought. Similarly, a standard data format and organization scheme for data storage and dissemination (both temporary and long term) should be developed. An excellent starting point for these considerations is the RSDP (Radio Science Data Protocol), suggested and described by Dr. Frank Lind [personal communication, 2004].

Next, the MRR should be calibrated in several different ways. First, we would like to be able to measure absolute backscattered power, so that the scattering cross sections of targets can be learned. This can be done with a calibrated noise source connected to the receiver(s), or even by observing the firmament: radio astronomers have determined the power densities arriving from thousands of stars (*e. g.*, the 408 MHz all-sky continuum survey performed by Haslam *et al.* [51]); the variation of received power with the Earth's rotation can be used in combination with such sky maps to distinguish gain and noise temperature in the receiver [105], after which absolute calibration can be attempted. Of course, it helps if the transmitter can be turned off for such an exercise; this may be the one drawback to exploiting commercial transmitters for radar applications.

Second, the interferometer should be calibrated, as we attempted in Chapter 6 (page 133). We have attempted the calibration with an opportunistic method that takes advantage of local transmitters. However, the antenna cable lengths (and thus their difference) could be measured directly through the use of a time domain reflec-

tometer.

Several antenna-related projects can benefit the MRR. First, to seriously address the instrument deconvolution of our data, we should thoroughly understand the gain patterns of our antennas and their interaction with local terrain. This may involve electromagnetic modeling of custom antenna performance, as with the NEC program [37], or antennas with manufacturer-specified patterns can be bought. Also, a pair of antennas should be positioned at MRO so that the horizontal interferometer (currently overmoded) can be used to determine absolute azimuth angles for scatterers. This will help with reliably locating targets within the MRR field of view. A vertical interferometer would also be a useful addition; this would allow the measurement of target altitudes, and combined with the horizontal interferometer, complete 3-D locations could be determined. Absolute locations of scatterers are required for many different ionospheric plasma experiments (*e. g.*, magnetic aspect angle studies and the comparison of radar observations with data from other instruments), and knowledge of location is essential for most aerospace-related applications, such as target tracking.

Many potential improvements in MRR sensitivity can be gained by applying signal processing algorithms toward clutter suppression and interference mitigation [133]. Since FM channels with a powerful transmitter at one receiver node and perfect quiet at another will not always be available, interference rejection solutions will become increasingly important as the MRR and ISIS grow into widespread receiver arrays. If multiple antennas are available at each receiver site, space-time adaptive processing (STAP) is an interesting possibility to investigate [62]. Other "signal processing" type projects fall into the data analysis stage. These include automatic target recognition (for both plasma turbulence as well as aircraft and other targets); target feature extraction; and aerospace tracking applications.

Finally, there are several electromagnetic theory and plasma physics projects that can be supported by the MRR. EM scattering from plasma density irregularities is still an open problem in many ways. For example, multiple scattering in the turbulent ionospheric medium is not well understood and seldom modeled or accounted for in the interpretation of radar data. Preliminary analyses show that waves of different polarizations seem to scatter differently from the primarily 2-D plasma density structures [Gidner and Sahr, unpublished work, 2002]; however, more can be learned about this subject, and cross-polarization experiments could be performed using the MRR as a platform. Last, but not least, the effect of ionospheric refraction on low elevation angle propagation at FM band (VHF) frequencies should be determined.

8.2 Future Projects for Passive Remote Sensing Arrays

The development of new meta-instruments such as the ISIS array (Intercepted Signals for Ionospheric Science, a planned national network of passive radar receivers) and DASI (Distributed Arrays of Small Instruments, a new initiative in ground-based geophysics [90]) will create great opportunities for experimental observations in space and ionospheric physics [67]. Large, distributed arrays of instruments can yield insights into global physics unattainable with single point measurements – no matter how wonderful the instrument at that single point is. The potential advantages of this new class of instrumentation are many, but harnessing them will require us to address many challenges as well. The main challenges we face fall into three categories: technical, logistical, and scientific.

Technical challenges concern making the instrument *possible* to operate, while logistical and scientific challenges deal with making an instrument that is *feasible* and *useful* to operate, respectively. The lines become somewhat blurred when one imagines encountering logistical problems so severe that the instrument cannot operate.

Also, if the instrument is not scientifically useful to operate, its ability to operate may be challenged by the funding agency!

The technical challenges involved in designing a distributed passive remote sensing array such as the MRR or ISIS include simply making all the receiver components work together properly. Solutions will involve both hardware (mostly off the shelf) and software design. Synchronization between individual receiver nodes is essential, and is solved with off the shelf GPS time and frequency reference modules. In general, we need to understand the entire system well enough to deconvolve the instrumental effects from the data.

Another technical challenge will be determining the optimal placement of receiver nodes in various geographical areas. Areas of interest may vary in topology, availability and quality of transmitters, and communication infrastructure (high speed internet access, for example). In Chapter 6, we proposed using geometric dilution of precision (GDOP) values in combination with magnetic aspect angle mappings as a metric by which to rank possible receiver locations. In order to determine such a metric, we must know the locations of suitable transmitters in the area.

The allocation of system resources – particularly computational processing power and network bandwidth – falls under the category of logistical challenges. So does building a robust, fault-tolerant system. This goal can be addressed by using uninterruptible power supplies and other similar protective hardware, and developing a suite of instrument diagnostics and a protocol for their regular assessment. In general, and especially for large arrays of instruments, we would like our system to be as autonomous as possible; algorithms aiding autonomy may be developed after the system has been in place for a while and we can define desired automatic behaviors (for example, automatic transmitter selection based on measurements of signal quality and co-channel interference). Developing a method for dealing with enormous

amounts of data will be probably the most important logistical challenge, especially for passive remote sensing instruments which must retain full reference and scatter datasets to enable reprocessing.

Finally, the scientific, or instrument usability, challenges we foresee mainly concern interpreting the large amounts of data in terms of geophysical models once we are successfully operating these instruments. Making sense of observations from multiple view geometries and diverse types of illumination (*e. g.*, transmitters of vastly different frequencies and bandwidths) will require new data fusion techniques. We will also need to design new experiments to take advantage of the unique opportunities afforded by this next generation of scientific instruments.

8.3 Conclusion

We claim that the experimental work presented in this dissertation is a preview of what is to come when the new ISIS (and eventually DASI) instrument arrays begin operation. High quality, but also high complexity, experiments will be enabled as more receivers are added and more transmitters of opportunity are tapped. In the context of magnetosphere-ionosphere coupling, distributed radio systems have great potential for understanding and supporting global models. Individually, passive radar systems are excellent and efficient tools for studying the behavior and instability of space plasmas. We hope that both the theoretical and experimental contributions of this work provide an insightful view of the micro-physics and macro-physics of the ionosphere.

BIBLIOGRAPHY

[1] M. Abramowitz and I. A. Stegun. Handbook of Mathematical Functions with Formulas, Graphs, and Mathematical Tables. U.S. Government Printing Office, Washington, D.C. 20402, 1972.

[2] K. Akimoto. Theory of pulse-particle interaction in one dimension. Phys. Plasmas, 4:3101, 1997.

[3] P. C. Anderson, D. L. Carpenter, K. Tsuruda, T. Mukai, and F. J. Rich. Multisatellite observations of rapid subauroral ion drifts (SAID). J. Geophys. Res., 106:29585, 2001.

[4] R. Andre and D. de Wit. Identification of the ionospheric footprint of magnetospheric boundaries using SuperDARN coherent HF radars. Planet. Space Sci., 51:813, 2003.

[5] H. Bahcivan, D. L. Hysell, M. F. Larsen, and R. F. Pfaff. 30 MHz imaging radar observations of auroral irregularities during the JOULE campaign. J. Geophys. Res., 100(A05):307, doi:10.1029/2004JA010975, 2005.

[6] V. S. Beley, V. G. Galushko, and Y. M. Yampolski. Traveling ionospheric disturbance diagnostics using HF signal trajectory parameter variations. Radio Sci., 30:1739–1752, 1995.

[7] W. J. G. Beynon and P. J. S. Williams. Incoherent scatter of radio waves from the ionosphere. Rep. Prog. Phys., 41:909, 1978.

[8] D. Bilitza. International reference ionosphere 2000. Radio Sci., 36:261, 2001.

[9] D. L. Book. NRL Plasma Formulary. Naval Research Laboratory, 1987.

[10] A. Boudouridis, E. Zesta, L. Lyons, P. Anderson, and D. Lummerzheim. The effect of solar wind pressure pulses on the size and strength of the auroral oval. J. Geophys. Res., 108:8012, doi:10.1029/2002JA009373, 2003.

[11] T. J. M. Boyd and J. J. Sanderson. The Physics of Plasmas. Cambridge University Press, 2003.

[12] O. Buneman. Excitation of field aligned sound waves by electron streams. Phys. Rev. Letters, 10:285–287, 1963.

[13] J. Burch, M. Schulz, and H. Spence (eds.). Inner magnetosphere interactions: new perspectives from imaging. Geophysical Monograph Series 159. American Geophysical Union, Washington, DC, 2005.

[14] Francis F. Chen. Introduction to Plasma Physics and Controlled Fusion. Plenum Press, 1984.

[15] G. Chisham, M. Pinnock, A. S. Rodger, and J.-P. Villain. High-time resolution conjugate SuperDARN radar observations of the dayside convection response to changes in IMF B-y. Ann. Geophys., 18:191, doi: 10.1007/s00585–000–0191–y, 2000.

[16] C. W. Clark and W. T. Ellison. Potential use of low-frequency sounds by baleen whales for probing the environment: evidence from models and empirical measurements. Echolocation in Bats and Dolphins, J. Thomas, C. Moss and M. Vater, eds. The University of Chicago Press, 2002.

[17] E. F. Donovan and D. R. Moorcroft. The effect of multiple scattering on the aspect sensitivity and polarization of radio auroral echoes. Radio Sci., 27:169, 1992.

[18] J. Drexler, J.-P. St.-Maurice, D. Chen, and D. R. Moorcroft. New insights from a nonlocal generalization of the farley-buneman instability problem at high latitudes. Ann. Geophys., 20:2003, 2002.

[19] Richard O. Duda, Peter E. Hart, and David G. Stork. Pattern Classification. John Wiley and Sons, 2001.

[20] J. W. Dungey. Interplanetary magnetic field and the auroral zones. Phys. Rev. Letters, 6:47, 1961.

[21] P. Eglitis, T. R. Robinson, I. W. McCrea, K. Schlegel, T. Nygren, and A. S. Rodger. Doppler spectrum statistics obtained from three different- frequency radar auroral experiments. Ann. Geophys., 13:56, 1995.

[22] P. J. Erickson, J. C. Foster, and J. M. Holt. Inferred electric field variability in the polarization jet from Millstone Hill E region coherent scatter observations. Radio Sci., 37:10.1029/2000RS002531, 2002.

[23] D. T. Farley. A plasma instability resulting in field-aligned irregularities in the ionosphere. J. Geophys. Res., 68:6083–6097, 1963.

[24] D. T. Farley and B. B. Balsley. Instabilities in the equatorial electrojet. J. Geophys. Res., 78:227, 1973.

[25] D. T. Farley, H. M. Ierkic, and B. G. Fejer. Radar interferometry: A new technique for studying plasma turbulence in the ionosphere. J. Geophys. Res., 86:1467, 1981.

[26] B. G. Fejer and M. C. Kelley. Ionospheric irregularities. Rev. Geophys. Space Phys., 18:401, 1980.

[27] B. G. Fejer, J. Providakes, and D. T. Farley. Theory of plasma waves in the auroral E region. J. Geophys. Res., 89:7487, 1984.

[28] B. G. Fejer and J. F. Providakes. High latitude E-Region irregularities: New results. Physica Scripta, T18:167, 1987.

[29] J. C. Foster, A. J. Coster, P. J. Erickson, J. M. Holt, F. D. Lind, W. Rideout, M. McCready, A. van Eyken, R. J. Barnes, R. A. Greenwald, and F. J. Rich. Multiradar observations of the polar tongue of ionization. J. Geophys. Res., 110:A09S31, doi:10.1029/2004JA010928, 2005.

[30] J. C. Foster and P. J. Erickson. Simultaneous observations of E region coherent backscatter and electric field amplitude at F region heights with the millstone hill UHF radar. Geophys. Res. Lett., 27:3177–3180, 2000.

[31] J. C. Foster, P. J. Erickson, A. J. Coster, J. Goldstein, and F. J. Rich. Ionospheric signatures of plasmaspheric tails. Geophys. Res. Lett., 29:doi:10.1029/2002GL015067, 2002.

[32] J. C. Foster, P. J. Erickson, F. D. Lind, and W. Rideout. Millstone Hill coherent-scatter radar observations of electric field variability in the sub-auroral polarization stream. Geophys. Res. Lett., 31:L21803, doi:10.1029/2004GL021271, 2004.

[33] J. C. Foster and W. Rideout. Midlatitude TEC enhancements during the October 2003 superstorm. Geophys. Res. Lett., 32:L12S04, doi:10.1029/2004GL021719, 2005.

[34] J. C. Foster, D. Tetenbaum, C. F. del Pozo, J.-P. St.-Maurice, and D. R. Moorcroft. Aspect angle variations in intensity, phase velocity, and altitude for high–latitude 34–cm E region irregularities. J. Geophys. Res., 97:8601–8617, 1992.

[35] J. C. Foster and H. B. Vo. Average characteristics and activity dependence of the subauroral polarization stream. J. Geophys. Res., 107:1475, 2002.

[36] M. Fukumoto, N. Nishitani, T. Ogawa, N. Sato, H. Yamagishi, and A. S. Yukimatu. Statistical analysis of echo power, Doppler velocity and spectral width obtained with the Syowa South HF radar. Adv. Polar Upper Atmos. Res., 13:37, 1999.

[37] Matthew. E. Grossman. Antennas for passive radar. Master's thesis, Univ. of Wash., Seattle, 1994.

[38] C. Haldoupis, M. C. Kelley, G. C. Hussey, and S. Shalimov. Role of unstable sporadic-E layers in the generation of midlatitude spread F. J. Geophys. Res., 108:1446, doi:10.1029/2003JA009956, 2003.

[39] C. I. Haldoupis. A review on radio studies of auroral E region ionospheric irregularities. Ann. Geophys., 7:239–258, 1989.

[40] C. I. Haldoupis and K. Schlegel. Direct comparison of 1-m irregularity phase velocities and ion acoustic speeds in the auroral E region ionosphere. J. Geophys. Res., 95:18989, 1990.

[41] G. E. Hall, D. Andre, D. W. Danskin, G. J. Sofko, and J. A. Koehler. Lifetime measurements of auroral scatterers. J. Geophys. Res., 98:17537, 1993.

[42] G. E. Hall and D. R. Moorcroft. Magnetic aspect angle effects in radar aurora at 48.5 MHz, corrected for refraction. J. Geophys. Res., 97:19471, 1992.

[43] P. W. Hammer, N. Platt, S. M. Hammel, J. F. Heagy, and B. D. Lee. Experimental observation of on-off intermittency. Phys. Rev. Letters, 73:1095, 1994.

[44] A. M. Hamza. A nonlinear theory for large aspect angle echoes in the auroral E region. J. Geophys. Res., 97:16981, 1992.

[45] A. M. Hamza and J.-P. St.-Maurice. A turbulent theoretical framework for the study of current–driven E region irregularities at high latitudes: Basic derivation and appliation to gradient–free situations. J. Geophys. Res., 98:11,587, 1993a.

[46] A. M. Hamza and J.-P. St.-Maurice. A self consistent fully turbulent theory of auroral E region irregularities. J. Geophys. Res., 98:11,601, 1993b.

[47] A. M. Hamza and J.-P. St.-Maurice. Large aspect angles in auroral E region echoes: A self-consistent turbulent fluid theory. J. Geophys. Res., 100:5723, 1995.

[48] J. M. Hansen. A new radar technique for remote sensing of atmospheric irregularities by passive observation of the scattering of commercial FM broadcasts. Master's thesis, Univ. of Wash., Seattle, 1994.

[49] C. Hanuise, J. P. Villain, J. C. Cerisier, C. Senior, J. M. Ruohoniemi, R. A. Greenwald, and K. B. Baker. Statistical study of high-latitude E-region Doppler spectra obtained with the SHERPA HF radar. Ann. Geophys., 9:273, 1991.

[50] J. K. Harmon. Planetary delay-Doppler radar and the long-code method. IEEE Trans. Geosci. and Remote Sensing, 40:1904, 2002.

[51] C. G. T. Haslam, C. J. Salter, H. Stoffel, and W. E. Wilson. A 408 MHz all-sky continuum survey II - The atlas of contour maps. Astron. Astrophys. Suppl. Ser., 47:1–143, 1982.

[52] P. E. Howland. Target tracking using television-based bistatic radar. IEEE Proceedings, Radar, Sonar Navigation, 146-3:166–174, 1999.

[53] D. L. Hysell and J. L. Chau. Imaging radar observations and nonlocal theory of large-scale plasma waves in the equatorial electrojet. Ann. Geophys., 20:1167, 2002.

[54] D. L. Hysell, M. Yamamoto, and S. Fukao. Simulations of plasma clouds in the mid-latitude E-region ionosphere with implications for type I and type II quasiperiodic echoes. J. Geophys. Res., 107:doi:10.1029/2002JA009291, 2002.

[55] B. J. Jackel, D. R. Moorcroft, and K. Schlegel. Characteristics of very large aspect angle E-region coherent echoes at 933 MHz. Ann. Geophys., 15:54, 1997.

[56] J. D. Jackson. Classical Electrodynamics. John Wiley and Sons, 1962.

[57] P. Janhunen. Three-dimensional stabilization mechanism for the auroral Farley-Buneman instability. J. Atmos. Terr. Phys., 54:1633, 1992.

[58] P. Janhunen. Perpendicular particle simulation of the E region Farley-Buneman instability. J. Geophys. Res., 99:11461, 1994.

[59] M. P. Johnson, U. S. Inan, and D. S. Lauben. Subionospheric VLF signatures of oblique (nonducted) whistler-induced precipitaion. Geophys. Res. Lett., 26:3569, 1999.

[60] Michael C. Kelley. The Earth's Ionosphere: Plasma Physics and Electrodynamics. Academic Press, San Diego, Calif., 1989.

[61] Margaret Kivelson and Christopher Russell (eds.). Introduction to Space Physics. Cambridge University Press, 1995.

[62] R. Klemm. Space-Time Adaptive Processing: principles and applications. The Institution of Electrical Engineers, 1998.

[63] V. Koch and R. Westphal. New approach to a multistatic passive radar sensor for air/space defense. IEEE Aerospace and Electronic Systems Magazine, 10:24, 1995.

[64] H. C. Koons and J. F. Fennell. Space weather effects on communications satellites. The Radio Science Bulletin, 316:27–41, 2006.

[65] E. Kudeki and G. R. Stitt. Frequency domain interferometry: A high resolution radar technique for studies of atmospheric turbulence. Geophys. Res. Lett., 14:198, 1987.

[66] Pijush Kundu and Ira Cohen. Fluid Mechanics. Elsevier Academic Press, 2004.

[67] L. J. Lanzerotti. The sun to the Earth - and beyond: A decadal research strategy in solar and space physics. National Academies Press, Washington, D.C., 2003.

[68] M. O. Leavitt. Lockheed martin silent sentry. Aviation Week & Space Technology, 150(19):75, 1999.

[69] K. Lee and C. F. Kennel. Effects of propagation parallel to the magnetic field on the type 1 electrojet irregularity instability. Planet. Space Sci., 21:1339, 1973.

[70] Nadav Levanon. Radar Principles. John Wiley, New York, 1988.

[71] F. D. Lind, J. D. Sahr, and D. M. Gidner. First passive radar observations of auroral E region irregularities. Geophys. Res. Lett., 26:2155–58, 1999.

[72] Frank D. Lind. Passive radar observations of the aurora. PhD thesis, Univ. of Wash., Seattle, 1999.

[73] A. J. Manucci, B. D. Wilson, and C. D. Edwards. A new method for monitoring the Earth's ionospheric total electron content using the GPS global network. ION GPS-93; Proceedings of the 6th International Technical Meeting of the Satellite Division of the Institute of Navigation, pages 1323–1332, 1993.

[74] M. G. Meyer and J. D. Sahr. Passive coherent scatter radar interferometer implementation, observations, and analysis. Radio Sci., 39:RS3008, doi:10.1029/2003RS002985, 2004.

[75] M. G. Meyer, J. D. Sahr, and Andrew Morabito. A statistical study of subauroral E-region coherent backscatter observed near 100 MHz with passive radar. J. Geophys. Res., 109:A07308, doi:10.1029/2004JA010396, 2004.

[76] Melissa G. Meyer. Passive VHF radar interferometer implementation, observations, and analysis. Master's thesis, Univ. of Wash., Seattle, 2003.

[77] S. E. Milan, M. Lester, and N. Sato. Multi-frequency observations of E-region HF radar aurora. Ann. Geophys., 21:761, 2003.

[78] D. R. Moorcroft. Propagation of plasma wave energy in the auroral E region. J. Geophys. Res., 89:2963, 1984.

[79] D. R. Moorcroft. An examination of radio-auroral aspect sensitivity. Can. J. Phys., 63:1005, 1985.

[80] D. R. Moorcroft. Estimates of absolute scattering coefficients of radar aurora. J. Geophys. Res., 92:8723, 1987.

[81] D. R. Moorcroft. Reflection and refraction by tilted layers - an explanation for VHF auroral backscatter at large aspect angles. Geophys. Res. Lett., 16(3):235, 1989.

[82] D. R. Moorcroft and K. Schlegel. E region coherent backscatter at short wavelength and large aspect angle. J. Geophys. Res., 93:2005, 1988.

[83] K. Mursla and T. Hiltula. Bashful ballerina: Southward shifted heliospheric current sheet. Geophys. Res. Lett., 30:doi:10.1029/2003GL018201, 2003.

[84] K. Mursla and T. Ulich. A new method to determine the solar cycle length. Geophys. Res. Lett., 25:1837, 1998.

[85] Dwight R. Nicholson. Introduction to Plasma Theory. John Wiley, 1983.

[86] E. Nielsen, C. F. del Pozo, and P. J. S. Williams. VHF coherent radar signals from the E region ionosphere and the relationship to electron drift velocity and ion acoustic velocity. J. Geophys. Res., 107:1012, doi:10.1029/2001JA900111, 2002.

[87] E. Nielsen and K. Schlegel. A first comparison of STARE and EISCAT electron drift velocity measurements. J. Geophys. Res., 88:5745, 1983.

[88] E. Nielsen and K. Schlegel. Coherent radar Doppler measurements and their relationship to the ionospheric electron drift velocity. J. Geophys. Res., 90:3498, 1985.

[89] E. C. Nielsen, C. I. Haldoupis, B. G. Fejer, and H. M. Ierkic. Dependence of auroral power spectra variations upon electron drift velocity in the eastward electrojet. J. Geophys. Res., 89:3819, 1984.

[90] Ad Hoc Committee on Distributed Arrays of Small Instruments: A Workshop Space Studies Board. Distributed Arrays of Small Instruments for Solar-Terrestrial Research: Report of a Workshop. National Academies Press, Washington, DC 20001, 2006.

[91] M. Oppenheim and Y. Dimant. Ion thermal effects on E-region instabilities: 2D kinetic simulations. J. Atmos. Terr. Phys., 66:1655, 2004.

[92] M. Oppenheim, N. Otani, and C. Ronchi. Hybrid simulation of the saturated Farley-Buneman instability in the ionosphere. Geophys. Res. Lett., 22:353, 1995.

[93] M. Oppenheim, N. Otani, and C. Ronchi. Saturation of the Farley-Buneman instability via nonlinear electron ExB drifts. J. Geophys. Res., 101:17273, 1996.

[94] N. Otani and M. Oppenheim. A saturation mechanism for the Farley-Buneman instability. Geophys. Res. Lett., 25:1833, 1998.

[95] George K. Parks. Physics of Space Plasmas. Addison Wesley, 1991.

[96] O. Penrose. Electrostatic instabilities of a uniform non-Maxwellian plasma. Phys. Fluids, 3:258, 1960.

[97] R. F. Pfaff, J. D. Sahr, J. F. Providakes, W. E. Swartz, D. T. Farley, P. M. Kintner, I. Häggström, Åke Hedberg, H. Opgenoorth, G. Holmgren, D. Wallis, A. McNamara, B. Whalen, A. Yau, S. Watanabe, F. Creutzberg, P. Williams, E. Nielsen, K. Schlegel, and T. R. Robinson. The E Region Rocket/Radar Instability Study (ERRRIS): Scientific objectives and campaign overview. J. Atmos. Terr. Phys., 54:779–808, 1992.

[98] William H. Press, Brian P. Flannery, Saul A. Teukolsky, and William T. Vetterling. Numerical Recipes in C. Cambridge University Press, Cambridge Mass., 1988.

[99] Eric Priest and Terry Forbes. Magnetic Reconection: MHD Theory and applications. Cambridge University Press, 2000.

[100] F. Primdahl. Ionospheric E-region plasma turbulence and instabilities observed in situ by sounding rockets. paper presented at 6th Scientific Assembly, Intl. Assoc. of Geomagn. and Aeron., 1989.

[101] J. A. Ratcliffe. Sun, Earth, and Radio. World University Library, London, 1970.

[102] L. A. Reinleitner and E. Nielsen. Self-consistent analysis of electron drift velocity measurements with the STARE/SABRE system. J. Geophys. Res., 90:8477, 1985.

[103] D. S. Robertson, D. T. Liddy, and W. G. Elford. Measurements of winds in the upper atmosphere by means of drifting meteor trails I. J. Atmos. Terr. Phys., 4:255, 1953.

[104] T. R. Robinson and F. Honary. A resonance broadening kinetic theory of the modified two-stream instability: Implications for radar auroral backscatter experiments. J. Geophys. Res., 95:1073, 1990.

[105] A. E. Rogers, P. Pratap, E. Kratzenberg, and M. A. Diaz. Calibration of active antenna arrays using a sky brightness model. Radio Sci., 39:RS2023, doi:10.1029/2003RS003016, 2004.

[106] C. Ronchi, P. L. Similon, and R. N. Sudan. A nonlocal linear theory of the graduent drift instability in the equatorial electrojet. J. Geophys. Res., 94:1317, 1989.

[107] C. T. Russell and R. L. McPherron. Semi-annual variation of geomagnetic activity. J. Geophys. Res., 78:92, 1973.

[108] J. D. Sahr, D. T. Farley, W. E. Swartz, J. F. Providakes, and R. F. Pfaff. Observations of 3 meter auroral irregularities during the ERRRIS campaigns. J. Atmos. Terr. Phys., 54:809, 1992.

[109] J. D. Sahr and B. G. Fejer. Auroral electrojet plasma irregularity theory and experiment: A critical review of present understanding and future directions. J. Geophys. Res., 101:26,893–26,909, 1996.

[110] J. D. Sahr and F. D. Lind. The Manastash Ridge Radar: A passive bistatic radar for upper atmospheric radio science. Radio Sci., 32:2345–58, 1997.

[111] John D. Sahr. Observation and theory of the radar aurora. PhD thesis, Cornell Univ., Ithaca, N. Y., 1990.

[112] F. L. Scarf, D. A. Gurnett, and W. S. Kurth. Measurements of plasma wave spectra in Jupiter's magnetosphere. J. Geophys. Res., 86:8181, 1981.

[113] K. Schlegel. Coherent backscatter from ionospheric E-region plasma irregularities. J. Atmos. Terr. Phys., 58:933–41, 1996.

[114] K. Schlegel and D. R. Moorcroft. EISCAT as a tristatic auroral radar. J. Geophys. Res., 94:1430, 1989.

[115] K. Schlegel, E. C. Thomas, and D. Ridge. A statistical study of auroral radar spectra obtained with SABRE. J. Geophys. Res., 91:13483, 1986.

[116] C. I. Haldoupis G. J. Sofko and J. A. Koehler. On ion acoustic plasma waves at large magnetic aspect angles in the high-latitude E region of the ionosphere. J. Geophys. Res., 91:5755, 1986.

[117] M. Spasojevic, G. Parks, M. Wilber, M. Fillingim, E. Lee, H. Reme, and M. Goldstein. Structure of the magnetospheric boundary layers during the extreme compression events of October-November 2003. American Geophysical Union, Spring Meeting 2004, Abstract SH41B-03, 2004.

[118] J.-P. St.-Maurice and A. M. Hamza. A new nonlinear approach to the theory of E region irregularities. J. Geophys. Res., 106(A2):1751, 2001.

[119] J.-P. St.-Maurice and K. Schlegel. A theory of coherent radar spectra in the auroral E region. J. Geophys. Res., 88:4087, 1983.

[120] E. C. Stone, A. M. Frandsen, R. A. Mewaldt, E. R. Christian, D. Margolies, J. F. Ormes, and F. Snow. The advanced composition explorer. Space Science Reviews, 86:1, 199.

[121] A. V. Streltsov and J. C. Foster. Electrodynamics of the magnetosphere-ionosphere coupling in the nightside subauroral zone. Phys. of Plasmas, 11:1260, doi:10.1063/1.1647139, 2004.

[122] R. N. Sudan. Nonlinear theory of type I irregularities in the equatorial electrojet. Geophys. Res. Lett., 10:983, 1983a.

[123] R. N. Sudan. Unified theory of type I and type II irregularities in the equatorial elecrojet. J. Geophys. Res., 88:4853, 1983b.

[124] R. N. Sudan, J. Akinrimisi, and D. T. Farley. Generation of small-scale irregularities in the equatorial electrojet. J. Geophys. Res., 78:240, 1973.

[125] M. Sugiura. Hourly values of equatorial Dst for IGY. Annals of the International Geophysical Year, 35:945, Pergamon Press, Oxford, 1964.

[126] A. Tarantola. Inverse Problem Theory: methods for data fitting and model parameter estimation. Elsevier, 1987.

[127] M. V. Uspensky, R. J. Pellinen, W. Baumjohann, G. V. Starkov, E. Nielsen, G. Sofko, and K. U. Kaila. Spatial variations of ionospheric cnoductivity anradar auroral amplitude in teastward electrojet region during pre-substorm conditions. J. Geophys., 52:40, 1983.

[128] J. Watermann. Refraction of 50-MHz radar waves in a realistic ionospheric model. Radio Sci., 25:805, 1990.

[129] J. Watermann, A. G. McNamara, G. J. Sofko, and J. A. Koehler. Distribution of mean doppler shift, spectral width, and skewness of coherent 50-mhz auroral radar backscatter. J. Geophys. Res., 94:6979, 1989.

[130] P. J. S. Williams, B. Jones, M. Uspensky, and G. Starkov. Multi-radar studies of auroral backscatter. J. Atmos. Terr. Phys., 50:315, 1988.

[131] P. J. S. Williams, G. O. L. Jones, and A. R. Jain. Methods of measuring plasma velocity with EISCAT. J. Atmos. Terr. Phys., 46:521, 1984.

[132] R. Yarlagadda, I. Ali, N. Al-Dhahir, and J. Hershey. GPS GDOP metric. IEE Proc. Radar, Sonar and Navigation, 147:259, 2000.

[133] C. C. Zhou. Application and Extension of Space-Time Adaptive Processing to Passive FM Radar. PhD thesis, Univ. of Wash., Seattle, 2003.

Appendix A

DERIVATIONS IN DETAIL

We provide details here for some of the derivations presented in the main text.

A.1 Ion Acoustic Dispersion Relation

Continuing from section 4.1.3 (page 45), we combine the electron and ion fluid equations by subtracting them. The two equations are reprinted here for convenience:

$$\frac{\partial}{\partial t}n + \nabla \cdot \left[\mathsf{R}^{-1} \left(-\frac{en}{m_e}\mathbf{E} - \frac{\gamma_e k_B T_e}{m_e}\nabla n \right) \right] = 0 \tag{A.1}$$

$$\frac{\nu_e}{\Omega_e \Omega_i}\left[-\frac{\partial}{\partial t}\left(\frac{\partial}{\partial t} + \nu_i \right) n = \frac{e}{m_i}\nabla \cdot (n\mathbf{E}) - \frac{\gamma_i k_B T_i}{m_i}\nabla^2 n \right] \tag{A.2}$$

To perform the subtraction (A.1)-(A.2), we explicitly write out the vector components:

$$\begin{aligned} \frac{\partial}{\partial t}n &= \frac{\nu_e}{B\Omega_e}\left(\frac{\partial}{\partial x}nE_x + \frac{\partial}{\partial y}nE_y \right) + \frac{\Omega_e}{B\nu_e}\frac{\partial}{\partial z}nE_z \\ &+ \frac{\gamma_e k_B T_e \nu_e}{m_e \Omega_e^2}\left(\frac{\partial^2}{\partial x^2}n + \frac{\partial^2}{\partial y^2}n \right) + \frac{\gamma_e k_B T_e}{m_e \nu_e}\frac{\partial^2}{\partial z^2}n \\ &- \frac{1}{B}\left(\frac{\partial}{\partial x}(nE_y) - \frac{\partial}{\partial y}(nE_x) \right) \end{aligned} \tag{A.3}$$

$$\begin{aligned} -\frac{\nu_e}{\Omega_e \Omega_i}\left(\frac{\partial^2}{\partial t^2}n + \nu_i \frac{\partial}{\partial t}n \right) &= \frac{\nu_e}{B\Omega_e}\left(\frac{\partial}{\partial x}nE_x + \frac{\partial}{\partial y}nE_y \right) + \frac{\nu_e}{B\Omega_e}\frac{\partial}{\partial z}nE_z \\ &- \frac{\gamma_i k_B T_i \nu_e}{m_i \Omega_e \Omega_i}\left(\frac{\partial^2}{\partial x^2}n + \frac{\partial^2}{\partial y^2}n \right) - \frac{\gamma_i k_B T_i \nu_e}{m_i \Omega_e \Omega_i}\frac{\partial^2}{\partial z^2}n \end{aligned} \tag{A.4}$$

Subtracting equation A.4 from A.3 yields

$$\frac{\partial}{\partial t}n + \frac{\psi}{\nu_i}\left(\frac{\partial^2}{\partial t^2}n + \nu_i \frac{\partial}{\partial t}n \right) = \left(\frac{\Omega_e}{B\nu_e} - \frac{\nu_e}{B\Omega_e} \right)\frac{\partial}{\partial z}(nE_z) + \nabla_\perp^2 n \left(\frac{\gamma_e k_B T_e \nu_e}{m_e \Omega_e^2} + \frac{\gamma_i k_B T_i \nu_e}{m_i \Omega_e \Omega_i} \right)$$

$$+ \left(\frac{\partial^2}{\partial z^2} n\right)\left(\frac{\gamma_e k_B T_e}{m_e \nu_e} + \frac{\gamma_i k_B T_i \nu_e}{m_i \Omega_e \Omega_i}\right) - \frac{1}{B}\left(\frac{\partial}{\partial x} n E_y - \frac{\partial}{\partial y} n E_x\right) \tag{A.5}$$

We recognize the ion acoustic speed in the $\nabla_\perp^2 n$ term:

$$\begin{aligned} \frac{\gamma_e k_B T_e \nu_e}{m_e \Omega_e^2} + \frac{\gamma_i k_B T_i \nu_e}{m_i \Omega_e \Omega_i} &= \frac{\psi}{\nu_i}\left(\frac{\gamma_i k_B T_i}{m_i} + \left(\frac{\Omega_i}{\Omega_e}\right)\frac{\gamma_e k_B T_e}{m_e}\right) \\ &= \frac{\psi}{\nu_i}\left(\frac{\gamma_i k_B T_i + \gamma_e k_B T_e}{m_i}\right) \\ &= \frac{\psi}{\nu_i} c_s^2 \end{aligned} \tag{A.6}$$

We can simplify the $(\partial^2/\partial z^2)n$ term:

$$\begin{aligned} \frac{\gamma_e k_B T_e}{m_e \nu_e} + \frac{\gamma_i k_B T_i \nu_e}{m_i \Omega_e \Omega_i} &= \left(\frac{1}{m_e \nu_e}\right)\gamma_e k_B T_e + \left(\frac{\nu_e}{m_i \Omega_e \Omega_i}\right)\gamma_i k_B T_i \\ &\approx \left(\frac{1}{\nu_e}\right)\frac{\gamma_e k_B T_e}{m_e} = \left(\frac{1}{\nu_e}\right) v_{\mathrm{Th,e}} \end{aligned} \tag{A.7}$$

as well as the $(\partial/\partial z) n E_z$ term:

$$\frac{\Omega_e}{B\nu_e} - \frac{\nu_e}{B\Omega_e} \approx \frac{\Omega_e}{B\nu_e} \tag{A.8}$$

The resulting equation is:

$$\begin{aligned} 0 &= \frac{\psi}{\nu_i}\left(\frac{\partial^2}{\partial t^2} - c_s^2 \nabla_\perp^2\right) n + (1+\psi)\frac{\partial}{\partial t} n - \frac{v_{\mathrm{Th,e}}}{\nu_e}\frac{\partial^2}{\partial z^2} n \\ &\quad + \frac{\partial}{\partial x}\frac{1}{B} n E_y - \frac{\partial}{\partial y}\frac{1}{B} n E_x - \frac{\partial}{\partial z}\frac{\Omega_e}{B\nu_e} n E_z \end{aligned} \tag{A.9}$$

$$0 = \frac{\psi}{\nu_i}\left(\frac{\partial^2}{\partial t^2} - c_s^2 \nabla_\perp^2\right) n + (1+\psi)\frac{\partial}{\partial t} n - \frac{v_{\mathrm{Th,e}}}{\nu_e}\frac{\partial^2}{\partial z^2} n + \nabla \cdot (n \mathbf{S} \mathbf{E}) \tag{A.10}$$

where

$$\mathsf{S} \equiv \begin{pmatrix} 0 & 1/B & 0 \\ -1/B & 0 & 0 \\ 0 & 0 & -\Omega_e/(B\nu_e) \end{pmatrix} \tag{A.11}$$

Next, we use the perturbation expansions $n \rightarrow n_0 + n_1$ and $\mathbf{E} \rightarrow \mathbf{E_0} + \mathbf{E_1} = E_0\hat{y} + \mathbf{E_1}$ to linearize the $\nabla \cdot (n\mathbf{SE})$ term:

$$\begin{aligned}
\nabla \cdot (n\mathbf{SE}) &= \nabla \cdot (n_0 + n_1)\mathsf{S}(\mathbf{E_0} + \mathbf{E_1}) && \text{(A.12)}\\
&= \nabla \cdot (n_0 + n_1)\left(\frac{E_0}{B}\hat{x} + \frac{E_{1y}}{B}\hat{x} - \frac{E_{1x}}{B}\hat{y} - \frac{\Omega_e E_{1z}}{B\nu_e}\hat{z}\right) && \text{(A.13)}\\
&= n_0\nabla \cdot (\mathbf{SE_1}) + \nabla \cdot n_1\frac{E_0}{B}\hat{x} + \underbrace{\nabla \cdot (n_1\mathbf{SE_1})}_{2^{\text{nd}}\text{ order}} && \text{(A.14)}\\
&= \frac{n_0}{B}\left(\frac{\partial}{\partial x}E_{1y} - \frac{\partial}{\partial y}E_{1x} - \frac{\Omega_e}{\nu_e}\frac{\partial}{\partial z}E_{1z}\right) + \frac{E_0}{B}\frac{\partial}{\partial x}n_1 && \text{(A.15)}\\
&= \frac{n_0}{B}\left((\nabla \times \mathbf{E_1}) \cdot \hat{z}\right) - n_0\frac{\Omega_e}{B\nu_e}\nabla \cdot (E_{1z}\hat{z}) + \nabla \cdot (n_1\mathbf{V_d}) && \text{(A.16)}\\
&= \frac{n_0}{B}\left((\nabla \times \mathbf{E_1}) \cdot \hat{z}\right) - n_0\nabla \cdot \mathbf{V}_{\|} + \mathbf{V_d} \cdot \nabla n_1 && \text{(A.17)}
\end{aligned}$$

The last term follows if we define $\mathbf{V}_{\|} = \Omega_e E_{1z}\hat{z}/(B\nu_e)$ and $\mathbf{V_d} = (\mathbf{E_0} \times \mathbf{B})/B^2$, with $\mathbf{E_0} = E_0\hat{y}$ and $\mathbf{B} = B\hat{z}$.

The final result (also given in equation 4.26) is

$$\begin{aligned}
\frac{\psi}{\nu_i}\left(\frac{\partial^2}{\partial t^2} - c_s^2\nabla_\perp^2\right)n_1 \;&+\; (1+\psi)\frac{\partial}{\partial t}n_1 - \frac{v_{\text{Th,e}}^2}{\nu_e}\frac{\partial^2}{\partial z^2}n_1\\
&+\; \frac{n_0}{B}\left(\nabla \times \mathbf{E_1}\right) \cdot \hat{z} - n_0\nabla \cdot \mathbf{V}_{\|} + \mathbf{V_d} \cdot \nabla n_1 = 0 \quad \text{(A.18)}
\end{aligned}$$

A.2 Derivatives of 3-D Gaussian Envelope Wave Packet

Here we present the details behind the Einstein notation derivatives (equations 5.45 and 5.46) given on page 90.

Since $\mathbf{r}$ is a vector containing the independent variables t, x, y, and z, we determine the derivatives of the 3-D Gaussian envelope wave packet (equation 5.44: $w(\mathbf{r}) = \exp(jk_n r_n)\exp(-2\mathsf{A}_{nm}r_n r_m)$) with respect to some r_l, which will work in the general case.

First we tackle the most complicated term (involving the matrix A) by itself:

$$\begin{aligned}
&\frac{\partial}{\partial r_l}\left(e^{-2\mathsf{A}_{nm}r_n r_m}\right) \\
&= \frac{\partial}{\partial r_l}\left(e^{-2\sum_n\sum_m \mathsf{A}_{nm}r_n r_m}\right) && \text{(A.19)}\\
&= \frac{\partial}{\partial r_l}\left(\prod_n\prod_m e^{-2\mathsf{A}_{nm}r_n r_m}\right) && \text{(A.20)}\\
&= \frac{\partial}{\partial r_l}\left(e^{-2\mathsf{A}_{lm}r_l r_m}\times e^{-2\mathsf{A}_{nl}r_n r_l}\times\prod_{n\neq l}\prod_{m\neq l} e^{-2\mathsf{A}_{nm}r_n r_m}\right) && \text{(A.21)}\\
&= \left(\prod_{n\neq l}\prod_{m\neq l} e^{-2\mathsf{A}_{nm}r_n r_m}\right)\times \\
&\qquad \left(e^{-2\mathsf{A}_{lm}r_l r_m}\times e^{-2\mathsf{A}_{nl}r_n r_l}\right)(-2\mathsf{A}_{nl}r_n - 2\mathsf{A}_{lm}r_m) && \text{(A.22)}\\
&= \left(\prod_n\prod_m e^{-2\mathsf{A}_{nm}r_n r_m}\right)(-4\mathsf{A}_{lm}r_m) && \text{(A.23)}\\
&= \left(e^{-2\mathsf{A}_{nm}r_n r_m}\right)(-4\mathsf{A}_{lm}r_m) && \text{(A.24)}
\end{aligned}$$

The step from equation A.22 to equation A.23 is valid as long as A is symmetric, and it is, since the inverse "covariance" matrix (the wave packet shaping matrix), Σ^{-1}, is symmetric.

Now we take the general derivative of the entire wave packet. The chain rule applies:

$$\begin{aligned}
\frac{\partial}{\partial r_l}w(\mathbf{r}) &= \frac{\partial}{\partial r_l}\left(e^{jk_n r_n}e^{-2\mathsf{A}_{nm}r_n r_m}\right) && \text{(A.25)}\\
&= w(\mathbf{r})\,(jk_l - 4\mathsf{A}_{lm}r_m) && \text{(A.26)}
\end{aligned}$$

We also compute the second derivative, again with respect to some general independent variable r_p:

$$\begin{aligned}
\frac{\partial^2}{\partial r_l \partial r_p}w(\mathbf{r}) &= w(\mathbf{r})\,(jk_l - 4\mathsf{A}_{lm}r_m)\,(jk_p - 4\mathsf{A}_{pq}r_q) + w(\mathbf{r})\,(-4A_{lp}) && \text{(A.27)}\\
&= w(\mathbf{r})\,[(jk_l - 4\mathsf{A}_{lm}r_m)(jk_p - 4\mathsf{A}_{pq}r_q) - 4\mathsf{A}_{lp}] && \text{(A.28)}
\end{aligned}$$

This brings us to the results given in equations 5.45 and 5.46.

VITA

Melissa Meyer grew up in southern middle Tennessee, graduating from Tullahoma High School in 1997. She attended the University of Tennessee at Knoxville and earned a Bachelor of Science in Electrical Engineering in 2001. She subsequently joined the Electrical Engineering program at the University of Washington in Seattle, and pursued studies leading to the Ph.D. in 2006. She will join the ECE faculty at Michigan Technological University in Autumn 2006.